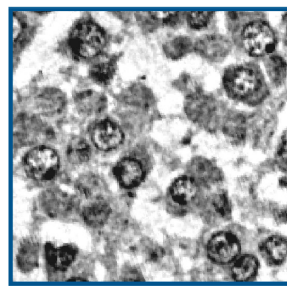
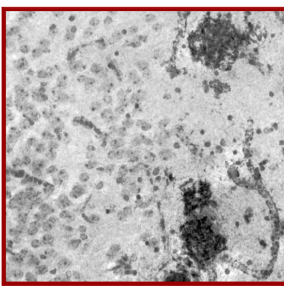
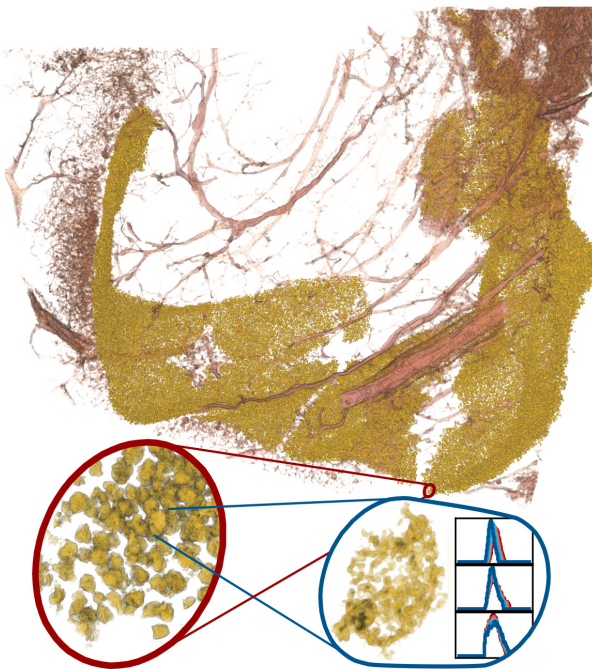
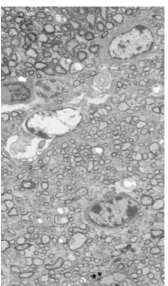
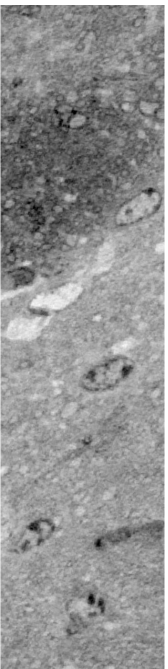
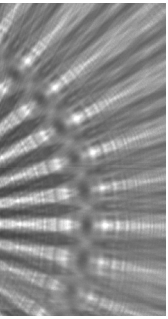




Göttingen Series in
X-ray Physics

Marina Eckermann

Advancing the Characterization of
Neuronal Cyto-Architecture by
X-ray Phase-Contrast Tomography



Universitätsverlag Göttingen

Marina Eckermann
Advancing the Characterization of Neuronal Cyto-Architecture by X-ray
Phase-Contrast Tomography

This work is licensed under a [Creative Commons
Attribution-ShareAlike 4.0 International License](https://creativecommons.org/licenses/by-sa/4.0/).



Published in 2021 by Universitätsverlag Göttingen
as volume 27 in the series “Göttingen series in X-ray physics”

Marina Eckermann

Advancing the
Characterization of
Neuronal Cyto-Architecture
by X-ray Phase-Contrast
Tomography

Göttingen series in X-ray physics
Volume 27



Universitätsverlag Göttingen
2021

Bibliographische Information der Deutschen Nationalbibliothek

The Deutsche Nationalbibliothek lists this publication in the Deutsche Nationalbibliografie; detailed bibliographic data are available on the Internet at <http://dnb.dnb.de>.

Funded by the German Research Foundation (DFG) under the Sonderforschungsbereich 755 “Nanoscale Photonic Imaging”,
Cluster of Excellence - EXC 2067/1- 390729940 “Multiscale Bioimaging”,
and the Sonderforschungsbereich 1456 “Mathematics of Experiment”.

Address of the author

Marina Eckermann

Email: marina.eckermann@phys.uni-goettingen.de

Dissertation

for the award of the degree “Doctor rerum naturalium”
of Georg-August-Universität Göttingen
within the doctoral program
“Physics of Biological and Complex Systems”
of the Georg-August University School of Science (GAUSS)

Thesis Advisory Committee

Prof. Dr. Tim Salditt, Institute for X-Ray Physics, Georg-August University,
Göttingen

Prof. Dr. Christine Stadelmann-Nessler, Institute for Neuropathology, University
Medical Center, Göttingen

Prof. Dr. Sarah Köster, Institute for X-Ray Physics, Georg-August University,
Göttingen

Date of the oral examination: 01.10.2021

This work is protected by German Intellectual Property Right Law.

It is also available as an Open Access version through the publisher’s homepage and the Göttingen University Catalogue (GUK) at the Göttingen State and University Library (<http://www.sub.uni-goettingen.de>).

The license terms of the online version apply.

Setting and layout: Marina Eckermann

Cover image: Marina Eckermann

© 2021 Universitätsverlag Göttingen

<https://univerlag.uni-goettingen.de>

ISBN: 978-3-86395-528-1

DOI: <https://doi.org/10.17875/gup2021-1830>

ISSN: 2191-9860

eISSN: 2512-6326

Preface of the series editors

The Göttingen series in x-ray physics is intended as a collection of research monographs in x-ray science, carried out at the Institute for X-ray Physics at the Georg-August-Universität in Göttingen, and in the framework of its related research networks and collaborations.

It covers topics ranging from x-ray microscopy, nano-focusing, wave propagation, image reconstruction, tomography, short x-ray pulses to applications of nanoscale x-ray imaging and biomolecular structure analysis.

In most but not all cases, the contributions are based on Ph.D. dissertations. The individual monographs should be enhanced by putting them in the context of related work, often based on a common long term research strategy, and funded by the same research networks. We hope that the series will also help to enhance the visibility of the research carried out here and help others in the field to advance similar projects.

Prof. Dr. Tim Salditt
Prof. Dr. Sarah Köster
Editors
Göttingen June 2014

Preface to the present volume

The three-dimensional cyto-architecture of the human brain and its inter-subject variation is still not sufficiently well known. A more quantitative micro-anatomy is required for the understanding of physiological functions and pathological mechanisms alike. Mapping the brain, however, requires further development in imaging methods, to visualize and quantify the architectonics of specific brain regions, and to compare data between individuals.

The present thesis contributes significantly towards this goal by boosting the performance of phase contrast X-ray tomography with regard to image quality, throughput and image processing. To this end, different instrumentation, sample preparation and imaging configurations are compared and optimized. Capitalizing on this progress, the author has been able to segment structural features of ten thousands of neurons by machine learning and has analyzed structural changes between individuals of a larger cohort, using tools of optimal transport theory.

In this way, she can show that nuclei of granular neurons in the hippocampus become more compact and heterogeneous in Alzheimer's disease. This study presents an ideal blueprint for subsequent work, showing scalability in data acquisition and exploitation!

Prof. Dr. Tim Salditt
Göttingen, December 2021

Contents

1	Introduction	1
1.1	The Healthy Brain	4
1.1.1	Selected Regions in the Human Brain	4
1.1.2	Neuronal and Glial Cells in the CNS	7
1.1.3	Open Questions and Challenges	9
1.2	The Pathological Brain	10
1.2.1	Alzheimer’s Disease	10
1.2.2	Multiple Sclerosis	12
1.2.3	Open Questions and Challenges	14
1.3	X-ray Interaction with Matter	15
1.3.1	The Complex Index of Refraction	17
1.3.2	Tuning the Interaction	18
1.3.3	Open Questions and Challenges	20
1.4	Phase-sensitive Imaging	21
1.4.1	Hologram Formation	21
1.4.2	A Note on Coherence	22
1.4.3	Wavefront Reconstruction I: Holographic Regime	23
1.4.4	Wavefront Reconstruction II: Edge-enhancement Regime	25
1.4.5	Open Questions and Challenges	27
1.5	Computed Tomography	28
1.5.1	Foundations	28
1.5.2	Tomographic Reconstruction	30
1.5.3	Sampling Criteria	32
1.5.4	Tomographic Artifacts	33
1.5.5	Image Quality Metrics	35
1.5.6	Open Questions and Challenges	36
1.6	Data Analysis by Means of Optimal Transport	37
1.6.1	Foundations	37
1.6.2	Embedding of OT in a Practical Analysis Workflow	39

2	Phase-contrast X-ray Tomography of Neuronal Tissue at Laboratory Sources with Submicron Resolution	63
2.1	Introduction	64
2.2	Methods	66
2.3	Results	70
2.4	Summary and Outlook	79
3	Three-dimensional Virtual Histology of the Cerebral Cortex based on Phase-Contrast X-ray Tomography	89
3.1	Introduction	89
3.2	Results	96
3.3	Discussion	105
3.4	Supplemental Document	109
4	Three-dimensional Virtual Histology of the Human Hippocampus based on Phase-Contrast Computed-Tomography	127
4.1	Introduction	128
4.2	Results I: Multiscale Tomography of the Hippocampus	132
4.3	Results II: Geometric and Statistical Analysis	138
4.4	Discussion	147
4.5	Materials and Methods	150
4.6	SI Appendix	153
5	Towards Correlative Imaging of Neuronal Tissue by Phase-Contrast X-ray Tomography and SEM	187
5.1	Introduction	188
5.2	Methods	190
5.3	Results	193
5.4	Discussion and Outlook	196
6	Conclusion and Outlook	203
A	Appendix	211
A.1	Towards X-ray Fluorescence Tomography	211
A.2	Further Details on Working with the Nanofocus PC-CT Setup TiNa	225
A.3	Measurements and Analysis of the X-ray Spectrum	241
	Author Contributions	255

List of Publications	257
Danksagung	261
Curriculum Vitae	263

Introduction

1

In Plato’s “Allegory of the Cave” [51], people imprisoned in a cave are restricted to view only the cave wall straight ahead, where they see diffuse objects, and hear the sounds thereof. Eventually, one of these prisoners gets free, gazes into other directions in the cave, notices the source of light, and can even step outside the cave and see the sun. The former prisoner realizes that the diffuse objects were no actual matter, but the shadows of matter, and the sounds were echos, reflected by the cave wall.

Towards the ultimate goal of fully deciphering the *brain*, it is indispensable to look at it from different perspectives, and also to incorporate different ways of collecting information - since “it is the multiscale structure of complex systems that is responsible for their major functional properties” [10]. “Multiscale” neuronal mechanisms are found in different domains, which can be grouped into three as proposed in [13]: (i) the *spatial domain* which refers to the level of detail (including molecules, synapses,

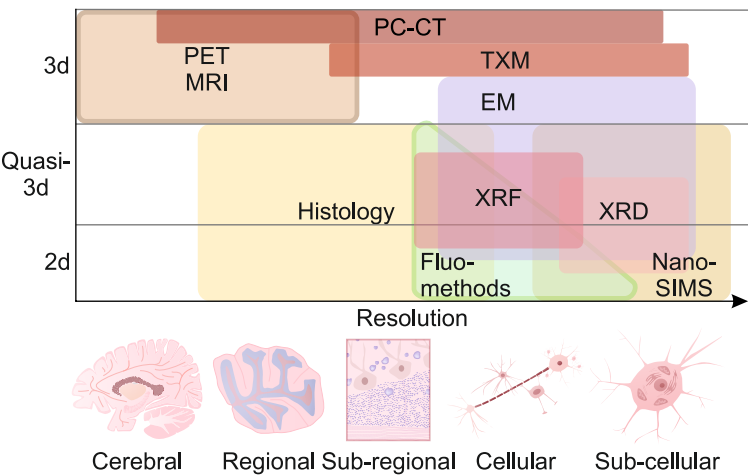


Fig. 1.1: Illustration of selected imaging methods used in neuroscience. The horizontal axis gives the spatial scale, and the vertical axis whether a tool is applied for planar or volumetric investigations. “Quasi-3d” indicates the extension from 2d to 3d by serial probing. A frame, if present, implies that a method is also applied to image the live state.

cells, regional segregations and beyond), (ii) the *temporal domain* which describes neuronal network dynamics at sub-seconds, over years and across species, and (iii) the *topological domain* which distinguishes the regionality of a network. It is essential to ultimately combine these three domains at different scales, in order to bring function into an anatomical context [47]. To this end, brain maps and models such as “BigBrain” [4] rely on the combination of data from a wealth of experimental modalities. Fig. 1.1 depicts the overlapping and complementary nature of such methods which are exemplified in the following.

The importance of the spatial domain (i) is demonstrated by the numerous top-down or level-up mechanisms in neuronal tissues. For instance, neurons are embedded in a network of glial cells which secrete molecules into the extracellular space. The composition of this extracellular milieu differs among cell layers and is detected by axonal growth cones, and thereby directs axons during neurogenesis [20, 131]. In neurogenesis, also the synaptic level is relevant: Synaptic connectivity follows high target specificity and is mediated by cell-surface proteins, which can be studied by joint *immunohistochemistry* and *genetic analysis* [165, 200]. The fact that aged synaptic vesicles are eventually removed from the release pool and degraded, raises questions on the link between synaptic activity and synaptic vesicle trafficking. These also involve the temporal domain (ii), and can be approached by *computational modeling* and subsequent multimodal experiments, such as correlative *NanoSIMS* (nanoscale secondary ion mass spectrometry) and *FM* (fluorescence microscopy) [94]. The synaptic vesicle supply in relation with activity is of particular importance for long-lived neurons, since they can not undergo cell division in most cases. In fact, neurodegeneration is of particular relevance in adult tissues and subcellular mechanisms can provide insight into the death of entire cell populations. For instance, pathological protein aggregates can be characterized by *cryo-EM* (electron microscopy) and *mass spectrometry* [5]. While neurodegeneration may occur across the brain, adult neurogenesis is restricted to few brain regions such as the olfactory bulb and the hippocampus [61]. In these regions, the integration (iii) of newly generated neurons can be of particular interest and studied by FIB-SEM (focused ion-beam scanning-EM) at the level of dendrites and synapses, at different time points (ii) [17]. Beside the apparent dynamics in the temporal domain (ii), information is processed among topological scales (iii), *i.e.* within confined regions, throughout the brain and beyond. The activity of single neurons within such long-ranging circuits can be studied to unravel their synaptic plasticity, using a variant of *FM* [91] based on optogenetics [137]. On the much coarser mm-spatial scale, also *PET* (positron-emission tomography [57]) and *MRI* (magnetic-resonance

imaging [199]) comprise different temporal and topological scales (ii,iii) in three dimensions (3d). PET, MRI, EM [17, 162] and histology or immunohistochemistry [4, 47] all cover a range of spatial and topological scales and hence provide anatomical landmarks for multimodal brain maps. The portfolio of experimental methods in neuroscience is supplemented by X-ray based methodologies. X-ray probing yields benefits as non-destructive (3d) testing at a comparatively high resolution. Subcellular details can be imaged by *TXM* (transmission X-ray microscopy), localized elemental quantification by *XRF* (X-ray fluorescence), and structure analyzed using *XRD* (X-ray diffraction) [32, 96]. Furthermore, *PC-CT* (phase-contrast computed-tomography) can cover the temporal domain (ii), but has more importantly been proven to enable 3d virtual histology at very different scales in the spatial and topological domains (i,iii) [35, 83, 105, 142, 145, 189, 202]. Recently, the gap between the different domains was narrowed by the correlation of functional *in vivo* FM-data of murine neuronal tissue with its anatomical maps from EM and PC-CT [16].

In this work, *propagation-based PC-CT*¹ is used to image neuronal tissues in three dimensions. PC-CT is non-destructive, can achieve isotropic resolution in the tens of nm, and can cover large (mm-range) fields-of-view, while being highly flexible in sample preparation. As demonstrated in Ch. 3, 4 and 5, *multiscale* PC-CT can be implemented in such a way that entire human brain regions and sub-cellular details are imaged with a single setup. In Ch. 4, this is utilized to study tissue samples from ≥ 20 *individuals* in 3d, taking advantage of the considerable volume throughput in imaging and in automatized *machine-learning based segmentation*. The image contrast reflects the local electron density, such that subcellular structures as chromatin can be studied and contextualized within neurodegenerative mechanisms by *optimal-transport analysis* (Ch. 4). Furthermore, dendritic connections can be *tracked through neuronal layers* (Ch. 3). PC-CT is also used in a correlative manner with SEM (Ch. 5) and XRF tomography (Sec. A.1). Such experiments can be implemented at accelerator-based or table-top X-ray sources, at sub- μm resolution (Ch. 2).

PC-CT of neuronal tissues is a highly interdisciplinary field, and the following sections are equally diverse: Sec. 1.1 and 1.2 give an introduction into neuroscience and a basis for the understanding of brain structure. Since PC-CT is an emerging technique, adequate sample preparation is raised in Sec. 1.3. Further, in PC-CT, the optimization of phase-retrieval and tomography are crucial, which are briefly described in Sec. 1.4 and 1.5, respectively. The foundations and a practical workflow for advanced feature analysis with optimal transport theory are addressed in Sec. 1.6. In each part, a variety

¹In the following, “PC-CT” will refer to propagation-based phase-contrast computed-tomography.

of aspects has to be reviewed, understood, and optimized in order to extend the operating range of PC-CT, such that it can substantially contribute to the understanding of the brain.

1.1 The Healthy Brain

The central nervous system (CNS) can be defined as that part of the nervous system, which lacks lymphatic structures and is isolated from potential internal perturbations by the blood-brain-barrier, while it is protected from external aggressions by bony structures [20]. Accordingly, the CNS comprises the brain and the spinal cord. Information is processed in a complex and rapidly interacting network with a hierarchically organization of specialized regions, spanning entire regions (tens of cm) down to individual differentiations of neural precursor cells (tens of μm) [172]. In this context, first the brain regions relevant for this work are introduced, followed by a description of the cellular components of the CNS.

1.1.1 Selected Regions in the Human Brain

In this work, the *cerebellum*, the *hippocampal formation*, and the *cerebral cortex* are of particular relevance, and depicted in Fig. 1.2.

Cerebellum The cerebellum is located in the *posterior cranial fossa* and is connected to the brainstem through three cerebellar peduncles, and separated from the cerebrum by the tentorium. It is responsible for the coordination of motion and can be associated with related disorders, such as ataxia or hypotonia [167].

The *gray matter* (GM) of the cerebellum, the *cerebellar cortex*, has a characteristic three-layer structure: the *molecular layer* (ML), which comprises stellate and basket cells; the *Purkinje-cell layer* (PCL) with massive cell soma; and the *granular layer* (GL), which shows Golgi cells and, most importantly, granule cells [167]. The neurons have a spatial orientation which is in agreement with their purpose in signal processing, and show afferent and efferent fibers throughout the layers. The GL is further bounded by the *white matter* (WM), where fibers are pooled, and only a small number of neuronal somata are present. ML, GL and WM can be identified in the histological section in Fig. 1.2(c).

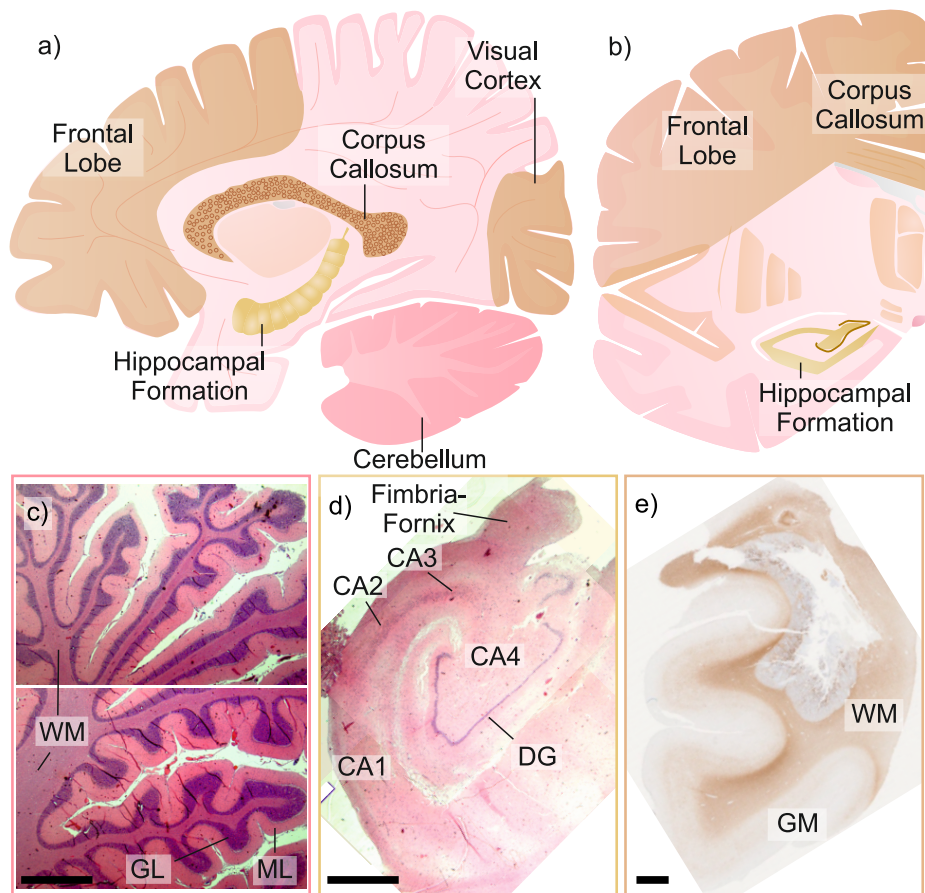


Fig. 1.2: Spatial categorization of the brain regions studied in this work. (a & b) Sketch of the human brain in sagittal and of one hemisphere in frontal plane, respectively. Regions are color labelled: (light pink) cerebellum, (golden) hippocampal formation, (brown) parts of the cerebral cortex which are of relevance for this thesis work, namely the frontal lobe, the corpus callosum and the visual cortex. (c-e) Histological slices of these regions, with labels on the significant neural structures: (c) cerebellum (stain: HE), (d) hippocampal formation (stain: HE), (e) cerebral cortex (stain: NABC1). Feature labels can be found in the respective paragraphs in Sec. 1.1.1. Scale bars: 2 mm.

Hippocampal Formation The hippocampal formation is part of the limbic system, embedded in the left and right temporal lobe of the cerebral cortex. It serves declarative long-term memory, emotions and vegetative functions, and is one of the regions first affected in Alzheimer's disease [167]. The hippocampal formation has an elongated shape and it is 4-5.2 cm in length in its anterior-posterior axis [119]. In lateral view in Fig. 1.2(d), the distinct layers of the hippocampal formation can be recognized: the *fimbria-fornix* serves as landmark to identify the adjacent *dentate gyrus* (DG), which is composed of granular neurons (10-18 μm diameter cell soma [36]). A further hippocampal layer is the *cornu ammonis* (CA), which is a band of pyramidal cells and can be divided into four subregions, CA1 through CA4. The DG forms a clamp around the CA4. The CA region runs from CA4 to CA1 into the *subicular cortex*. Both in the CA and the subicular cortex, neurons have a pyramidal shape of 25-35 μm in diameter [3]. For information processing, these strata are interconnected, for the most part in a unidirectional manner [3].

Cerebral Cortex The cerebral cortex represents 40% of the human brain by weight [177] and comprises a number of different subregions. It is responsible for human-specific competences, which include language, somatosensory and structural detection tasks and conceptual thinking [177]. Matching these evolutionary achievements, the major part of the cerebral cortex is referred to as *neocortex*, a six-layered structure which is sketched in Fig. 1.3. Projection neurons represent 80% of all neurons [76], and are primarily found in cortical layers for short- and long-range signaling [172]. Fig. 1.2(e) shows a histology image of cortical tissue.

The *frontal cortex* is located in the anteriority of the cerebral brain (cf. Fig. 1.2(a & b), "Frontal Lobe"), whose neocortical neurons are afferent in layer I-IV for signals from monoamine neurons, thalamus and other cortical parts, and efferent in layer V-VI to conduct towards the spinal cord, thalamus, cranial nerve motor nuclei, neostriatum or in III to other cortical regions [167]. Fig. 1.2 comprises two further cortical regions: In the posterior pole, the *visual cortex* is responsible for tasks such as the combination of images from both eyes and its analysis [167]. The two contralateral hemispheres of the human brain are connected by the *corpus callosum* (CC), which is the major white matter tract [172].

With a significant proportion of myelinated fibers, the cerebral cortex is affected in Multiple Sclerosis, which is an inflammatory disease accompanied with demyelination [173]. Further, in view of its massive and complex neuronal structure, the cerebral cortex also shows signs of pathology in Alzheimer's and Huntington's disease [167].

1.1.2 Neuronal and Glial Cells in the CNS

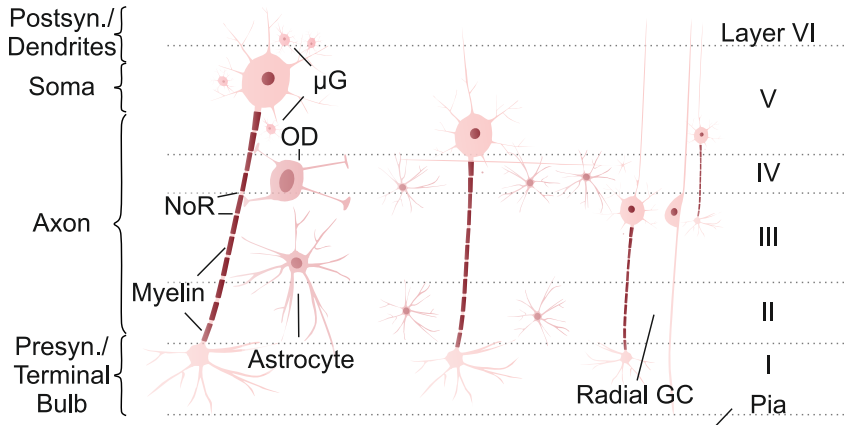


Fig. 1.3: Brain tissue cells, arranged in layers as in the cerebral cortex: Depending on their target brain region, neurons extend from layer I over multiple layers (labels on the right), embedded in a network of glial cells. During neurogenesis, radial glial cells (GC) guide the neuronal projections from the pia, which is a layer of membranes surrounding nervous tissue, and oligodendrocytes (OD), astrocytes and microglia (μ G) serve maintenance until cellular maturity is reached. Labels on the left indicate the components of the leftmost neuron.

Two main groups of cells reside in the brain tissue: *neuronal* and *glial cells*, as depicted in Fig. 1.3 with the indication of cortical layers I-VI [131].

Neuronal cells serve the storage and transmission of information by membrane protein synthesis, generation of action potentials (APs) and release of neurotransmitters [131]. In addition to neurons, 50% of the cells in the human brain are glia (lat. *nerve glue*, Rudolph Virchow) [6], also referred to as *satellite cells*, which tightly enclose each single neuron to within 20 nm [131]. They hence organize neuronal connections, and do not generate APs but rather have a modulating role: they interact with neurons by segregation into the extracellular matrix, which is referred to as *cerebrospinal fluid* [20, 100, 131]. Thereby, in principal all glial cells can modulate axonal growth, for instance. Glial cells can be grouped into *oligodendrocytes*, *astrocytes*, *microglia* and *ependymal cells* [20]. Glia-glia communication occurs directly via low-resistance gap junctions. Importantly, glial cells are not postmitotic after differentiation, *i.e.* they are still capable of cell division [20].

Neuronal Cells

Neurons have been described as the computational units of the brain [118]. They are very diverse in shape and function, for instance they secrete different neurotransmitters [20]. Still, all neurons present the same kind of basic subcellular components, such as soma and (ramified) dendrites, which are both unmyelinated, and an axon (cf. Fig. 1.3 left). Axons can be *excitatory*, *inhibitory* or *modulatory*, and transport nutrients along their microtubules [20]. Excitatory neuron-neuron communication happens at well-defined synaptic junctions, from the axon of the efferent to the dendrite of the afferent neuron, and is inhibitory in axo-somatic or axo-axonic connections. *Presynaptically*, synaptic vesicles carry neurotransmitters, which are released at synaptic junctions and activate highly specific receptors *postsynaptically*.

Apart from the contribution of ionotropic receptors at synaptic sites, the composition of the ionic milieu in neurons is regulated by ionic channels [20]. These are evenly distributed along the neuron, except for the axon: the axon is surrounded by a continuously renewed sheath of central myelin [87], which has an isolating effect due to its impermeability to ions. In turn, Na^{2+} channels accumulate along the axon at the nodes of Ranvier (NoR), which are regular myelin interceptions [131]. The action potentials propagate in a so-called “saltatory manner” and electrical conduction properties of the axons are enhanced. Note that in general, neurons in the CNS become postmitotic after differentiation.

Glial Cells

Oligodendrocytes Oligodendrocytes (OD) serve the myelination of axons [20]. Also, they provide metabolic supply. ODs have a diverse appearance, however, they are all characterized by a rather round cell soma of 10-20 μm in diameter and an oval nucleus [20]. Further, ODs show slow proliferation, which might be an important aspect in the context of neurodegeneration.

Astrocytes Astrocytes serve the physical structure of the brain, and together with ODs, also contribute to the metabolic supply of synapses [20]. They show a high variability in morphology, ranging from fibrous to protoplasmic soma. Astrocytes form connections with capillaries and neurons, in close proximity to synapses and neuronal cell bodies, where they regulate the concentration of neurotransmitters.

Radial Glial Cells Radial glial cells (Radial GC) take an essential role during the maturation of the mammalian CNS [131], in particular in the cerebrum and the cerebellum. Notably elongated, these cells guide the neurons throughout the tissue, perpendicularly to the neuronal layers under development, as indicated in Fig. 1.3.

Microglial Cells Microglia (μ G) differ from other glia in structure and origin, playing a phagocytic role as they target debris such as misfolded proteins. They derive from still controversial precursors from the yolk sac [112], and can differentiate into macrophages upon activation. In the healthy, mature CNS, μ G are found in a resting state and become activated and adopt a phagocytic phenotype during disease [20].

Ependymal Cells Ependymal cells are located at the ventricular surfaces, and show a distinct morphology with apical cilia and microvilli [20, 131].

1.1.3 Open Questions and Challenges

The study of the human brain is accompanied by intrinsic limitations compared to small animals, regarding fundamentally ethical aspects which compromise *in vivo* experiments or tissue preservation protocols (delayed and prolonged chemical fixation, inapplicability of perfusion). In addition, further factors such as the availability of laboratory models, differences in overall size, physiochemical characteristics and cellular densities present challenges in the context of brain pathology research [81]. For this reason, neuroscientific questions have often recourse to small-animal models with controversial translation to humans [110]: These questions may address the formation of neuronal networks, the identification of neuronal or glial cell types, and the role thereof in a temporal and spatial context. As such, cell types can be characterized by three attributes: (i) morphology, (ii) electrophysiology and (iii) gene expression [146, 203]. For instance, methods exist to identify single μ G and study them *in vivo* over time [95, 132]. In this way, the understanding of single cell types can be expanded, and further their role in progressive neurodegenerative disorders. Beyond the cellular level, scientific questions further span protein and synaptic scales, as well as long-range centimetric neural circuitry and tissue architecture. Further, the understanding of neurogenerative mechanisms is a crucial part, also in view of neurodegeneration. The importance of not only multiscale, but also multimodal approaches, is emphasized by the three steps of neuronal network development according to [161]: (i) axon guidance to target areas (transcriptomes), (ii) synaptic coupling within these target

areas (connectomes), and (iii) formation of functional synapses (transcriptomes and interactomes), where in brackets the respective methodology is given.

Methodological advancements, as pointed out in [131], continuously help to deepen the understanding and will raise questions which can not be imagined today.

1.2 The Pathological Brain

Beside healthy, human brain tissue affected by Alzheimer's Disease or Multiple Sclerosis is studied in this work, in view of better quantifying the respective pathologies on the cellular level.

1.2.1 Alzheimer's Disease

Alzheimer's Disease (AD) is a neurodegenerative disorder with a complex and multifactorial etiology [7]. Since neuropathological changes in the initial stages of the disease are not reflected by clinical symptoms, a clear, three-step (AT-N) biological definition based in novel biomarkers for *in vivo* diagnostics has been proposed recently [93]: (A) the presence of beta-amyloid ($A\beta$) plaques defines the Alzheimer's continuum, and if this is true, (T) the burden of tau tangles (τ) determines if AD is present, and finally, (N) the severeness of AD is staged through neurodegenerative indicators or cognitive syndroms. Note that this staging scheme is a suggestion, but not established in clinical routine diagnostics. For *ex vivo* neuropathological diagnostics [126], the (ABC) staging consists of assessing (A) the overall $A\beta$ burden according to Thal [183], (B) the presence of τ -tangles following Braak [19], and (C) the actual plaques among $A\beta$ as per CERAD [124].

Under pathological conditions, the amyloid precursor protein (APP) is cleaved by the β and γ secretases, releasing $A\beta$ -peptides of different lengths to the extracellular space through β -secretase [204]. $A\beta$ -peptide monomers eventually misfold and aggregate into oligomers, forming insoluble $A\beta$ -plaques, deposited *extracellularly* to neurons. In Fig. 1.4(a,c,d), the brown-colored structures are $A\beta$ -plaques. Note that in the virtual histology data in (c & d, right), no $A\beta$ -correlated increase in electron density can be found, which has also been reported in [188].

In axons, the microtubules are stabilized by regulated phosphorylation of the τ -protein [150]. Under pathological conditions, τ -hyperphosphorylation causes detachment from the microtubules and formation of insoluble aggregates *in neuronal cytosol*,

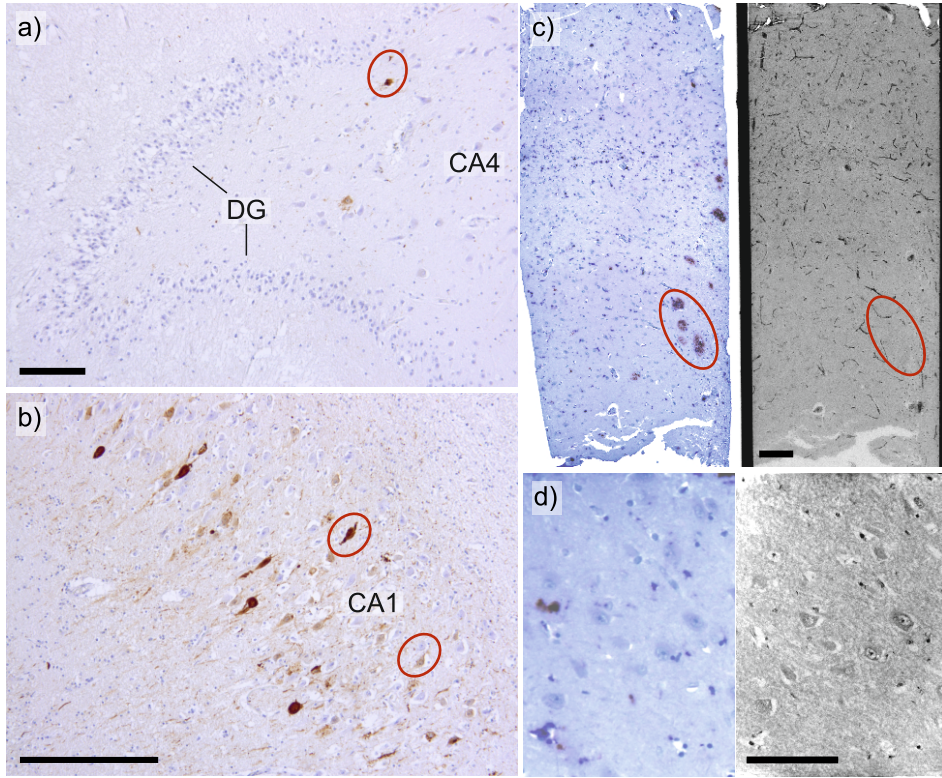


Fig. 1.4: Histology of hippocampal tissue affected by Alzheimer's disease: (a & b) In conventional histology, Tau (brown) & ki-m1p (blue) stain accentuates the (a) DG-cell band with parts of CA4, and (b) pyramidal neurons in CA1 which show a dominant τ -pathology. (c & d, left) Conventional histology of hippocampal tissue using $A\beta_4$ (brown) and ki-m1p (blue) stain, with (right) the correlative virtual histology (PC-CT of the unstained and paraffin-embedded tissue, (c) laboratory μ CT and (d) synchrotron nanoCT). Scale bars: 100 μ m.

referred to as τ -tangles. In Fig. 1.4(b), affected neurons emerge with brown color. Further, it has been proposed that τ -tangles can propagate across synaptic junctions, inducing misfolding of τ -protein downstream. As part of inflammation, glia are also involved [150]. Multiple factors may contribute to neurodegeneration: presumably, $A\beta$ -plaques occupy and terminate synaptic junctions, and further, the destabilization of microtubules induces deformation and lack of nutritional supply [150]. Generally, AD is considered as *$A\beta$ -induced tauopathy*.

Further, disease hypotheses involving chromatin have been posited [41, 58, 59, 63, 120]. In the cell nuclei, genetic information is encoded in deoxyribonucleic acid

(DNA) molecules. The complex of DNA and histones is referred to as chromatin. *Heterochromatin* indicates a tight association of DNA to the histones, while in *euchromatin*, DNA is loosely packed and genetic information is largely accessible [114]. Such chromatin-related hypotheses regarding AD-pathology may be considered as “granular pathology” and ascribed to similar basic concepts. τ -protein is linked to the protection of DNA by regulation of euchromatin gene expression, which in turn is reduced due to τ -hyperphosphorylation and oxidative stress [63, 72]. It has been reported that while 75% of the DNA is packed as euchromatin in controls, it is only 55% in AD brains [41]. Potential subsequent DNA-damage may result in slowed metabolism or may induce cell cycle re-entry, which leads to apoptosis for post-mitotic adult neurons (i.e. neurodegeneration) [63, 72]. This concept can be expanded to the theory of *laminopathy* [58]. In controls, the nuclear envelope is smooth, while mutations induce disruptions and invaginations in the nuclei of diseased neurons. Since the nuclear envelope acts as an anchor for heterochromatin, the nucleo-cytoskeleton organization is affected, resulting in perturbations of the nucleoskeleton and neuronal death [58, 120]. Beyond chromatin, subcellular organelles such as mitochondria are sought to be related with early stages of AD [84].

1.2.2 Multiple Sclerosis

Multiple Sclerosis (MS) is an inflammatory and neurodegenerative disease with autoimmune origin, which is pathologically characterized by chronic inflammatory demyelination, accompanied with axonal loss and glial scar formation [173]. Pathology emerges most prominently in the densely myelinated WM tracts, while its staging in GM is particularly challenging [173].

Inflammation induces astrocytic proliferation through upregulation of glial fibrillary acidic protein (GFAP) [168]. Increased abundance of astrocytes is associated with repair by uptake of excitotoxic substances and limitation of damage propagation by rigidification of tissue as well as revascularization. When this reaction is disproportionate to the initial trigger, it becomes pathological and is referred to as *astrogliosis* [173], defined as cellular hypertrophy and disruption of individual astrocytic domains, i.e. *glial scar* [156, 168]. Furthermore, astrocytic factors impede the differentiation of OD-progenitor cells [22]. Compromised myelination affects neuronal activity and survival. Damage to the myelin sheath followed by scar formation is also referred to as “MS-plaques”. Such regions with late MS plaques display some perivascular inflammatory infiltrates, newly formed myelin sheaths with reduced thickness and reduced

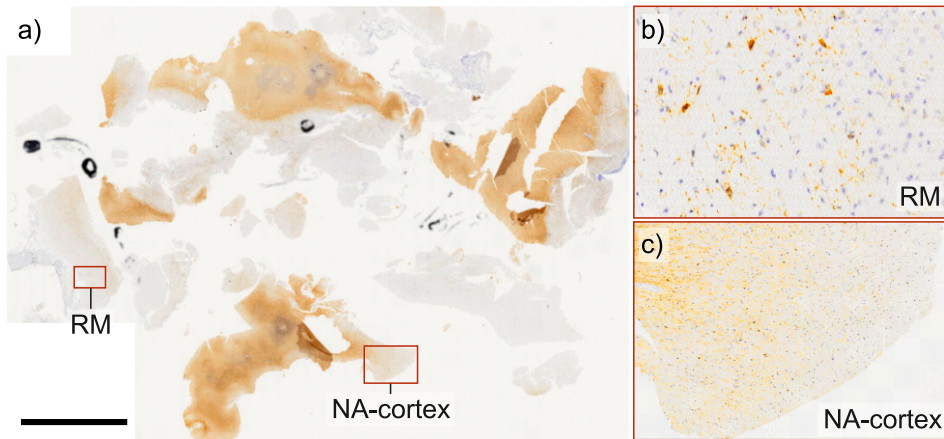


Fig. 1.5: Conventional histology of Multiple Sclerosis diseased cortical tissue stained with NABC1 antibody, biopsy collected during surgery: (a) in overview, where MS-relevant areas (RM, NA) are labelled, (b & c) with zoom-ins thereof. NABC1 serves the delineation of myelin, premyelinating and actively myelinating oligodendrocytes. Scale bar: 0.5 cm.

axonal density [143]. Furthermore, macrophages and products of myelin degradation are absent. Fig. 1.5(a,b) depicts histopathological images of such remyelinated regions (RM), characterized by MS-plaques which show a reduced myelin density [143]. Note that this is distinct from normally appearing (NA) tissue, which shows normal axon myelination in immunohistochemistry, *i.e.* no plaques in a radius of ≥ 10 mm and also no further signs of abnormality [55], as depicted in Fig. 1.5(a,c).

Various stages of MS can be defined according to the histopathological aspect of the lesions. The early stages are characterized by active myelin degradation and phagocytosis, while late stages are characterized by the absence of inflammatory infiltrates and the presence of chronically unmyelinated axons [108, 143], which all show axonal degradation [22]. Following the histopathological stages, MS can be categorized as acute or chronic, with chronic MS presenting more cortical demyelination and more extensive spreading [173]. Further, while white matter MS pathology features pronounced signs of inflammation and gliosis, cortical MS directly affects neuronal cell bodies due to their direct proximity. Finally, MS can be additionally classified by the degree of OD regeneration and remyelination [22, 143].

1.2.3 Open Questions and Challenges

The preceding sections outline the complex and multi-factorial processes in AD and MS, in which causalities are still elusive.

MS, for instance, is generally considered as an inflammatory demyelinating disease leading to impairment of axonal function, but simultaneously shows phases of progressive neurodegeneration [173]. Also, the onset of MS-pathology in the GM is so far unclear [31]. The roles of astrocytes, showing regional specificity [75], and of μ G, segregating cytokines which have been proven neurotoxic but also neuroprotective [92, 129], are unresolved. With regard to therapeutical strategies, the understanding of the glial scar in function [168], and the individual-specific degree of remyelination present challenges [143]. Beyond the pathological mechanisms, the ultimate cause of MS is controversial. Hypothesis aiming to explain this disorder range from inflammation, for instance with viral origin [121], and autoimmunity, to a degenerative disorder, and can be summarized as “immunological convolution” [178]. As a consequence, in [173], the authors explicitly ask for “more sensitive imaging techniques”.

Also in AD, the disease pattern is still unresolved. The correlation between neuropathology and behavioural and cognitive symptoms is incoherent, in particular in view of A β -plaque formation [23, 24] and its link to neurofibrillary deposits [175]. As in MS, μ G show ambivalent impact on neural networks, with a possible relation to patient age, and urge investigations in 3d (Ch. 3). μ G close to A β -plaques may potentially curb neurotoxicity, while away from these they could induce neuronal damage [176]. Further open questions target for instance the microtubule-actin-interplay [196] or the role of nucleoli in disease mechanism. With their cellular importance and pathomorphological changes, nucleoli receive much attention in AD-research. Still, the exact mechanisms and their link to clinical symptoms are unidentified [133].

As stated in Sec. 1.1.3, innovative investigation methodologies raise novel questions and pinpoint new directions (Ch. 4). Likewise, data analysis schemes are under discussion in order to appropriately delineate diseases with such complex patterns.

In general, understanding disease mechanisms requires multilevel studies, in particular the association of *post mortem* with *in vivo* temporal findings [55]. Guidelines exist to diagnose AD and MS in patients, based on respective biomarkers [93, 184]. However, MRI-based misdiagnosis frequently occurs due to insufficiently defined diagnostic criteria [55], calling for even more profound correlative imaging. The combination of methodologies can also help to better understand the induced neurotoxicity by accumulation of trace elements in the brain [34, 84]. A possible approach is outlined

in Sec. A.1.

Beyond human *in vivo* studies, animal models based on targeted genetic modifications have made a decisive contribution to the current state of knowledge in neurodegenerative diseases [44, 97]. Frequently used animal models focus on single pathologies of a disease, which would mimic APP-, $A\beta$ - or τ -alterations for AD-related research. Such models show overexpressed phenotypes on a confined region compared to humans. General limitations of small animals include the reduced complexity of neuronal circuits and glial network, deficiency of vascular and immunologic components, as well as short life-time, reduced genetic diversity and intrinsic differences in brain development and function [44]. Animal models are generally considered appropriate to develop disease hypotheses, while their translation to humans often fails due to poorly defined preclinical studies [44, 97]. Studying single pathologies is advantageous to understand their precise and isolated functioning, but, at the same time, misses the complex patterns of human diseases. Combinations of models show exceeding complexity due to interrelationships between the models. Such interrelationships are hardly distinguished from desired disease-related effects, and combinations of models are hence less utilized [97]. Human-like phenotyping in models and human phenotyping itself require sensitive methods and multiomics approaches [7, 44]. Analysis methods which attempt to capture the neurodegenerative disease complexity are part of this work: (MS) Ch. 3, (AD) Ch. 4.

1.3 X-ray Interaction with Matter

In this thesis, neuronal tissues are studied by phase-contrast projection-imaging. Typically, such experiments are conducted with hard X-rays, *i.e.* on the order of 6-100 keV. In this range, two interaction processes are significant: X-rays undergo *photoelectric absorption* or *Rayleigh scattering*, with relative cross section depending on the energy E of the probe and the atomic number Z of the object. Fig. 1.6a) shows their cross sections for three materials relevant in this work taken as examples. The underlying X-ray interaction processes serve a basis for quantitative understanding of the contrast mechanisms in image formation, and can be found in more detail in [1, 138, 160]. However, the overall X-ray interaction with extended objects is better represented by the complex refractive index, as defined in Sec. 1.3.1 and plotted in Fig. 1.6b). Sample preparation protocols can be adjusted accordingly, which is described in Sec. 1.3.2. Note that *Compton scattering*, which describes inelastic processes between photons

and matter, is dominant at > 100 keV only and hence not relevant for this work.

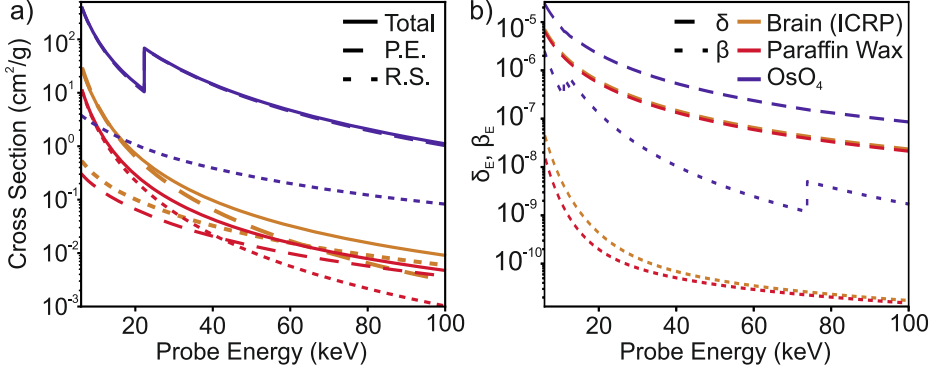


Fig. 1.6: X-ray interaction for three exemplary materials: brain tissue (ICRP), paraffin wax and OsO₄. (a) Plot of the cross sections of photoelectric absorption (P.E.) and Rayleigh scattering (R.S.), and their total. (b) Plot of the complex refractive index increments δ and β . Values were taken from [166], using the NIST compound catalog.

Photoelectric Absorption In photoelectric absorption, atoms take up discrete photon quantiles, resulting in transitions of bound to unbound electron states and excessive momentum, hence *photoionization*. Away from absorption edges, absorption occurs with a cross section of

$$\sigma_{\text{p.a.}} \propto \frac{Z^m}{E^3},$$

with $m = 4.5$ for light, $m = 4$ for heavy atoms [160].

Rayleigh Scattering Elastic interaction between photons and stationary electrons is referred to as Rayleigh scattering. It describes the phase response of oscillating electrons which are disturbed by an incoming electromagnetic field. Note that the cross section of Rayleigh scattering is related to E via the form factor, but more importantly it depends on the presence of electrons. At the level of detail considered in this work, this scales up to the integrated electron density distribution $\rho_e(x, y, z)\Delta z dx dy$ [138]. Further, Rayleigh scattering serves as a basis for the derivation of the refractive index.

1.3.1 The Complex Index of Refraction

The complex index of refraction n is defined as the ratio of the speed of light in vacuum and its phase velocity in a given material [1, 160]

$$\begin{aligned} n := \frac{c}{v} &= 1 - \frac{r_e \rho_e}{\lambda^2} \left[1 + f'_S(\Delta \vec{k}) + i f''_S(\Delta \vec{k}) \right] \\ &= 1 - \delta_E + i \beta_E, \end{aligned} \quad (1.1)$$

with the classical electron radius r_e and the spatial frequency \vec{k} . In this presentation, n is expressed in terms of electron density ρ_e and the scattering length $f_S = f'_S + i \cdot f''_S$. Here, the decomposition into the real part f'_S and the complex part f''_S indicates the induced phase shift and photon absorption, respectively. Fig. 1.6b) shows the real and complex value increments δ_E and β_E for three materials relevant in this work taken as examples. n_E indicates the energy-dependence of n , if relevant, implying $E = \frac{hc}{\lambda} = \frac{hck}{2\pi}$ (h : Planck's constant, λ : wave length, k : wave number).

Assume a single-material object which is sufficiently thin to fulfill both *projection approximation*² and the *first Born approximation*³. Then, away from absorption edges, the real part of the refractive index is obtained as [1]

$$\delta_E = \frac{\lambda^2 \cdot r_e \rho_e}{2\pi} \propto \frac{\rho_e}{E^2}, \quad (1.2)$$

such that feature contrast forms as $\Delta \delta_E \propto \Delta \rho_e$. For the complex part, again away from absorption edges,

$$\beta_E = \frac{\lambda \mu_E}{4\pi} \propto \rho_{\text{atom}} \frac{Z^{m-1}}{E^4} \quad (1.3)$$

can be found, with the absorption coefficient μ_E [160].

²In the projection approximation, the material is regarded as an extended, single scatterer, whose overall scattering properties are the sum along its in-depth extension Δz : $\bar{\delta}_E = \int_{\Delta z} \delta_E dz$ and $\bar{\beta}_E = \int_{\Delta z} \beta_E dz$. Note that an alternative expression for $\bar{\delta}_E, \bar{\beta}_E$ can be found in the *Alvarez-Macovski basis* [2]. Further, scattering events within the object, which change the optical path, are neglected [138, 195]. This assumption holds in the regime of $\Delta z < \frac{2\Delta x^2}{\lambda}$, with Δx the smallest resolution element. For $\Delta x = 200$ nm and $E = 8$ keV, the maximum object thickness would be $516 \mu\text{m}$, for $E = 13.8$ keV it is $890 \mu\text{m}$.

³In the *first Born approximation*, only single scattering events are considered, *i.e.* each photon of the unperturbed incident wavefield is scattered once at most [138].

1.3.2 Tuning the Interaction

Eq. (1.1), (1.2) and (1.3) convey that in radiography, the image contrast is formed according to the complex refractive index, which is dependent on the probe energy E . Since $\delta_E \propto E^{-2}$ and $\beta_E \propto E^{-4}$, an object can be sampled with relatively low E and close to absorption edges to exploit β_E [106], or with increased E to elevate the relative amount of phase shift δ_E compared to X-ray absorption β_E [154, 180]. Apart from the probe energy, X-ray interaction can be further directed *by the choice of sample material* (cf. Fig. 1.6b): (i) the electron density ρ_e affects the *real* part of n and (ii) the atomic number Z the *complex* part. This can be exploited for targeted weighting of either or both parts. In particular regarding biological specimens, many sample preparation techniques exist, whose steps affect – intentionally or unintentionally – the feature properties ρ_e and Z . For instance, procedures from conventional histology have been adapted for PC-CT [25, 26, 127]. In the following, X-ray interaction is considered with a special attention paid to the sample properties, *i.e.* to brain tissue.

Modification of the Electron Density Standard protocols from historically established techniques, such as histology and electron microscopy, involve chemical fixation, dehydration, optional staining, and embedding. The manipulation with chemical reagents comes with modifications in ρ_e as a side effect, which can be exploited in X-ray imaging. For one, it has been shown that fixation of brain tissue with *formalin* induces a weight increase of about 3-40% [103, 109], depending on the solution concentration, the optional addition of salts and the temperature. This weight increase is composed of an initial phase of shrinkage because of tonicity, followed by tissue swelling due to a bunch of factors, one of which consists in osmotic effects in aqueous media [8]. Fixation with *osmium* leads to an increase in diameter of nerve fibers by 2-7% [48, 88]. The additional volume correlates with the specific weight in the sample, suggesting aggregation of heavy metal [8]. In dehydration, the degree of tissue shrinkage is essentially conditioned by the solvent, and slightly affected by the succession of dehydration [21]. It may also be bypassed completely, by choosing water-based stains or embeds [28]. Consequently, volumetric changes and solvent displacements affect the electron density ρ_e . Tab. 1.1 outlines examples of reported tissue deformation during preparation, in comparison with the solvents' intrinsic electron density. Preparation protocols can hence be adapted to direct ρ_e and thereby n .

	Sample Type	PBS	Ethanol	Paraffin
d (μm)	Purkinje Cells	15.8	14.7	14.7
	Granular Cells	6.3	4.4	4
V (μm^3)	Purkinje Cells	2065	1663	1663
	Granular Cells	130.9	44.6	33.5
V/V_{PBS} (%)	Purkinje Cells	100	81	81
	Granular Cells	100	34	26
V/V_{PBS} (%)	Brain tissue	115 ^{*1}	80	68
V/V_{PBS} (%)	Brain tissue	125 ^{*2}	90	87 ^{*3}
ρ_e (nm^{-3})		337	269	311
$\rho_e/\rho_{e,\text{PBS}}$ (%)		100	80	92

^{*1} Infiltration with formalin, ^{*2} infiltration with osmium,

^{*3} infiltration with methacrylate.

Table 1.1: Reported values on tissue deformation, (top) for murine cerebellum tissue [187] under the assumption of spherical features with diameter d and volume $V = \frac{\pi}{6}d^3$, (center) for guinea pig brain tissue (values have been read off the plots in [8]), and (bottom) electron density ρ_e for different solvents according to [187].

Modification of the Atomic Number For brain tissue, relatively low atomic numbers $Z \approx 6$ [107], with accordingly low degree of photoelectric absorption, are found. Chemical compounds can be bound to sample features of interest with high specificity, in order to elevate the absorption locally. Traditionally, from electron and light microscopy (EM, LM), such stains are applied as metal treatments, namely OsO_4 , PTA , UA and HgS , which intrinsically show high molecular weights of 190.2, 183.9, 238.1, and 232.7, respectively [78, 151]. In addition to contrasting, they also accomplish tissue fixation.

Osmium tetroxide (OsO_4) binds to phospholipid headgroups, emphasizing membrane-rich cortical structures such as fiber tracts particularly [78]. Referred to as “rOTO” (reduced OsO_4 , thiocarbonylhydrazide (TCH), OsO_4) [122, 123, 198], protocols from EM have been optimized for bulk tissue processing, resulting in adequate feature contrast and uniform tissue penetration [86]. rOTO serves state-of-the-art connectomic studies in SBF-SEM [79, 80] or X-ray tomography [105]. As a supplement to OsO_4 -preparation or as a standalone, phosphotungstic acid (PTA) or uranyl acetate (UA) can be added to contrast synaptic complexes, fibers or membranes [78]. The performance of both

substances depends on parameters as pH-levels, impregnation duration, chemical fixative, the stain being water- or alcohol-based, and temperature, each regulating staining intensity. Compared to its dry state, tissue weight may double [89, 90].

Early neuronal connectivity studies with LM have been accomplished using the *Golgi* method [65, 66, 67], elaborated in view of penetration to *Golgi-Cox* [43, 149]. In a sequence involving mercurid chloride, potassium chromate and potassium dichromate, *metallic mercuric sulfides* (HgS) label about 3-10% of the neuronal axons and dendrites [30].

1.3.3 Open Questions and Challenges

The goal of studying neuronal connectivity and structure in mm^3 -sized volumes at the synaptic level in 3d imposes constraints on sample preparation at two levels: (i) structural preservation and (ii) structural contrasting in view of the imaging method. Concerning (i), special attention is given to the preservation of DNA, RNA, proteins and lipids, to which end brain banks constantly question standard preparation protocols [54]. Autolysis sets in shortly *post mortem* [37], where protein dephosphorylation can be observed within minutes [54]. Conventional fixation of *ex vivo* tissues occurs by infiltration, and relies on uniform tissue penetration by the fixative, and on sufficient fixation capabilities by the fixative itself. Further, this has to be achieved in a reasonable time. This approach is deficient in ultrastructure preservation, and *perfusion* or *high-pressure freezing* can be utilized instead [157]. In this context, correlative imaging can help to ensure the presence of delicate structures (cf. Ch. 5). Further, tissue preparation protocols are often first developed for animals, and later translated to human samples. In this context, ethics, the agonal state, *post mortem* delay, and storage temperature are critical and limiting factors [54]. It is also important to bear in mind that there are differences in protein degradation: they can be classified as “resistant” (e.g. hyperphosphorylated τ , present in AD) or “vulnerable” (e.g. normal τ) [54]. On the cellular level, soft-tissue processing can induce feature deformation (cf. Tab. 1.1, or a recent study in [155]), which is possibly also observed in Ch. 4, Fig. 4.14. Regarding (ii), it remains an open discussion whether it is preferential for phase-contrast imaging to mix and elevate contributions from δ_E and β_E by heavy-metal staining, or to solely tune δ_E by embedding, for instance.

1.4 Phase-sensitive Imaging

Contrast formation according to the real and the complex part of the refractive index n leads to fringy intensity patterns⁴ caused by self-interfering wavefronts in the detector plane, which are translated to the object plane by phase-retrieval algorithms. In this work, phase-contrast is exploited in particular for imaging of unstained neuronal tissue (low Z).

1.4.1 Hologram Formation

The propagation of a monochromatic plane wave $\Psi_E(x, y, z)$ from $z = z_{01} = 0$ to $z = z_{12} \geq 0$ in the three-dimensional space is described by the *free-space Fresnel (aka. diffraction or propagation) operator* [138]

$$\mathcal{D}_{Fr}[\cdot] = \mathcal{F}_2^{-1} \left[\exp \left(\frac{-i|\vec{k}_\perp|^2}{2\pi \cdot Fr} \right) \cdot \mathcal{F}_2[\cdot] \right], \quad (1.4)$$

where compared to [138], one part of the propagation factor is approximated to be constant and hence disregarded. A further adaptation is to write eq. 1.4 in terms of unitless quantities [74]: this affects the spatial frequency $\vec{k}_\perp = \left(\frac{2\pi n_x}{N_x}, \frac{2\pi n_y}{N_y} \right)$ and the *Fresnel number* $Fr = \frac{\Delta x^2}{\lambda z_{12}} (N_x, N_y$: number of discrete sampling points, and $n_i \in [-N_i/2, N_i/2]$, Δx : pixel size in the sample plane, λ : X-ray wave length, and z_{12} : propagation distance). $\mathcal{F}_2[\cdot]$ denotes the 2d-Fourier transform (cf. Sec. 1.5.1).

Importantly, Fr classifies the optical regimes, which are (i) the contact regime for $Fr \gg 1$, (ii) the Fresnel regime for $Fr \lesssim 1$, and (iii) the Fraunhofer regime for $Fr \lll 1$. The relevant imaging regime in this thesis is the Fresnel regime, and which can be further distinguished into the *holographic* (cf. Sec. 1.4.3) and the *edge-enhancement* regime (cf. Sec. 1.4.4).

If an object is positioned at z_{01} , the wavefield $\Psi_E(x, y, z_{01})$ is disturbed according to the local optical properties $n_E(x, y, z)$ of the object. If this object is sufficiently thin, the respective wavefield can then be described as

$$\Psi_E(x, y, z_{12}) = \mathcal{D}_{Fr} [\Psi_E(x, y, z_{01}) \cdot \exp(-\mu_E(x, y) - i\Phi_E(x, y))] ,$$

⁴Holographic intensity fringes are observed in the defocused detector plane, if phase-contrast CT is implemented via *free-space propagation*, as introduced below.

where the probe and the object transmission property $\mu_E(x, y) = 2k\bar{\beta}_E(x, y)$ determine the amplitude, and the diffraction the complex phase factor $\Phi_E(x, y) = k\bar{\delta}_E(x, y)$. However, the phase property is not directly measurable, but, as predicted by Gabor's self-interference [60], encoded in the intensity pattern

$$I_E(x, y, z_{12}) = |\Psi_E(x, y, z_{12})|^2. \quad (1.5)$$

The propagator \mathcal{D}_{Fr} , eq. (1.4), forms the basis to develop a number of methods utilized in this work in order to retrieve the phase Φ [74, 116, 160, 186].

The observation that for $z_{12} = 0$ follows $Fr \rightarrow \infty$ and the measured intensity $I_E(x, y, z_{12}) = |\Psi_E(x, y, 0)|^2 \cdot \exp(-2\bar{\mu}_E(x, y))$ comprises only absorption information of the object, and no phase, demonstrates the need for free-space propagation in order to exploit contrast based on variations of $\delta_E(x, y)$ and hence ρ_e in the object. Eq. 1.5 is a nonlinear mapping, which allows for more generic phase retrieval algorithms, such as NLT and AP in Sec. 1.4.3.

Provided a slowly varying phase and weak absorption, the Fourier transform of eq. 1.5 can be approximated as the *contrast-transfer function* (CTF)

$$\frac{\hat{I}_E(\vec{k}_\perp, \chi)}{\hat{I}_0} = 2\pi\delta_D(\vec{k}_\perp) + 2\sin(\chi)\hat{\Phi}_E(\vec{k}_\perp) - \frac{1}{2}\cos(\chi)\hat{\mu}_E(\vec{k}_\perp), \quad (1.6)$$

with $\chi = \frac{\Delta x^2 |k_\perp|^2}{4\pi \cdot Fr}$ and $\hat{\cdot}$ denotes the Fourier transform. The CTF serves as the basis for the *linearized* phase-retrieval algorithm in Sec. 1.4.3, also referred to as “CTF-approach”.

1.4.2 A Note on Coherence

At this point, a note on the energy spectrum, symbolized with index E , shall be made: from the nature of sin-cos-behavior in eq. 1.6 (or as also found for the more general case), where χ , Φ and μ are energy-dependent, a polychromatic spectrum would lead to poorly defined contrast. Monochromaticity is required in order to achieve contrast according to eq. 1.5 or 1.6 (or see the respective phase-retrieval schemes in Sec. 1.4.3), but not in order to observe interference *per se*. Hence, X-ray phase-contrast experiments in the holographic regime find application in setups with considerable monochromaticity⁵, *i.e.* in synchrotron setups. Accelerator-based X-ray sources are often

⁵Monochromaticity is distinct from temporal coherence for pulsed radiation. Practically, also pink beams ($\Delta E \gtrsim 10$ keV) can show significant temporal coherence, referring to wave packets being “in phase”.

utilized in combination with a Si(111) monochromator which reduces the bandwidth ΔE (for instance, the P10 beamline at DESY has a bandwidth of $\Delta E = 1$ eV at 10 keV [136]). In laboratory X-ray sources, the bandwidth can easily span $\Delta E = 35$ -100 keV. Hence, for phase-contrast imaging with polychromatic X-ray sources, the assumption of holographic contrast formation (\rightarrow CTF) is not suitable. Instead, the edge-enhancement regime (\rightarrow near-field TIE, transport of intensity equation) is more appropriate: As described in Sec. 1.4.4, the TIE reveals a simple linear $1/E$ -dependent scaling, and otherwise encodes the X-ray energy only in I_E , such that spatial coherence becomes much more important [140, 197].

Spatial coherence can be defined as $\xi_{\perp} = \frac{\lambda}{2 \cdot s/z_{01}}$ [1]: Due to the low divergence of synchrotron radiation, coherence-beamlines have a source spot s much smaller than its distance to the endstation z_{01} (again, for P10 as an example of a primary source at the GINIX-endstation in parallel-beam (PB) geometry: $s = 39 \mu\text{m}$ (h) or $s = 250 \mu\text{m}$ (v) [134], $z_{01} \approx 86.1$ m, $E = 12$ keV; or with a secondary source (waveguide, WG) in cone-beam (CB) geometry: $s = 30$ nm, $z_{01} = 125$ mm, $E = 8$ keV [171]). They exhibit high spatial coherence $\xi_{\perp} = 114 \mu\text{m}$ (h, PB) or $\xi_{\perp} = 323 \mu\text{m}$ (CB), respectively, which is 100-1000 times the sampling length, allowing for deep-holographic imaging at $Fr \approx 10^{-4}$. Such small Fresnel numbers give access to more modulations in eq. 1.6 (or in its more general case), and allow for increased maximum spatial resolution. Laboratory nanofocus setups, such as the TiNa setup in Ch. 2, are typically operated with $s = 300$ nm and $z_{01} = 1.1$ mm (at $E = 11.46$ keV), resulting in $\xi_{\perp} = 198$ nm $\ll \xi_{\perp, \text{GINIX}}$. Laboratory ξ_{\perp} is on the order of the spatial sampling length, such that the Fresnel regime is restricted to $Fr \approx 1$. Therefore, holographic applications are mostly implemented at large-scale facilities, while edge-enhancement is implemented at both accelerator-based and laboratory X-ray sources. For further readings on coherence properties, [69, 138, 192] are suggested.

1.4.3 Wavefront Reconstruction I: Holographic Regime

In the holographic regime, i.e. for $Fr \ll 1$ or when $\sin(\chi) \neq \chi$ in eq. 1.6, for instance, CTF, NLT and AP phase retrieval find application in this work.

Contrast-Transfer Function (CTF) For *homogeneous objects*, a linear behavior between absorption and phase shift within the object can be assumed: $\hat{\mu}_E = \frac{2\beta_E}{\delta_E} \hat{\Phi}_E$. Provided that the object is further *weakly* absorbing and $\frac{\beta_E}{\delta_E}$ is known, least-square minimization relates the experimentally measured intensity $I_E^{\text{exp}}(x, y, z_{12})$ to the CTF-

expression in eq. 1.6, and delivers a unique solution from which the phase is directly accessible [40]:

$$\Phi_E^{\text{CTF}}(x, y, z_{01}) = \mathcal{F}_2^{-1} \left[\frac{\sum_{n=1}^N (\sin(\chi_n) + \frac{\beta_E}{\delta_E} \cos(\chi_n)) \cdot \mathcal{F}_2 [I_E^{\text{exp}}(x, y, z_n) - 1]}{\sum_{n=1}^N 2(\sin(\chi_n) + \frac{\beta_E}{\delta_E} \cos(\chi_n))^2 + \alpha(x, y)} \right].$$

This reconstruction scheme has been introduced by Peter Cloetens and colleagues, and gained popularity due to its practicability (low cost at high quality for weakly interacting objects). Note that $\sum_{n=1}^N$ serves the combination of data sets recorded at N different Fr_n , by modification of z_{12} . As also described in [40], reconstruction with a range of Fr_n is advisable in order to account for (i) zero-crossings in the CTF due to the Talbot effect [39, 181], and (ii) the twin-image problem⁶, at best for four carefully chosen Fr_n [201]. In particular for $N = 1$, a suitable choice of the two regularization parameters in $\alpha(\vec{k}_\perp)$ can account for residual absorption and poorly represented spatial frequencies [38].

Non-Linear Tikhonov (NLT) For a more general case, which is based on the non-linear version of eq. 1.6 but still assuming $\frac{\delta_E}{\beta_E}$ -coupling (the *homogeneous-object assumption*), or when the application of constraints is desirable (cf. next paragraph on AP), the least-square minimization in phase reconstruction can be extended by non-linear Tikhonov regularization, and is referred to as NLT. Such phase-retrieval schemes require the integration of an iterative solver, due to the non-linearity in eq. 1.5 in contrast to the linear CTF (eq. 1.6). The choice of initialization determines whether a local or global minimum will be reached. The $\frac{\delta_E}{\beta_E}$ -coupling allows for the exact computation of derivatives in gradient descent optimization, which makes the algorithm particularly efficient in convergence and hence in computational effort. The NLT is implemented in [115], while the publication by Simon Maretzke and colleagues on this NLT-scheme is in preparation. Note that non-linear phase-retrieval schemes are gaining in popularity, and that a similar approach has been developed by scientists at the ID16A-beamline at ESRF, Grenoble (publication in preparation).

⁶Due to geometrical optics, there is not only the real image at z_{12} , but also its virtual twin at $-z_{12}$. Phase retrieval results in a sharp image in the object plane with, depending on the well-posedness of the problem in terms of experimental parameters, an overlay of the defocused twin [68].

Alternating Projections (AP) AP algorithms are generally used to compute a best approximation point on two intersecting or non-intersecting sets (*i.e.* the experimental data and the respective assumptions), by serial projecting onto these sets⁷ [18]. Hence, the derivative is not computed analytically, but approached via these projections. The AP phase-retrieval scheme is another example of iterative reconstruction algorithms, and only the most basic representative of the group of projection algorithms. It reconstructs wavefronts via

$$\Psi_{n+1}^{\text{AP}} = P_S(P_M(\Psi_n)),$$

where the operator $P_M(\cdot)$ matches the iterated (guessed/computed) with the recorded intensities, and $P_S(\cdot)$ comprises object-space constraints, including the support, or some prior knowledge on phase or amplitude magnitude [73, 193].

For the holographic data in this thesis, AP-reconstruction may take 100-times more iterations than NLT, at potentially “better quality”. AP is less restrictive on the phase problem as it does not rely on the $\frac{\delta_E}{\beta_E}$ -coupling, and therefore, the AP-initialization should be reconsidered: initialization with ones (or random values) instead of the CTF-solution can be advantageous to approach the global minimum, since it might lead to optimization in a local side-minimum otherwise.

1.4.4 Wavefront Reconstruction II: Edge-enhancement Regime

The CTF-equation can be further simplified, by assuming small propagation distances z_{12} (*i.e.* $\sin(\chi) \approx \chi$) and a weak and homogeneous object (*i.e.* $\nabla_{\perp} I_E \approx 0$), resulting in the *near-field transport of intensity equation (TIE)* [138, 182]:

$$\frac{I_E(\vec{k}_{\perp}, z_{12})}{I_E(\vec{k}_{\perp}, 0)} = 1 - \frac{z_{12}}{k} \nabla_{\perp}^2 \Phi_E(\vec{k}_{\perp}, z_{12}). \quad (1.7)$$

The near-field TIE provides the basis for phase retrieval in the edge-enhancement regime.

Single-Material Object (SMO) Under the assumption of an object with a fixed ratio $\delta_E(x, y)/\beta_E(x, y) = \delta_E/\beta_E$ in eq. (1.7), the SMO-equation according to David

⁷Here, “projection” refers to the dimensionality reduction in a purely mathematical sense and not in the practical tomographic.

Paganin and colleagues can be derived [139]:

$$\Phi_E^{\text{SMO}}(x, y) = \frac{\delta_E}{2\beta_E} \cdot \ln \left(\mathcal{F}_2^{-1} \left(\frac{\mathcal{F}_2 \left(\frac{I_E(x, y, z_{12})}{I_0} \right)}{\frac{\delta_E k}{2\beta_E Fr} \cdot |k_\perp|^2 + 1} \right) \right).$$

Note that theoretically, δ_E/β_E is selected specifically for each energy, but with broad X-ray spectra in practice chosen as a single effective value $\delta_E/\beta_E = \delta/\beta$. Depending on the severeness of violating these presumptions, image quality may be degraded due to smear.

Modified Bronnikov Algorithm (MBA) Proceeding from the near-field TIE with the assumptions of a pure phase (*i.e.* $\mu_E(x, y) = 0$) and weakly interacting object, and a plane wave with initial intensity I_0 , the *simplified TIE* leads to

$$\Phi_E^{\text{MBA}}(x, y) = 2\pi \cdot Fr \cdot \mathcal{F}_2^{-1} \left(\frac{\mathcal{F}_2 \left(\frac{I_E(x, y, z_{12})}{I_0} - 1 \right)}{|k_\perp|^2 + \alpha} \right),$$

according to Amela Groso and colleagues [70, 71]. From comparison with SMO, residual absorption can be incorporated in the MBA-approach, and a theoretical estimate of $\alpha = \frac{4\pi\beta_E Fr}{\delta_E}$ is found. However, as for SMO, mismatched assumptions in view of object texture or X-ray spectrum still limit image quality.

Bronnikov-Aided Correction (BAC) Towards overcoming the idealized assumptions in object or experimental settings, the near-field TIE can again be consulted. Based on a phase map and the intensity in the detector plane z_{12} , the intensity in the object plane $z_{01} = 0$ is computed (in analogy to back-propagation in holographic reconstruction schemes) [46]:

$$I_E^{\text{BAC}}(x, y, 0) = \frac{I_E(x, y, z_{12})}{1 - \gamma \nabla_\perp^2 \Phi_E(x, y)},$$

with the regularization parameter $\gamma = \frac{z_{12}}{k}$ in the ideal case. Note that in this work, $\Phi_E(x, y) \approx \Phi_E^{\text{MBA}}(x, y)$ as suggested by Yoni De Witte and colleagues [46]. Computing $\Phi_E^{\text{MBA}}(x, y)$, which is valid for pure phase objects, and then correcting this phase map by the BAC-ansatz which considers weak absorption, extends the applicability of phase-contrast imaging in the edge-enhancement regime. Note that the MBA step resembles a low-pass filter, while the additional BAC step corresponds to a high-pass filter. This

results in sharper intensity maps compared to the SMO- and MBA-scheme. A similar scheme has been developed recently, based on Paganin's SMO-reconstruction, which is referred to as "generalized Paganin" [141].

1.4.5 Open Questions and Challenges

While propagation-based phase-contrast imaging is under strong development, in particular for studying biomedical objects, phase-retrieval algorithms are subject to restrictive assumptions, as introduced above. Here, one may ask the question: Should the experiment (including sample and setup) meet the algorithm or the algorithm the experiment?

One idealization is the plane/spherical wave assumption in empty-beam correction [85]. Finite spot sizes and aberrated optics (*e.g.* KB-mirrors) flaw the probe, such that empty-beam correction may induce a diffuse haze in the reconstructed phase map. *Near-field ptychography* addresses this problem by reconstructing probe *and* object [153]. This technique is particularly suitable for high-resolution nanotomography, beyond the weak object assumption (*e.g.* stained samples, cf. Sec. 1.3), and the related computational effort can benefit from advanced GPU architecture [171, 174]. Concerning near-field holography, the portfolio of iterative phase-retrieval methods goes far beyond those presented above. Iterative schemes impose less restrictions on the experiment, in general, but allow for selective specification of parameters by constraints: The *modified Hybrid-Input-Output*, for instance, has been demonstrated to achieve spatial resolution on the order of 20 nm for biological samples [9, 62]. However, these results rely on the definition of a support to set a reference and solve the twin-image problem. This is problematic for tissue samples which usually exceed the field-of-view (FOV) at high geometric magnification. In such cases, the support can be defined within the cleverly padded area [73], and the twin-image problem is solved based on multi-shot recordings. The maximum suitable sample diameter which would otherwise flaw the hologram is additionally limited by a number of factors: (i) the projection approximation [138, 195], (ii) the uncertainty in the Fresnel number when the sample covers an extended range of z_{01} , and (iii) the Fresnel-scaling theorem [138]. Under violation of these conditions, 3d multi-slice phase-retrieval can help, which is already available for far-field ptychography [179], but yet to be developed for near-field imaging. However, if (i) the projection approximation is fulfilled, 3d near-field phase-retrieval schemes have been proposed in the TIE-approximation [185], and for a more general case [159].

In “standard” nanotomography conditions (*i.e.* in this work: moderate voxel size of $\gtrsim 100$ nm, $Fr \approx 10^{-3}$ - 10^{-4} , weak object), the CTF-scheme has proven adequate. However, beyond the idealized assumptions in the CTF, iterative schemes perform superiorly [73]. Also, multi-defocus reconstructions can flaw image quality due to rescaling and registration of the datasets. Multi-energy reconstruction schemes address this issue and retrieve more quantitative electron-density maps, and induce a variation in Fresnel numbers by changing the energy instead of the propagation distance [11, 111, 154]. In order to access the 2d-map (δ_E, β_E) of an object, spectral methods can also rely on energy-selective detectors. They can be applied to setups with broad bandwidths, such as laboratory sources, in particular in view of heavy-metal stainings [163].

1.5 Computed Tomography

In order to study neuronal tissue in three dimensions, computed tomography is utilized in this work. The concepts of tomography are outlined in the following, including the foundations, reconstruction schemes, sampling conditions, quality metrics and relevant artifacts. The aspects are largely based on [29, 99, 160].

1.5.1 Foundations

Radon Transformation In tomography, an nd object f is studied from different angles $\vec{\theta} \in \mathbb{R}^{n-1}$, and is reduced to 1d by summation of single resolution elements along n -1-dimensional hyperplanes $\vec{L}_{\vec{\theta}}$. These summations are referred to as *projections* $p(\vec{\theta}, x')$. Fig. 1.7(a) outlines this concept for $n = 2$: an object f in real space (x, z) is sampled at the angle θ by a source-detector-system in (x') , which records the object-induced change⁸ of the probe s along $\vec{L}_{\theta} = \begin{pmatrix} x \cos(\theta) + z \sin(\theta) \\ -x \sin(\theta) + z \cos(\theta) \end{pmatrix}$, referred to as *Radon transformation*⁹ [147]:

$$p(\theta, x') = \mathcal{R}(f(x, z)) = \int_{\vec{r} \in \vec{L}_{\theta}} f(x, z) \cdot \delta(\vec{r} \cdot \vec{e}_x - x') dx dz.$$

The projection data $p(\vec{\theta}, x')$ which are collected at a number of projection angles θ during tomographic acquisition form a *sinogram*, see Fig. 1.7(c).

⁸It is presumed that the process of projecting is *linear*.

⁹From the nature of detector pixel arrays, discrete sampling suggests matrix notation: $p = A \cdot f$, with the system's sampling matrix A . This representation will be helpful in algebraic reconstruction.

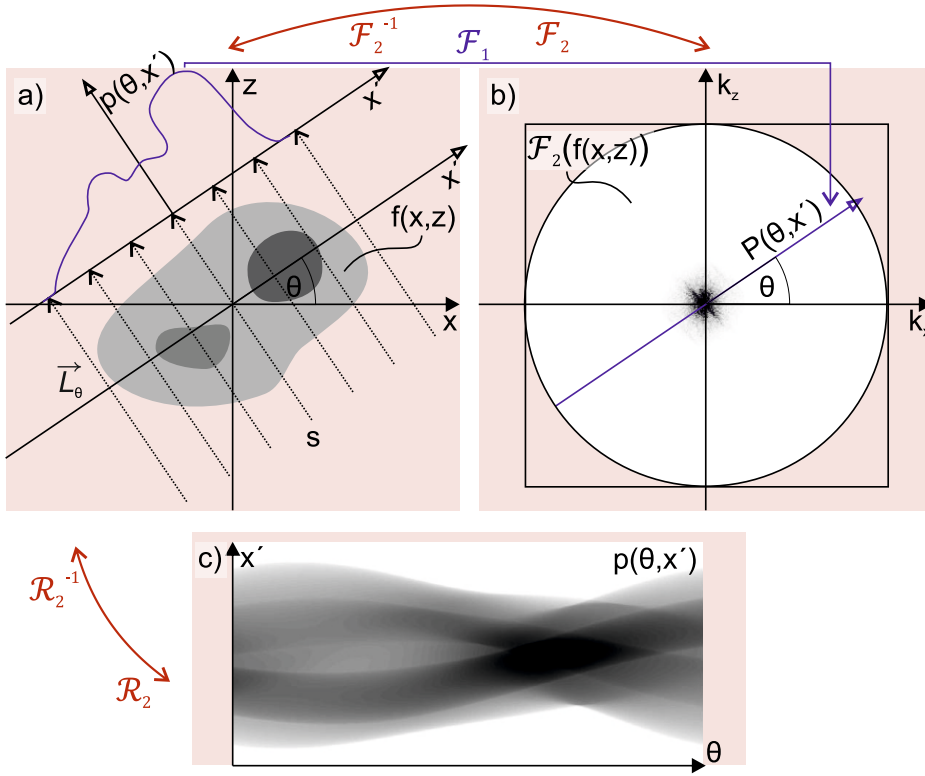


Fig. 1.7: The principle of the Fourier-slice-theorem in 2d tomography. (a) An object $f(x, z)$ is sampled with a probe s in the source-detector-system (x') at angle θ . Voxel elements of $f(x, z)$ are summed along the integration path \vec{L}_θ . Its 1d-Fourier transform $\mathcal{F}_1(f(\theta, x')) = P(\theta, x')$ is plotted in blue and marked in (b) in Fourier space. In the direct Fourier method, for a number of projection angles θ , the 2d-Fourier domain of $f(x, z)$ is filled up. (c) In the backprojection scheme, projection data are collected in a sinogram $p(\theta, x')$. Radon-backtransformation of $p(\theta, x')$ yields the object $f(x, z)$ (under consideration of a filter step, see FBP). Adapted from [29, 160].

Fourier Transformation The n d-Fourier transform of f is defined as [29]

$$F(\vec{k}) = \mathcal{F}_n(f(\vec{r})) := \int_{\mathbb{R}^n} f(\vec{r}) e^{-2\pi i \vec{k} \cdot \vec{r}} d^n r,$$

cf. Fig. 1.7(b). The Fourier transformation has a number of properties which are detailed in e.g. [33], and the *convolution theorem* is of particular importance: it states that the convolution of two signals in real space equals their multiplication in Fourier

space.

Fourier-Slice-Theorem The Fourier-slice-theorem (FST) describes a fundamental property of the Radon transformation [130]:

$$\mathcal{F}_1(\mathcal{R}(f(x, z))) = \mathcal{F}_1(p(\theta, x')) = P(\theta, k_{x'}) = F_\theta(k_x, k_z) = \mathcal{F}_{2,\theta}(f(x, z)) ,$$

where the index of $\mathcal{F}(\cdot)$ indicates the dimensionality. Fig. 1.7 illustrates the FST: the Radon transform of an object f at θ is Fourier-transformed, which is identical to extracting the line through the 2d Fourier transform of f at θ . Hence, the *direct Fourier method* is justified: the collection of lines $P(\theta, k_{x'})$ at a number of angles θ in 2d Fourier space, allows for the retrieval of the object f in real space (x, z) by inverse 2d Fourier transformation.

The Regridding Problem with the Direct Fourier Method Fig. 1.8(a) visualizes the *circular* tomographic sampling scheme of the direct Fourier method (red dots), while in numerical implementations, the final output $f(k_x, k_z)$ is defined on a *cartesian* grid (gray dots). This requires data interpolation in Fourier space, which can lead to severe artifacts due to the operation on spatial frequencies instead of real space coordinates. Instead, the *backprojection* scheme is preferably used in practice.

The Backprojection and the Sampling Problem In the backprojection (BP) method, tomographic projections are collected in real space, and smeared back along the integration paths [99]. However, the Fourier space representation of the data sampling in Fig. 1.8(a) demonstrates that the *line density* (sampling density) is higher for low spatial frequencies. This sampling ramp introduces structure blurring. A prominent solution to this problem is the introduction of a filtering step in Fourier space, referred to as *filtered backprojection* (FBP).

1.5.2 Tomographic Reconstruction

The sampling problem introduced above has a negative impact on the spatial frequency domains. Taking this into account, different approaches exist for tomographic reconstruction [29, 99].

Filtered Backprojection (FBP) and the FDK Scheme A simple, mathematically consistent tomographic reconstruction scheme is the *filtered backprojection* (FBP), which has also been independently proposed by Radon [147]. From the nature of BP with its intrinsic point-spread function $\text{PSF}(k_x, k_y) = |(k_x, k_y)|^{-1}$, it is conclusive to implement a spatial frequency filter of $|k_x, k_y|$. Since the inverse Fourier transform of non-square-integrable functions does not exist, this filter is preferentially applied to the projection data in Fourier space.

In general, tomographic reconstruction schemes are designed for parallel-beam (PB) geometry, *i.e.* parallel line integrals. However, X-rays propagating in fan-beam (FB) or cone-beam (CB) geometry¹⁰ may be preferred, either for the purpose of higher throughput or finer sampling, or also due to the divergent nature of table-top X-ray sources. With *FDK*, Feldkamp, Davis and Kress propose a method to rescale single slices in CB-geometry to their FB-equivalents, exploiting the fact that a 2d-plane of a cone beam is a tilted FB (tilted with respect to the tomographic axis) for small cone-beam angles Ψ [53]. By rescaling, each projection is mimicked as if it was recorded in

¹⁰FB-geometry refers to divergent beam paths in the 2d-space, as sketched in Fig. 1.8(b), blue. Its 3d extension is termed CB-geometry, with divergence not only in (x', z') but also in (x', y') .

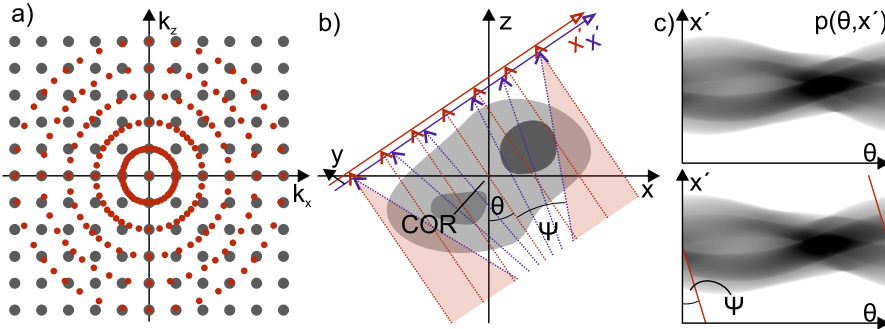


Fig. 1.8: Sampling in tomographic imaging. (a) Representation of tomography sampling points (red) in Fourier space demonstrates that low spatial frequencies are relatively overrepresented. Specifically for the direct Fourier method, the mismatch between the sampled datapoints (red) and the computation on a cartesian grid (gray) requires interpolation in Fourier space, which is prone to artifacts. (b & c) Irradiation discrepancies in (red) PB- and (blue) FB-geometry. (b) Compared to PB-geometry, single FB-rays trespass different voxels at different path lengths. “COR” marks the center of rotation. The extension to 3d divergent illumination (CB-geometry) is indicated by the two detector lines x' . (c) These deviations result in a Radon space which is skewed by the propagation opening angle Ψ (top: PB-geometry, bottom: FB- or central slice in CB-geometry). Adapted from [29].

the center along the x' -axis in FB-geometry. Subsequently, a modified FBP scheme is applied. Fig. 1.8(b) shows the concept of PB-acquisition (red) in compliance with FB-geometry (or central slice in CB; blue): divergent rays propagate with an opening angle $2 \cdot \Psi$, and result in a sampling mismatch (red-shaded areas). Hence, line integrals in PB- and FB-geometry do not coincide, but the opening angle Ψ induces a shift in the sinogram compared to PB-geometry, see Fig. 1.8(c). The concept is detailed in [29, 99].

Algebraic Reconstruction As noted above, the projection scheme can be written in matrix notation, as $\mathbf{p} = \mathbf{A} \cdot \mathbf{f}$. Here, the system matrix \mathbf{A} comprises the entire experimental geometry, *i.e.* which object elements are traversed by a single line integral, and by which amount. In realistic experimental implementations, this straightforward definition is ill-posed for noise-flawed data and large detector arrays leading to \mathbf{A} being vastly singular. The object \mathbf{f} can hence be retrieved iteratively, minimizing a norm $\|\mathbf{A}\mathbf{f} - \mathbf{p}\|$, with initialization $\mathbf{f}_0 = \mathbf{0}$ for instance. In the most basic approach, the *algebraic reconstruction technique* (ART), based on [98], the solution \mathbf{f}_m is updated at each iteration step m , under consideration of a relaxation parameter [50]. While convergence is potentially fast, the result may suffer from noisy data and inappropriate choice of relaxation parameter. In such cases, the *simultaneous iterative reconstruction technique* (SIRT) can be used [64, 82]. Opposed to ART, in SIRT, higher consistency is achieved by ART-reconstruction of single voxels, whose values \mathbf{f}_m are only updated after consideration of *all* projection rays traversing the respective voxel. The update results from the average suggested from all projection integrals. As a consequence, in general, convergence with SIRT is slower than with ART. In literature, the *simultaneous algebraic reconstruction technique* (SART) is traded as a method to combine the advantages from ART and SIRT: the procedure uses bilinear elements instead of voxels, leading to smoother outputs, and further, the correction terms are applied ad-hoc, under consideration of a Hamming window to weight the update locally [99]. An example of SIRT-reconstructed CT-data after 400 iterations can be found in Ch. 3, Fig. 3.5(b.vii-viii).

1.5.3 Sampling Criteria

Angular Sampling Range in Cone-Beam Geometry In contrast to PB-geometry, line integrals follow diverging paths in CB¹¹. This results in sampling discrepancies,

¹¹This artifact can be likewise found in FB-geometry. Since CB-geometry is found in most experiments in this work, which are rescaled to FB in FDK-reconstruction, here CB is referred to.

which are indicated by red-shaded areas in Fig. 1.8(b). The respective sinograms are plotted in (c). In order to sample the entire angular PB-range of $\theta \in [0, 180)$ from CB-data, the acquisition range θ needs to be expanded by the CB-opening angle: $\theta \in [0^\circ, 180^\circ + \psi)$ [29]. The CB-sampling issue can be extended to the third dimension, *i.e.* along the rotation axis, and different techniques exist to cope with it [29]. According to the *Tuy-Smith's sufficiency condition*, an object is sufficiently sampled if all planes which intersect the object in Radon space also traverse the X-ray source-detector path at least once [29]. Note that in CB-geometry, sampling on a circular trajectory does not fulfill this requirement, exhibiting so-called “shadow zones”¹².

Angular Sampling Intervals According to the FST, the entire Fourier space may be sampled from projections $p(\theta, x')$ [29]. The *Nyquist-limit* gives the minimum number of angular positions N_p which is required such that the tomographic problem has a unique solution: $N_p \approx \frac{\pi}{2} N_{x'}$, with $N_{x'}$ denoting the number of detector pixels in horizontal direction. A more abstract approach is provided by *Orlov's sufficiency condition* [160].

1.5.4 Tomographic Artifacts

In tomographic images, reconstruction artifacts are easily introduced for various causes. The most important ones in this thesis are briefly described in the following paragraphs and exemplified in Fig. 1.9 for acquisitions covering $\theta \in [0, 180^\circ)$ with $N_p = 540$, using the “dicty”-phantom from [115]. (a) shows the artifact-free tomographic reconstruction of $f(x, z)$.

Center of Rotation When the position of the center of rotation during reconstruction does not match the one from the experiment, the line integrals are attributed to the wrong voxel elements during backprojection. According to the amount of misplacement Δ , structures at $\theta = 0^\circ$ and 180° are smeared back with an offset of $-\Delta/2$ and $+\Delta/2$ in object plane (x, z) , respectively, resulting in so-called “half-moon artifacts” (cf. Fig. 1.9(b)). For $\theta \in [0^\circ, 360^\circ)$ acquisitions, this artifact emerges as double-edged structures.

Motion during Acquisition Motion during data acquisition implies that the source-object-detector system has not been consistent but shows some additional temporal

¹²The effect of shadow zones along the rotation axis is observed in data from Ch. 2.

translation. As a consequence, projection line integrals do not follow straight paths, eventually leading to *local* half-moon artifacts (cf. Fig. 1.9(c)).

Insufficient Projection Sampling If the angular sampling criterion is not met, a lack of spatial information leads to stripe artifacts along the missing line integrals. Fig. 1.9(d) shows that this is particularly severe along edges, at which undersampling results in dominant streak artifacts (red arrow).

Partial Volume Partial volume artifacts arise when the entire object exceeds the field-of-view in tomographic projections. Fig. 1.9(e) depicts the resulting truncation artifact. If this can not be averted, the sinogram can be *edge-padded* to mitigate the artifact.

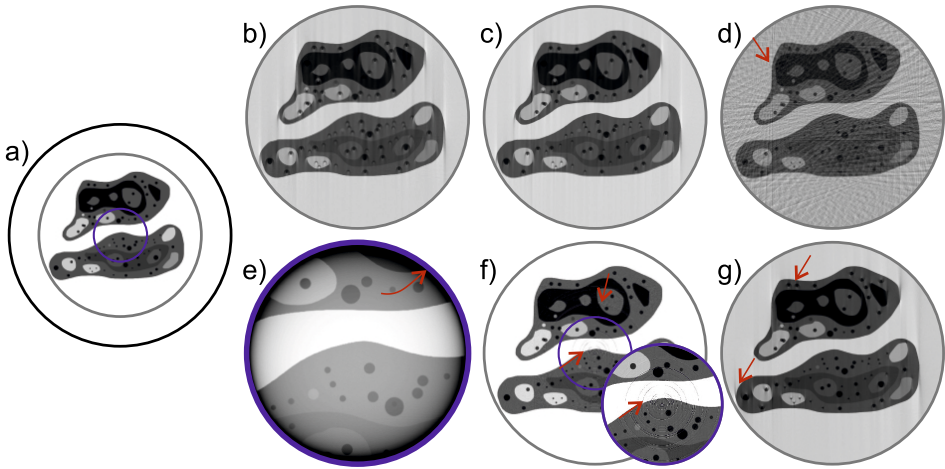


Fig. 1.9: Relevant artifacts in tomographic reconstruction, at the example of $\theta \in [0^\circ, 180^\circ)$. (a) Phantom, (b) reconstruction with mismatched center of rotation by 8 pixel, (c) motion-flawed reconstruction (successive motion according to the rising edge of a Gaussian distribution with $\mu = 5$ pixel, $\sigma = 5$ pixel), (d) reconstruction as (a), but with only 10% of N_p , (e) partial volume acquisition of the subregion marked by the blue circle in (a) shows truncation artifact without padding of the sinogram, (f) reconstruction affected by (half-)ring artifacts, and (g) CB-reconstruction with mismatched geometry (FDK-reconstruction with $\frac{z_{02}/z_{01}|_{\text{rec}}}{z_{02}/z_{01}|_{\text{sim}}} = 0.95$) leads to local half-moon artifacts.

Ring Artifacts Ring artifacts arise from persistent irregular values throughout the tomographic acquisition. Mostly, the root of cause lies in the non-linear response of single detector pixels, and can be mitigated with so-called outlier-filters as implemented in [115], an additive-correction approach [102], or based on wavelet-filters [128]. In $\theta \in [0^\circ, 180^\circ)$ acquisitions, ring artifacts emerge as half-rings, as shown in Fig. 1.9(f).

Geometry Artifacts When the experimental parameters to compute the CB-opening angle are ill-posed, line integrals do not follow straight but curved paths in FB, and the effective, CB-to-FB paths are resampled incorrectly. Again, local half-moon artifacts emerge (cf. Fig. 1.9(g)). The same underlying phenomenon causes artifacts if the center of the cone-beam does not coincide with the center of the detector (“nick-angle”).

1.5.5 Image Quality Metrics

Different tools exist to access the quality of the reconstructed object information f , which is conditioned by the system’s PSF h .

Modulation-Transfer Function (MTF) The normalized Fourier transform of h yields the *Optical Transfer Function (OTF)*. The MTF is defined as: $\text{MTF}(k_{\vec{r}}) = \left| \frac{\mathcal{F}(h(\vec{r}))}{\mathcal{F}(h(0))} \right|$ [160]. From analyzing the MTF as a function of the spatial frequency $k_{\vec{r}}$, the spatial resolution can be accessed.

Contrast-to-Noise Ratio (CNR) The CNR quantifies the degree of object-specific signal contained in image data, namely its *contrast* [160]. Various definitions exist, and in this work, it was used as: $\text{CNR} = \frac{\mu_{\text{ft}} - \mu_{\text{bg}}}{\sigma_{\text{bg}}}$, with μ_{ft} and μ_{bg} the mean gray values of the feature and the background, respectively, and σ_{bg} the standard deviation of the background signal. The CNR has been studied for a range of PC-CT settings in Ch. 2.

Fourier-Shell-Correlation (FSC) The FSC is a metric to capture both the spatial resolution and the contrast in 3d-data (2d-equivalent: *Fourier-ring-correlation (FRC)*) [160]. Its basic concept is to determine the degree of correlation, *i.e.* the signal consistency, found in two independent image sets I_1, I_2 over shells k_i in Fourier space. The

FSC is defined as [77, 190]

$$\text{FSC}(k_i) = \frac{\sum_{k \in k_i} \mathcal{F}_3(I_1(k)) \cdot \mathcal{F}_3^*(I_2(k))}{\sqrt{\sum_{k \in k_i} |\mathcal{F}_3(I_1(k))|^2 \cdot \sum_{k \in k_i} |\mathcal{F}_3(I_2(k))|^2}}.$$

Note that the definition of the underlying threshold curve needs to be borne in mind when inspecting the FSC-metric. In this work, the half-bit threshold criterion was utilized:

$$T_{1/2}(k_i) = \frac{0.2071 + 1.9102 \cdot n(k_i)^{-1/2}}{1.2071 + 0.9102 \cdot n(k_i)^{-1/2}}.$$

Further definitions can be found in [191]. In CT, two independent data sets are usually achieved by splitting the projection data into two sets, and performing two tomographic reconstructions, each with one of the half data sets. FSC-results hence give an upper limit for the spatial resolution, and examples are given in Ch. 2 and 4.

1.5.6 Open Questions and Challenges

Recently, nanotomography using a transmission X-ray microscope (TXM) has been reported to reveal 10.4 nm resolution (FSC 1/2-bit) in a reasonably short scan time, *i.e.* in 250 min [45]. Achievement of such high-quality data requires particular stability during acquisition and an advanced reconstruction scheme, which was iterative in this case. Still, single components in the workflow can be further optimized: these include a more efficient and higher-resolution detection system, and storage ring upgrades to fourth generation synchrotron leading to elevated photon flux in a narrowed emission angle.

Beyond iterative optimization techniques, machine- and deep-learning implementations are becoming more popular in tomographic reconstruction in order to compensate for missing data [49] or for noise reduction and resolution enhancement [56, 113]. To this point, even such novel reconstruction schemes could not bridge the resolution discrepancy between 2d and 3d images [45, 56], which is demanding but theoretically achievable. However, machine- or deep-learning schemes are limited to the reconstruction of features which are included in the training data. Time-resolved tomography acquisitions (4d) have a reduced photon yield due to short exposure times, and can particularly benefit from noise-compensating or noise-robust methods [125, 158]. With continuous advancements in X-ray source and detector technologies, such

as synchrotron storage ring upgrades, scan efficiency increases and hence both the 3d and 4d scan throughput. The implementation of reasonably fast tomographic reconstruction becomes increasingly important, both for post-acquisition and online reconstruction [14, 27, 117].

Finally, an important point in nanotomography is made: for practical reasons, (biological) samples mostly exceed the rather small FOV in nanoimaging (“ROI-problem”). As a consequence, $p(\theta, x')$ is not known for all hyperplanes in Radon space, such that the tomographic problem is underdetermined and image quality is potentially flawed [148]. Algorithms have been established to account for this [52, 152], which include deep-learning implementations, or the joint reconstruction of overview- and ROI-tomography [42]. Apart from algorithms, on the experimental side, continuous acquisition during rotation instead of step-and-shoot can exploit blurring of structures which are farther away from the center of rotation (cf. Ch. 4, Fig. 4.2(a)).

1.6 Data Analysis by Means of Optimal Transport

In the previous sections, the principles and challenges in neuronal PC-CT have been addressed. Following sample preparation, data acquisition and tomographic reconstruction of phase maps, post-processing often includes the segmentation of features of interest. To this end, annotations can be made manually, using dedicated machine-learning software such as Ilastik [12], or based on deep-learning V-net architecture as in Ch. 4, for instance. Subsequently, *optimal transport (OT)* theory can find application as an emerging tool for advanced statistical analysis. The high dimensionality in PC-CT data, which is not restricted to the spatial dimensions, can be exploited by OT in order to access successive changes in large point clouds, as presented in Ch. 4.

1.6.1 Foundations

OT-theory can be dated back to the 18th century, when Monge was confronted with transitioning a sand pile with minimal effort, which is today referred to as a basic “optimal transport problem” [104, 144]. Piles of sand grains, or more general *data point clouds*, are *probability measures*, and can be approximated by Gaussians $\alpha = \mathcal{N}(\mu_\alpha, \Sigma_\alpha)$, $\beta = \mathcal{N}(\mu_\beta, \Sigma_\beta) \in \mathbb{R}^d$, with means $\mu_\alpha, \mu_\beta \in \mathbb{R}^d$ and covariance matrices $\Sigma_\alpha, \Sigma_\beta \in \mathbb{R}^{d \times d}$ in the example of two. In this simplification [144], an analytical solution

to the optimal transport problem exists, which is the transport plan $\mathbf{T}_{\alpha,\beta} \in \mathbb{R}_+^{d \times d}$:

$$\mathbf{T}_{\alpha,\beta} : x \mapsto \boldsymbol{\mu}_\beta + \boldsymbol{\Sigma}_\alpha^{-1/2} \left(\boldsymbol{\Sigma}_\alpha^{1/2} \boldsymbol{\Sigma}_\beta \boldsymbol{\Sigma}_\alpha^{1/2} \right)^{1/2} \boldsymbol{\Sigma}_\alpha^{-1/2} \cdot (x - \boldsymbol{\mu}_\alpha) . \quad (1.8)$$

$\mathbf{T}_{\alpha,\beta}$ is a deterministic transport map of single, specific data points, whose transport cost is given by the *Wasserstein metric*:

$$\mathcal{W}_2(\alpha, \beta) = \sqrt{\|\boldsymbol{\mu}_\alpha - \boldsymbol{\mu}_\beta\|^2 + \mathcal{B}(\boldsymbol{\Sigma}_\alpha, \boldsymbol{\Sigma}_\beta)^2} ,$$

with the Bures metric \mathcal{B} :

$$\mathcal{B}(\boldsymbol{\Sigma}_\alpha, \boldsymbol{\Sigma}_\beta) = \sqrt{\text{tr} \left(\boldsymbol{\Sigma}_\alpha + \boldsymbol{\Sigma}_\beta - 2 \left(\boldsymbol{\Sigma}_\alpha^{1/2} \boldsymbol{\Sigma}_\beta \boldsymbol{\Sigma}_\alpha^{1/2} \right)^{1/2} \right)} .$$

The field has been importantly shaped by Kantorovich in the 1940s [101], who suggested to relax the picture of permutation of single, specific data points and their *deterministic* transport map \mathbf{T} , and instead consider a coupling matrix $\mathbf{P} \in \mathbb{R}_+^{n \times m}$ of *probabilistic* mass flow [144]. This concept is also referred to as “mass splitting”, and introduces data point clouds $\boldsymbol{\alpha} \in \mathbb{R}^m, \boldsymbol{\beta} \in \mathbb{R}^n$, with m, n the number of data points. The key geometric properties of the underlying ground space are preserved, such that the distance between $\boldsymbol{\alpha}$ and $\boldsymbol{\beta}$ is again defined by the Wasserstein metric $\mathcal{W}_p(\boldsymbol{\alpha}, \boldsymbol{\beta}) := L_{\mathbf{C},p}(\boldsymbol{\alpha}, \boldsymbol{\beta})^{1/p}$ with p th moment and cost matrix \mathbf{C} . The optimization problem is defined as [144]

$$L_{\mathbf{C}}(\boldsymbol{\alpha}, \boldsymbol{\beta}) := \min_{\mathbf{P} \in \mathbf{U}(\boldsymbol{\alpha}, \boldsymbol{\beta})} \langle \mathbf{C}, \mathbf{P} \rangle := \sum_{i,j} \mathbf{C}_{i,j} \mathbf{P}_{i,j} , \quad (1.9)$$

with a set of maps connecting $\boldsymbol{\alpha}$ and $\boldsymbol{\beta}$ [144]:

$$\mathbf{U}(\boldsymbol{\alpha}, \boldsymbol{\beta}) := \{ \mathbf{P} \in \mathbb{R}_+^{n \times m} : \mathbf{P} \mathbf{1}_m = \boldsymbol{\alpha} \text{ and } \mathbf{P}^T \mathbf{1}_n = \boldsymbol{\beta} \} ,$$

where $\mathbf{P} \mathbf{1}_m = \left(\sum_j \mathbf{P}_{i,j} \right)_i \in \mathbb{R}^n$ and $\mathbf{P}^T \mathbf{1}_n = \left(\sum_i \mathbf{P}_{i,j} \right)_j \in \mathbb{R}^m$. Computational OT is dedicated to the determination of the optimal transport plan \mathbf{T} or \mathbf{P} and its cost \mathcal{W}_p . In contrast to the Gaussian case which has an analytical solution (eq. 1.8), the general OT-problem on point clouds in the Kantorovich formulation is approached *numerically*. First of all, $L_{\mathbf{C}}(\boldsymbol{\alpha}, \boldsymbol{\beta})$ is extended by the additive term $-\epsilon \mathbf{H}(\mathbf{P})$, referred to as “entropic regularization” [144]. As a consequence, the optimization problem has a unique solution and is eligible for the application of simple alternate minimization

algorithms [144]. In general, higher values of ϵ result in stronger smoothing and elevated convergence, and approach the exact solution up to the ϵ -induced inaccuracy. The *Sinkhorn* algorithm is an established method to solve the regularized form of eq. 1.9 [169]. Note that today, it is applied with several modifications compared to its original scheme [164]: iterations are conducted in the log-domain to prevent overflow, further the kernel matrix is sparsified by adaptive truncation, and, finally, the iterations are carried out in a top-down-approach with simultaneous ϵ -adaptation.

Finally, for both cases (point clouds and Gaussians), each probability measure can be described by a single data point. The ensemble of data points is a “set”, which together with the “metric” \mathcal{W}_p on this set forms the “metric space” [101]. Note that in general, the metric space is a Riemannian manifold and not cartesian. However, this particular metric space shows properties of an ∞ -dimensional, curved plane [135], on which each probability measure is represented by the single data point. This property allows for a local approximation of the metric space by a *tangent space* [101], and is readily understandable described in [194]. Each point in this tangent space defines a direction and a velocity with respect to the metric space. The operation from tangent to metric space is referred to as “exponential map”, its inverse as “logarithmic map”. Hence, based on the data points along a direction in the tangent space, the logarithmic map can be used to yield a *curve of data point clouds/Gaussians* (since the point cloud/Gaussian of each probability measure is reduced to a single data point). This concept is also termed “geodesic” or “dynamic”, and allows the analysis of temporal evolution of populations between α and β [104, 144]. In this work, this concept has been exploited to access the pathological trend from a normal state α towards a diseased state β (Ch. 4, [Fig. 8(e)]). OT-analysis is particularly powerful as it is not only based on single metrics such as size or gray values in images, but rather determines and discriminates texture and shape properties in a broader sense [194].

1.6.2 Embedding of OT in a Practical Analysis Workflow

Suppose that we have data from N probability measures (e.g. individuals in a medical study), which may be assigned to either of two groups (e.g. diseased or control). Each of these single individuals consists of any number of data points (*point cloud*), and each data point has M features (M -dimensional *feature space*). Importantly, OT-analysis allows for different numbers of data points among the individuals. Here, the question arises on which path these point clouds can be transferred into each other. In the following, first the Gaussian case, and then the point cloud generalization are considered,

supported by the illustration in Fig. 1.10 for $N = 4$ and $M = 2$.

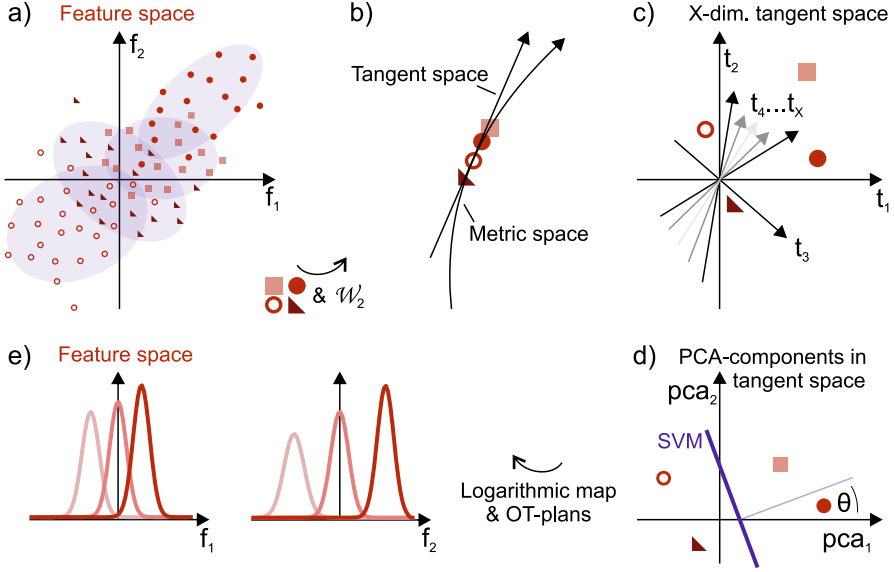


Fig. 1.10: Illustration of a data analysis workflow with optimal transport, for an example of four individuals and two features. (a) Data point clouds of the individuals are plotted in a 2d feature space, with their Gaussian approximations (shaded ellipsoids). (b) The set of probability measures and the Wasserstein metric \mathcal{W}_2 define the metric space. Each individual is represented by one data point. Local linearization yields the tangent space, (c) which is of dimension X . (d) PCA of this tangent space reveals the modes of dominant difference between the individuals. Based on the prior group classification, SVM (support vector machine) provides a hyperplane which separates both groups. The angle θ between the normal on the hyperplane and the main PCA-mode “pca1” indicates to which degree pca1 can serve group assignment *without* prior group classification. (e) Logarithmic map and OT-plans bring the mode (normal on SVM-hyperplane or pca1) back to feature space and make the OT-path along single features accessible.

Gaussian Case As a first step, each point cloud is approximated by a M -dimensional Gaussian with μ_n and Σ_n , as introduced in Sec. 1.6.1 and exemplified in Fig. 1.10(a). According to eq. 1.8, optimal transport plans \mathbf{T} between these Gaussians are generated. The costs related to the OT-plans are defined by the Wasserstein metric \mathcal{W}_2 . The set, in which each individual is represented by one data point, and the corresponding distances \mathcal{W}_2 define the *metric space*. Fig. 1.10(b) shows a simplification of this metric space, which resembles an ∞ -dimensional, curved plane. Local linearization of the

metric space leads to a $M^2 + M$ -dimensional¹³ subspace, *i.e.* the tangent space (cf. Fig. 1.10(c)). Principal component analysis (PCA) reveals the dominant axes of the tangent space, *i.e.* the modes of maximum change between the N data points of the individuals (cf. Fig. 1.10(d)). In order to relate this maximum change in tangent space to the M -dimensional feature space, first the logarithmic map and finally the OT-maps \mathbf{T} are consulted. At this point, data are again available as probability measures on the feature space, as plotted in Fig. 1.10(e). This step conveys that in the metric and tangent space, each individual is described by a single point, and that each single point in fact comprises a Gaussian distribution. Up to this point, *no* group classification has been included in the analysis.

Point Cloud Generalization The workflow for point clouds is very similar to the procedure for Gaussians introduced above. On the N point clouds, transport plans can be generated according to eq. 1.9. The coupling matrix $\mathbf{P} \in \mathbb{R}_+^{n \times m}$ specifies how each single data point in a cloud of m points is transported to the other cloud of n points, and vice versa. As described in Sec. 1.6.1 and as for the Gaussian case, a metric space is defined, which is locally approximated by a tangent space. Fig. 1.10(b) illustrates the approximation of the metric space by the tangent space. The tangent space consists of a direction and a velocity for each point. Fig. 1.10(c) indicates the high dimensionality (X) of the tangent space. As for the Gaussian case, PCA gives access to the main modes of change in the tangent space, and can be associated with the feature space by application of the logarithmic map and the OT-plans \mathbf{P} . Again, a single data point in the metric and tangent space contains an entire point cloud in feature space. The analysis of point clouds potentially reveals structural changes which can not be captured by Gaussian distributions *per se*. However, for truly Gaussian-distributed point clouds, OT-analysis in the Gaussian case leads to the exact same results as in the point cloud case.

Classification of Groups The agreement between the prior group-classification and the OT-analysis based on the M selected features can be quantified. To this end, the data points in PCA-space can be separated according to their group classification by a hyperplane, using a (linear) support vector machine (SVM) [15, 170] as plotted in Fig. 1.10(d). The distance between a data point and the SVM-plane yields the *SVM-score*, *i.e.*

¹³The dimensionality of the tangent space results from the $M \times M$ -dimensional covariance matrix, plus $M \times 1$ -dimensional array of mean values. It is possible to reduce its dimensionality by taking advantage of the symmetry of the covariance matrix, but computations on its full dimensionality are numerically more straightforward.

the separability of the individuals based on the M features. Further, it is demonstrated in Ch. 4 that the main PCA-mode can be in close agreement with the normal on the SVM-hyperplane: in this way, groups can be classified purely based on the features, without taking any prior group assignments into account. The agreement between the main PCA-mode and the normal on the SVM-hyperplane can be quantified by their scalar product (angle θ in Fig. 1.10(d)).

Bibliography

- [1] J. Als-Nielsen and D. McMorrow. *Elements of modern X-ray physics*. John Wiley & Sons, 2011.
- [2] R. E. Alvarez and A. Macovski. “Energy-selective reconstructions in x-ray computerised tomography.” In: *Physics in Medicine & Biology* 21.5 (1976), p. 733.
- [3] D. G. Amaral, H. E. Scharfman, and P. Lavenex. “The dentate gyrus: fundamental neuroanatomical organization.” In: *The Dentate Gyrus: A Comprehensive Guide to Structure, Function, and Clinical Implications*. Elsevier, 2007, pp. 3–790.
- [4] K. Amunts, C. Lepage, L. Borgeat, H. Mohlberg, T. Dickscheid, M.-É. Rousseau, S. Bludau, P.-L. Bazin, L. B. Lewis, A.-M. Oros-Peusquens, et al. “BigBrain: an ultrahigh-resolution 3D human brain model.” In: *Science* 340.6139 (2013), pp. 1472–1475.
- [5] T. Arakhamia, C. E. Lee, Y. Carlomagno, D. M. Duong, S. R. Kunder, K. Wang, D. Williams, M. DeTure, D. W. Dickson, C. N. Cook, et al. “Posttranslational modifications mediate the structural diversity of tauopathy strains.” In: *Cell* 180.4 (2020), pp. 633–644.
- [6] F. A. Azevedo, L. R. Carvalho, L. T. Grinberg, J. M. Farfel, R. E. Ferretti, R. E. Leite, W. J. Filho, R. Lent, and S. Herculano-Houzel. “Equal numbers of neuronal and nonneuronal cells make the human brain an isometrically scaled-up primate brain.” In: *Journal of Comparative Neurology* 513.5 (2009), pp. 532–541.
- [7] A. Badhwar, G. P. McFall, S. Sapkota, S. E. Black, H. Chertkow, S. Duchesne, M. Masellis, L. Li, R. A. Dixon, and P. Bellec. “A multiomics approach to heterogeneity in Alzheimer’s disease: focused review and roadmap.” In: *Brain* 143.5 (2020), pp. 1315–1331.
- [8] G. Bahr, G. Bloom, and U. Friberg. “Volume changes of tissues in physiological fluids during fixation in osmium tetroxide or formaldehyde and during subsequent treatment.” In: *Experimental Cell Research* 12.2 (1957), pp. 342–355.

- [9] M. Bartels, M. Krenkel, J. Haber, R. Wilke, and T. Salditt. “X-ray holographic imaging of hydrated biological cells in solution.” In: *Physical Review Letters* 114.4 (2015), p. 048103.
- [10] D. S. Bassett and F. Siebenhühner. “Multiscale network organization in the human brain.” In: *Multiscale Analysis and Nonlinear Dynamics* (2013), pp. 179–204.
- [11] M. Beltran, D. M. Paganin, K. Siu, A. Fouras, S. Hooper, D. Reser, and M. Kitchen. “Interface-specific x-ray phase retrieval tomography of complex biological organs.” In: *Physics in Medicine & Biology* 56.23 (2011), p. 7353.
- [12] S. Berg, D. Kutra, T. Kroeger, C. N. Straehle, B. X. Kausler, C. Haubold, M. Schiegg, J. Ales, T. Beier, M. Rudy, et al. “Ilastik: interactive machine learning for (bio) image analysis.” In: *Nature Methods* 16 (2019), pp. 1–7.
- [13] R. F. Betzel and D. S. Bassett. “Multi-scale brain networks.” In: *NeuroImage* 160 (2017), pp. 73–83.
- [14] T. Bicer, D. Gursoy, R. Kettimuthu, I. T. Foster, B. Ren, V. De Andrede, and F. De Carlo. “Real-time data analysis and autonomous steering of synchrotron light source experiments.” In: *2017 IEEE 13th International Conference on e-Science (e-Science)*. IEEE. 2017, pp. 59–68.
- [15] C. M. Bishop. “Pattern recognition.” In: *Machine Learning* 128.9 (2006).
- [16] C. Bosch, T. Ackels, A. Pacureanu, Y. Zhang, C. J. Peddie, M. Berning, N. Rzepka, M.-C. Zdora, I. Whiteley, M. Storm, et al. “Functional and multiscale 3D structural investigation of brain tissue through correlative in vivo physiology, synchrotron micro-tomography and volume electron microscopy.” In: *bioRxiv* (2021).
- [17] C. Bosch, A. Martínez, N. Masachs, C. M. Teixeira, I. Feraud, F. Ulloa, E. Pérez-Martínez, C. Lois, J. X. Comella, J. DeFelipe, et al. “FIB/SEM technology and high-throughput 3D reconstruction of dendritic spines and synapses in GFP-labeled adult-generated neurons.” In: *Frontiers in Neuroanatomy* 9 (2015), p. 60.
- [18] S. Boyd, J. Dattorro, et al. “Alternating projections.” In: *EE392o, Stanford University* (2003).

- [19] H. Braak, I. Alafuzoff, T. Arzberger, H. Kretschmar, and K. Del Tredici. "Staging of Alzheimer disease-associated neurofibrillary pathology using paraffin sections and immunocytochemistry." In: *Acta Neuropathologica* 112.4 (2006), pp. 389–404.
- [20] S. Brady, G. Siegel, R. W. Albers, and D. Price. *Basic neurochemistry: principles of molecular, cellular, and medical neurobiology*. 7th ed. Academic press, 2011.
- [21] M. Brown, R. Reed, and R. Henry. "Effects of dehydration mediums and temperature on total dehydration time and tissue shrinkage." In: *Journal of the International Society for Plastination* 17 (2002), pp. 28–33.
- [22] W. Brück and C. Stadelmann. "Inflammation and degeneration in multiple sclerosis." In: *Neurological Sciences* 24.5 (2003), s265–s267.
- [23] M. A. Busche, X. Chen, H. A. Henning, J. Reichwald, M. Staufenbiel, B. Sakmann, and A. Konnerth. "Critical role of soluble amyloid- β for early hippocampal hyperactivity in a mouse model of Alzheimer's disease." In: *Proceedings of the National Academy of Sciences* 109.22 (2012), pp. 8740–8745.
- [24] M. A. Busche, C. Grienberger, A. D. Keskin, B. Song, U. Neumann, M. Staufenbiel, H. Förstl, and A. Konnerth. "Decreased amyloid- β and increased neuronal hyperactivity by immunotherapy in Alzheimer's models." In: *Nature Neuroscience* 18.12 (2015), pp. 1725–1727.
- [25] M. Busse, J. P. Marcinišzyn, S. Ferstl, M. A. Kimm, F. Pfeiffer, and T. Gulder. "3D-Non-destructive Imaging through Heavy-Metal Eosin Salt Contrast Agents." In: *Chemistry (Weinheim an der Bergstrasse, Germany)* 27.14 (2021), p. 4561.
- [26] M. Busse, M. Müller, M. A. Kimm, S. Ferstl, S. Allner, K. Achterhold, J. Herzen, and F. Pfeiffer. "Three-dimensional virtual histology enabled through cytoplasm-specific X-ray stain for microscopic and nanoscopic computed tomography." In: *Proceedings of the National Academy of Sciences* 115.10 (2018), pp. 2293–2298.
- [27] J.-W. Buurlage, F. Marone, D. M. Pelt, W. J. Palenstijn, M. Stampanoni, K. J. Batenburg, and C. M. Schlepütz. "Real-time reconstruction and visualisation towards dynamic feedback control during time-resolved tomography experiments at TOMCAT." In: *Scientific Reports* 9.1 (2019), pp. 1–11.
- [28] J. Buytaert, J. Goyens, D. De Greef, P. Aerts, and J. Dirckx. "Volume shrinkage of bone, brain and muscle tissue in sample preparation for micro-CT and light sheet fluorescence microscopy (LSFM)." In: *Microscopy and Microanalysis* 20.4 (2014), pp. 1208–1217.

- [29] T. Buzug. *Computed Tomography: From Photon Statistics to Modern Cone-Beam CT*. Springer Berlin Heidelberg, 2008.
- [30] S. Cajal. “¿Neuronismo o reticularismo? Las pruebas objetivas de la unidad anatómica de las células nerviosas.” In: *Arch. Neurobiol.* 13 (1933), pp. 1–44.
- [31] M. Calabrese, R. Magliozzi, O. Ciccarelli, J. J. Geurts, R. Reynolds, and R. Martin. “Exploring the origins of grey matter damage in multiple sclerosis.” In: *Nature Reviews Neuroscience* 16.3 (2015), pp. 147–158.
- [32] E. Carboni, J.-D. Nicolas, M. Töpperwien, C. Stadelmann-Nessler, P. Lingor, and T. Salditt. “Imaging of neuronal tissues by x-ray diffraction and x-ray fluorescence microscopy: evaluation of contrast and biomarkers for neurodegenerative diseases.” In: *Biomedical optics express* 8.10 (2017), pp. 4331–4347.
- [33] D. C. Champeney and D. Champeney. *A handbook of Fourier theorems*. Cambridge University Press, 1987.
- [34] P. Chen, M. R. Miah, and M. Aschner. “Metals and neurodegeneration.” In: *F1000Research* 5 (2016).
- [35] M. Chourrout, H. Rositi, E. Ong, V. Hubert, A. Paccalet, L. Foucault, A. Autret, B. Fayard, C. Olivier, R. Bolbos, et al. “Brain virtual histology with X-ray phase-contrast tomography Part I: whole-brain myelin mapping in white-matter injury models.” In: *bioRxiv* (2021).
- [36] B. J. Claiborne, D. G. Amaral, and W. M. Cowan. “Quantitative, three-dimensional analysis of granule cell dendrites in the rat dentate gyrus.” In: *The Journal of Comparative Neurology* 302.2 (1990), pp. 206–219.
- [37] M. A. Clark, M. B. Worrell, and J. E. Pless. “Postmortem changes in soft tissues.” In: *Forensic Taphonomy: the postmortem Fate of Human Remains* (1997), pp. 151–164.
- [38] P. Cloetens. “Contribution to phase contrast imaging, reconstruction and tomography with hard synchrotron radiation: principles, implementation and applications.” PhD thesis. VUB (Faculteit Toegepaste Wetenschappen), 1999.
- [39] P. Cloetens, J. Guigay, C. De Martino, J. Baruchel, and M. Schlenker. “Fractional Talbot imaging of phase gratings with hard x rays.” In: *Optics Letters* 22.14 (1997), pp. 1059–1061.

- [40] P. Cloetens, W. Ludwig, J. Baruchel, D. Van Dyck, J. Van Landuyt, J. Guigay, and M. Schlenker. “Holotomography: Quantitative phase tomography with micrometer resolution using hard synchrotron radiation x rays.” In: *Applied Physics Letters* 75.19 (1999), pp. 2912–2914.
- [41] D. Crapper, S. Quittkat, and U. De Boni. “Altered chromatin conformation in Alzheimer’s disease.” In: *Brain: a Journal of Neurology* 102.3 (1979), p. 483.
- [42] J. C. Da Silva, M. Guizar-Sicairos, M. Holler, A. Diaz, J. A. van Bokhoven, O. Bunk, and A. Menzel. “Quantitative region-of-interest tomography using variable field of view.” In: *Optics Express* 26.13 (2018), pp. 16752–16768.
- [43] G. Das, K. Reuhl, and R. Zhou. “The golgi-cox method.” In: *Neural Development*. Springer, 2013, pp. 313–321.
- [44] T. M. Dawson, T. E. Golde, and C. Lagier-Tourenne. “Animal models of neurodegenerative diseases.” In: *Nature Neuroscience* 21.10 (2018), pp. 1370–1379.
- [45] V. De Andrade, V. Nikitin, M. Wojcik, A. Deriy, S. Bean, D. Shu, T. Mooney, K. Peterson, P. Kc, K. Li, S. Ali, K. Fezzaa, D. Gürsoy, C. Arico, S. Ouendi, D. Troadec, P. Simon, F. De Carlo, and C. Lethien. “Fast X-ray Nanotomography with Sub-10 nm Resolution as a Powerful Imaging Tool for Nanotechnology and Energy Storage Applications.” In: *Advanced Materials* 33.21 (2021), p. 2008653.
- [46] Y. De Witte, M. Boone, J. Vlassenbroeck, M. Dierick, and L. Van Hoorebeke. “Bronnikov-aided correction for x-ray computed tomography.” In: *JOSA A* 26.4 (2009), pp. 890–894.
- [47] S.-L. Ding, J. J. Royall, S. M. Sunkin, L. Ng, B. A. Facer, P. Lesnar, A. Guillozet-Bongaarts, B. McMurray, A. Szafer, T. A. Dolbeare, et al. “Comprehensive cellular-resolution atlas of the adult human brain.” In: *The Journal of Comparative Neurology* 525.2 (2017), p. 407.
- [48] H. H. Donaldson and G. Hoke. “On the areas of the axis cylinder and medullary sheath as seen in cross sections of the spinal nerves of vertebrates.” In: *Journal of Comparative Neurology and Psychology* 15.1 (1905), pp. 1–16.
- [49] J. Dong, J. Fu, and Z. He. “A deep learning reconstruction framework for X-ray computed tomography with incomplete data.” In: *PloS one* 14.11 (2019), e0224426.
- [50] P. P. B. Eggermont, G. T. Herman, and A. Lent. “Iterative algorithms for large partitioned linear systems, with applications to image reconstruction.” In: *Linear Algebra and its Applications* 40 (1981), pp. 37–67.

- [51] S. Eyer. "Translation from Plato's Republic 514b–518d ("Allegory of the Cave")." In: *Ahiman: A Review of Masonic Culture and Tradition* 1 (2009), pp. 73–78.
- [52] A. Faridani, K. A. Buglione, P. Huabsomboon, O. D. Iancu, J. McGrath, et al. "Introduction to local tomography." In: *Contemporary Mathematics* 278 (2001), pp. 29–48.
- [53] L. A. Feldkamp, L. C. Davis, and J. W. Kress. "Practical cone-beam algorithm." In: *Josa a* 1.6 (1984), pp. 612–619.
- [54] I. Ferrer, A. Martinez, S. Boluda, P. Parchi, and M. Barrachina. "Brain banks: benefits, limitations and cautions concerning the use of post-mortem brain tissue for molecular studies." In: *Cell and Tissue Banking* 9.3 (2008), p. 181.
- [55] M. Filippi, W. Brück, D. Chard, F. Fazekas, J. J. Geurts, C. Enzinger, S. Hametner, T. Kuhlmann, P. Preziosa, À. Rovira, et al. "Association between pathological and MRI findings in multiple sclerosis." In: *The Lancet Neurology* 18.2 (2019), pp. 198–210.
- [56] S. Flenner, M. Storm, A. Kubec, E. Longo, F. Döring, D. M. Pelt, C. David, M. Müller, and I. Greving. "Pushing the temporal resolution in absorption and Zernike phase contrast nanotomography: enabling fast in situ experiments." In: *Journal of Synchrotron Radiation* 27.5 (2020).
- [57] C. la Fougère, S. Grant, A. Kostikov, R. Schirmacher, P. Gravel, H. M. Schipper, A. Reader, A. Evans, and A. Thiel. "Where in-vivo imaging meets cytoarchitectonics: the relationship between cortical thickness and neuronal density measured with high-resolution [18F] flumazenil-PET." In: *NeuroImage* 56.3 (2011), pp. 951–960.
- [58] B. Frost. "Alzheimer's disease: An acquired neurodegenerative laminopathy." In: *Nucleus* 7.3 (2016), pp. 275–283.
- [59] B. Frost, M. Hemberg, J. Lewis, and M. B. Feany. "Tau promotes neurodegeneration through global chromatin relaxation." In: *Nature Neuroscience* 17.3 (2014), pp. 357–366.
- [60] D. Gabor. "A new microscopic principle." In: *Nature* 161 (1948), pp. 777–778.
- [61] F. H. Gage. "Mammalian neural stem cells." In: *Science* 287.5457 (2000), pp. 1433–1438.
- [62] K. Giewekemeyer, S. Krüger, S. Kalbfleisch, M. Bartels, C. Beta, and T. Salditt. "X-ray propagation microscopy of biological cells using waveguides as a quasi-point source." In: *Physical Review A* 83.2 (2011), p. 023804.

- [63] L. Gil, S. A. Niño, E. Chi-Ahumada, I. Rodríguez-Leyva, C. Guerrero, A. B. Rebolledo, J. A. Arias, and M. E. Jiménez-Capdeville. “Perinuclear Lamin A and Nucleoplasmic Lamin B2 Characterize Two Types of Hippocampal Neurons through Alzheimer’s Disease Progression.” In: *International Journal of Molecular Sciences* 21.5 (2020), p. 1841.
- [64] P. Gilbert. “Iterative methods for the three-dimensional reconstruction of an object from projections.” In: *Journal of Theoretical Biology* 36.1 (1972), pp. 105–117.
- [65] C. Golgi. “Di una nuova reasione apparentemente nera delle cellule nervose cerebrali ottenuta col bichloruro di mercurio.” In: *Arch. Med. Sci.* 3 (1879), pp. 1–7.
- [66] C. Golgi. “Modificazione del metodo di colorazione deli elementi nervosi col bichloruru Di mercurio.” In: *La Rivista Italiana della Medicina di Laboratorio* 7 (1891), pp. 193–194.
- [67] C. Golgi. “Sulla struttura della sostanza grigia del cervello.” In: *Gazz. Med. Ital. - Lombardia* 6 (1873), pp. 244–246.
- [68] J. W. Goodman. *Introduction to Fourier optics*. 4th ed. Roberts and Company Publishers, 2005.
- [69] J. W. Goodman. *Statistical optics*. John Wiley & Sons, 2015.
- [70] A. Groso, R. Abela, and M. Stampanoni. “Implementation of a fast method for high resolution phase contrast tomography.” In: *Optics Express* 14.18 (2006), pp. 8103–8110.
- [71] A. Groso, M. Stampanoni, R. Abela, P. Schneider, S. Linga, and R. Müller. “Phase contrast tomography: an alternative approach.” In: *Applied Physics Letters* 88.21 (2006), p. 214104.
- [72] T. Guo, W. Noble, and D. P. Hanger. “Roles of tau protein in health and disease.” In: *Acta Neuropathologica* 133.5 (2017), pp. 665–704.
- [73] J. Hagemann, M. Töpperwien, and T. Salditt. “Phase retrieval for near-field X-ray imaging beyond linearisation or compact support.” In: *Applied Physics Letters* 113.4 (2018), p. 041109.
- [74] J. Hagemann. *Johannes Hagemann X Ray Near Field Holography: Beyond Idealized Assumptions of the Probe*. Vol. 24. Göttingen series in X-ray physics. Universitätsverlag Göttingen, 2017.

- [75] M. T. Haindl, U. Köck, M. Zeitelhofer-Adzemovic, F. Fazekas, and S. Hochmeister. “The formation of a glial scar does not prohibit remyelination in an animal model of multiple sclerosis.” In: *Glia* 67.3 (2019), pp. 467–481.
- [76] W. Han and N. Šestan. “Cortical projection neurons: sprung from the same root.” In: *Neuron* 80.5 (2013), pp. 1103–1105.
- [77] G. Harauz and M. van Heel. “Exact filters for general geometry three dimensional reconstruction.” In: *Optik* 73.4 (1986), pp. 146–156.
- [78] M. A. Hayat et al. *Principles and techniques of electron microscopy. Biological applications*. Edward Arnold., 1981.
- [79] M. Helmstaedter. “Cellular-resolution connectomics: challenges of dense neural circuit reconstruction.” In: *Nature Methods* 10.6 (2013), pp. 501–507.
- [80] M. Helmstaedter, K. L. Briggman, S. C. Turaga, V. Jain, H. S. Seung, and W. Denk. “Connectomic reconstruction of the inner plexiform layer in the mouse retina.” In: *Nature* 500.7461 (2013), pp. 168–174.
- [81] S. Herculano-Houzel. “The human brain in numbers: a linearly scaled-up primate brain.” In: *Frontiers in Human Neuroscience* 3 (2009), p. 31.
- [82] G. T. Herman. “Image reconstruction from projections.” In: *The Fundamental of Computerized Tomography* (1980), pp. 260–276.
- [83] S. E. Hieber, C. Bikis, A. Khimchenko, G. Schweighauser, J. Hench, N. Chicherova, G. Schulz, and B. Müller. “Tomographic brain imaging with nucleolar detail and automatic cell counting.” In: *Scientific Reports* 6.1 (2016), pp. 1–11.
- [84] K. Hirai, G. Aliev, A. Nunomura, H. Fujioka, R. L. Russell, C. S. Atwood, A. B. Johnson, Y. Kress, H. V. Vinters, M. Tabaton, et al. “Mitochondrial abnormalities in Alzheimer’s disease.” In: *Journal of Neuroscience* 21.9 (2001), pp. 3017–3023.
- [85] C. Homann, T. Hohage, J. Hagemann, A.-L. Robisch, and T. Salditt. “Validity of the empty-beam correction in near-field imaging.” In: *Physical Review A* 91.1 (2015), p. 013821.
- [86] Y. Hua, P. Laserstein, and M. Helmstaedter. “Large-volume en-bloc staining for electron microscopy-based connectomics.” In: *Nature Communications* 6.1 (2015), p. 7923.
- [87] E. G. Hughes, J. L. Orthmann-Murphy, A. J. Langseth, and D. E. Bergles. “Myelin remodeling through experience-dependent oligodendrogenesis in the adult somatosensory cortex.” In: *Nature Neuroscience* 21.5 (2018), pp. 696–706.

- [88] J. Hursh. "Conduction velocity and diameter of nerve fibers." In: *American Journal of Physiology-Legacy Content* 127.1 (1939), pp. 131–139.
- [89] H. Huxley. "Some aspects of staining of tissue for sectioning." In: *Journal of the Royal Microscopical Society* 78.1-2 (1958), pp. 30–34.
- [90] H. Huxley and G. Zubay. "Preferential staining of nucleic acid-containing structures for electron microscopy." In: *The Journal of Cell Biology* 11.2 (1961), pp. 273–296.
- [91] J. B. Issa, B. D. Haefele, A. Agarwal, D. E. Bergles, E. D. Young, and D. T. Yue. "Multiscale optical Ca²⁺ imaging of tonal organization in mouse auditory cortex." In: *Neuron* 83.4 (2014), pp. 944–959.
- [92] C. Jack, F. Ruffini, A. Bar-Or, and J. P. Antel. "Microglia and multiple sclerosis." In: *Journal of Neuroscience Research* 81.3 (2005), pp. 363–373.
- [93] C. R. Jack Jr, D. A. Bennett, K. Blennow, M. C. Carrillo, B. Dunn, S. B. Haeblerlein, D. M. Holtzman, W. Jagust, F. Jessen, J. Karlawish, et al. "NIA-AA research framework: toward a biological definition of Alzheimer's disease." In: *Alzheimer's & Dementia* 14.4 (2018), pp. 535–562.
- [94] S. Jähne, F. Mikulasch, H. G. Heuer, S. Truckenbrodt, P. Agüi-Gonzalez, K. Grewe, A. Vogts, S. O. Rizzoli, and V. Priesemann. "Presynaptic activity and protein turnover are correlated at the single-synapse level." In: *Cell Reports* 34.11 (2021), p. 108841.
- [95] D. T. Jones, D. S. Knopman, J. L. Gunter, J. Graff-Radford, P. Vemuri, B. F. Boeve, R. C. Petersen, M. W. Weiner, and C. R. Jack Jr. "Cascading network failure across the Alzheimer's disease spectrum." In: *Brain* 139.2 (2016), pp. 547–562.
- [96] K. Joppe, J.-D. Nicolas, T. A. Grünewald, M. Eckermann, T. Salditt, and P. Lingor. "Elemental quantification and analysis of structural abnormalities in neurons from Parkinson's-diseased brains by X-ray fluorescence microscopy and diffraction." In: *Biomedical Optics Express* 11.7 (2020), pp. 3423–3443.
- [97] M. Jucker. "The benefits and limitations of animal models for translational research in neurodegenerative diseases." In: *Nature Medicine* 16.11 (2010), pp. 1210–1214.
- [98] S. Kaczmarz. "Angenäherte Auflösung linearer Gleichungssysteme." In: *Bulletin International de l'Académie Polonaise des Sciences et des Lettres. Classe des Sciences Mathématiques et Naturelles. Série A, Sciences Mathématiques* (1937), pp. 355–357.

- [99] A. C. Kak, M. Slaney, and G. Wang. *Principles of computerized tomographic imaging*. 2002.
- [100] E. R. Kandel, J. H. Schwartz, T. M. Jessell, S. Siegelbaum, A. J. Hudspeth, and S. Mack. *Principles of neural science*. Vol. 4. McGraw-hill New York, 2000.
- [101] L. Kantorovich. “On the transfer of masses (in Russian).” In: *Doklady Akademii Nauk*. Vol. 37. 2. 1942, pp. 227–229.
- [102] R. A. Ketcham. “New algorithms for ring artifact removal.” In: *Proc. SPIE* 6318 (2006), 63180O.
- [103] H. D. King. “The effects of formaldehyde on the brain.” In: *Journal of Comparative Neurology* 23 (1913), p. 283.
- [104] S. Kolouri, S. R. Park, M. Thorpe, D. Slepcev, and G. K. Rohde. “Optimal mass transport: Signal processing and machine-learning applications.” In: *IEEE Signal Processing Magazine* 34.4 (2017), pp. 43–59.
- [105] A. T. Kuan, J. S. Phelps, L. A. Thomas, T. M. Nguyen, J. Han, C.-L. Chen, A. W. Azevedo, J. C. Tuthill, J. Funke, P. Cloetens, et al. “Dense neuronal reconstruction through X-ray holographic nano-tomography.” In: *Nature Neuroscience* 23.12 (2020), pp. 1637–1643.
- [106] S. Kulpe, M. Dierolf, B. Günther, J. Brantl, M. Busse, K. Achterhold, B. Gleich, F. Pfeiffer, and D. Pfeiffer. “Dynamic K-edge Subtraction fluoroscopy at a compact inverse-compton Synchrotron X-ray Source.” In: *Scientific Reports* 10.1 (2020), pp. 1–9.
- [107] M. Kurudirek. “Effective atomic numbers and electron densities of some human tissues and dosimetric materials for mean energies of various radiation sources relevant to radiotherapy and medical applications.” In: *Radiation Physics and Chemistry* 102 (2014), pp. 139–146.
- [108] A. Kutzelnigg, C. F. Lucchinetti, C. Stadelmann, W. Brück, H. Rauschka, M. Bergmann, M. Schmidbauer, J. E. Parisi, and H. Lassmann. “Cortical demyelination and diffuse white matter injury in multiple sclerosis.” In: *Brain* 128.11 (2005), pp. 2705–2712.
- [109] H. Lagerlöf and T. Torgersruud. “Zur Kenntnis der Gewichts- und Volumenveränderungen bei Formalinfixation von Gehirngewebe und der Einwirkung von NaCl-Zusatz darauf.” In: *J Psychol Neurol* 46 (1934), pp. 178–188.

- [110] H. M. Lai, A. K. L. Liu, H. H. M. Ng, M. H. Goldfinger, T. W. Chau, J. DeFelice, B. S. Tilley, W. M. Wong, W. Wu, and S. M. Gentleman. “Next generation histology methods for three-dimensional imaging of fresh and archival human brain tissues.” In: *Nature Communications* 9.1 (2018), pp. 1–12.
- [111] H. T. Li, F. Schaff, L. C. Croton, K. S. Morgan, and M. J. Kitchen. “Quantitative material decomposition using linear iterative near-field phase retrieval dual-energy x-ray imaging.” In: *Physics in Medicine & Biology* 65.18 (2020), p. 185014.
- [112] Q. Li and B. A. Barres. “Microglia and macrophages in brain homeostasis and disease.” In: *Nature Reviews Immunology* 18.4 (2018), pp. 225–242.
- [113] Z. Liu, T. Bicer, R. Kettimuthu, D. Gürsoy, F. D. Carlo, and I. T. Foster. “TomoGAN: Low-Dose X-Ray Tomography with Generative Adversarial Networks.” In: *CoRR* abs/1902.07582 (2019).
- [114] H. Lodish, A. Berk, S. L. Zipursky, P. Matsudaira, D. Baltimore, and J. E. Darnell. “Molecular cell biology.” In: *Biochemistry and Molecular Biology Education* (2001).
- [115] L. M. Lohse, A.-L. Robisch, M. Töpperwien, S. Maretzke, M. Krenkel, J. Hagemann, and T. Salditt. “A phase-retrieval toolbox for X-ray holography and tomography.” In: *Journal of Synchrotron Radiation* 27.3 (2020).
- [116] S. Maretzke. “Inverse Problems in Propagation-based X-ray Phase Contrast Imaging and Tomography: Stability Analysis and Reconstruction Methods.” PhD thesis. Niedersächsische Staats-und Universitätsbibliothek Göttingen, 2019.
- [117] F. Marone and M. Stampanoni. “Regridding reconstruction algorithm for real-time tomographic imaging.” In: *Journal of Synchrotron Radiation* 19.6 (2012), pp. 1029–1037.
- [118] W. S. McCulloch and W. Pitts. “A logical calculus of the ideas immanent in nervous activity.” In: *The Bulletin of Mathematical Biophysics* 5.4 (1943), pp. 115–133.
- [119] T. L. McHugh, A. J. Saykin, H. A. Wishart, L. A. Flashman, H. B. Cleavinger, L. A. Rabin, A. C. Mamourian, and L. Shen. “Hippocampal Volume and Shape Analysis in an Older Adult Population.” In: *The Clinical Neuropsychologist* 21.1 (2007), pp. 130–145.

- [120] I. Méndez-López, I. Blanco-Luquin, J. Sánchez-Ruiz de Gordo, A. Urdániz-Casado, M. Roldán, B. Acha, C. Echavarri, V. Zelaya, I. Jericó, and M. Mendioroz. “Hippocampal LMNA Gene Expression is Increased in Late-Stage Alzheimer’s Disease.” In: *International Journal of Molecular Sciences* 20.4 (2019), p. 878.
- [121] A.-F. Mentis, E. Dardiotis, N. Grigoriadis, E. Petinaki, and G. Hadjigeorgiou. “Viruses and endogenous retroviruses in multiple sclerosis: From correlation to causation.” In: *Acta Neurologica Scandinavica* 136.6 (2017), pp. 606–616.
- [122] S. Mikula and W. Denk. “High-resolution whole-brain staining for electron microscopic circuit reconstruction.” In: *Nature Methods* 12.6 (2015), p. 541.
- [123] S. Mikula, J. Binding, and W. Denk. “Staining and embedding the whole mouse brain for electron microscopy.” In: *Nature Methods* 9.12 (2012), pp. 1198–1201.
- [124] S. S. Mirra, A. Heyman, D. McKeel, S. Sumi, B. J. Crain, L. Brownlee, F. Vogel, J. Hughes, G. Van Belle, L. Berg, et al. “The Consortium to Establish a Registry for Alzheimer’s Disease (CERAD): Part II. Standardization of the neuropathologic assessment of Alzheimer’s disease.” In: *Neurology* 41.4 (1991), pp. 479–479.
- [125] R. Mokso, F. Marone, D. Haberthür, J. Schittny, G. Mikuljan, A. Isenegger, and M. Stampanoni. “Following dynamic processes by X-ray tomographic microscopy with sub-second temporal resolution.” In: *AIP conference proceedings*. Vol. 1365. 1. American Institute of Physics. 2011, pp. 38–41.
- [126] T. J. Montine, C. H. Phelps, T. G. Beach, E. H. Bigio, N. J. Cairns, D. W. Dickson, C. Duyckaerts, M. P. Frosch, E. Masliah, S. S. Mirra, et al. “National Institute on Aging–Alzheimer’s Association guidelines for the neuropathologic assessment of Alzheimer’s disease: a practical approach.” In: *Acta Neuropathologica* 123.1 (2012), pp. 1–11.
- [127] M. Müller, M. A. Kimm, S. Ferstl, S. Allner, K. Achterhold, J. Herzen, F. Pfeiffer, and M. Busse. “Nucleus-specific X-ray stain for 3D virtual histology.” In: *Scientific Reports* 8.1 (2018), pp. 1–10.
- [128] B. Münch, P. Trtik, F. Marone, and M. Stampanoni. “Stripe and ring artifact removal with combined wavelet-Fourier filtering.” In: *Optics Express* 17.10 (2009), pp. 8567–8591.
- [129] I. Napoli and H. Neumann. “Protective effects of microglia in multiple sclerosis.” In: *Experimental Neurology* 225.1 (2010), pp. 24–28.
- [130] F. Natterer. *The mathematics of computerized tomography*. SIAM, 2001.

- [131] J. G. Nicholls, A. R. Martin, B. G. Wallace, and P. A. Fuchs. *From neuron to brain*. 4th ed. Vol. 271. Sinauer Associates Sunderland, MA, 2001.
- [132] A. Nimmerjahn and D. E. Bergles. “Large-scale recording of astrocyte activity.” In: *Current Opinion in Neurobiology* 32 (2015), pp. 95–106.
- [133] C. Nyhus, M. Pihl, P. Hyttel, and V. J. Hall. “Evidence for nucleolar dysfunction in Alzheimer’s disease.” In: *Reviews in the Neurosciences* 30.7 (2019), pp. 685–700.
- [134] M. Osterhoff. *Wave optical simulations of x-ray nano-focusing optics*. Vol. 9. Universitätsverlag Göttingen, 2012.
- [135] F. Otto. “The geometry of dissipative evolution equations: the porous medium equation.” In: *Comm. Partial Differential Equations* 26.1-2 (2001), pp. 101–174.
- [136] *P10 - Coherence Application Beamline Unified Data Sheet*. URL: https://photon-science.desy.de/facilities/petra_iii/beamlines/p10_coherence_applications/unified_data_sheet_p10/index_eng.html (visited on 07/20/2021).
- [137] A. M. Packer, D. S. Peterka, J. J. Hirtz, R. Prakash, K. Deisseroth, and R. Yuste. “Two-photon optogenetics of dendritic spines and neural circuits.” In: *Nature Methods* 9.12 (2012), pp. 1202–1205.
- [138] D. Paganin et al. *Coherent X-ray optics*. 6. Oxford University Press on Demand, 2006.
- [139] D. Paganin, S. C. Mayo, T. E. Gureyev, P. R. Miller, and S. W. Wilkins. “Simultaneous phase and amplitude extraction from a single defocused image of a homogeneous object.” In: *Journal of Microscopy* 206.1 (2002), pp. 33–40.
- [140] D. Paganin and K. A. Nugent. “Noninterferometric phase imaging with partially coherent light.” In: *Physical Review Letters* 80.12 (1998), p. 2586.
- [141] D. M. Paganin, V. Favre-Nicolin, A. Mirone, A. Rack, J. Villanova, M. P. Olbinado, V. Fernandez, J. C. da Silva, and D. Pelliccia. “Boosting spatial resolution by incorporating periodic boundary conditions into single-distance hard-x-ray phase retrieval.” In: *Journal of Optics* 22.11 (2020), p. 115607.
- [142] F. Palermo, N. Pieroni, L. Maugeri, G. B. Provinciali, A. Sanna, L. Massimi, M. Catalano, M. P. Olbinado, I. Bukreeva, M. Fratini, et al. “X-ray Phase Contrast Tomography Serves Preclinical Investigation of Neurodegenerative Diseases.” In: *Frontiers in Neuroscience* 14 (2020), p. 1137.

- [143] P. Patrikios, C. Stadelmann, A. Kutzelnigg, H. Rauschka, M. Schmidbauer, H. Laursen, P. S. Sorensen, W. Brück, C. Lucchinetti, and H. Lassmann. “Remyelination is extensive in a subset of multiple sclerosis patients.” In: *Brain* 129.12 (2006), pp. 3165–3172.
- [144] G. Peyré, M. Cuturi, et al. “Computational optimal transport: With applications to data science.” In: *Foundations and Trends® in Machine Learning* 11.5-6 (2019), pp. 355–607.
- [145] B. R. Pinzer, M. Cacquevel, P. Modregger, S. McDonald, J. Bensadoun, T. Thuerling, P. Aebischer, and M. Stampanoni. “Imaging brain amyloid deposition using grating-based differential phase contrast tomography.” In: *NeuroImage* 61.4 (2012), pp. 1336–1346.
- [146] J.-F. Poulin, B. Tasic, J. Hjerling-Leffler, J. M. Trimarchi, and R. Awatramani. “Disentangling neural cell diversity using single-cell transcriptomics.” In: *Nature Neuroscience* 19.9 (2016), pp. 1131–1141.
- [147] J. Radon. “Über die Bestimmung von Funktionen durch ihre Integralwerte längs gewisser Mannigfaltigkeiten.[On the determination of functions from their integrals along certain manifolds].” In: *SBLepzig* 29 (1917), p. 69.
- [148] A. G. Ramm and A. I. Katsevich. *The Radon transform and local tomography*. CRC press, 2020.
- [149] E. Ramón-Moliner. “The Golgi-Cox Technique.” In: *Contemporary Research Methods in Neuroanatomy*. Springer Berlin Heidelberg, 1970, pp. 32–55.
- [150] W. J. Ray and V. Buggia-Prevot. “Novel Targets for Alzheimer’s Disease: A View Beyond Amyloid.” In: *Annual Review of Medicine* 72 (2021).
- [151] W. L. Roberts, T. J. Campbell, G. R. Rapp, et al. *Encyclopedia of minerals*. Van Nostrand Reinhold, 1990.
- [152] A. Robisch, J. Frohn, and T. Salditt. “Iterative micro-tomography of biopsy samples from truncated projections with quantitative gray values.” In: *Physics in Medicine & Biology* 65.23 (2020), p. 235034.
- [153] A. Robisch, K. Kröger, A. Rack, and T. Salditt. “Near-field ptychography using lateral and longitudinal shifts.” In: *New Journal of Physics* 17.7 (2015), p. 073033.
- [154] A.-L. Robisch, M. Eckermann, M. Töpperwien, F. van der Meer, C. Stadelmann-Nessler, and T. Salditt. “Nanoscale x-ray holotomography of human brain tissue with phase retrieval based on multienergy recordings.” In: *Journal of Medical Imaging* 7.1 (2020), p. 013501.

- [155] G. Rodgers, C. Tanner, G. Schulz, A. Migga, T. Weitkamp, W. Kuo, M. Scheel, M. Osterwalder, V. Kurtcuoglu, and B. Müller. “Impact of fixation and paraffin embedding on mouse brain morphology: a synchrotron radiation-based tomography study.” In: *Developments in X-Ray Tomography XIII*. International Society for Optics and Photonics. 2021.
- [156] A. Rolls, R. Shechter, and M. Schwartz. “The bright side of the glial scar in CNS repair.” In: *Nature Reviews Neuroscience* 10.3 (2009), pp. 235–241.
- [157] P. Rostaing, E. Real, L. Siksou, J.-P. Lechaire, T. Boudier, T. M. Boeckers, F. Gertler, E. D. Gundelfinger, A. Triller, and S. Marty. “Analysis of synaptic ultrastructure without fixative using high-pressure freezing and tomography.” In: *European Journal of Neuroscience* 24.12 (2006), pp. 3463–3474.
- [158] A. Ruhlandt, M. Töpperwien, M. Krenkel, R. Mokso, and T. Salditt. “Four dimensional material movies: High speed phase-contrast tomography by back-projection along dynamically curved paths.” In: *Scientific Reports* 7.1 (2017), pp. 1–9.
- [159] A. Ruhlandt and T. Salditt. “Three-dimensional propagation in near-field tomographic X-ray phase retrieval.” In: *Acta Crystallographica Section A: Foundations and Advances* 72.2 (2016), pp. 215–221.
- [160] T. Salditt, T. Aspelmeier, and S. Aeffner. *Biomedical Imaging: Principles of Radiography, Tomography and Medical Physics*. Walter de Gruyter GmbH & Co KG, 2017.
- [161] J. R. Sanes and S. L. Zipursky. “Synaptic specificity, recognition molecules, and assembly of neural circuits.” In: *Cell* 181.3 (2020), pp. 536–556.
- [162] A. Sartori-Rupp, D. C. Cervantes, A. Pepe, K. Gousset, E. Delage, S. Corroyer-Dulmont, C. Schmitt, J. Krijnse-Locker, and C. Zurzolo. “Correlative cryo-electron microscopy reveals the structure of TNTs in neuronal cells.” In: *Nature Communications* 10.1 (2019), pp. 1–16.
- [163] F. Schaff, K. S. Morgan, D. M. Paganin, and M. J. Kitchen. “Spectral propagation-based x-ray phase-contrast imaging.” In: *Developments in X-Ray Tomography XIII*. International Society for Optics and Photonics. 2021.
- [164] B. Schmitzer. “Stabilized sparse scaling algorithms for entropy regularized transport problems.” In: *SIAM Journal on Scientific Computing* 41.3 (2019), A1443–A1481.

- [165] D. Schmucker, J. C. Clemens, H. Shu, C. A. Worby, J. Xiao, M. Muda, J. E. Dixon, and S. L. Zipursky. "Drosophila Dscam is an axon guidance receptor exhibiting extraordinary molecular diversity." In: *Cell* 101.6 (2000), pp. 671–684.
- [166] T. Schoonjans, A. Brunetti, B. Golosio, M. S. del Rio, V. A. Solé, C. Ferrero, and L. Vincze. "The xraylib library for X-ray–matter interactions. Recent developments." In: *Spectrochimica Acta Part B: Atomic Spectroscopy* 66.11-12 (2011), pp. 776–784.
- [167] A. Siegel and H. N. Saprú. *Essential neuroscience*. 2nd ed. Lippincott Williams & Wilkins, 2006.
- [168] J. Silver and J. H. Miller. "Regeneration beyond the glial scar." In: *Nature Reviews Neuroscience* 5.2 (2004), pp. 146–156.
- [169] R. Sinkhorn and P. Knopp. "Concerning nonnegative matrices and doubly stochastic matrices." In: *Pacific Journal of Mathematics* 21.2 (1967), pp. 343–348.
- [170] A. J. Smola and B. Schölkopf. "A tutorial on support vector regression." In: *Statistics and Computing* 14.3 (2004), pp. 199–222.
- [171] J. Soltau, M. Vassholz, M. Osterhoff, and T. Salditt. "Inline holography with hard x-rays at sub-15 nm resolution." In: *Optica* 8 (2021), pp. 818–823.
- [172] O. Sporns and J. D. Zwi. "The small world of the cerebral cortex." In: *Neuroinformatics* 2.2 (2004), pp. 145–162.
- [173] C. Stadelmann, M. Albert, C. Wegner, and W. Brück. "Cortical pathology in multiple sclerosis." In: *Current Opinion in Neurology* 21.3 (2008), pp. 229–234.
- [174] M. Stockmar, M. Hubert, M. Dierolf, B. Enders, R. Clare, S. Allner, A. Fehringer, I. Zanette, J. Villanova, J. Laurencin, et al. "X-ray nanotomography using near-field ptychography." In: *Optics Express* 23.10 (2015), pp. 12720–12731.
- [175] W. J. Streit, H. Braak, K. Del Tredici, J. Leyh, J. Lier, H. Khoshbouei, C. Eisenlöffel, W. Müller, and I. Bechmann. "Microglial activation occurs late during preclinical Alzheimer's disease." In: *Glia* 66.12 (2018), pp. 2550–2562.
- [176] W. J. Streit, H. Braak, Q.-S. Xue, and I. Bechmann. "Dystrophic (senescent) rather than activated microglial cells are associated with tau pathology and likely precede neurodegeneration in Alzheimer's disease." In: *Acta Neuropathologica* 118.4 (2009), pp. 475–485.

- [177] N. L. Strominger, R. J. Demarest, and L. B. Laemle. *Noback's human nervous system: structure and function*. Springer Science & Business Media, 2012.
- [178] P. K. Stys, G. W. Zamponi, J. Van Minnen, and J. J. Geurts. "Will the real multiple sclerosis please stand up?" In: *Nature Reviews Neuroscience* 13.7 (2012), pp. 507–514.
- [179] A. Suzuki, S. Furutaku, K. Shimomura, K. Yamauchi, Y. Kohmura, T. Ishikawa, and Y. Takahashi. "High-resolution multislice x-ray ptychography of extended thick objects." In: *Physical Review Letters* 112.5 (2014), p. 053903.
- [180] A. Sztrókay, P. Diemoz, T. Schlossbauer, E. Brun, F. Bamberg, D. Mayr, M. Reiser, A. Bravin, and P. Coan. "High-resolution breast tomography at high energy: a feasibility study of phase contrast imaging on a whole breast." In: *Physics in Medicine & Biology* 57.10 (2012), p. 2931.
- [181] H. F. Talbot. "LXXXVI. Facts relating to optical science. No. IV." In: *The London, Edinburgh, and Dublin Philosophical Magazine and Journal of Science* 9.56 (1836), pp. 401–407.
- [182] M. R. Teague. "Deterministic phase retrieval: a Green's function solution." In: *JOSA* 73.11 (1983), pp. 1434–1441.
- [183] D. R. Thal, U. Rüb, M. Orantes, and H. Braak. "Phases of A β -deposition in the human brain and its relevance for the development of AD." In: *Neurology* 58.12 (2002), pp. 1791–1800.
- [184] A. J. Thompson, B. L. Banwell, F. Barkhof, W. M. Carroll, T. Coetzee, G. Comi, J. Correale, F. Fazekas, M. Filippi, M. S. Freedman, et al. "Diagnosis of multiple sclerosis: 2017 revisions of the McDonald criteria." In: *The Lancet Neurology* 17.2 (2018), pp. 162–173.
- [185] D. A. Thompson, Y. I. Nesterets, K. M. Pavlov, and T. E. Gureyev. "Fast three-dimensional phase retrieval in propagation-based X-ray tomography." In: *Journal of Synchrotron Radiation* 26.3 (2019), pp. 825–838.
- [186] M. Töpperwien. *3d virtual histology of neuronal tissue by propagation-based x-ray phase-contrast tomography*. Vol. 25. Göttingen series in X-ray physics. Universitätsverlag Göttingen, 2018.
- [187] M. Töpperwien, A. Markus, F. Alves, and T. Salditt. "Contrast enhancement for visualizing neuronal cytoarchitecture by propagation-based x-ray phase-contrast tomography." In: *NeuroImage* 199 (2019), pp. 70–80.

- [188] M. Töpperwien, F. van der Meer, C. Stadelmann, and T. Salditt. “Correlative x-ray phase-contrast tomography and histology of human brain tissue affected by Alzheimer’s disease.” In: *NeuroImage* 210 (2020), p. 116523.
- [189] M. Töpperwien, F. van der Meer, C. Stadelmann, and T. Salditt. “Three-dimensional virtual histology of human cerebellum by X-ray phase-contrast tomography.” In: *Proceedings of the National Academy of Sciences* 115.27 (2018), pp. 6940–6945.
- [190] M. Van Heel. “Similarity measures between images.” In: *Ultramicroscopy* 21.1 (1987), pp. 95–100.
- [191] M. Van Heel and M. Schatz. “Fourier shell correlation threshold criteria.” In: *Journal of Structural Biology* 151.3 (2005), pp. 250–262.
- [192] I. A. Vartanyants and A. Singer. “Coherence properties of hard x-ray synchrotron sources and x-ray free-electron lasers.” In: *New Journal of Physics* 12.3 (2010), p. 035004.
- [193] J. Von Neumann. “On rings of operators. Reduction theory.” In: *Annals of Mathematics* (1949), pp. 401–485.
- [194] W. Wang, D. Slepčev, S. Basu, J. A. Ozolek, and G. K. Rohde. “A linear optimal transportation framework for quantifying and visualizing variations in sets of images.” In: *International Journal of Computer Vision* 101.2 (2013), pp. 254–269.
- [195] U. Weierstall, Q. Chen, J. Spence, M. Howells, M. Isaacson, and R. Panepucci. “Image reconstruction from electron and X-ray diffraction patterns using iterative algorithms: experiment and simulation.” In: *Ultramicroscopy* 90.2-3 (2002), pp. 171–195.
- [196] I. T. Whiteman, L. S. Minamide, D. L. Goh, J. R. Bamburg, and C. Goldsbury. “Rapid changes in phospho-MAP/tau epitopes during neuronal stress: cofilin-actin rods primarily recruit microtubule binding domain epitopes.” In: *PLoS One* 6.6 (2011), e20878.
- [197] S. Wilkins, T. E. Gureyev, D. Gao, A. Pogany, and A. Stevenson. “Phase-contrast imaging using polychromatic hard X-rays.” In: *Nature* 384.6607 (1996), pp. 335–338.
- [198] M. C. Willingham and A. V. Rutherford. “The use of osmium-thiocarbohydrazide-osmium (OTO) and ferrocyanide-reduced osmium methods to enhance membrane contrast and preservation in cultured cells.” In: *Journal of Histochemistry and Cytochemistry* 32.4 (1984), pp. 455–460.

- [199] D. Wu and J. Zhang. “In vivo mapping of macroscopic neuronal projections in the mouse hippocampus using high-resolution diffusion MRI.” In: *NeuroImage* 125 (2016), pp. 84–93.
- [200] S. Xu, Q. Xiao, F. Cosmanescu, A. P. Sergeeva, J. Yoo, Y. Lin, P. S. Katsamba, G. Ahlsen, J. Kaufman, N. T. Linaval, et al. “Interactions between the Ig-Superfamily proteins DIP- α and Dpr6/10 regulate assembly of neural circuits.” In: *Neuron* 100.6 (2018), pp. 1369–1384.
- [201] S. Zabler, P. Cloetens, J.-P. Guigay, J. Baruchel, and M. Schlenker. “Optimization of phase contrast imaging using hard x rays.” In: *Review of Scientific Instruments* 76.7 (2005), p. 073705.
- [202] M.-C. Zdora, P. Thibault, W. Kuo, V. Fernandez, H. Deyhle, J. Vila-Comamala, M. P. Olbinado, A. Rack, P. M. Lackie, O. L. Katsamenis, et al. “X-ray phase tomography with near-field speckles for three-dimensional virtual histology.” In: *Optica* 7.9 (2020), pp. 1221–1227.
- [203] H. Zeng and J. R. Sanes. “Neuronal cell-type classification: challenges, opportunities and the path forward.” In: *Nature Reviews Neuroscience* 18.9 (2017), pp. 530–546.
- [204] X. Zhang and W. Song. “The role of APP and BACE1 trafficking in APP processing and amyloid- β generation.” In: *Alzheimer’s Research & Therapy* 5.5 (2013), pp. 1–8.

Phase-contrast X-ray Tomography of Neuronal Tissue at Laboratory Sources with Submicron Resolution

2

Marina Eckermann, Mareike Töpperwien, Anna-Lena Robisch, Franziska van der Meer, Christine Stadelmann and Tim Salditt

Reproduced from Journal of Medical Imaging (2020), 7(1), 013502.

Purpose: Recently, progress has been achieved in implementing phase-contrast tomography of soft biological tissues at laboratory sources. This opens up opportunities for three-dimensional (3d) histology based on x-ray computed tomography (μ - and nanoCT) in direct vicinity of hospitals and biomedical research institutions. Combining advanced x-ray generation and detection techniques with phase reconstruction algorithms, 3d histology can be obtained even of unstained tissue of the central nervous system, as shown for example for biopsies and autopsies of human cerebellum. Depending on the setup, *i.e.* source, detector, and geometric parameters, laboratory-based tomography can be implemented at very different sizes and length scales.

Here, we investigate to which extent 3d histology of neuronal tissue can exploit the cone-beam geometry at high magnification M using a nanofocus transmission x-ray tubes (nanotube) with 300 nm minimal spot size (Excillum), combined with a single-photon counting camera. Tightly approaching the source spot with the biopsy punch, we achieve high $M \approx 10^1$ - 10^2 , high flux density and exploit the superior efficiency of this detector technology.

Approach: Different nanotube configurations such as spot size and flux, M as well as exposure time, Fresnel number and coherence are varied and selected in view of resolution, field of view, and/or phase contrast requirements.

Results: The data show that the information content for the cyto-architecture is enhanced by the phase effect. Comparison of results to those obtained at a microfocus rotating-anode x-ray tomography setup with a high resolution detector, *i.e.* at low- M geometry, reveals similar to slightly superior data quality for the nanotube setup. Besides its compactness, reduced power consumption by a factor of 10^3 and shorter scan duration, the particular advantage of the nanotube setup also lies in its suitability with pixel detector technology, enabling an increased range of opportunities for applications in laboratory phase-contrast x-ray tomography.

Conclusions: The phase retrieval scheme utilized here mixes amplitude and phase contrast, with results being robust with respect to reconstruction parameters. Structural information content is comparable to previous results achieved with a microfocus rotating-anode setup, but can be obtained in shorter scan time. Beyond advantages as compactness, lowered power consumption and flexibility, the nanotube setup's scalability in view of progress in pixel detector technology is particularly beneficial. Further progress is thus likely to bring 3d virtual histology to the performance in scan time and throughput required for clinical practice in neuropathology.

2.1 Introduction

Phase-contrast x-ray tomography offers a unique potential to realize 3d virtual histology, with cellular and even sub-cellular resolution, and for 3d volumes which are inaccessible by more established techniques. While volume and throughput in conventional histology are limited by slicing and staining, volume penetration for both light- and electron-based microscopy techniques is unsuitable for larger tissue volumes. A substantial amount of propagation-based x-ray phase-contrast tomography studies with synchrotron radiation has demonstrated this potential, both for stained [3, 31, 34] and unstained [29, 37] soft tissues, and including mouse models [36] as well as human tissue [19, 37]. Many different types of tissues have been imaged, including heart and cardiovascular systems [9, 11, 40], skin [42], cancerous tissue in particular for mamma [43], the peripheral nervous system [3, 30], and tissues of the central nervous system (CNS) [18, 19, 20, 21].

Towards a broader accessibility and use of the technique in a clinical setting, translation from synchrotron to laboratory sources is an important goal of ongoing technique and

instrumentation development. Laboratory-based phase-contrast μ CT has already been implemented at different sources: transmission microfocus sealed tubes [27], liquid metal-jet anodes [4, 21, 38, 39, 44], as well as microfocus rotating-anode sources [28, 32]. The detection technology has been equally diverse. Nanotubes offer yet another opportunity to implement phase-contrast tomography, with possible advantages in particular in view of increased spatial coherence length. For stained tissue, high resolution tomography of different tissues has been demonstrated in [5, 23]. A particular challenge is to reach sufficient image quality for unstained soft tissues with laboratory radiation. To this end, we have recently demonstrated the capabilities of optimized image acquisition (by geometry and detection) and reconstruction, using liquid-anode metal jet sources as well as a microfocus rotating-anode sources [28, 33].

In this work, we want to investigate the suitability of a home-built setup installed at a nanotube (NanoTube N1 60kV, Excillum AB, Stockholm, Sweden) for 3d histology of unstained *post mortem* human brain tissue. As in our earlier study [37], we chose cerebellar tissue, as a reference structure for phase-contrast tomography data evaluation, due to its well-known anatomy and features covering various relevant length scales and e^- -densities. Fig. 2.1 illustrates its basic anatomical features, in order to place the tomographic results obtained on biopsy punches from paraffin-embedded tissue blocks with typical diameter of a mm into proper anatomical perspective. The *white matter* (WM) consists of myelinated neuronal structures as *axons* in *fiber tracts* (FT). From there, fibers traverse the *granular layer* (GL), consisting of *granular cells* (GC) and *Golgi cells* (GgC). Bounding the GL, a single layer of *Purkinje cells* (PC, PCL) with sparse occurrences of *basket cells* (BC) is situated. PC's long, planar and widely branched dendritic trees reach into the *molecular layer* (ML), which distinguishes itself from the GL by the *molecular cells* (MC), being more sparsely spread neurons and having larger nuclei.

The manuscript is organized as follows: after this introduction, the setup realization and data processing of the nanotube x-ray source are outlined in 2.2.1, complemented by a brief presentation of a yet well-established rotating-anode microfocus setup in 2.2.2. The results section 2.3 start with the inspection of commissioning test measurements regarding stability and spectrum in 2.3.1. However, the analysis of the tomographic data occupies the main part of this work, for one being devoted to the variation of physical parameters as source spot size, lateral coherence length, dose or Fresnel number in 2.3.2.1 and 2.3.2.2, but also to the comparison with a yet well-established microfocus setup in 2.3.2.3. This manuscript closes with a summary and outlook in 2.4.

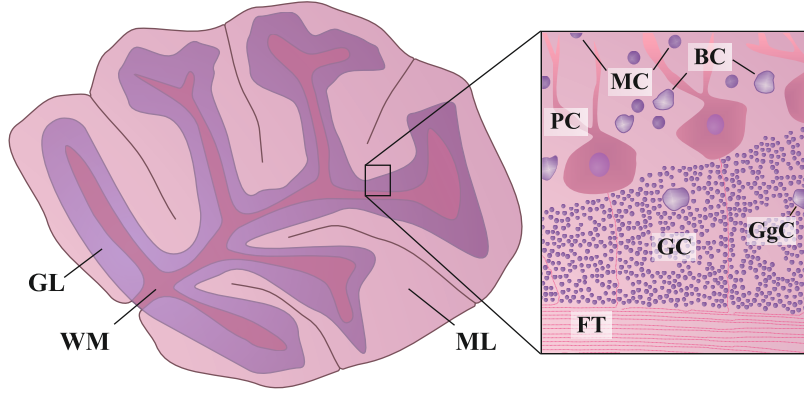


Fig. 2.1: Depiction of the cerebellum anatomy, giving a rather macroscopic perspective on the left and a zoom-in to the cellular scale on the right. Notations correspond to the ones defined in the text.

2.2 Methods

2.2.1 NanoTube Implementation

Experimental Setup We have designed a nanofocus x-ray setup for propagation-based x-ray phase-contrast tomography, depicted in Fig. 2.2. Its central component is the NanoTube N1 60 kV (Excillum AB) x-ray source, with two-dimensional (2d) spatial resolution down to 150 nm, according to manufacturer (lines-and-spaces, metal test objects in absorption contrast). The source is operated at 60 keV, with a power between 0.2 and 1.2 W, depending on the spot size. The NanoTube system was calibrated for three different spot sizes s (full width at half maximum, FWHM): “big spot, high flux” at $1\ \mu\text{m}$, “middle spot, middle flux” at $0.5\ \mu\text{m}$ and “small spot, low flux” at $0.3\ \mu\text{m}$ (FWHM). Fig. 2.2a) shows the schematic of the transmission-anode target, which consists of a $0.50\ \mu\text{m}$ tungsten-film (chemical symbol “W”) providing a rather high e^- -stopping power S ($S = 54.4\ \text{MeV}/\text{cm}$ [22]) on a $100\ \mu\text{m}$ -layer of diamond, serving as carrier layer and for heat mitigation at fewer e^- -interactions ($S = 18.1\ \text{MeV}/\text{cm}$). As shown in the zoomed optical micrograph in Fig. 2.2c), samples can be positioned in direct proximity to the target, since it also serves as vacuum exit window. The cone-shaped front end of the NanoTube allows to position the sample tower underneath the X-ray target, and to achieve small source-to-sample distances down to $z_{01} \geq 100\ \mu\text{m}$. Due to the small sub- μm spot size s , high geometrical magnification $M = z_{02}/z_{01} \gg 1$

can be realized without source blurring, making it possible to use direct (photon-counting) pixel detectors, which are available only with relatively large pixel size px . Accordingly, the effective pixel size in the sample plane is reduced to [25]

$$px_{\text{eff}} = \frac{1}{M} \cdot px = \frac{z_{01}}{z_{02}} \cdot px .$$

At the same time, phase contrast is still feasible, since small s also assures the spatial coherence length ζ [2] to be of the same order of magnitude as px_{eff}

$$\zeta = \frac{\lambda \cdot z_{01}}{s} \geq px_{\text{eff}} ,$$

where λ denotes the x-ray wavelength. The sample tower is equipped with three translational motors at the bottom (x,y,z), to position the tomographic rotation axis. The FOV on the sample is selected by two further translational motors (x,z) on top of the rotation, enabling automated alignment routines as described in [28]. For high-resolution optical monitoring of the sample environment, a Manta camera (Allied Vision Technologies GmbH, Stadtroda, Germany) is installed with a view along the x-axis, as shown in 2.2(b) & (c). Broad overviews of the scene are provided by an Axis camera (Axis Communications AB, Lund, Sweden). A single-photon counting Timepix Hexa H05-W0154 detector (XIE, Freiburg, Germany) was used, with a $500 \mu\text{m}$ Si-sensor, $px = 55 \mu\text{m}$ and 768×512 pixels (w x h) distributed over six modules, to record the 2d projections.

Data recording settings For tomographic acquisition, 2d X-ray projections were recorded at 1201 rotation angles, equally distributed over 192° ¹, with sets of 25 flat field images before and after each scan. $z_{02} \approx 20 \text{ cm}$ was kept fixed, varying z_{01} and s . The detector was operated with a lower-limit cut-off energy of 4 keV. The acquisition time was adjusted depending on the spot size s to avoid overexposure, which is at maximum counts of 11 810 ph. Most scans were split into four consecutive tomographic scans with $\frac{1}{4}$ exposure time each, and then recombined via cross-correlation in Fourier space[14]. Thus, for these cases, four different exposures were recorded and averaged for each projection. All scan parameters are tabulated in Tab. 2.1, 2.2 and 2.3. This acquisition scheme was found to reduce ring artifacts arising from a statistically varying response of the modules.

¹Due to the cone-beam angle being 12° , an increased angular sampling range was required.

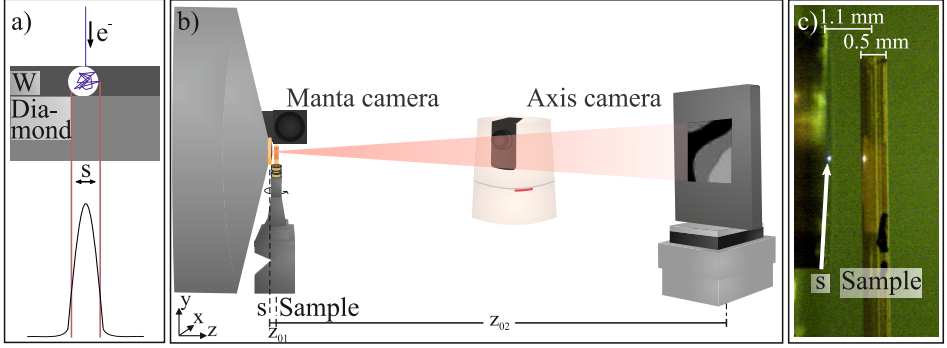


Fig. 2.2: Illustration of the nanotube setup: a) Schematic of the transmission target X-ray source. b) Recording geometry: the cone-shaped front end of the nanotube allows for small distances z_{01} between source s and the sample. The detector is aligned at z_{02} from the source. The axis camera allows for visual inspection of the setup in general, while the manta camera gives a microscopic control of the tight z_{01} environment, see exemplary view in c).

Phase retrieval The data are recorded in the *direct contrast* or *edge enhancement regime* at Fresnel numbers

$$F = \frac{px_{\text{eff}}^2}{z_{\text{eff}}\lambda} = \frac{px^2}{z_{12}M\lambda} \approx 1,$$

where $px_{\text{eff}} = px/M$ for the effective pixel size, and $z_{\text{eff}} = z_{12}/M$ for the effective propagation distance have been used (Fresnel scaling theorem [25]). As demonstrated in [4, 35], in this regime, even data from low coherence sources can be successfully reconstructed based on the *Bronnikov-aided correction* (BAC) scheme. To this end, the *transport of intensity equation* (TIE) serves a starting point to describe the propagation of a paraxial wave along \vec{z} with intensity $I(\vec{r})$ and phase distribution $\phi(\vec{r})$: $\nabla_{\perp}(I(\vec{r}) \cdot \nabla_{\perp}\phi(\vec{r})) = -k\partial_z I(\vec{r})$, k being the wavenumber. Under the assumption of small propagation distances z_{eff} and a purely phase shifting object, the TIE can be linearized, and an approximate phase $\tilde{\phi}$ can be computed as [12, 13]

$$\tilde{\phi}(\vec{r}_{\perp}) = 2\pi F \cdot \mathcal{F}_{\perp}^{-1} \left[\frac{\mathcal{F}_{\perp} \left[\frac{I(\vec{r}_{\perp}, z) - I_0}{I_0} \right]}{|\vec{k}_{\perp}|^2 + \alpha} \right],$$

where \mathcal{F} denotes the Fourier transform and I_0 the (uniform) intensity distribution. The parameter α is introduced to regularize the singularity at zero spatial frequencies, and in practice is chosen such that edge enhancement is cancelled. In a second step,

the approximate phase $\tilde{\phi}$ is used to compute a (corrected) sharp intensity distribution in the object exit plane, according to [8]

$$I(\vec{r}_\perp, z = 0) = \frac{I(\vec{r}_\perp, z)}{1 - \gamma \nabla_\perp^2 \tilde{\phi}(\vec{r}_\perp)}.$$

In practice, the art of using the BAC is to choose the two regularization parameters α and γ such that the resulting somewhat hypothetical intensity distribution contains contributions from intensity and phase contrast, even though expressed only in terms of transmitted intensity. As for reconstructions assuming a homogeneous object, the two contributions cannot be separated. For high resolution laboratory μ - and nanoCT, this scheme yields unparalleled image quality. After, the phase-retrieved 2d projection data are processed for ring artifact mitigation according to [24] and then recombined to a 3d volume using the ASTRA-toolbox[1, 26]. Visualization was done with Avizo (Thermo Fisher Scientific, Waltham MA, USA).

2.2.2 Rotating-Anode Setup

For comparison, the samples were also scanned at a (home-built) laboratory μ CT setup installed at a rotating Cu-anode x-ray source (Rigaku, Tokyo, Japan) with main line 8.048 keV (K_α) and source size $s = 70 \mu\text{m}$ [28]. It was operated at 40 keV and 30 mA. A high resolution, lens-coupled single crystal scintillator CCD detector (Xsight, Rigaku, Prague, Czech Republic), with $px = 0.54 \mu\text{m}$ was used. Images were recorded at $M = \frac{500 \text{ mm}}{494 \text{ mm}} \approx 1$ to achieve a spatial coherence $\zeta \approx 1 \mu\text{m}$ reasonable for μm -resolution (after 2x2 pixel-binning).

The number of projection angles was identical to that of the nanotube scans, distributed over an angular range of 180° from the cone-beam angle being $\approx 0^\circ$. The exposure time, however, needed to be increased significantly due to the very different detector technology, *i.e.* to 50 s. In addition to the flat fields, 10 dark images were recorded prior to each scan, to account for the dark current of the CCD. With $F = 1.24$, BAC applies also here.

2.3 Results

2.3.1 Commissioning Tests

Prior to performing high-resolution tomography scans, the stability of the source and its environment was verified. To this end, the source was operated at spot size $s = 0.56 \mu\text{m}$, and images of a custom-fabricated JIMA target ($1.5 \mu\text{m}$ W; ZonePlates Ltd, London, UK) positioned at $z_{01} = 19.6 \text{ mm}$, were recorded at $z_{02} = 900 \text{ mm}$, using a sCMOS camera (Photonic Science, UK) with a $5 \mu\text{m}$ Gadox scintillator 2208×2744 pixels (w x h) and $px = 4.54 \mu\text{m}$. As indicated in Fig. 2.3(a), images of 600 nm lines-and-spaces were acquired every 12 min for 5 min of exposure over the course of 6.6 h. Fig. 2.3(b) shows the modulations of the lines-and-spaces corresponding to the marked area in a) after 0 h, 3 h and 6 h (from top to bottom). Only a minor shift on the order of 30 nm/h is observed. At the same time, the variations of the total intensity (integrated flat fields) shown in (c) are about 0.6 % (rms-value).

Next, the spectrum of the X-ray source was assessed using an energy-resolving XR-100CdTe detector (Amptek, Bedford, USA) with a sensor thickness of 1 mm, positioned at $z_{02} = 1.2 \text{ m}$ to avoid saturation. Spectral bins were calibrated based on the K_{α} and K_{β} fluorescence signals of Mo, Ni and Ag foils. The spectrum is plotted in red in Fig. 2.3(d). The counts-weighted mean energy of this spectrum E_w is 21.40 keV. However, at the given distance, absorption in air is already substantial, and has to be corrected for using the tabulated values (Henke tables), accessed through the CXRO data base[17] and matched to the detector bins with a Matlab-implementation of shape-preserving piecewise cubic extrapolation. The resulted corrected curve is shown in yellow, representing the source emission spectrum, with a correspondingly lower mean energy $E_w = 11.46 \text{ keV}$. Since the detector for the tomographic scans had a $500 \mu\text{m}$ Si-sensor, and hence reduced sensitivity at high photon energy, this was also corrected[22], along with the absorption in air, for the corresponding detector position $z_{02} \approx 20 \text{ cm}$, see the blue curve. It is characterized by $E_w = 9.11 \text{ keV}$, and therefore represents the mean photon energy for the tomography data (without taking beam hardening in the sample into account).

The photon flux is dependent of s and the actual, specific source calibration. For $s = 0.95 \mu\text{m}$, it was found to be in the order of $\sim 2 \cdot 10^{11} \text{ ph/s}$ in 2π -space, $\sim 4 \cdot 10^{10} \text{ ph/s}$ for $s = 0.51 \mu\text{m}$ and $\sim 1 \cdot 10^{10} \text{ ph/s}$ for $s = 0.30 \mu\text{m}$.

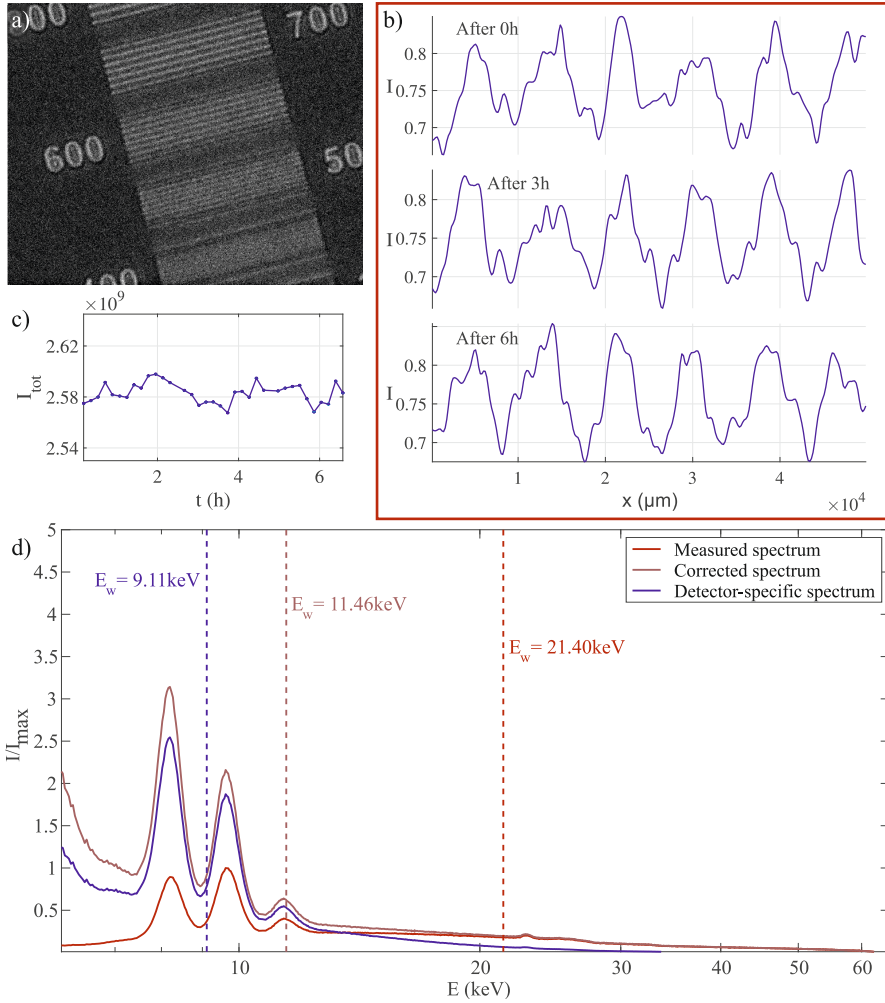


Fig. 2.3: Pre-characterization of the imaging setup. (a-c) Test of stability by recording a time series for a test pattern, recorded at $s = 0.56 \mu\text{m}$ and $\text{px}_{\text{eff}} = 0.099 \mu\text{m}$. (a) Image of the JIMA-target ($1.5 \mu\text{m}$ W). The annotation “600” refers to the structure measured, *i.e.* 600 nm lines and 600 nm spaces. The red rectangle indicates the area, for which line profiles are shown in (b) at three time points: (top) 0h, (center) 3h, and (bottom) 6h. (c) Integrated intensity over time. (d) Source spectrum: (red) measured data (detector output), (yellow) corrected for absorption in air, and (blue) the spectrum taking into account the energy dependence in the quantum efficiency of the detector used for the tomographic scans.

2.3.2 Phase-Contrast Tomography of Unstained Human Brain Tissue

In this work, paraffin-embedded human cerebellum was used to investigate suitability of the setup for 3d virtual histology and neuropathology. From the tissue block, a 0.5 mm biopsy punch was extracted and transferred into a 0.5 mm polyimide tube (Professional Plastics, Fullerton CA, USA) on a custom-fabricated Huber brass pin (Huber Diffractionstechnik GmbH & Co. KG, Rimsting, Germany), as illustrated in Fig. 2.2.

2.3.2.1 Variation of s/ζ at Constant F

We have first investigated the influence of the lateral coherence length ζ on the tomographic image quality, by setting two different spot sizes (I) $s = 0.95 \mu\text{m}$ and (II) $s = 0.51 \mu\text{m}$, respectively, while keeping $F \approx 2.0$ constant, and the dose also approximately at the same level. Hence the larger source size resulted in a significantly reduced total scan time. All experimental and phase reconstruction parameters are listed in Tab. 2.1. In this work, radiation dose was calculated combining the photon counts from the projection data with the spectra in Fig. 2.3. Fig. 2.4 illustrates data reconstruction steps, from projection to orthoslices through the reconstructed volume. The projections in (a) reveal slight edge enhancement in both cases, especially for the polyimide-air-interface, as plotted in (b). As expected, the higher coherence for the $0.501 \mu\text{m}$ source spot yields a more pronounced edge enhancement compared to $0.934 \mu\text{m}$. In the same plot, the blue curves show the profiles after phase retrieval, and the respective 2d images are given in (c). Virtual slices through the same position in the xz-plane and xy-plane are shown in (d) and (f), respectively, with a corresponding zoom shown in (e). Data for (I) were recorded as a single tomographic scan, acquisition for (II) was split into four as described in 2.2.1. By fractionating the dose over four scans, ring artifacts were found to be reduced. Based on visual inspection, both data sets appear to be of very similar quality. Different cerebellum-specific regions as outlined in Fig. 2.1 are clearly identifiable: as for the zoom-ins (I.e) and (II.e), the cell-dense GL on the right and the ML on the left are separated by the sparsely-distributed, bold PCL-cells (red arrows). The resolution was quantified exploiting Fourier-Shell-Correlation (FSC) [15, 41]. In this analysis scheme, two independently recorded Kaiser-Bessel-filtered data are evaluated for their consistency, defined via the intersection of the cross-correlation in Fourier space with a threshold criteria,

s (μm)	F	z_{01} (mm)	$p x_{\text{eff}}$ (μm)	ζ (μm)	Exp. time (s)	P (W)	Scan time (h)	Dose (kGy)
0.95	1.97	3.5	0.959	0.501	$1 \cdot 3.5 = 3.5$	1.18	2.0	10.6
0.51	1.96	3.5	1.067	0.934	$4 \cdot 5 = 20$	0.24	8.0	14.3

s (μm)	F	α_{BAC}	γ_{BAC}	FSC (μm)	CNR		
					GCL	PC _n	PC _b
0.95	1.97	0.12	0.16	1.83	5.46	5.49	0.74
0.51	1.96	0.10	0.16	1.76	6.39	9.25	2.74

Table 2.1: Parameters and quality measured for the tomographic scans at fixed F : (top) experimental parameters, (bottom) quality measures. Exposure times also indicate whether the scan was performed as a single or multiple ones. *Fourier-shell correlation* (FSC) is based on volumes of 400^3 voxels, with a Kaiser-Bessel window of 7 pixels[6]. The signal-to-noise ration (CNR) was calculated as $(\mu_{\text{ft}} - \mu_{\text{bg}})/\sigma_{\text{bg}}$ on 5 GCs, 4 PC bodies (PC_b) and their nuclei (PC_n), respectively. Scan time refers to the full scan, including readout and motor positioning.

being 1/2-bit in this case[16]. Therefore, FSC-values are not only governed by spatial resolution, but also the overall noise level. In this work, two independent data sets are reached performing the tomographic reconstruction twice, using half of the angular projections each. Hence, FSC-based resolution evaluation serves as an upper limit estimate. For both scans inspected here, the analysis results in similar values of around $1.8\mu\text{m}$. However, case (I) for $s = 0.51\mu\text{m}$ has superior feature contrast, see Tab. 2.1.

2.3.2.2 Variations of F at Constant Source Spot Size s

Next we investigate the influence of F on tomographic image quality, as controlled by the source-to-sample distance z_{01} , while keeping z_{02} fixed. Hence $p x_{\text{eff}}$ (Eq. 2.2.1) and ζ (Eq. 2.2.1) vary accordingly. Most scans were recorded at $s = 0.51\mu\text{m} = \text{const.}$ In addition we include a scan at the minimally achievable $s = 0.30\mu\text{m}$, as well as at $s = 0.95\mu\text{m}$. For the latter, the $0.95\mu\text{m}$ -scan from Tab. 2.1 was repeated four times to reach an equal overall scan time of 8 h. All parameters are detailed in Tab. 2.2. Fig. 2.5 shows the virtual slices along the xy-plane through the reconstruction volume, in similar positions. By repeating the 2 h- $0.95\mu\text{m}$ -scan from Tab. 2.1 four times, and increasing the dose accordingly, the 3d resolution (FSC) is increased to $1.00\mu\text{m}$, i.e. close to the voxel size. The CNR also increased for GCs and PC nuclei, but only marginally for PC bodies. In order to increase the CNR of PC bodies substantially, it was necessary to double ζ (via reduction of s) at constant F (constant z_{01}). Despite

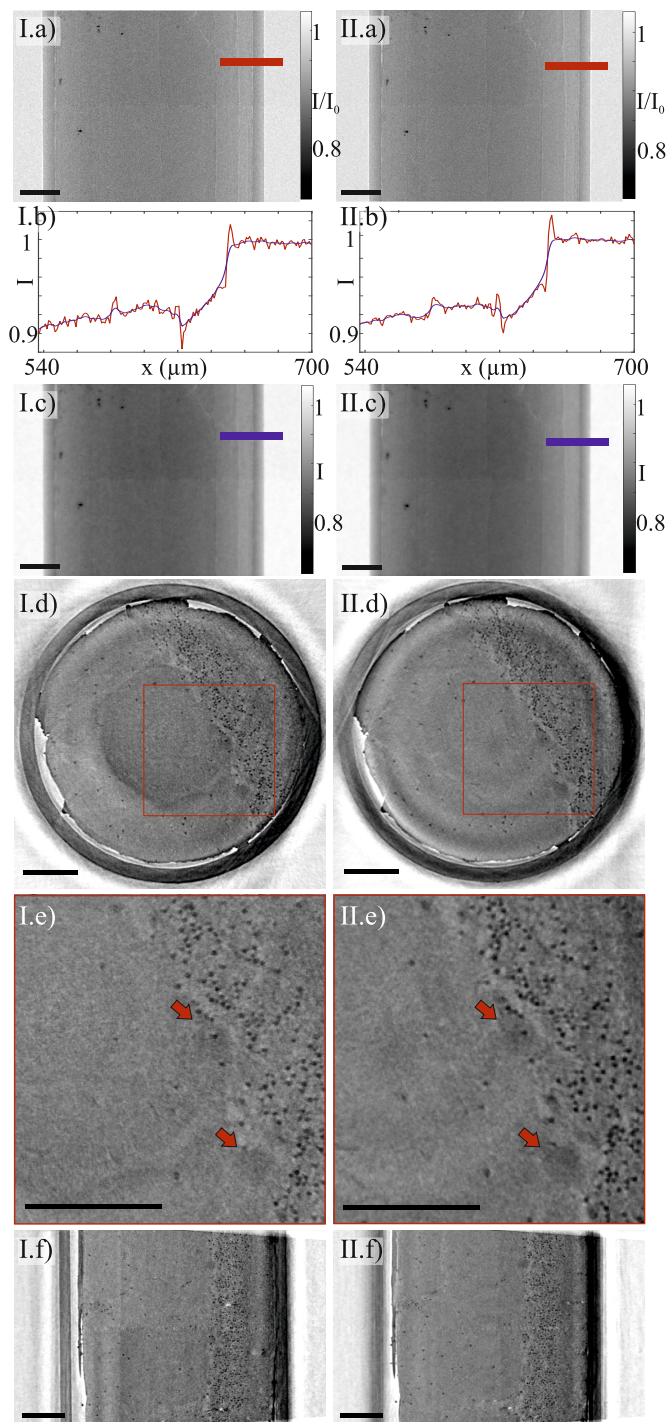


Fig. 2.4: (caption next page)

Fig. 2.4 (previous page): Data from tomography scans at fixed Fresnel number of 2.0, at (I) $s = 0.95 \mu\text{m}$ ($\zeta = 0.501 \mu\text{m}$) and (II) $0.51 \mu\text{m}$ ($\zeta = 0.934 \mu\text{m}$). (a) Respective flat-field corrected projections and (c) BAC-reconstructed projections. Colored bars indicate the position of the profiles shown in (b). The same virtual slice (d) in the xz-plane with a zoom-in in (e) and (f) in the xy-plane. Red arrows mark PCs. Data from quantitative analysis are summarized in table 2.1. Scale bars: $100 \mu\text{m}$.

s (μm)	F	z_{01} (mm)	px_{eff} (μm)	ζ (μm)	Exp. time (s)	P (W)	Scan time (h)	Dose (kGy)
0.95	1.97	3.5	0.959	0.501	$4 \cdot 3.5 = 14$	0.91	8.0	40.5
0.51	1.96	3.5	1.067	0.934	$4 \cdot 5 = 20$	0.24	8.0	14.3
0.51	1.40	2.5	0.687	0.667	$4 \cdot 5 = 20$	0.22	8.0	26.0
0.51	0.83	1.5	0.410	0.400	$4 \cdot 5 = 20$	0.24	8.0	77.1
0.30	0.60	1.1	0.300	0.680	$4 \cdot 20 = 80$	0.91	32.5	189.2

s (μm)	F	α_{BAC}	γ_{BAC}	FSC (μm)	CNR		
					GCL	PC_n	PC_b
0.95	1.97	0.12	0.16	$1.00^{K=100}$	6.47	5.93	0.86
0.51	1.96	0.10	0.16	$1.76^{K=400}$	6.39	9.25	2.74
0.51	1.40	0.03	0.16	$1.13^{K=130}$	6.18	6.91	1.24
0.51	0.83	0.015	0.16	$1.19^{K=200}$	5.57	5.52	1.38
0.30	0.60	0.015	0.16	$1.02^{K=200}$	3.82	3.81	0.83

Table 2.2: Analysis of image quality as a function of s and F : (top) experimental, (bottom) image quality parameters. Exposure times also indicate whether the scan was performed as a single or multiple ones. FSC evaluation is based on volumes of K^3 voxels, with a Kaiser-Bessel window of 7 pixels[6]. CNR was calculated as $(\mu_{\text{ft}} - \mu_{\text{bg}})/\sigma_{\text{bg}}$ on 5 GCs, 4 PC bodies (PC_b) and their nuclei (PC_n), respectively.

the significantly lower dose, which compromised resolution, the contrast for the rather large cell bodies is higher. As an overall trend, reducing F (via z_{01}) results in increased resolution, which is expected based on higher dose (smaller px_{eff}). At the same time, despite rise in dose, the CNRs are lower, indicating that the increase in ζ is more important, in particular for intrinsically low-contrasted features such as PC bodies. This conclusion is also confirmed by comparing the results in Tab. 2.2 for $s = 0.95 \mu\text{m}$ and $s = 0.30 \mu\text{m}$. In these scans, a roughly similar coherence length $\zeta \approx 0.5\text{-}0.7 \mu\text{m}$ results in a constant $\text{CNR} \approx 0.83\text{-}0.86$ for PC bodies, even though the radiation dose deviates by more than a factor of four.

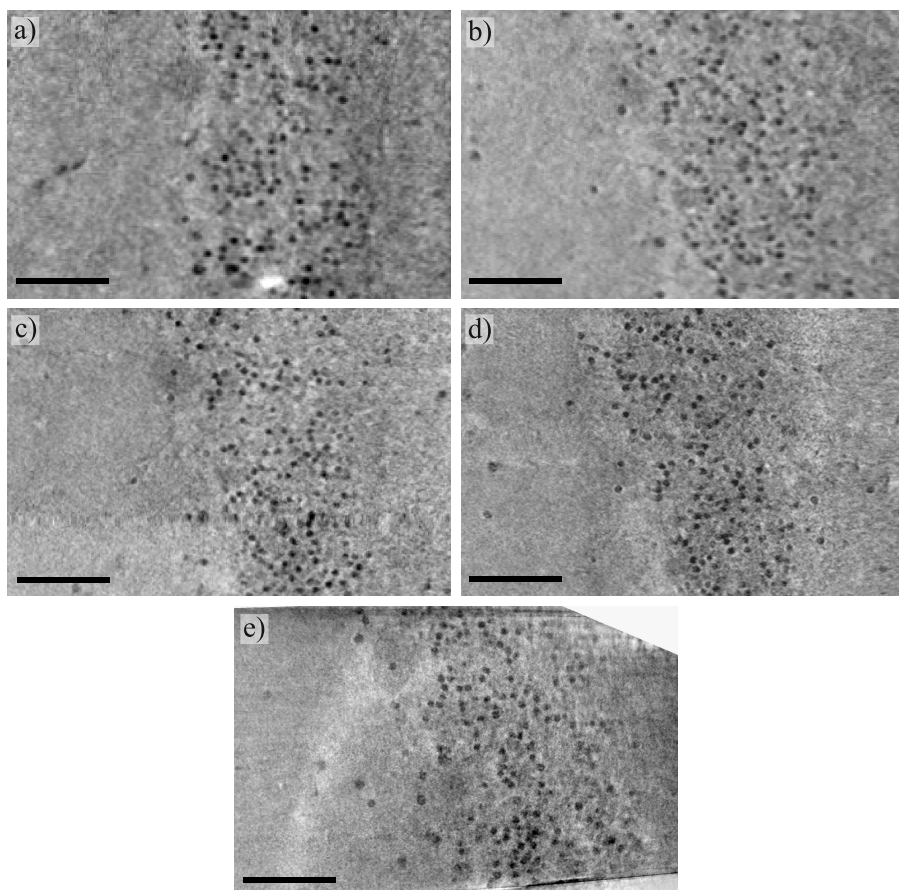


Fig. 2.5: Virtual xy-slices through the tomographic reconstruction, at similar positions in the biopsy punch, for (a) spot size of $0.95\ \mu\text{m}$, (b-d) $0.51\ \mu\text{m}$ and (e) $0.30\ \mu\text{m}$ and Fresnel numbers of (from (a) to (e)) 1.97, 1.96, 1.40, 0.83 and 0.60. Note the rise in geometrical magnification from (a&b) to (e). The respective analysis parameters are given in table 2.2. Scale bars: $50\ \mu\text{m}$.

s (μm)	F	z_{01} (mm)	px_{eff} (μm)	ζ (μm)	Exp. time (s)	P (W)	Scan time (h)
0.51	1.96	3.5	1.067	0.934	$4 \cdot 5 = 20$	0.24	8.0
70.0	1.24	494.0	1.070	1.094	$1 \cdot 50 = 50$	1400	16.7

s (μm)	F	α_{BAC}	γ_{BAC}	FSC (μm)	CNR		
					GCL	PC_n	PC_b
0.51	1.96	0.10	0.16	1.76	6.39	9.25	2.74
70.0	1.24	0.07	0.16	1.82	5.36	6.80	2.55

Table 2.3: Analysis of the tomographic scans for the nanofocus setup with $px_{\text{eff}} \approx 1.07 \mu\text{m}$, in comparison to a rotating anode scan with the same px_{eff} : (top) experimental parameters, (bottom) image quality parameters. Exposure times also indicate whether the scan was performed as a single or multiple ones. FSC-analysis is based on volumes of 400^3 voxels, with a Kaiser-Bessel window of 7 pixels[6]. CNR was calculated as $(\mu_{\text{ft}} - \mu_{\text{bg}})/\sigma_{\text{bg}}$ on 5 GCs, 4 PC bodies (PC_b) and their nuclei (PC_n), respectively.

2.3.2.3 Comparison with Data from a Microfocus Laboratory Setup

In order put the NanoTube results into perspective with earlier implementations of 3d histology with laboratory x-ray phase-contrast tomography, Fig. 2.6 and Tab. 2.3 presents a comparison to a reconstruction obtained at the microfocus rotating-anode x-ray source, with instrumentation described in 2.2.2. For the comparison, we selected the NanoTube dataset recorded for $s = 0.51 \mu\text{m}$ and $F = 1.96$, in order to achieve similar effective pixel size $px_{\text{eff}} \approx 1.07 \mu\text{m}$ and coherence length $\zeta \approx 0.93\text{-}1.09 \mu\text{m}$. The NanoTube setup achieves slightly higher resolution (FSC-based) and increased CNRs (for the features considered), but requires only half of the scan time. However, as directly apparent from Fig. 2.6(a), this comes at the cost of reduced FOV, reflecting the different detector technologies. For sufficiently narrow samples, this could be compensated for by scanning two volumes consecutively and stacking them, which would result in similar overall scan time for both setups. The plots in (b) show profiles across the capillary edges indicated in (a). The two setups give very similar intensity profiles; absorption and edge enhancement is slightly more pronounced for the microfocus rotating-anode data. Finally, (c) and (d) show virtual slices through the xz- and xy-plane to judge image quality by visual inspection.

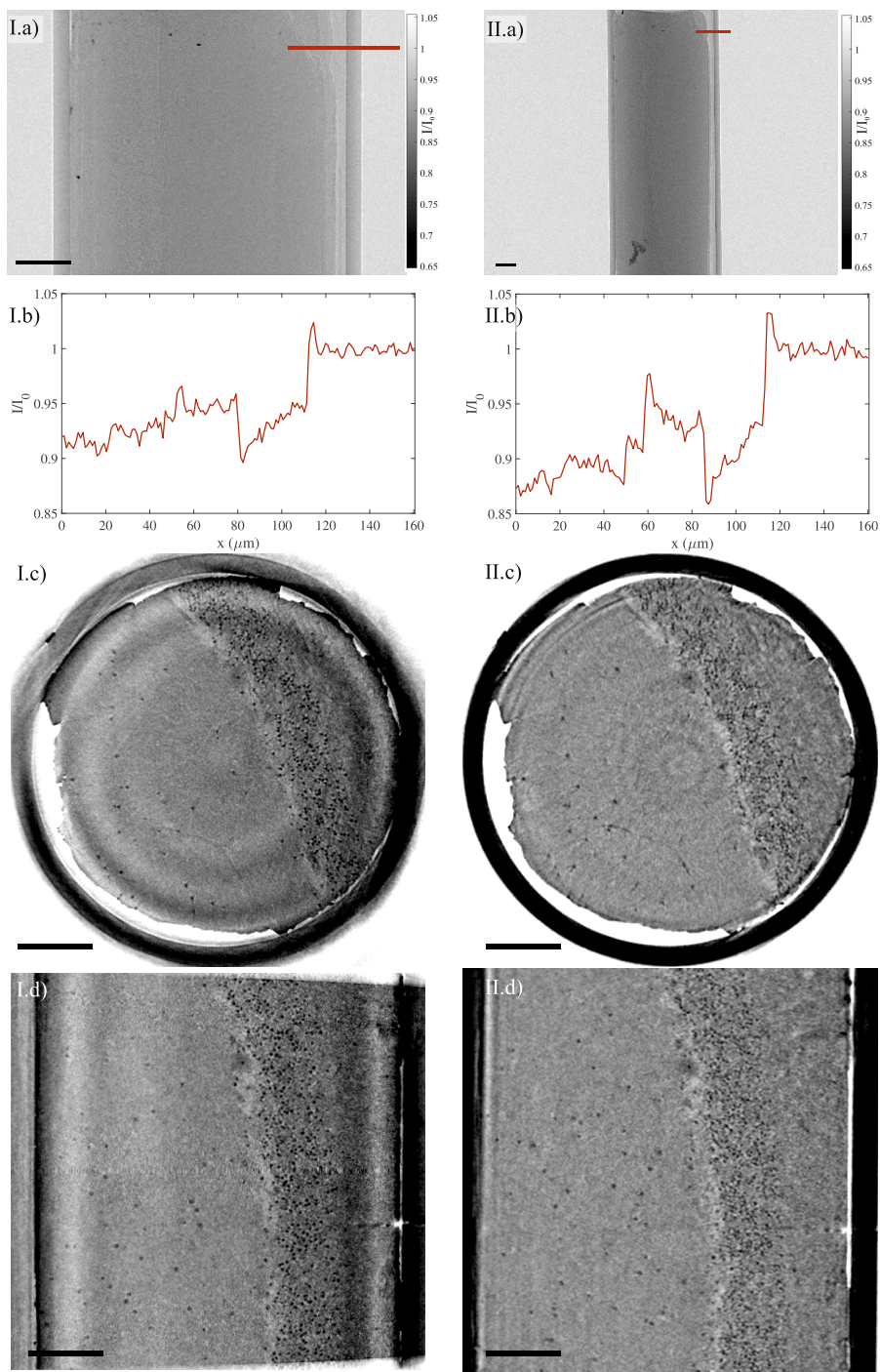


Fig. 2.6: (caption next page)

Fig. 2.6 (previous page): Comparison of (I) nanotube tomography with (II) microfocus rotating-anode results. Settings were chosen such that $px_{\text{eff}} \approx 1.07 \mu\text{m}$ same for both data sets. (a) Flat-field corrected projections. The colored bars show the position of the intensity profile plots in (b). Note the identical ranges of the y-axis. Virtual slices through the same position in the reconstructed sample volume are shown in (c) for the xz-plane and (d) the xy-plane. Scale bars: $100 \mu\text{m}$.

2.4 Summary and Outlook

In summary, we have successfully demonstrated phase-contrast tomography of unstained neuronal tissue, using a home-built laboratory setup with a nanofocus x-ray transmission tube (nanotube) and a photon counting pixel detector. Sufficient image quality for the detection of neurons and hence representation of the cyto-architecture was achieved. In particular, FSC analysis indicated a resolution of $0.90 \mu\text{m}$ for a source setting of $s = 0.30 \mu\text{m}$. The phase retrieval and reconstruction scheme presented here mixes amplitude and phase information, but is very suited to visualize the small electron density differences in unstained tissue and hence the cyto-architecture, for example of neuronal tissue. Final results can be represented as β or δ up to a factor of k , expressing the amplitude (real-valued transmission function) or the phase shift, respectively. Importantly, the information content for the cyto-architecture is enhanced by the phase effect, as evidenced by the variation of F , see also Fig. 2.7. Experimental determination of α_{BAC} as illustrated in Fig. 2.7 is unproblematic and results are robust with respect to variations up to about $\pm 40\%$. Since magnification and cone-beam angle are high, cone-beam tomographic reconstruction according to [10] is required. Effects of the cone-beam geometry can easily appear in form of distortions, such as at the edges of the source-facing side of the reconstructed volume (cf. Fig. 2.6 (I.d) & (II.d)). Compared to a microfocus rotating-anode setup, data quality and information content appear to be on a similar level. However, the particular advantage of the nanotube setup (apart from its more compact size and much reduced power consumption) is in its scalability with respect to progress in pixel detector technology. While already performing on the same level for a relatively thin silicon sensor, future replacement by 1 mm thick Si sensors or even $GaAs$ sensors, along with an increase in the detection panels may result in significantly reduced scan times. We also note that new pixel detector technology allows for registration of counting with sub-pixel registration and for photon energy determination [7], opening up an entirely new opportunity for laboratory phase-contrast tomography. Further progress is hence

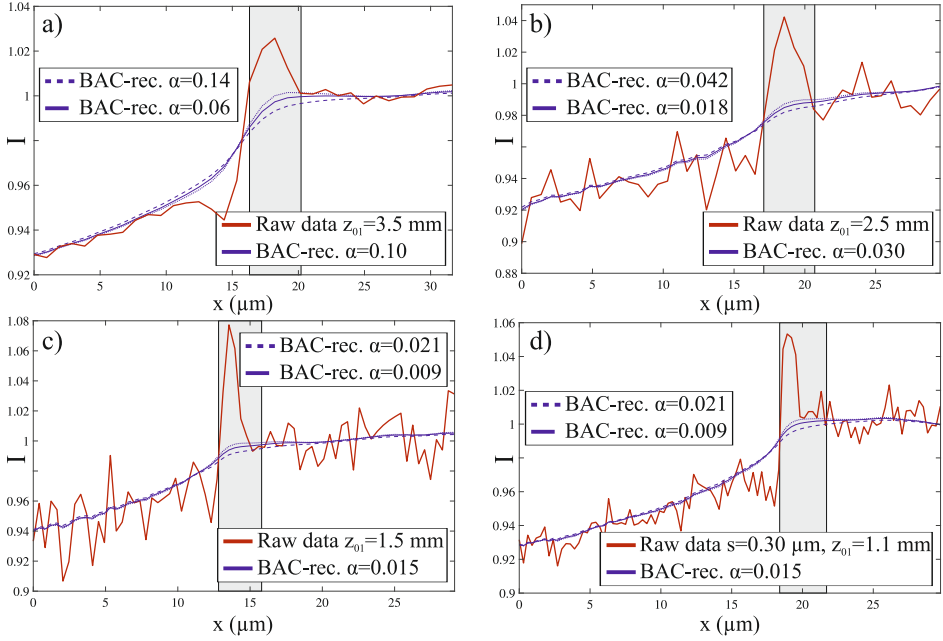


Fig. 2.7: Edge enhancement and choice of reconstruction parameters. The plots correspond to the data shown in Fig. 2.5 and give the image profiles before reconstruction (red) exhibiting pronounced edge enhancement between air and kapton tubes as a hallmark of phase contrast. In addition, profiles are shown after BAC-reconstruction, carried out for three different values of α_{BAC} , to illustrate the process of finding the best suited parameter value.

likely to bring virtual 3d histology to the performance in scan time and throughput required for clinical practice in neuropathology. This, however, would be useful only in combination with automated evaluation of cyto-architecture as in [37] and more knowledge on alterations associated with pathologies. Importantly, the demonstrated laboratory-based image quality would already be sufficient for this task.

Disclosures

This work was presented at SPIE Optics and Photonics 2019 as contribution 11113-21 “Phase contrast x-ray tomography of neuronal tissue at laboratory sources with submicron resolution”. Presentation Date: 12 August 2019. It is published in the corresponding conference proceedings (Optics and Photonics 2019: X-Ray, Gamma-

Ray, and Particle Technologies). Apart from that, there are no relevant financial interests in the manuscript and no other potential conflicts of interest to disclose. Human cerebellar tissue was retrieved at routine autopsy in agreement with the ethics committee of the University Medical Center Göttingen. Furthermore, the authors declare no conflict of interest.

Acknowledgments

We thank Excillum AB for their support with the NanoTube x-ray source, Peter Luley and Matthias Meister for engineering support, and Jasper Frohn for assistance with the microfocus rotating-anode x-ray source. Funded by the Deutsche Forschungsgemeinschaft (DFG, German Research Foundation) under Germany's Excellence Strategy - EXC 2067/1- 390729940.

This work has also been presented at SPIE Optics and Photonics 2019 and published in SPIE Conference Proceedings (Optics and Photonics 2019: X-Ray, Gamma-Ray, and Particle Technologies).

Bibliography

- [1] W. van Aarle, W. J. Palenstijn, J. De Beenhouwer, T. Altantzis, S. Bals, K. J. Batenburg, and J. Sijbers. “The ASTRA Toolbox: A platform for advanced algorithm development in electron tomography.” In: *Ultramicroscopy* 157 (2015), pp. 35–47.
- [2] H. Barrett and K. Myers. *Foundations of Image Science*. Wiley Series in Pure and Applied Optics. Wiley, 2013.
- [3] M. Bartels, M. Krenkel, P. Cloetens, W. Möbius, and T. Salditt. “Myelinated mouse nerves studied by X-ray phase contrast zoom tomography.” In: *Journal of Structural Biology* 192.3 (2015), pp. 561–568.
- [4] M. Bartels, V. H. Hernandez, M. Krenkel, T. Moser, and T. Salditt. “Phase contrast tomography of the mouse cochlea at microfocus x-ray sources.” In: *Appl. Phys. Lett.* 103.8, 083703 (2013), p. 083703.
- [5] M. Busse, M. Müller, M. A. Kimm, S. Ferstl, S. Allner, K. Achterhold, J. Herzen, and F. Pfeiffer. “Three-dimensional virtual histology enabled through cytoplasm-specific X-ray stain for microscopic and nanoscopic computed tomography.” In: *Proceedings of the National Academy of Sciences* 115.10 (2018), pp. 2293–2298.
- [6] T. Butz. *Fouriertransformation für Fußgänger*. Vieweg+Teubner Verlag / Springer Fachmedien Wiesbaden GmbH, Wiesbaden, 2012.
- [7] S. Cartier, A. Bergamaschi, R. Dinapoli, D. Greiffenberg, I. Johnson, J. H. Jungmann, D. Mezza, A. Mozzanica, B. Schmitt, X. Shi, M. Stampanoni, J. Sun, and G. Tinti. “Micron resolution of MÖNCH and GOTTHARD, small pitch charge integrating detectors with single photon sensitivity.” In: *Journal of Instrumentation* 9.05 (2014), pp. C05027–C05027.
- [8] Y. De Witte, M. Boone, J. Vlassenbroeck, M. Dierick, and L. Van Hoorebeke. “Bronnikov-aided correction for x-ray computed tomography.” In: *JOSA A* 26.4 (2009), pp. 890–894.

- [9] H. Dejea, P. Garcia-Canadilla, M. Stampanoni, M. Zamora, F. Crispi, B. Bijmens, and A. Bonnin. "Microstructural Analysis of Cardiac Endomyocardial Biopsies with Synchrotron Radiation-Based X-Ray Phase Contrast Imaging." In: *Functional Imaging and Modelling of the Heart*. Springer International Publishing, 2017, pp. 23–31.
- [10] L. A. Feldkamp, L. C. Davis, and J. W. Kress. "Practical cone-beam algorithm." In: *Josa a* 1.6 (1984), pp. 612–619.
- [11] P. Garcia-Canadilla, H. Dejea, A. Bonnin, V. Balicevic, S. Loncaric, C. Zhang, C. Butakoff, J. Aguado-Sierra, M. Vázquez, L. H. Jackson, D. J. Stuckey, C. Rau, M. Stampanoni, B. Bijmens, and A. C. Cook. "Complex Congenital Heart Disease Associated With Disordered Myocardial Architecture in a Midtrimester Human Fetus." In: *Circulation: Cardiovascular Imaging* 11.10 (2018).
- [12] A. Groso, R. Abela, and M. Stampanoni. "Implementation of a fast method for high resolution phase contrast tomography." In: *Optics Express* 14.18 (2006), pp. 8103–8110.
- [13] A. Groso, M. Stampanoni, R. Abela, P. Schneider, S. Linga, and R. Müller. "Phase contrast tomography: an alternative approach." In: *Applied Physics Letters* 88.21 (2006), p. 214104.
- [14] M. Guizar-Sicairos, S. T. Thurman, and J. R. Fienup. "Efficient subpixel image registration algorithms." In: *Optics Letters* 33.2 (2008), pp. 156–158.
- [15] G. Harauz and M. van Heel. "Exact filters for general geometry three dimensional reconstruction." In: *Proceedings of the IEEE Computer Vision and Pattern Recognition Conf.* Vol. 73. 1986, pp. 146–156.
- [16] M. van Heel and M. Schatz. "Fourier shell correlation threshold criteria." In: *Journal of Structural Biology* 151.3 (2005), pp. 250–262.
- [17] B. Henke, E. Gullikson, and J. Davis. *X-ray interactions: photoabsorption, scattering, transmission, and reflection at E=50-30000 eV, Z=1-92, Atomic Data and Nuclear Data Tables*. Database 2. Center for X-Ray Optics, Lawrence Berkeley National Laboratory, 1993.
- [18] S. E. Hieber, C. Bikis, A. Khimchenko, G. Schweighauser, J. Hench, N. Chicherova, G. Schulz, and B. Müller. "Tomographic brain imaging with nucleolar detail and automatic cell counting." In: *Scientific Reports* 6 (2016), p. 32156.

- [19] A. Khimchenko, C. Bikis, A. Pacureanu, S. E. Hieber, P. Thalmann, H. Deyhle, G. Schweighauser, J. Hench, S. Frank, M. Müller-Gerbl, et al. "Hard X-Ray Nanoholotomography: Large-Scale, Label-Free, 3D Neuroimaging beyond Optical Limit." In: *Advanced Science* 5 (2018), p. 1700694.
- [20] A. Khimchenko, H. Deyhle, G. Schulz, G. Schweighauser, J. Hench, N. Chicherova, C. Bikis, S. E. Hieber, and B. Müller. "Extending two-dimensional histology into the third dimension through conventional micro computed tomography." In: *NeuroImage* 139 (2016), pp. 26–36.
- [21] M. Krenkel, M. Töpperwien, M. Bartels, P. Lingor, D. Schild, and T. Salditt. "X-ray phase contrast tomography from whole organ down to single cells." In: *Proc. SPIE* 9212 (2014), 92120R.
- [22] P. Linstrom. *NIST Chemistry WebBook, NIST Standard Reference Database* 69. 1997.
- [23] M. Müller, I. de Sena Oliveira, S. Allner, S. Ferstl, P. Bidola, K. Mechlem, A. Fehringer, L. Hehn, M. Dierolf, K. Achterhold, B. Gleich, J. U. Hammel, H. Jahn, G. Mayer, and F. Pfeiffer. "Myoanatomy of the velvet worm leg revealed by laboratory-based nanofocus X-ray source tomography." In: *Proceedings of the National Academy of Sciences* (2017), p. 201710742.
- [24] B. Münch, P. Trtik, F. Marone, and M. Stampanoni. "Stripe and ring artifact removal with combined wavelet-Fourier filtering." In: *Optics Express* 17.10 (2009), pp. 8567–8591.
- [25] D. Paganin et al. *Coherent X-ray optics*. 6. Oxford University Press on Demand, 2006.
- [26] W. J. Palenstijn, K. J. Batenburg, and J. Sijbers. "The ASTRA tomography toolbox." In: *13th International Conference on Computational and Mathematical Methods in Science and Engineering. CMMSE*. 2013.
- [27] F. Pfeiffer, T. Weitkamp, O. Bunk, and C. David. "Phase retrieval and differential phase-contrast imaging with low-brilliance X-ray sources." In: *Nature Physics* 2.4 (2006), pp. 258–261.
- [28] M. Reichardt, J. Frohn, M. Toepperwien, J.-D. Nicolas, A. Markus, F. Alves, and T. Salditt. "Nanoscale holographic tomography of heart tissue with x-ray waveguide optics." In: *Developments in X-Ray Tomography XI*. Vol. 10391. International Society for Optics and Photonics. 2017, p. 1039105.

- [29] M. Saccomano, J. Albers, G. Tromba, M. D. Radmilović, S. Gajović, F. Alves, and C. Dullin. “Synchrotron inline phase contrast CT enables detailed virtual histology of embedded soft-tissue samples with and without staining.” In: *Journal of Synchrotron Radiation* 25.4 (2018), pp. 1153–1161.
- [30] J. F. Scopel, L. de Souza Queiroz, F. P. O’Dowd, M. C. F. Júnior, A. Nucci, and M. G. Hönnicke. “Are Human Peripheral Nerves Sensitive to X-Ray Imaging?” In: *PLOS ONE* 10.3 (2015), e0116831.
- [31] M. C. Strotton, A. J. Bodey, K. Wanelik, M. C. Darrow, E. Medina, C. Hobbs, C. Rau, and E. J. Bradbury. “Optimising complementary soft tissue synchrotron X-ray microtomography for reversibly-stained central nervous system samples.” In: *Scientific Reports* 8.1 (2018), p. 12017.
- [32] A. Tkachuk, F. Duewer, H. Cui, M. Feser, S. Wang, and W. Yun. “X-ray computed tomography in Zernike phase contrast mode at 8 keV with 50-nm resolution using Cu rotating anode X-ray source.” In: *Z. Kristallogr. Cryst. Mater.* 222.11/2007 (2007), pp. 650–655.
- [33] M. Töpperwien, T. R. Doeppner, B. Zechmeister, M. Bähr, and T. Salditt. “Multiscale x-ray phase-contrast tomography in a mouse model of transient focal cerebral ischemia.” In: *Biomedical Optics Express* 10.1 (2019), pp. 92–103.
- [34] M. Töpperwien, M. Krenkel, K. Müller, and T. Salditt. “Phase-contrast tomography of neuronal tissues: from laboratory-to high resolution synchrotron CT.” In: *Proc. SPIE* 9967 (2016), 99670T.
- [35] M. Töpperwien, M. Krenkel, D. Vincenz, F. Stöber, A. M. Oelschlegel, J. Goldschmidt, and T. Salditt. “Three-dimensional mouse brain cytoarchitecture revealed by laboratory-based x-ray phase-contrast tomography.” In: *Scientific Reports* 7.1 (2017), pp. 1–8.
- [36] M. Töpperwien, A. Markus, F. Alves, and T. Salditt. “Contrast enhancement for visualizing neuronal cytoarchitecture by propagation-based x-ray phase-contrast tomography.” In: *NeuroImage* 199 (2019), pp. 70–80.
- [37] M. Töpperwien, F. van der Meer, C. Stadelmann, and T. Salditt. “Three-dimensional virtual histology of human cerebellum by X-ray phase-contrast tomography.” In: *Proceedings of the National Academy of Sciences* 115.27 (2018), pp. 6940–6945.
- [38] T. Tuohimaa, M. Otendal, and H. M. Hertz. “Phase-contrast x-ray imaging with a liquid-metal-jet-anode microfocus source.” In: *Appl. Phys. Lett.* 91.7, 074104 (2007), p. 074104.

- [39] W. Vågberg, D. H. Larsson, M. Li, A. Arner, and H. M. Hertz. “X-ray phase-contrast tomography for high-spatial-resolution zebrafish muscle imaging.” In: *Scientific Reports* 5.16625 (2015), pp. 1–6.
- [40] W. Vågberg, J. Persson, L. Szekely, and H. M. Hertz. “Cellular-resolution 3D virtual histology of human coronary arteries using x-ray phase tomography.” In: *Scientific Reports* 8.1 (2018), p. 11014.
- [41] M. Van Heel. “Similarity measures between images.” In: *Ultramicroscopy* 21.1 (1987), pp. 95–100.
- [42] L. A. Walton, R. S. Bradley, P. J. Withers, V. L. Newton, R. E. B. Watson, C. Austin, and M. J. Sherratt. “Morphological Characterisation of Unstained and Intact Tissue Micro-architecture by X-ray Computed Micro- and Nano-Tomography.” In: *Scientific Reports* 5.1 (2015).
- [43] Y. Zhao, E. Brun, P. Coan, Z. Huang, A. Sztrokay, P. C. Diemoz, S. Liebhardt, A. Mittone, S. Gasilov, J. Miao, and A. Bravin. “High-resolution, low-dose phase contrast X-ray tomography for 3D diagnosis of human breast cancers.” In: *Proceedings of the National Academy of Sciences* 109.45 (2012), pp. 18290–18294.
- [44] T. Zhou, U. Lundström, T. Thüring, S. Rutishauser, D. H. Larsson, M. Stamparoni, C. David, H. M. Hertz, and A. Burvall. “Comparison of two x-ray phase-contrast imaging methods with a microfocus source.” In: *Optics Express* 21.25 (2013), pp. 30183–30195.

Three-dimensional Virtual Histology of the Cerebral Cortex based on Phase-Contrast X-ray Tomography

3

Marina Eckermann, Franziska van der Meer, Peter Cloetens, Torben Ruhwedel, Wiebke Möbius, Christine Stadelmann and Tim Salditt

Reproduced from Biomedical Optics Express (2021), **12**, 7582-7598.

In this work, we optimize the setups and experimental parameters of X-ray phase-contrast computed-tomography for three-dimensional imaging of the cyto- and myeloarchitecture of cerebral cortex, including both human and murine tissue. We present examples for different optical configurations using state-of-the art synchrotron instruments for holographic tomography, as well as compact laboratory setups for phase-contrast tomography in the direct contrast (edge-enhancement) regime. Apart from unstained and paraffin-embedded tissue, we tested hydrated tissue, as well as heavy metal stained and resin-embedded tissue using two different protocols. Further, we show that the image quality achieved allows to assess the neuropathology of multiple sclerosis in a biopsy sample collected during surgery.

3.1 Introduction

The human brain is formed by a complex and rapidly interacting network, with information processing within and across specialized subregions [66]. In order to decipher how the brain functions and how function is compromised in different pathological states, structural information is required, covering many length scales. On the macro- and

microscale, the cytoarchitecture and myeloarchitecture account for the different types, morphologies, and concentrations of neurons, glial cells and connective fibers, and their connectivity, and is typically assessed by optical microscopy based on histological thin section or cultured tissue slices [36, 37, 47, 56]. Optical microscopy in combination with immunohistochemistry constitutes a routine technique of neuropathology and pre-clinical research, for example in neurodegenerative diseases. Small-angle X-ray scattering has also proven to be suitable for studying the myelostructure in murine and human brain tissue [32, 33]. On the nanoscale level, neuronal circuits can be probed by modern electron microscopy (EM), in particular serial block face scanning electron microscopy (SBEM) [26, 27] or volume-EM by automated transmission-EM (TEM) [50], enabled by advanced heavy metal staining, notably the adapted rOTO-protocols [31, 44, 45].

More recently, X-ray phase-contrast computed-tomography (PC-CT) has joined the toolset to study human brain tissue [5, 18, 25, 53, 78], as well as small animal models of mammalian brain tissue [13, 29, 72, 73, 77]. Similar to conventional CT, PC-CT offers three-dimensional (3d) reconstructions without any need for sectioning, while offering much higher contrast to soft tissues and also resolution, when free-wave propagation is exploited for contrast formation. PC-CT can be implemented both with synchrotron radiation (SR) and compact laboratory sources (μ CT). Tissue volumes can be scanned with adjustable field-of-view and resolution. For larger overviews, parallel-beam (PB) illumination is most efficient, scanning entire biopsy punches within minutes [24] at a resolution limited by the detector pixels size (*i.e.* down to the sub- μ m range). Selected subregions can then be probed in cone-beam (CB) geometry down to the sub-100 nm range, below the diffraction limit of optical microscopy. Here, a resolution given by the half-width of the source spot can be achieved, *i.e.* at the level of the focused synchrotron radiation. Applications of PC-CT in human brain sample imaging, in particular of unstained formalin-fixed and paraffin-embedded (FFPE) tissues, have recently been demonstrated. Cellular and sub-cellular structural details can be observed in these preparations [20, 35, 75]. Further sample preparation techniques for PC-CT of unstained neuronal tissue exist, including formalin-fixed, dehydrated or hydrated tissue in solution or tissue fixed and embedded in paraffin [2, 3, 55, 73]. In order to create enhanced contrast for small cellular features and in particular nerve fibers, osmium-based protocols have also been used for PC-CT of tissue from the central nervous system of murine and from the peripheral nervous system both of human and murine tissue [4, 21, 70, 71].

Following preceding PC-CT studies on human cerebellum and hippocampus [74, 75],

the main goal of the current work is to explore to which extent PC-CT could contribute to imaging of the cerebral cortex of the mammalian brain, and in particular of the human brain, which shows a complex neuroanatomy with 10^{15} neuronal connections [66]. We include the corpus callosum (CC), which is the major tract of commissural fibers, with 10^8 nerve filaments connecting both hemispheres of the brain [1]. For the essential neuroscience background, we refer to [58, 66]. In this context, we ask to which degree advanced staining protocols can help to increase contrast and resolution. In view of the aforementioned recent progress in heavy metal staining and the preceding advent of SBEM, which has made it possible to address the connectivity problem in small brain volumes [17, 34, 61], the question arises whether PC-CT can extend this toolset towards larger brain volumes. If so, it may contribute in future to integrate data from different smaller volumes scanned by SBEM. A recent proof-of-concept demonstrates the potential of PC-CT in this context [11, 39]. Here, we investigate which instrumental and optical settings, both at synchrotron and inhouse laboratory sources, can take advantage of different stains: To this end, both conventional- OsO_4 and rOTO staining protocols are applied. At the same time, we further include unstained hydrated, (partially) dehydrated, and FFPE-tissue of the cerebral cortex, as well as OsO_4 -stained and epon-embedded sample blocks (cf. Fig. 3.1 (d) and Fig. 3.1 (e & f), and supplemental document for experimental concepts of data acquisition).

Fig. 3.1 shows a schematic of the cortical regions, from which tissue autopsies and biopsies are scanned in the present PC-CT study. The sagittal view in Fig. 3.1 (a) shows the CC in cross section, while its frontal view is depicted in (b). Various types of neurons exist throughout the cerebral cortex, detailed in [42]. 80% of the cortical neurons are projection neurons, and they are responsible both for short- and long-range signaling. Fig. 3.1 (c) shows a sketch of such a projection neuron, which receives input through its dendrites (top), and processes via its myelinated axon to the axon terminal (bottom). Close to the neuron's dendrites, microglial cells are sketched (μG). μG ensure brain maintenance, and target for example misfolded proteins leading to plaques, or damaged neuronal portions. Astrocytes serve the physical organization of the brain, and together with oligodendrocytes (OD) provide the metabolic supply of synapses. Importantly, ODs wrap axons with concentric myelin sheaths.

Apart from neuroimaging of healthy brain tissue, we also want to focus on the assessment of PC-CT for studies in neurodegenerative diseases. Following our recent PC-CT works on human hippocampal tissue affected by Alzheimer's disease, we here include first scans of human brain tissue biopsies obtained during surgery of a patient suffering from *Multiple Sclerosis* (MS). MS is an inflammatory and neurodegenerative disease,

which is pathologically characterized by chronic inflammatory demyelination, accompanied with axonal loss and glial scar formation [67]. Glial scar can occur in any type of brain damage, not restricted to inflammation, and reflects an increased number of astrocytes through hyper-proliferation, which rigidifies the tissue. While white matter lesions are rather prominent with clinical routine imaging techniques, pathologies in gray matter emerge unobtrusively. Pathohistological assessment thereof remains a technical challenge [67]. To-date, the insufficient feature contrast is eluded by special myelin protein immunohistochemistry, but also PC-CT could be a potential tool. The astrocyte proliferation is a reaction to stabilize lesions and to keep inflammatory cell

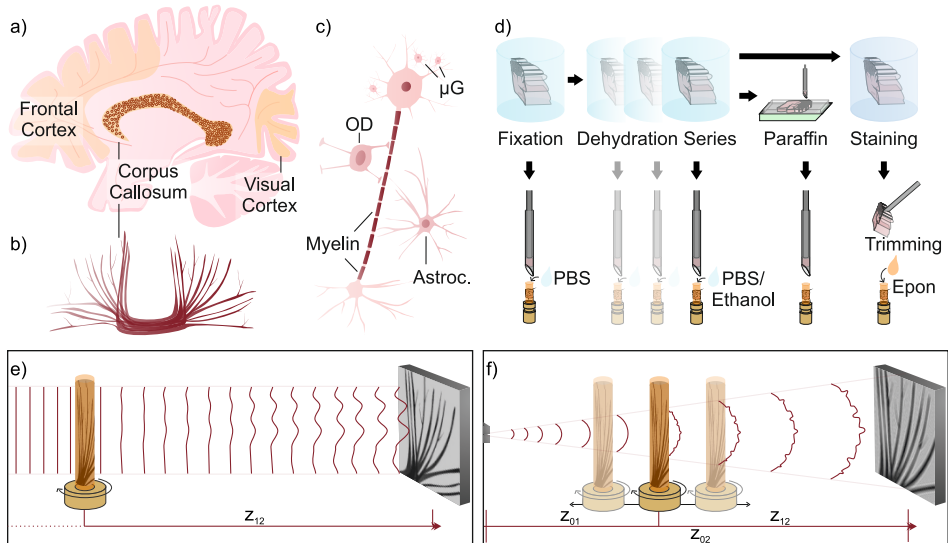


Fig. 3.1: Basic anatomy, structural features of interest, sample preparation, and measurement principle. (a) Schematic of the human brain in sagittal plane, yellow colors indicate relevant cortical regions for this work: Frontal cortex, visual cortex, and corpus callosum, which is also outlined in coronal plane (b). (c) Schematic of selected cortical structures on a cellular level: neuron with a myelinated axon, microglial cells (μG) in the vicinity of the dendritic tree, oligodendrocytes (OD), and astrocytes (Astroc.). (d) A range of sample preparation protocols are applied, ranging from solely chemical fixation, (partial) dehydration, to (un-)stained solid embedding. PC-CT data are collected (e) in parallel-beam (PB) mode to quickly scan rather large tissue volumes (cf. supplemental document), or (f) exploiting geometrical magnification to zoom into selected regions of interest in cone-beam (CB) geometry (cf. methods in supplemental document). Note that setup-characteristic parameters are indicated: (z_{01}) source-to-sample distance, (z_{02}) source-to-detector distance, and (z_{12}) sample-to-detector distance.

from spreading, but at the same time is believed to hinder new neuronal growth [60, 62]. Furthermore, astrocytic factors impede the differentiation of OD-progenitor cells. Signs of glial scar formation are completed by increased emergence of μ G, resulting in angiogenesis and fibrosis. Damage of the myelin sheath followed by scar formation is also referred to as "MS-plaques". Overall, various forms (chronic, acute) and stages of MS exist [8, 40], in which OD even regenerate and remyelinate. According to the definition in [23], normally appearing white matter (WM) refers to tissue with normal axon myelination, without plaques in a radius of ≥ 10 mm and no further signs of abnormality, while normally appearing gray matter (GM) shows no signs of demyelination using immunohistochemistry. Normally appearing tissue is distinct from remyelination region, in which shadow plaques (plaques with myelin sheath, "remyelinated lesions") and newly formed myelin sheaths with reduced thickness are found [49]. Here we want to investigate, at which quality structural features can be identified in PC-CT reconstructions.

Next, we briefly introduce the topics of relevance in this work: instrumentation and optics for synchrotron and laboratory PC-CT, sample preparation including unstained, hydrated, and heavy metal stained tissues, and the important role of mouse models, notwithstanding the fact that human brain tissue remains the main incentive of this work.

Laboratory μ CT In view of future applications in pathohistology, it is important to assess to which extent phase-contrast imaging of unstained human tissue can be implemented with laboratory μ CT. With recent advancements in both reconstruction schemes suitable for low coherence and novel instrumentation, such as transmission-anode X-ray sources with small source spots and sufficient power (for example approx. 300 nm and 0.3 W, respectively, for the N2 NanoTube, Excillum Inc.), partially-coherent illumination can now be implemented at compact laboratory setups for 3d virtual histology analysis [20], even without liquid-jet anode technology which was used in [71, 75] or a compact laser-driven synchrotron source [22]. Details on implementations can be found in the supplemental document.

Synchrotron Radiation The much higher brilliance and in particular spatial coherence enables focusing to spot sizes in the 10-100 nm range, while preserving high photon flux, now routinely exceeding $> 10^9$ ph/s [14, 54, 59, 63, 68]. Synchrotron scans in such a cone-beam geometry (SR-CB) with nanometric virtual source offer the highest resolution and potential for further scaling. Due to the correspondingly

smaller effective pixel size in the sample plane, data acquisition typically takes place in the so-called deep holographic regime, defined by a very small Fresnel number $F \ll 1$ (cf. supplemental document). Further, using monochromatic illumination, this regime offers highest sensitivity to small phase differences. Consequently, it allows for quantitative interpretation of reconstructed density, based on well-defined optical constants. For recordings in the holographic regime, these are decisive advantages of SR, where single X-ray energies are selected based on multilayer or crystal monochromators, while laboratory PC is always restricted to broad bandpass due to its limited brilliance. Also filtered white or pink SR can be used for PC-CT, offering elevated photon flux. Most SR parallel-beam data (SR-PB) are recorded in the so-called direct contrast regime ($F \leq 1$), which is compatible with broad bandpass. However, for high-resolution studies in the holographic regime, a higher monochromaticity is required. Furthermore, radiation damage can occur more easily for pink beams.

Hydrated and in Solution In conventional histopathological analysis, FFPE-sample blocks are prepared by chemical fixation, gradual dehydration and subsequent paraffin infiltration, and further processed through slicing, rehydration, and staining before inspection by optical microscopy. Aside from its 3d capability, virtual histology and pathohistology based on PC-CT can be motivated by the following properties: a different and complementary image contrast based on electron density, compatibility with sample preparations beyond the standard FFPE-scheme, which is known to be associated with pronounced tissue modifications [7, 10, 38], and finally the wish to reduce effort and time in sample preparation. To this end, the image quality and performance of PC-CT for liquid-embedded samples has to be further assessed.

Heavy-metal Staining Beyond the contrast based on (native) electron density obtained from unstained tissues, feature-specific contrast can be achieved by staining. Osmium tetroxide (OsO_4), for instance, binds to the phospholipid headgroups, and hence gives particular contrast to plasma membranes, multi-vesicular structures, ribosomes and Golgi complexes. Membrane-rich cortical structures such as fiber tracts should therefore emerge particularly. Further to contrast enhancement, chemical fixation of sample tissue is an important property of OsO_4 [51]. Sophisticated classical OsO_4 -based protocols exist for EM applications, and have been finetuned for bulk tissue staining, notably as adapted *rOTO* ("reduced osmium, thiocarbohydrazide (TCH), osmium") [44, 45], resulting in contrast levels compatible with SBF-SEM connectomic studies [26, 27]. Reducing agents, such as potassium ferrocyanide, are one key aspect of

rOTO, converting Os^{VIII} to reduced oxidation states [31]. As a result, larger amounts of osmium are deposited onto the membrane. However, in conventional rOTO [81], the penetration depth typically does not exceed 200 μm . In order to overcome this limitation, the reducing agent can be applied only right after deep osmium penetration. Consequently, this rOTO modification [31] can surmount staining rings at the tissue periphery and limited penetration depth, making it possible to process mm-thick tissue blocks. While this is well-established for EM, for PC-CT, osmium-based staining gave good results for tissue of the peripheral nervous system [4, 15, 69, 79], and, to some extent, of the central nervous system [3, 6, 21, 43, 48]. However, staining protocols specifically optimized for PC-CT, *i.e.* in view of volume suitability and contrast agent density, are still lacking. Recently, well-established procedures from conventional histology have been adapted for PC-CT [9, 46]. Regarding heavy metal protocols from EM, it is less clear how heavy metals are the most suitable approach for PC-CT. There are still many open questions regarding the most suitable protocols for given tissue type, photon energy, instrumentation (SR versus laboratory μCT) and phase retrieval approach. First findings demonstrate that the modified rOTO protocol from [31] is also well suited for SR-PC [39]. Still, to-date, PC-CT applications using heavy metal stains for tissue of the central nervous system have been reported only for small animal models, and not for human tissue.

Murine Brain Tissue The mouse brain is an indispensable example for the neurobiology of the mammalian brain in order to unravel mechanisms of different neurodegenerative diseases in genetically well-controlled mutants. As far as imaging is concerned, small animal models offer some advantages in tissue preparations as compared to human tissues. Optimized fixation, such as perfusion of the mouse brain and more control of the preparation protocol, can be expected to result in better preservation of the tissue's ultrastructure [65]. At the same time, neurons of the mouse brain are smaller and of lower (native) electron density, compared to human, which can pose a greater challenge for PC-CT, see for example the image quality of human [75] and murine cerebellum [73] for recordings of similar experimental settings. Furthermore, studies of murine brain tissue are adequate to develop and refine sample preparation protocols, which can later be partially translated to human tissue, under the constraints given by clinical pathology.

At the end of this introduction, we briefly outline the further organization of this manuscript. In the following results section, we first address unstained human brain

tissue, comparing paraffin-embedded and hydrated samples, as well as results obtained with synchrotron radiation (SR) and laboratory instrumentation (μ CT), before we focus on heavy metal stains both in human and murine cortical tissue. We close with a discussion section presenting the main conclusions and an application outlook.

3.2 Results

First, we turn to PC-CT results obtained for unstained tissue of the human cortex, comparing formalin-fixed, dehydrated and paraffin-embedded (FFPE) with hydrated samples, as well as synchrotron radiation (SR) and compact laboratory sources (μ CT). The image quality and volume information in each image configuration can be assessed in view of future applications for histopathological inspection and analysis. For these and all further datasets, details on sample preparation and experimental setups are given in the supplemental document, with data acquisition and reconstruction settings listed in Tab. S1-S3.

Fig. 3.2 presents an overview over PC-CT reconstructions and segmentation of neurons from parallel and cone-beam synchrotron radiation (SR1-PB and SR1-CB configuration, cf. supplemental document). All samples are unstained and embedded in paraffin, collected as 1 mm biopsy punches from FFPE-tissue blocks. While all panels indicated by (a) refer to tissue collected during *post mortem* routine autopsy from a (neuropathologically) normal subject, panels indicated by (b & c) refer to biopsy tissues samples from a patient diagnosed with MS, and collected during surgery. Notably, sample (c) has been extracted from a region of normal appearing gray matter, and (b) from a remyelinated region of an individual with MS, as defined in the introduction. With regard to the feature pathology in the remyelinated region, the normally appearing sample can be considered as a control presenting the same subject-specific and tissue processing conditions, while (a) represents a control in a wider-range pathological sense. Fig. 3.2 (a-c.i) shows overview orthoslices from the 1 mm biopsy punches, recorded in SR1-PB configuration, with (a-c.ii) showing corresponding volume renderings of neuronal structures, and (a-c.iii) planar slices. For the remyelinated sample, (b.iv) shows a region-of-interest (ROI) corresponding to the marked region in (b.i), which has subsequently been scanned in SR1-CB configuration. (b.v & vi) present volume renderings of the ROI, with neuron shapes and axons showing a strong orientation. In the two lower rows, single neurons are highlighted, recorded in SR1-CB configuration for all three samples. In each data set, neurons with both a particularly

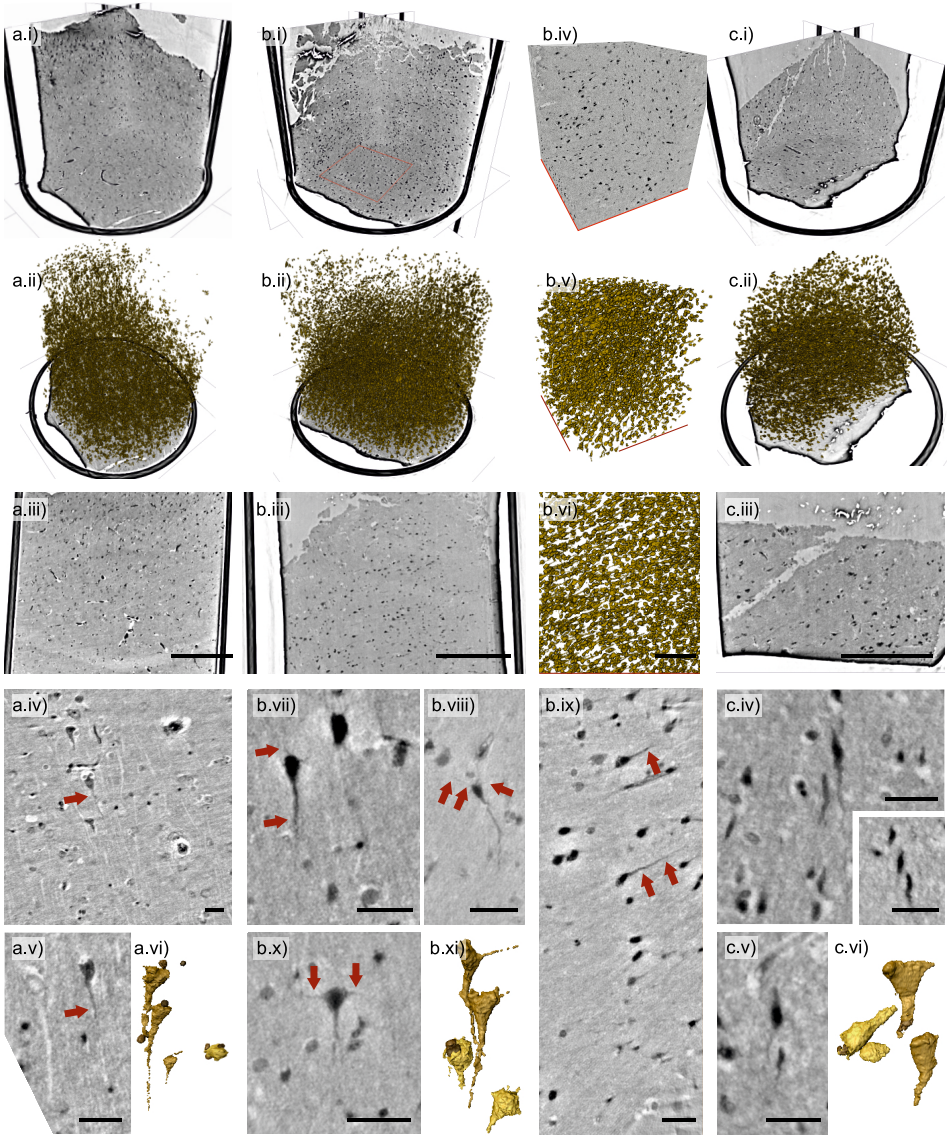


Fig. 3.2: (caption next page)

high and low electron density can be found. Axonal fibers are well-contrasted based on their native electron density, and even the dendrites can be distinguished in some cases. Further, for the control sample data shown in (a.iv), the spatially oriented fibers emerge with a lower electron density (lighter color) compared to the surrounding tissue, as opposed to the biopsy samples. In all three samples, the image quality and

Fig. 3.2 (previous page): Human cortical tissue, unstained FFPE-preparation, SR1 scans. (a) cortex control tissue sample, collected *post mortem*, (b & c) cortex tissue samples collected from a subject diagnosed with Multiple Sclerosis (MS) during surgery: (b) from a remyelination region, (c) from normally appearing cortex. Top three rows show slices and volume renderings of neurons from SR1 data: (a.i-iii, b.i-iii, c.i-iii) present reconstructions from SR1-PB scans, (otherwise) higher resolution reconstruction from a SR1-CB scan of the region marked in (b.i). Fiber structures and neurons with delicate dendrites (exemplary highlighted by arrows), and associated cells are depicted as single slices or Maximum Intensity Projections (MIPs), with projection thickness given by: (a.iv & v, c.iv-inset) 2 μm , (b.vii & ix) 1 μm , (c.v) 1.6 μm . (a.vi, b.xi, c.vi) Volume renderings of four representative neurons and microglia. Scale bars: (a.iii, b.iii, c.iii) 300 μm , (b.vi) 100 μm , (otherwise) 30 μm .

resolution is sufficient for gray-value based segmentation, as illustrated by selected segmentations of neurons along with smaller bordering cells, which can tentatively be identified as microglia. The corresponding renderings (a.vi, b.xi, c.vi) were all obtained manually using Avizo Lite (Thermo Fisher Sci.).

As discussed in the introduction, it is of interest to explore to which extent PC-CT can be applied to unstained tissue beyond the standard FFPE-scheme, which can suffer from dehydration artifacts, and for which more preparation steps are required compared to simple fixation and embedding of tissue in buffer or solvent. Here we examine the image quality and performance of PC-CT for liquid-embedded human cortical tissue, following up our previous work on cerebellum [73]. To this end, Fig. 3.3 presents results obtained for cortical tissue of a single human (control), scanned in SR1-CB configuration in three different liquids, representing a *dehydration series*: (a) fully hydrated in PBS (0% dehydration), (b) 30% PBS 70% ethanol, and finally (c) in 100% ethanol. Overview slices in (a-c.i) show reasonable tissue contrast for all steps of preparation. Fig. 3.3 (middle row) features single cells: cell bodies, nuclei and nucleoli can be clearly distinguished, and even also cellular dendrites. Inspection of the data gives an impression of cellular shrinkage with increasing ethanol infiltration. Overall tissue volume reduction from dehydration is well-known. However, the observation also depends on the exact cellular type. For example, cells marked in (a.ii) and (c.iii) both emerge particularly strong and with similar size despite the different solvents. In Fig. 3.3 (lower row), the pronounced impact of dehydration on vessel architecture stands out.

Next, we assess to which extent phase-contrast of unstained human tissue can be

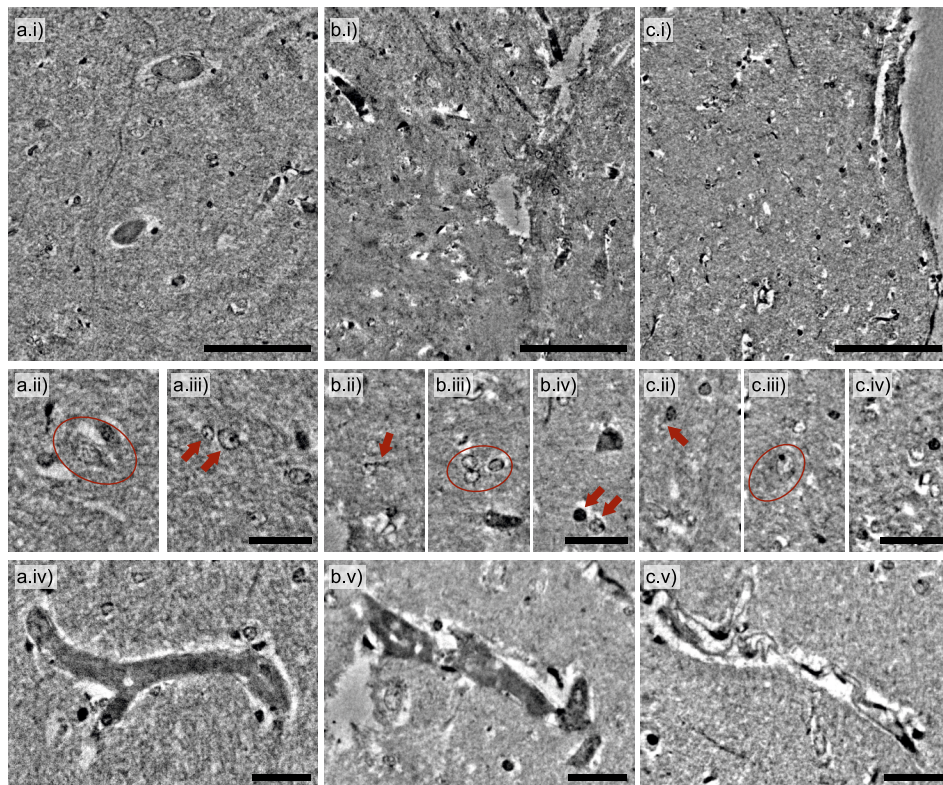


Fig. 3.3: Human cortical tissue, unstained in liquid, SR1 scans: (a) Fully hydrated in PBS (0% dehydration), (b) in 30% PBS 70% ethanol, and (c) in 100% ethanol. (Top row) Depiction of the overall tissue structure, (middle row) selected regions highlighting single cells and dendritic structures, (bottom row) vasculature changing appearance during dehydration. Scale bars: (a-c.i) 100 μm , (otherwise) 30 μm .

exploited in laboratory μCT (cf. supplemental document). Fig. 3.4 demonstrates that this approach can indeed yield convincing image quality for unstained human cortical tissue, with sufficient contrast for neurons and axons. Note that this example is presented for the biopsy samples collected during surgery, pointing out the potential for future use of PC-CT in clinical pathological diagnostics. Both setups yield very similar feature visibility and comparatively high resolution, owing to the sub- μm spot size of both sources, but differ in the detector technology, *i.e.* indirect fibre-coupled CCD (μCT1) versus direct detection with a single-photon counting pixel detector (μCT2). This also accounts for the observed differences in the ring artifacts, observed in μCT2 data, which can be attributed to the inter-module gaps of the single-photon counting

detector.

We move from unstained tissue, *i.e.* PC-CT with contrast based on (native) electron density, to contrast-enhancement from heavy metal staining. Previous PC-CT studies of the central nervous system using heavy metal stains have been reported only for small animal models, and not for human tissue. In Fig. 3.5, the conventional OsO_4 -staining procedure (cf. supplemental document) has been applied to human *post mortem* tissue, notably (a) gray and (b) white matter (GM, WM). (a.i & ii) show volume renderings of myelinated structures and corresponding virtual sections. By adjusting geometric magnification and source size, the tissue was scanned at 350 nm voxel size, see (a.iii-iv) for examples with μCT1 . A tool developed for segmentation of single myelinated axons in synchrotron nanotomography data [15] was also applied here for

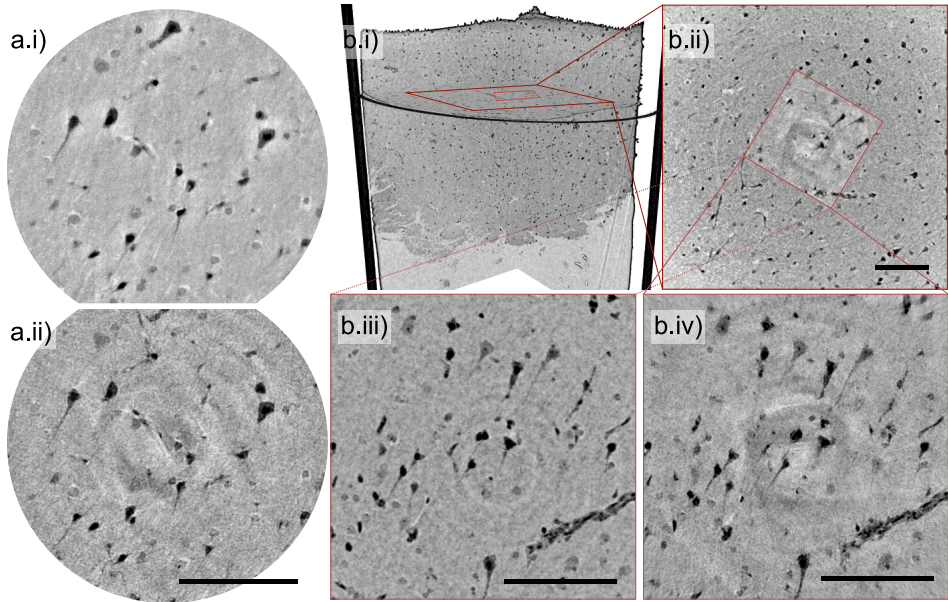


Fig. 3.4: Human cortical biopsies, unstained FFPE-preparation, laboratory-based PC-CT. Reconstructions are shown for a tissue biopsy collected during surgery from the remyelinated region of a subject diagnosed with MS. (a) Comparison between SR and laboratory: reconstruction of the same regions from (a.i) SR1-CB data, and (a.ii) L2-data, both represented as Maximum Intensity Projections (MIPs) over 1.4 μm thickness. (b) Overview scans and ROIs, reconstructed from (b.i & ii) μCT1 data. Squares mark regions recorded with 350 nm voxel size, using μCT2 , pasted into the μCT1 reconstruction as an inset. (b.iii & iv) MIPs with 6 μm thickness of the same region, scanned with μCT1 & μCT2 , respectively. Scale bars: (b.ii) 140 μm , (otherwise) 100 μm .

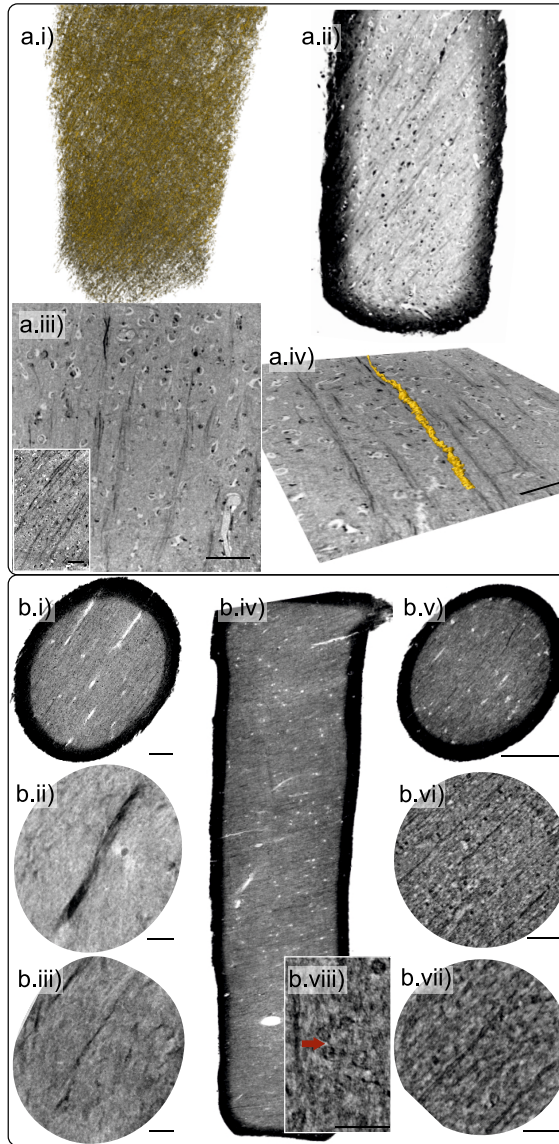


Fig. 3.5: Human cortical tissue, OsO_4 -stained, SR1-PB, SR1-CB, $\mu\text{CT}2$. The examples show *post mortem* human cortical tissues from: (a) GM and (b) WM. After overview scans recorded at (a.i-ii & b.i) the $\mu\text{CT}1$, (b.ii-iii) the $\mu\text{CT}2$, and (b.iv-v) the SR1-PB setup, more detailed scans were recorded with (a.iii-iv) $\mu\text{CT}1$ and (b.vi-viii) SR1-CB configuration. (a.i) Volume rendering of stained fibrous structures within the entire punch. In (a.iv), a neuron was tracked and segmented based on its contrasted myelin sheath. MIPs over (b.i) $11.5\ \mu\text{m}$, (b.v) $2\ \mu\text{m}$, (b.vii) $0.35\ \mu\text{m}$, (b.viii) $0.5\ \mu\text{m}$ thickness. Scale bars: (b.v) $300\ \mu\text{m}$, (b.vi-viii) $50\ \mu\text{m}$, (otherwise) $100\ \mu\text{m}$.

a proof-of-concept that fiber tracing can be performed at the level of quality achievable from laboratory PC-CT of stained tissue, see the rendering in (a.iv). OsO₄-stained human WM is shown in Fig. 3.5(b), for data from (b.i) μ CT2 (0.99 μ m voxels), and from (b.iv-v) SR1-PB, and in more detail for (b.ii-iii) data obtained at μ CT2 (0.65 μ m voxels) and (b.vi-viii) SR1-CB. Even in rather large FOV-scans, the delicate myelinated fibers which are on the order of a few microns in width can be identified based on the contrast provided by the conventional OsO₄-stain. Note that in (b.vii & viii), the source-to-sample-distance has been decreased, affecting the geometric magnification of single resolution elements from 159 nm to 49 nm.

After having presented examples of human tissue above, we now turn to PC-CT of small animal models, more explicitly murine tissue of the central nervous system. In particular, we present PC-CT results of murine brain tissue for the conventional-OsO₄ protocol, and the rOTO-technique, both applied to K&S-fixed murine cortical tissue (cf. supplemental document). As expected, the heavy metal staining helps to extend the application range of laboratory μ CT.

Fig. 3.6 shows reconstructions from laboratory μ CT1-data, for (a) rOTO- and (b) conventional-OsO₄ staining. The samples depicted in (a.i-b.ii) have been extracted along the craniocaudal axis, and comprise a number of different brain regions. With the CC as the most massive part of the commissural fibers, it emerges particularly contrasted. This region is further depicted in Fig. 3.6 (middle & bottom row), with (a.iii-b.iv) showing virtual sections, and (a & b.v) reconstructed volumes rendered purely based on the voxel gray-values. With high-resolution settings for setup μ CT1, inter-layer connections are studied locally in (a.vi-b.vii).

Heavy-metal stains can also help to increase resolution and image contrast in synchrotron PC-CT. Fig. 3.7 presents an overview of SR1-PB (parallel-beam) and SR1-CB (cone-beam configuration) data obtained on the same murine samples as in Fig. 3.6, again labeled (a) for rOTO-protocol and (b) for conventional OsO₄-staining. Panels (a-b.i) have been acquired with the SR1-PB setting. The fibroid nature of the CC is very clearly represented already on larger scale for rOTO. Neuronal cell bodies emerge with lighter contrast in both protocols. In (a.ii & b.ii-iii) and (a.iii-iv & b.iv) higher resolution scans are presented, acquired in the SR1-CB and SR2 setup, respectively. In these reconstructions, the cylindrical myelin sheath around the axons is clearly resolved and single axons can be traced in 3d. Not all myelinated fibers in the CC are oriented along the same direction, as exemplary indicated by the elongated arrows. In

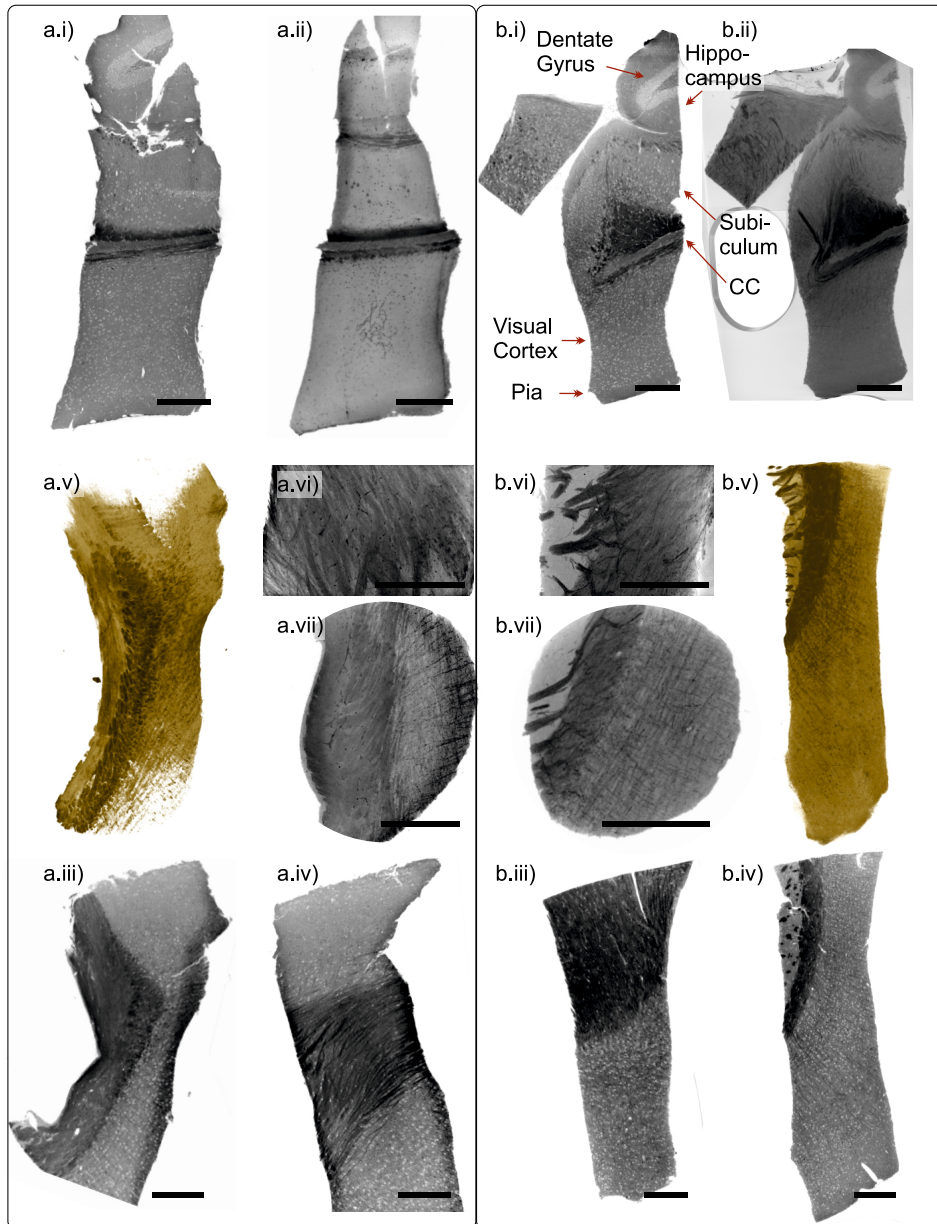


Fig. 3.6: Murine brain tissue, different heavy metal stains, laboratory CT. Virtual sections, MIPs and volume renderings are shown for (a) rOTO-protocol, and (b) conventional OsO_4 -staining. (a.ii & b.ii) MIP over 100 μm , (a.vi) MIP 20 over μm , and (a.vii, b.vi & vii) MIP over 35 μm thickness. (a.v & b.v) volume renderings, (otherwise) virtual sections. Scale bars: 300 μm .

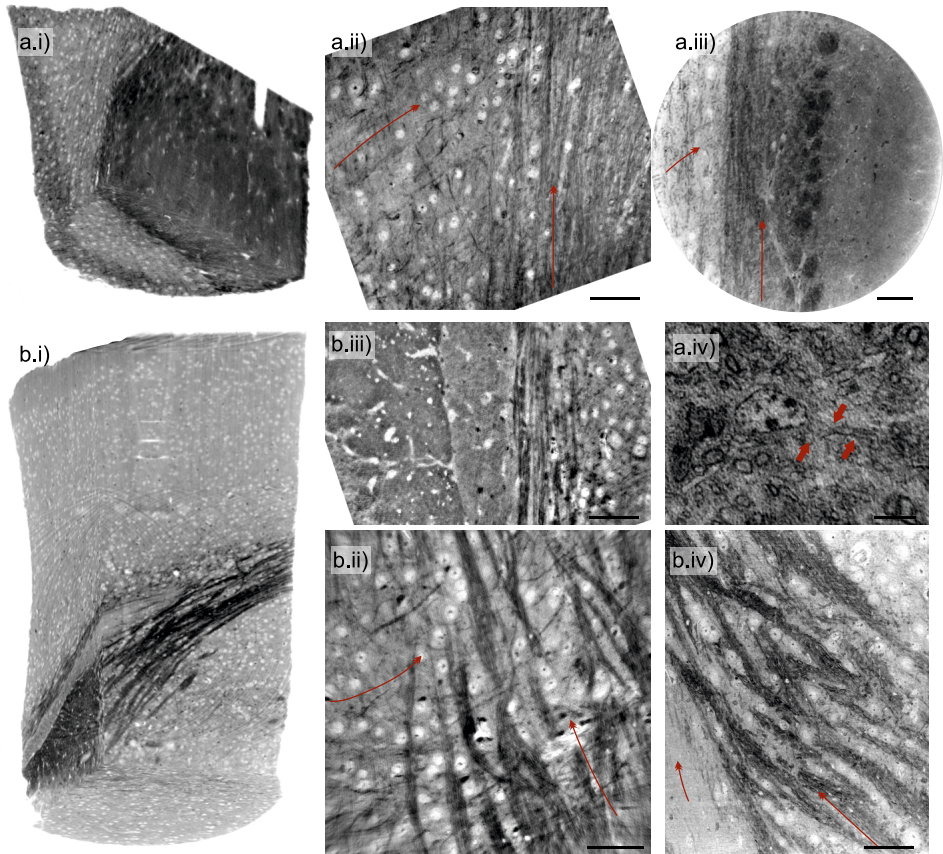


Fig. 3.7: Murine corpus callosum (CC), stained with the (a) rOTO protocol and (b) conventional-OsO₄ (cf. supplemental document), using (a.i & b.i) the SR1-PB, (a.ii & b.ii-iii) SR1-CB and (a.iii-iv & b.iv) SR2. Elongated arrows indicate the general fiber orientation, accentuating the cross-fiber organization of the CC, and bold arrows mark cell body membrane with axonal extensions. Scale bars: (a.iv) 5 μ m, (otherwise) 50 μ m.

the scans shown in (a.iv), the voxel size was further reduced from 130 nm to 50 nm. The myelinated axon shapes are well-resolved and contrasted. They are recognized in longitudinal section, and in cross-sectional view, as marked by arrows. Further, pronounced variations in electron density are resolved in the nucleus, indicative of heterochromatin. Again, the exact settings of all scans are listed in Tab. S1 & S2.

Finally, Fig. 3.8 closes the presentation by highlighting the results obtained for the rOTO-stain at high magnification, both with synchrotron radiation (SR1-CB, SR2), and high resolution laboratory (μ CT1). Panels (a) and (b) show two virtual sections of rOTO-stained murine CC tissue, while (c) presents a rendering of a μ CT1 laboratory dataset (visualization with NVIDIA IndeX). The wealth of neural cell bodies and the complex fiber structures in the CC, jointly with negatively contrasted vasculature, emerge particularly in this presentation.

3.3 Discussion

In summary, the examples presented above demonstrate the capability of PC-CT to cover mm³-sized tissue volumes with convincing image details regarding the neuronal cyto- and myeloarchitecture. Different imaging demands require different field-of-view, voxel size and resolution, as well as contrast. In most general terms, this can be met by adaptation of the tissue preparation, staining, choice of photon energy and flux, the instrumental and geometric settings, and reconstruction algorithms. The present work gives some examples how settings and parameters can hence be tuned and shifted accordingly. We draw the following conclusions:

- Following previous PC-CT of human cerebellum and hippocampus, the present work demonstrates that the technique is well-suited to address also the highly-structured and interconnected cytoarchitecture of human cerebral cortex, see Fig. 3.2-3.5.
- Beyond *post mortem* autopsies, biopsies of human brain tissue collected during surgery can be scanned for histopathological assessment, see Fig. 3.4.
- Hydrated neuronal tissue can be reconstructed with considerable image quality, see Fig. 3.3. Liquid embedding requires the SR1 setting, and is currently incompatible with vacuum settings such as in SR2.
- The higher photon energy of 17.1 keV possible at SR2 in combination with elevated photon flux of $2 \cdot 10^{11}$ ph/s allows for very convincing scans of neuronal

tissue stained according to the rOTO protocol. Rather than SR1, these properties allow for more reasonable cross sections in the range of 300-400 μm .

- Staining can augment laboratory μCT to the sub- μm range.
- The instrumental stability and unprecedented high flux in KB nanofocus results in less noise and higher resolution for SR2 compared to SR1, see for example the highly resolved neuronal nuclei in Fig. 3.7 (a.iv).
- The high coherence (longitudinal and spatial due to WG filtering) at SR1 enables reconstruction at favorable dose-to-resolution ratios, and is particularly well-suited for unstained tissue, also based on its lower photon energy. Dose estimates are given in Tab. S2.
- A major asset of SR, apart from much smaller scan times and higher throughput, is monochromaticity, and the resulting quantitative contrast based on meeting the assumptions of phase retrieval algorithms [53].
- At the same time, laboratory μCT becomes quite competitive for larger scan volumes and stained specimen, as in Fig. 3.6, since the broad bandpass enables a versatile image contrast, with contributions both from phase and absorption.
- The full potential of SR for PC-CT of neuronal tissue could best be exploited by combining the full-field CT acquisition with further stitching protocols. The goal to increase the volume up to three orders of magnitude seems not unrealistic, if dose-induced sample degradation and local tomography errors could be mitigated, e.g. by advanced local tomography algorithms [52].
- Shifting the measurement window in the other direction, the resolution of SR-CB recordings should be further scaled up, for example by the super-resolution holography approach and pixel detectors [63].

Concerning applications, we note down the following reflections:

- For neuropathology and pre-clinical research, in particular on neurodegenerative diseases, unstained FFPE- or solvent-embedded tissue is suitable, and the laboratory CT can be a valuable tool.
- For research in neuroscience, and in particular for addressing the connectivity problem, PC-CT requires high-magnification and high-resolution SR-CB settings, and has to be further scaled up in performance. The challenge is to achieve higher resolution and contrast to identify synapses while maintaining a field-of-view which offers an advantage with respect to EM.
- For the current datasets at high resolution, synapses should be visible, but the

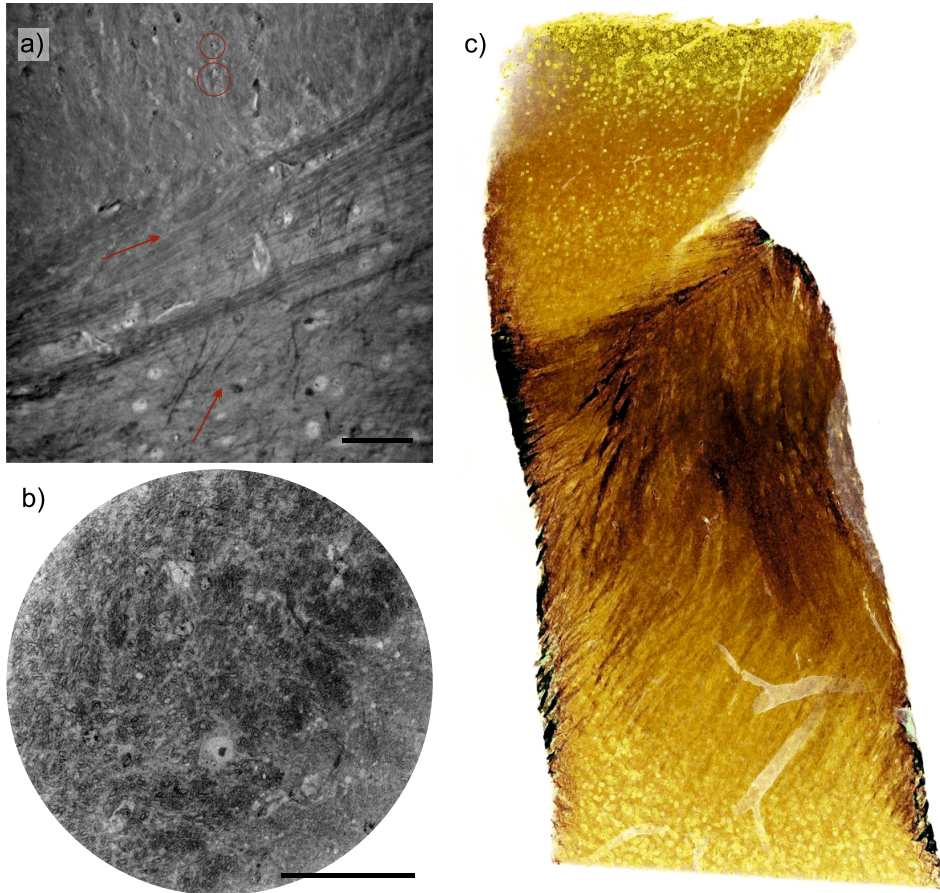


Fig. 3.8: Murine CC, rOTO-stained, recorded with (a) SR1-CB, (b) SR2 and (c) μ CT1. Arrows indicate general fiber orientation in the section, emphasizing the organization of the CC, and circles exemplary highlight single neurons. Scale bars: 50 μ m.

identification would require guidance and validations by correlative imaging, in particular by EM. Datasets of the current work will be made available upon request for independent inspection.

Note that all of the above statements have to be taken with a grain of salt. They also reflect the choices and preferences of the authors in view for future work and directions, based on the presented results. Of course, we expect that other valuable perspectives and ideas will be expressed in the field, and that technical progress in optics, instrumentation, reconstruction algorithms and finally sample preparation will provide further progress in the near future.

Funding

Support by the Deutsche Forschungsgemeinschaft (DFG, German Research Foundation) under Germany's Excellence Strategy - EXC 2067/1-390729940 *Multiscale Bioimaging* and the German Federal Ministry of Education and Research (BMBF) through grant No. 05K19MG2 *NeuroTomo*, are gratefully acknowledged.

Acknowledgments

We thank Michael Sprung, Markus Osterhoff and Bastian Hartmann for support at GINIX, and Peter Luley for support with TINa. We thank Johannes Hagemann for his expertise and for fruitful discussions on holographic phase reconstruction. Further, we thank ESRF for granting beamtime on ID16A (SR2 setup) through experiment LS-2980. We also acknowledge assistance in visualization with NVIDIA IndeX (NVIDIA Corporation, USA).

Disclosures

The authors declare no conflicts of interest.

Data Availability Statement

Data underlying the results presented in this paper are not publicly available at this time but may be obtained from the authors upon request. ESRF data (SR2 setup) will become public in 2024.

Supplemental Document

See the supplemental document for supporting content.

3.4 Supplemental Document

Sample Preparation

Human Hippocampal Tissue Human hippocampal tissue was retrieved by surgery or routine autopsy, in agreement with the ethics committee of the University Medical Center Göttingen. Following established clinical pathology protocols, autopsy dissection blocks were fixed in 10% PFA.

For unstained tissue preparations, samples were subsequently dehydrated and paraffin-embedded (FFPE) (if applicable, for non-liquid embedding of samples). A single FFPE-block measured about $2 \times 3 \times 0.3 \text{ cm}^3$. In all cases, cylindrical samples for PC-CT were extracted using a 1 mm-biopsy punch and inserted into polyimide tubes. For heavy metal staining, tissue blocks were incubated in 1 % OsO_4 (1-2 h at room temperature, RT), and then infiltrated with propylene oxide in PBS in an increasing series. For embedding, tissue samples were placed in Renlam resin in propylene oxide (1:1, 2:1) prior to incubation in pure resin and polymerization (twice overnight).

Murine Brain Tissue Male C57Bl6N mice at the age of 10 days were sacrificed in agreement with the ethics committee of Max-Planck-Institute for Experimental Medicine by cervical dislocation. Tissue was fixed by immersion in solution containing 2.5% glutaraldehyde, 4% formaldehyde and 0.5% NaCl in 0.1 M phosphate buffer (PB). Staining procedure followed either the *conventional-OsO₄* protocol [80], or a modification referred to as *reduced osmium, thiocarbohydrazide, osmium* (rOTO), which further elevates membrane penetration of OsO_4 [31]. The so-called conventional protocol comprised following steps and parameters: Samples were washed in 0.1 M PB (3×10 min at 4°C). After post-fixation and staining in 2% OsO_4 in 0.1 M PB (4 h at 4°C), tissue samples then were washed, dehydrated with increasing concentrations of acetone in water (30%, 50%, 70% and 90%, for 20 mins each at RT), and incubated in 100% acetone (3×15 min). For embedding, tissues were incubated with increasing concentrations of EPON resin mixed with acetone (2:1, 1:1 1:2, for 2 h each at RT) prior to incubation with pure EPON resin (overnight at RT) and polymerization (24 h at 60°C), for which the sample was mounted in a 1 mm-kapton tube.

The rOTO protocol has been conducted as follows: Samples were washed in 0.1 M PB buffer (3×15 mins at 4°C), and then incubated in 2% OsO_4 and 0.25% $\text{K}_4[\text{Fe}(\text{CN})_6]$ (3 h at 4°C) to reduce the OsO_4 to OsO_2 . After washing with ddH_2O , samples were incubated with 0.1% thiocarbohydrazide (in ddH_2O , for 1 h at RT). Samples were

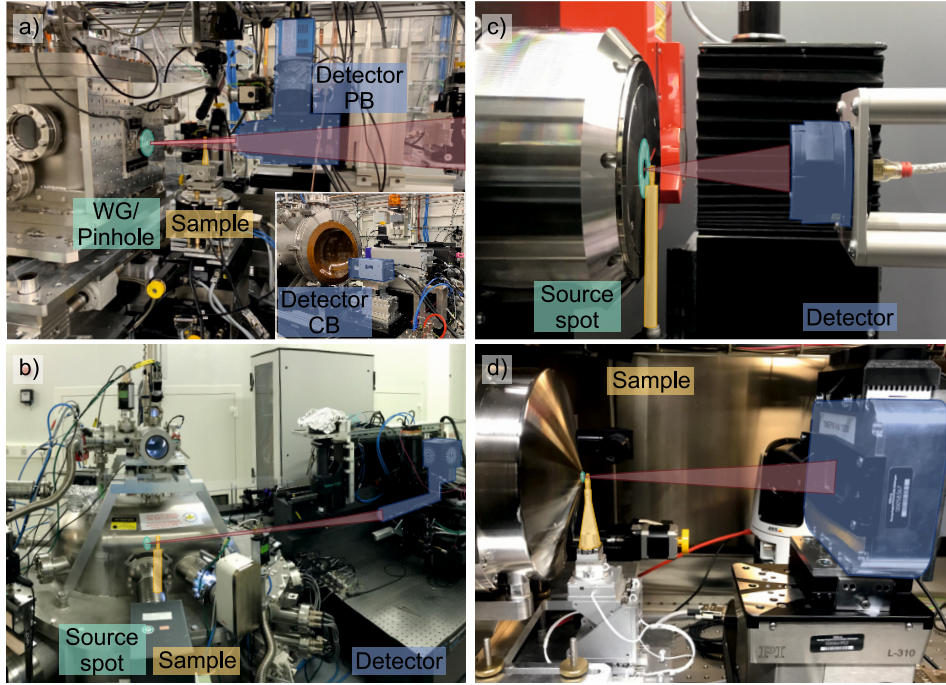


Fig. 3.9: Annotated photographs of the experimental setups. (Green) marks the X-ray focal plane, (orange) the sample stage, (blue) the detectors. (a) GINIX endstation at P10 beamline, DESY, Hamburg (SR1). In PB-configuration, the PCO.Edge-detector is used ("Detector PB"). The inset shows the detector stage approx. 5 m down stream ("Detector CB" sCMOS-cameras, Photonic Science & Andor). (b) ID16A beamline, ESRF, Grenoble (SR2). (c) EasyTom Nano setup (RX Solutions), with the CCD-camera in use (μ CT1). (d) Home-built nanoPC-CT setup TiNa, with Excillum NanoTube N2 X-ray source and a single photon counting detector (Timepix) (μ CT2).

subsequently treated with 2% OsO_4 (90 min), and after washing with ddH_2O , further contrasted with 2.5% uranyl acetate (overnight at 4°C), followed by several washes with ddH_2O . Samples were then dehydrated and resin-embedded, as for the rOTO-preparation.

The sample preparation techniques are illustrated in Fig. 1(d).

Experimental Setups - Synchrotron Beamlines

The synchrotron-based data presented in this work were collected at two beamlines dedicated to propagation-based holo-tomography: (SR1) the GINIX endstation of the

P10 beamline, Petra III, DESY, Hamburg [54], and (SR2) the nano-imaging beamline ID16A, ESRF, Grenoble [14, 59], cf. Fig. 3.9(a & b).

- **SR1:** GINIX is equipped with two different setups for PC-CT. Overview scans covering FOVs of about 1.5 mm are scanned in *parallel-beam configuration* (PB) [24], depicted in Fig. 1(e). In a continuous rotation, 3000 projections and 200 flat images are recorded with the PCO.edge detector (50 μm Lu:Ag scintillator, $px = 0.65 \mu\text{m}$ 10 \times objective, $M = 1$) in a full 360 $^\circ$ rotation. With 35 ms exposure time, a total scan takes about 70 s. Opposing projections are used for projection correction in order to mitigate ring-artifacts, and 1500 processed projections serve tomographic reconstruction to fulfill the sampling criteria. In the data shown here, $z_{12} \approx 40$ mm and the further settings detailed in Tab. 3.1 were used. Fig. 1(f) depicts the *cone-beam geometry* (CB), serving high-resolution data acquisition using a compound optics of KB-mirrors and X-ray waveguides (WG). Data were recorded with a fiber-plate CCD-camera with a 15 μm thick Gadox-scintillator at $z_{02} \approx 5$ m. By changing the distance z_{01} between WG and sample, the geometric magnification M is adjusted: with $M \approx 40 \dots 138$, different voxel sizes between $px \approx 200$ nm and $px \approx 50$ nm were chosen in this work. Scan-specific details are given in Tab. 3.2.

	Human, unstained FFPE	Mouse OsO ₄ conv.	Mouse rOTO	Human WM OsO ₄
Figure	2	7(a.i)	7(b.i)	5(b.iv-v)
E (keV)	13.8	10.8	21.0	10.8
τ (s)	0.035	0.035	0.035	0.035
z_{12} (mm)	41	40	17.5	17.5
px (μm)	0.65	0.65	0.65	0.65
FOV (mm^2) (h \times v)	1.7×1.3	1.7×1.3	1.7×1.3	1.7×1.3
d ($\cdot 10^{-3}$ m)	3.0	0.2	3.6	0.2
D ($\cdot 10^4$ Gy)	1.1	2.4	0.2	2.4
F	0.1148	0.0920	0.4089	0.0898
Phase retrieval	NLT	NLT	NLT	NLT
lim1	$8 \cdot 10^{-4}$	$8 \cdot 10^{-4}$	$8 \cdot 10^{-4}$	$8 \cdot 10^{-4}$
lim2	0.05	0.05	0.05	0.05
δ/β	30	15	15	10

Table 3.1: Scan and reconstruction parameters of GINIX-data recorded in SR1-PB configuration. E denotes the X-ray energy, τ the exposure time, z_{12} the sample-to-detector distance, px the pixel size, FOV the field-of-view in the sample plane, d the attenuation length, D the estimated radiation dose, and F the Fresnel number. lim1/2 are the regularization parameters, and δ/β the ratio of dispersion to absorption decrement of the refractive index.

Ex. Figure	Human, unstained FFPE	Human, unstained Dehyd. Series	Mouse OsO ₄ conv.	Mouse rOTO	Human OsO ₄	Human OsO ₄
# projections	1442	1501	1501	1001	1501	1501
# defocus dist.	1	2 (70% Eth.: 3)	4	4	3	2 1/2
E (keV)	8.0	8.0	13.8	13.8	10.8	10.0
τ (s)	2	1	0.7	1	2	0.4
z_{01} (mm)	150	130	125	125	125	40
z_{02} (mm)	5113	5073	5113	5113	5113	5113
px (nm)	200	161	159	159	159	49.2
FOV (mm ²) (h×v)	0.51×0.43	0.33×0.33	0.33×0.33	0.33×0.33	0.41×0.34	0.13×0.11
d (·10 ⁻³ m)	0.59	0.45	4.20	1.30	0.19	0.16
D (·10 ⁴ Gy)	1.1	1.6	9.4	2.8	34.7	71.3
Phase retrieval	NLT	NLT	NLT	NLT	NLT	NLT
lim1	$8 \cdot 10^{-4}$	$8 \cdot 10^{-3}$	$2 \cdot 10^{-2}$	$2 \cdot 10^{-2}$	$1.8 \cdot 10^{-3}$	$5.3 \cdot 10^{-4}$
lim2	0.4	0	0.8	0.8	$5 \cdot 10^{-2}$	$5 \cdot 10^{-2}$
δ/β	90	35	30	30	0.05	0.01
					15	25

Ex. Figure	Mouse OsO ₄ conv.	Mouse rOTO	Mouse rOTO
# projections	2000	2000	2000
# defocus dist.	4	4	4
E (keV)	17.1	17.1	17.1
τ (s)	0.2	0.2	0.2
z_{01} (mm)	48.6	48.6	16.4
z_{02} (mm)	1208	1208	1208
px (nm)	130	130	50
FOV (mm ²) (h×v)	0.26×0.26	0.26×0.26	0.10×0.10
d (·10 ⁻³ m)	0.75	2.4	2.4
D (·10 ⁶ Gy)	7.4	2.4	15.9
Phase retrieval	CG	CG	CG
lim1	0	0	0
lim2	0.01	0.01	0.01
δ/β	15	15	15

Table 3.2: Experimental and reconstruction settings and parameters for (top) SR1-CB and (bottom) SR2 data, recorded in CB-configuration. E denotes the X-ray energy, τ the exposure time, z_{01} the source-to-sample and z_{02} the sample-to-detector distance, px the pixel size, FOV the field-of-view in the sample plane, d the attenuation length, D the estimated radiation dose, and F the Fresnel number. lim1/2 are the regularization parameters, and δ/β the ratio of dispersion to absorption decrement of the refractive index.

- **SR2:** ID16A beamline is specialized in nano-holotomography, with voxel sizes down to 10 nm. X-rays are provided either at 17.1 or 33.6 keV photon energy, and focused by KB-mirrors. Here we used 17.1 keV and a propagation distance $z_{12} = 1.2$ m in cone-beam geometry (cf. Fig. 1(f)). Magnified projections were recorded by a lens-coupled FReLoN CCD-camera (23 μm GGG:Eu scintillator). The acquisitions can take advantage of a particularly high flux (approx. $2 \cdot 10^{11}$ ph/s) and a cryo environment under vacuum. The present study was conducted at room temperature under vacuum. Further details are listed in Tab. 3.2, and the experiment is referenced as [19].

Dose Estimation The accumulated dose D in the sample-FOV was estimated as

$$D = \frac{I_0 \tau E}{d \rho_m \text{FOV}},$$

with the usual approximations as discussed in [30, 57], based on photon flux I_0 , which was approximated as $I_0 \approx 5 \cdot 10^{11}$ ph/s for SR1-PB, $I_0 \approx 10^9$ ph/s for SR1-CB and $I_0 \approx 2 \cdot 10^{11}$ ph/s for SR2, exposure time τ , X-ray energy E , attenuation length d , mass density ρ_m . For paraffin-embedded samples $\rho_m = 2.2 \text{ g/cm}^3$ was used, and d as computed by [28] for a representative protein and tissue composite with stoichiometry $C_{50}C_{30}N_9O_{10}S_1$ [30]. For stained samples, ρ_m was kept constant, since the dose-damage relationship refers to the energy uptake per tissue mass, rather than label mass. To this end, however, we neglect the additional dose uptake by photoelectrons of larger range, emitted from heavy atom labels into their environment. Instead, the attenuation length d was calculated from the measured X-ray transmission T in the respective projections, based on d_{FFPE} for unstained FFPE-preparations, i.e.

$$d_{\text{stain}} = \frac{\log(T_{\text{FFPE}})}{\log(T_{\text{stain}})} \cdot d_{\text{FFPE}}.$$

Experimental Setups - Laboratory Implementations

Laboratory PC-CT (μCT) was conducted with two setups configured for sub- μm imaging: (μCT1) the commercial EasyTom Nano (RX Solutions) [64], and (μCT2) the home-built TiNa-setup [20], cf. Fig. 3.9(c & d).

- **μCT1 :** With EasyTom Nano, X-rays were generated by a Hamamatsu transmission-target source (W), and projections were recorded by a CCD-camera (Gadox-scintillator, 9 μm pixels, 2×2 -binning) with magnification in the range $M \approx 18...52$. Best feature contrast was found at 60 kV acceleration voltage. This setup

was used in overview alignment, with $px=0.99 \mu\text{m}$ and middle focal spot mode, or for higher magnification, with $px=0.35 \mu\text{m}$ and small focal spot mode. Further experimental details are given in Tab. 3.3.

- **μCT2 :** With the TINA-setup, the Excillum NanoTube N2 and a Timepix detector (500 μm Si, 55 μm pixels) were used. Also here, the acceleration voltage was set to 60 kV. The source-to-sample distance was particularly small ($z_{01} = 1.4 \text{ mm}$), resulting in $M \approx 157$ (as required by the larger detector pixel size). Further details are given in Tab. 3.3.

	μCT1 , Overview	μCT1 , ROI	μCT2 , ROI
# projections	1568	3008	1201
z_{01} (mm)	5	5	1.4
z_{02} (mm)	98	278	218
px (μm)	0.99	0.35	0.35
FOV (mm^2) ($h \times v$)	$2.0 \times 0.14^*$	0.7×0.47	0.27×0.18
τ (s)	12×1.7	5×10	14×9
Source spot mode	middle	small	0.3 μm
Total scan time (h)	9	46	46

Table 3.3: Experimental and reconstruction parameters for μCT scans. z_{01} denotes the source-to-sample and z_{02} the sample-to-detector distance, px the pixel size, FOV the field-of-view in the sample plane, and τ the exposure time. No pre-filtering of the beams was used. * denotes the FOV of a single tomographic scan; multiple scans have been acquired and combined in this work.

Holographic & Tomographic Reconstruction

Projections were first corrected for empty beam and dark images. For synchrotron-based datasets, phase retrieval was carried out using either the linearized *contrast-transfer-function* (CTF) algorithm [12] or a non-linear implementation thereof, both assuming homogeneous object composition. At (SR1), this is implemented via the *non-linear Tikhonov* (NLT) scheme [41], while at (SR2), a conjugate gradient approach is used [82]. These phase retrieval approaches are well-suited for reconstruction of holographic images at small Fresnel numbers $F = \frac{px^2}{z_{\text{eff}}\lambda} \ll 1$, with wavelength λ , and the effective propagation distance $z_{\text{eff}} = z_{12}/M$. Note that these algorithms provide optimal image quality when applied to data sets recorded at four slightly different Fresnel numbers, i.e. at four different defocus distances as indicated in Fig. 1(f) [83]. Phase reconstruction of laboratory data was performed (μCT1) with a simple phase filter (provided by RX-Solutions software), or (μCT2) using the Bronnikov-aided

correction (BAC) [16], as also implemented in [41]. Reconstruction parameters are listed in Tab. 3.1, 3.2 and 3.3.

Phase-retrieved projections were used for tomographic reconstruction, performed either by filtered back-projection (FBP, PB-configuration), or a cone-beam (FDK, CB-configuration) algorithm. Note that the GINIX-dataset recorded at $px = 49.2$ nm (cf. Tab 3.2) was reconstructed with the simultaneous iterations reconstruction technique (SIRT, 400 iterations). All three tomographic reconstruction schemes are implemented in the ASTRA-toolbox [76].

Bibliography

- [1] M. Banich. *Interhemispheric interaction: Mechanisms of unified processing*. fl kitterle (ed.). *Hemispheric communication: Mechanisms and models*. Hillsdale, NJ: Erlbaum, 1995, pp. 271–300.
- [2] G. E. Barbone, A. Bravin, A. Mittone, S. Grosu, J. Ricke, G. Cavaletti, V. Djonov, and P. Coan. “High-Spatial-Resolution Three-dimensional Imaging of Human Spinal Cord and Column Anatomy with Postmortem X-ray Phase-Contrast Micro-CT.” In: *Radiology* 298.1 (2021), pp. 135–146.
- [3] G. E. Barbone, A. Bravin, A. Mittone, M. J. Kraiger, M. H. de Angelis, M. Bossi, E. Ballarini, V. Rodriguez-Menendez, C. Ceresa, G. Cavaletti, et al. “Establishing sample-preparation protocols for X-ray phase-contrast CT of rodent spinal cords: Aldehyde fixations and osmium impregnation.” In: *Journal of Neuroscience Methods* 339 (2020), p. 108744.
- [4] M. Bartels, M. Krenkel, P. Cloetens, W. Möbius, and T. Salditt. “Myelinated mouse nerves studied by X-ray phase contrast zoom tomography.” In: *Journal of Structural Biology* 192.3 (2015), pp. 561–568.
- [5] C. Bikis, G. Rodgers, H. Deyhle, P. Thalmann, A. Hipp, F. Beckmann, T. Weitkamp, S. Theocharis, C. Rau, G. Schulz, et al. “Sensitivity comparison of absorption and grating-based phase tomography of paraffin-embedded human brain tissue.” In: *Applied Physics Letters* 114.8 (2019), p. 083702.
- [6] C. Bosch, T. Ackels, A. Pacureanu, Y. Zhang, C. J. Peddie, M. Berning, N. Rzepka, M.-C. Zdora, I. Whiteley, M. Storm, et al. “Functional and multiscale 3D structural investigation of brain tissue through correlative in vivo physiology, synchrotron micro-tomography and volume electron microscopy.” In: *bioRxiv* (2021).
- [7] M. Brown, R. Reed, and R. Henry. “Effects of dehydration mediums and temperature on total dehydration time and tissue shrinkage.” In: *Journal of the International Society for Plastination* 17 (2002), pp. 28–33.

- [8] W. Brück and C. Stadelmann. "Inflammation and degeneration in multiple sclerosis." In: *Neurological Sciences* 24.5 (2003), s265–s267.
- [9] M. Busse, M. Müller, M. A. Kimm, S. Ferstl, S. Allner, K. Achterhold, J. Herzen, and F. Pfeiffer. "Three-dimensional virtual histology enabled through cytoplasm-specific X-ray stain for microscopic and nanoscopic computed tomography." In: *Proceedings of the National Academy of Sciences* 115.10 (2018), pp. 2293–2298.
- [10] J. Buytaert, J. Goyens, D. De Greef, P. Aerts, and J. Dirckx. "Volume shrinkage of bone, brain and muscle tissue in sample preparation for micro-CT and light sheet fluorescence microscopy (LSFM)." In: *Microscopy and Microanalysis* 20.4 (2014), pp. 1208–1217.
- [11] A. Cedola, A. Bravin, I. Bukreeva, M. Fratini, A. Pacureanu, A. Mittone, L. Massimi, P. Cloetens, P. Coan, G. Campi, et al. "X-ray phase contrast tomography reveals early vascular alterations and neuronal loss in a multiple sclerosis model." In: *Scientific reports* 7.1 (2017), pp. 1–11.
- [12] P. Cloetens, W. Ludwig, J. Baruchel, D. Van Dyck, J. Van Landuyt, J. Guigay, and M. Schlenker. "Holotomography: Quantitative phase tomography with micrometer resolution using hard synchrotron radiation x rays." In: *Applied Physics Letters* 75.19 (1999), pp. 2912–2914.
- [13] L. C. Croton, K. S. Morgan, D. M. Paganin, L. T. Kerr, M. J. Wallace, K. J. Crossley, S. L. Miller, N. Yagi, K. Uesugi, S. B. Hooper, et al. "In situ phase contrast X-ray brain CT." In: *Scientific Reports* 8.1 (2018), pp. 1–12.
- [14] J. C. Da Silva, A. Pacureanu, Y. Yang, S. Bohic, C. Morawe, R. Barrett, and P. Cloetens. "Efficient concentration of high-energy x-rays for diffraction-limited imaging resolution." In: *Optica* 4.5 (2017), pp. 492–495.
- [15] L. B. Dahlin, K. R. Rix, V. A. Dahl, A. B. Dahl, J. N. Jensen, P. Cloetens, A. Pacureanu, S. Mohseni, N. O. Thomsen, and M. Bech. "Three-dimensional architecture of human diabetic peripheral nerves revealed by X-ray phase contrast holographic nanotomography." In: *Scientific reports* 10.1 (2020), pp. 1–8.
- [16] Y. De Witte, M. Boone, J. Vlassenbroeck, M. Dierick, and L. Van Hoorebeke. "Bronnikov-aided correction for x-ray computed tomography." In: *JOSA A* 26.4 (2009), pp. 890–894.

- [17] W. Denk and H. Horstmann. “Serial block-face scanning electron microscopy to reconstruct three-dimensional tissue nanostructure.” In: *PLoS Biol* 2.11 (2004), e329.
- [18] T. Donath, F. Pfeiffer, O. Bunk, C. Grünzweig, E. Hempel, S. Popescu, P. Vock, and C. David. “Toward clinical X-ray phase-contrast CT: demonstration of enhanced soft-tissue contrast in human specimen.” In: *Investigative Radiology* 45.7 (2010), pp. 445–452.
- [19] M. Eckermann, P. Cloetens, J. Reichmann, M. Osterhoff, T. Salditt, and M. Osterhoff. *3d structure of the human dentate gyrus by holo-tomography: Alzheimer disease vs Control*.
- [20] M. Eckermann, M. Töpperwien, A.-L. Robisch, F. van der Meer, C. Stadelmann, and T. Salditt. “Phase-contrast X-Ray Tomography of Neuronal Tissue at Laboratory Sources With Submicron Resolution.” In: *Journal of medical imaging (Bellingham, Wash.)* 7.1 (2020), p. 013502.
- [21] M. Eckermann, M. Töpperwien, T. Ruhwedel, W. Möbius, and T. Salditt. “Evaluation of different heavy-metal stains and embedding media for phase contrast tomography of neuronal tissue.” In: *Developments in X-Ray Tomography XII*. Vol. 11113. International Society for Optics and Photonics. 2019, 111130N.
- [22] E. Eggli, S. Schleede, M. Bech, K. Achterhold, R. Loewen, R. D. Ruth, and F. Pfeiffer. “X-ray phase-contrast tomography with a compact laser-driven synchrotron source.” In: *Proceedings of the National Academy of Sciences* 112.18 (2015), pp. 5567–5572.
- [23] M. Filippi, W. Brück, D. Chard, F. Fazekas, J. J. Geurts, C. Enzinger, S. Hametner, T. Kuhlmann, P. Preziosa, À. Rovira, et al. “Association between pathological and MRI findings in multiple sclerosis.” In: *The Lancet Neurology* 18.2 (2019), pp. 198–210.
- [24] J. Frohn, D. Pinkert-Leetsch, J. Missbach-Güntner, M. Reichardt, M. Osterhoff, F. Alves, and T. Salditt. “3D virtual histology of human pancreatic tissue by multiscale phase-contrast X-ray tomography.” In: *Journal of Synchrotron Radiation* 27.6 (2020), pp. 1707–1719.
- [25] R. Gradl, M. Dierolf, B. Günther, L. Hehn, W. Möller, D. Kutschke, L. Yang, M. Donnelley, R. Murrie, A. Erl, et al. “In vivo dynamic phase-contrast X-ray imaging using a compact light source.” In: *Scientific Reports* 8.1 (2018), pp. 1–8.

- [26] M. Helmstaedter. “Cellular-resolution connectomics: challenges of dense neural circuit reconstruction.” In: *Nature Methods* 10.6 (2013), pp. 501–507.
- [27] M. Helmstaedter, K. L. Briggman, S. C. Turaga, V. Jain, H. S. Seung, and W. Denk. “Connectomic reconstruction of the inner plexiform layer in the mouse retina.” In: *Nature* 500.7461 (2013), pp. 168–174.
- [28] B. Henke, E. Gullikson, and J. Davis. *X-ray interactions: photoabsorption, scattering, transmission, and reflection at E=50-30000 eV, Z=1-92, Atomic Data and Nuclear Data Tables*. Database 2. Center for X-Ray Optics, Lawrence Berkeley National Laboratory, 1993.
- [29] M. Hoshino, K. Uesugi, T. Tsukube, and N. Yagi. “Quantitative and dynamic measurements of biological fresh samples with X-ray phase contrast tomography.” In: *Journal of Synchrotron Radiation* 21.6 (2014), pp. 1347–1357.
- [30] M. R. Howells, T. Beetz, H. N. Chapman, C. Cui, J. Holton, C. Jacobsen, J. Kirz, E. Lima, S. Marchesini, H. Miao, et al. “An assessment of the resolution limitation due to radiation-damage in x-ray diffraction microscopy.” In: *Journal of Electron Spectroscopy and Related Phenomena* 170.1-3 (2009), pp. 4–12.
- [31] Y. Hua, P. Laserstein, and M. Helmstaedter. “Large-volume en-bloc staining for electron microscopy-based connectomics.” In: *Nature Communications* 6.1 (2015), p. 7923.
- [32] T. H. Jensen, M. Bech, O. Bunk, A. Menzel, A. Bouchet, G. Le Duc, R. Feidenhans, and F. Pfeiffer. “Molecular X-ray computed tomography of myelin in a rat brain.” In: *NeuroImage* 57.1 (2011), pp. 124–129.
- [33] K. Joppe, J.-D. Nicolas, T. A. Grünwald, M. Eckermann, T. Salditt, and P. Lingor. “Elemental quantification and analysis of structural abnormalities in neurons from Parkinson’s-diseased brains by X-ray fluorescence microscopy and diffraction.” In: *Biomedical Optics Express* 11.7 (2020), pp. 3423–3443.
- [34] E. Jurrus, M. Hardy, T. Tasdizen, P. T. Fletcher, P. Koshevoy, C.-B. Chien, W. Denk, and R. Whitaker. “Axon tracking in serial block-face scanning electron microscopy.” In: *Medical image analysis* 13.1 (2009), pp. 180–188.
- [35] A. Khimchenko, C. Bikis, A. Pacureanu, S. E. Hieber, P. Thalmann, H. Deyhle, G. Schweighauser, J. Hench, S. Frank, M. Müller-Gerbl, et al. “Hard X-Ray Nanoholotomography: Large-Scale, Label-Free, 3D Neuroimaging beyond Optical Limit.” In: *Advanced Science* 5 (2018), p. 1700694.

- [36] J. Kim, T. Zhao, R. S. Petralia, Y. Yu, H. Peng, E. Myers, and J. C. Magee. “mGRASP enables mapping mammalian synaptic connectivity with light microscopy.” In: *Nature methods* 9.1 (2012), pp. 96–102.
- [37] S.-Y. Kim, K. Chung, and K. Deisseroth. “Light microscopy mapping of connections in the intact brain.” In: *Trends in cognitive sciences* 17.12 (2013), pp. 596–599.
- [38] H. D. King. “The effects of formaldehyde on the brain.” In: *Journal of Comparative Neurology* 23 (1913), p. 283.
- [39] A. T. Kuan, J. S. Phelps, L. A. Thomas, T. M. Nguyen, J. Han, C.-L. Chen, A. W. Azevedo, J. C. Tuthill, J. Funke, P. Cloetens, et al. “Dense neuronal reconstruction through X-ray holographic nano-tomography.” In: *Nature Neuroscience* 23.12 (2020), pp. 1637–1643.
- [40] A. Kutzelnigg, C. F. Lucchinetti, C. Stadelmann, W. Brück, H. Rauschka, M. Bergmann, M. Schmidbauer, J. E. Parisi, and H. Lassmann. “Cortical demyelination and diffuse white matter injury in multiple sclerosis.” In: *Brain* 128.11 (2005), pp. 2705–2712.
- [41] L. M. Lohse, A.-L. Robisch, M. Töpperwien, S. Maretzke, M. Krenkel, J. Hagemann, and T. Salditt. “A phase-retrieval toolbox for X-ray holography and tomography.” In: *Journal of Synchrotron Radiation* 27.3 (2020).
- [42] R. H. Masland. “Neuronal cell types.” In: *Current Biology* 14.13 (2004), R497–R500.
- [43] L. Massimi, I. Bukreeva, G. Santamaria, M. Fratini, A. Corbelli, F. Brun, S. Fumagalli, L. Maugeri, A. Pacureanu, P. Cloetens, et al. “Exploring Alzheimer’s disease mouse brain through X-ray phase contrast tomography: From the cell to the organ.” In: *NeuroImage* 184 (2019), pp. 490–495.
- [44] S. Mikula and W. Denk. “High-resolution whole-brain staining for electron microscopic circuit reconstruction.” In: *Nature Methods* 12.6 (2015), p. 541.
- [45] S. Mikula, J. Binding, and W. Denk. “Staining and embedding the whole mouse brain for electron microscopy.” In: *Nature Methods* 9.12 (2012), pp. 1198–1201.
- [46] M. Müller, M. A. Kimm, S. Ferstl, S. Allner, K. Achterhold, J. Herzen, F. Pfeiffer, and M. Busse. “Nucleus-specific X-ray stain for 3D virtual histology.” In: *Scientific Reports* 8.1 (2018), pp. 1–10.

- [47] L. J. Nicolai, A. Ramaekers, T. Raemaekers, A. Drozdzecki, A. S. Mauss, J. Yan, M. Landgraf, W. Annaert, and B. A. Hassan. “Genetically encoded dendritic marker sheds light on neuronal connectivity in *Drosophila*.” In: *Proceedings of the National Academy of Sciences* 107.47 (2010), pp. 20553–20558.
- [48] P. Parlanti, V. Cappello, F. Brun, G. Tromba, R. Rigolio, I. Tonazzini, M. Cecchini, V. Piazza, and M. Gemmi. “Size and specimen-dependent strategy for x-ray micro-ct and tem correlative analysis of nervous system samples.” In: *Scientific Reports* 7.1 (2017), pp. 1–12.
- [49] P. Patrikios, C. Stadelmann, A. Kutzelnigg, H. Rauschka, M. Schmidbauer, H. Laursen, P. S. Sorensen, W. Brück, C. Lucchinetti, and H. Lassmann. “Remyelination is extensive in a subset of multiple sclerosis patients.” In: *Brain* 129.12 (2006), pp. 3165–3172.
- [50] J. S. Phelps, D. G. C. Hildebrand, B. J. Graham, A. T. Kuan, L. A. Thomas, T. M. Nguyen, J. Buhmann, A. W. Azevedo, A. Sustar, S. Agrawal, et al. “Reconstruction of motor control circuits in adult *Drosophila* using automated transmission electron microscopy.” In: *Cell* 184.3 (2021), pp. 759–774.
- [51] D. G. Robinson, U. Ehlers, R. Herken, B. Herrmann, F. Mayer, and F.-W. Schürmann. *Methods of Preparation for Electron Microscopy*. Springer Berlin Heidelberg, 1987.
- [52] A. Robisch, J. Frohn, and T. Salditt. “Iterative micro-tomography of biopsy samples from truncated projections with quantitative gray values.” In: *Physics in Medicine & Biology* 65.23 (2020), p. 235034.
- [53] A.-L. Robisch, M. Eckermann, M. Töpperwien, F. van der Meer, C. Stadelmann-Nessler, and T. Salditt. “Nanoscale x-ray holotomography of human brain tissue with phase retrieval based on multienergy recordings.” In: *Journal of Medical Imaging* 7.1 (2020), p. 013501.
- [54] T. Salditt, M. Osterhoff, M. Krenkel, R. N. Wilke, M. Priebe, M. Bartels, S. Kalbfleisch, and M. Sprung. “Compound focusing mirror and X-ray waveguide optics for coherent imaging and nano-diffraction.” In: *Journal of Synchrotron Radiation* 22.4 (2015), pp. 867–878.
- [55] G. Schulz, A. Morel, M. S. Imholz, H. Deyhle, T. Weitkamp, I. Zanette, F. Pfeiffer, C. David, M. Müller-Gerbl, and B. Müller. “Evaluating the microstructure of human brain tissues using synchrotron radiation-based micro-computed to-

- mography.” In: *Developments in X-ray Tomography VII*. Vol. 7804. International Society for Optics and Photonics. 2010, 78040F.
- [56] F. Y. Shen, M. M. Harrington, L. A. Walker, H. P. J. Cheng, E. S. Boyden, and D. Cai. “Light microscopy based approach for mapping connectivity with molecular specificity.” In: *Nature communications* 11.1 (2020), pp. 1–12.
- [57] Q. Shen, I. Bazarov, and P. Thibault. “Diffractive imaging of nonperiodic materials with future coherent X-ray sources.” In: *Journal of Synchrotron Radiation* 11.5 (2004), pp. 432–438.
- [58] A. Siegel and H. N. Saprú. *Essential neuroscience*. 2nd ed. Lippincott Williams & Wilkins, 2006.
- [59] J. C. da Silva, A. Pacureanu, Y. Yang, F. Fus, M. Hubert, L. Bloch, M. Salome, S. Bohic, and P. Cloetens. “High-energy cryo x-ray nano-imaging at the ID16A beamline of ESRF.” In: *X-Ray Nanoimaging: Instruments and Methods III*. Vol. 10389. International Society for Optics and Photonics. 2017, 103890F.
- [60] J. Silver and J. H. Miller. “Regeneration beyond the glial scar.” In: *Nature Reviews Neuroscience* 5.2 (2004), pp. 146–156.
- [61] D. Smith and T. Starborg. “Serial block face scanning electron microscopy in cell biology: Applications and technology.” In: *Tissue and Cell* 57 (2019), pp. 111–122.
- [62] M. V. Sofroniew and H. V. Vinters. “Astrocytes: biology and pathology.” In: *Acta Neuropathologica* 119.1 (2010), pp. 7–35.
- [63] J. Soltau, M. Vassholz, M. Osterhoff, and T. Salditt. “Inline holography with hard x-rays at sub-15 nm resolution.” In: *Optica* 8 (2021), pp. 818–823.
- [64] R. Solutions. *EasyTom Nano*. 2021.
- [65] G. E. Sosinsky, J. Crum, Y. Z. Jones, J. Lanman, B. Smarr, M. Terada, M. E. Martone, T. J. Deerinck, J. E. Johnson, and M. H. Ellisman. “The combination of chemical fixation procedures with high pressure freezing and freeze substitution preserves highly labile tissue ultrastructure for electron tomography applications.” In: *Journal of Structural Biology* 161.3 (2008), pp. 359–371.
- [66] O. Sporns and J. D. Zwi. “The small world of the cerebral cortex.” In: *Neuroinformatics* 2.2 (2004), pp. 145–162.
- [67] C. Stadelmann, M. Albert, C. Wegner, and W. Brück. “Cortical pathology in multiple sclerosis.” In: *Current Opinion in Neurology* 21.3 (2008), pp. 229–234.

- [68] M. Stampanoni, R. Mokso, F. Marone, J. Vila-Comamala, S. Gorelick, P. Trtik, K. Jefimovs, and C. David. "Phase-contrast tomography at the nanoscale using hard x rays." In: *Physical Review B* 81.14 (2010), p. 140105.
- [69] M. Töpperwien, M. Krenkel, T. Ruhwedel, W. Möbius, A. Pacureanu, P. Cloetens, and T. Salditt. "Phase-contrast tomography of sciatic nerves: image quality and experimental parameters." In: *Journal of Physics: Conference Series*. Vol. 849(1). IOP Publishing. 2017, p. 012001.
- [70] M. Töpperwien, M. Krenkel, T. Ruhwedel, W. Möbius, A. Pacureanu, P. Cloetens, and T. Salditt. "Phase-contrast tomography of sciatic nerves: image quality and experimental parameters." In: *J. Phys: Conf. Ser.* 849.1 (2017), p. 012001.
- [71] M. Töpperwien, M. Krenkel, F. Quade, and T. Salditt. "Laboratory-based x-ray phase-contrast tomography enables 3D virtual histology." In: *Proc. SPIE* 9964 (2016), p. 99640I.
- [72] M. Töpperwien, M. Krenkel, D. Vincenz, F. Stöber, A. M. Oelschlegel, J. Goldschmidt, and T. Salditt. "Three-dimensional mouse brain cytoarchitecture revealed by laboratory-based x-ray phase-contrast tomography." In: *Scientific Reports* 7.1 (2017), pp. 1–8.
- [73] M. Töpperwien, A. Markus, F. Alves, and T. Salditt. "Contrast enhancement for visualizing neuronal cytoarchitecture by propagation-based x-ray phase-contrast tomography." In: *NeuroImage* 199 (2019), pp. 70–80.
- [74] M. Töpperwien, F. van der Meer, C. Stadelmann, and T. Salditt. "Correlative x-ray phase-contrast tomography and histology of human brain tissue affected by Alzheimer's disease." In: *NeuroImage* 210 (2020), p. 116523.
- [75] M. Töpperwien, F. van der Meer, C. Stadelmann, and T. Salditt. "Three-dimensional virtual histology of human cerebellum by X-ray phase-contrast tomography." In: *Proceedings of the National Academy of Sciences* 115.27 (2018), pp. 6940–6945.
- [76] W. Van Aarle, W. J. Palenstijn, J. Cant, E. Janssens, F. Bleichrodt, A. Dabrovolski, J. De Beenhouwer, K. J. Batenburg, and J. Sijbers. "Fast and flexible X-ray tomography using the ASTRA toolbox." In: *Optics Express* 24.22 (2016), pp. 25129–25147.
- [77] M. Viermetz, L. Birnbacher, M. Willner, K. Achterhold, F. Pfeiffer, and J. Herzen. "High resolution laboratory grating-based X-ray phase-contrast CT." In: *Scientific Reports* 8.1 (2018), pp. 1–8.

- [78] C. Walsh, P. Tafforeau, W. L. Wagner, D. J. Jafree, A. Bellier, C. Werlein, M. P. Kühnel, E. Boller, S. Walker-Samuel, J. L. Robertus, et al. “Multiscale three-dimensional imaging of intact human organs down to the cellular scale using hierarchical phase-contrast tomography.” In: *bioRxiv* (2021).
- [79] M.-T. Weil, S. Heibeck, M. Töpperwien, S. tom Dieck, T. Ruhwedel, T. Salditt, M. C. Rodicio, J. R. Morgan, K.-A. Nave, W. Möbius, et al. “Axonal ensheathment in the nervous system of lamprey: implications for the evolution of myelinating glia.” In: *Journal of Neuroscience* 38.29 (2018), pp. 6586–6596.
- [80] M.-T. Weil, T. Ruhwedel, M. Meschkat, B. Sadowski, and W. Möbius. “Transmission electron microscopy of oligodendrocytes and myelin.” In: *Oligodendrocytes*. Springer, 2019, pp. 343–375.
- [81] M. C. Willingham and A. V. Rutherford. “The use of osmium-thiocarbohydrazide-osmium (OTO) and ferrocyanide-reduced osmium methods to enhance membrane contrast and preservation in cultured cells.” In: *Journal of Histochemistry and Cytochemistry* 32.4 (1984), pp. 455–460.
- [82] B. Yu, L. Weber, A. Pacureanu, M. Langer, C. Olivier, P. Cloetens, and F. Peyrin. “Evaluation of phase retrieval approaches in magnified X-ray phase nano computerized tomography applied to bone tissue.” In: *Optics Express* 26.9 (2018), pp. 11110–11124.
- [83] S. Zabler, P. Cloetens, J.-P. Guigay, J. Baruchel, and M. Schlenker. “Optimization of phase contrast imaging using hard x rays.” In: *Review of Scientific Instruments* 76.7 (2005), p. 073705.

Three-dimensional Virtual Histology of the Human Hippocampus based on Phase-Contrast Computed-Tomography

4

Marina Eckermann, Bernhard Schmitzer, Franziska van der Meer, Jonas Franz, Ove Hansen, Christine Stadelmann and Tim Salditt

Reproduced from Proceedings of the National Academy of Sciences of the USA (2021), **118** (48), e2113835118.

We have studied the three-dimensional (3d) cytoarchitecture of the human hippocampus in neuropathologically healthy and Alzheimer's disease (AD) individuals, based on phase-contrast X-ray computed-tomography of *post mortem* human tissue punch biopsies. In view of recent findings suggesting a nuclear origin of AD, we target in particular the nuclear structure of the dentate gyrus (DG) granule cells. Tissue samples of 20 individuals were scanned and evaluated using a highly-automated approach of measurement and analysis, combining multiscale recordings, optimized phase retrieval, segmentation by machine learning, representation of structural properties in a feature space, and classification based on the theory of optimal transport. Accordingly, we find that the prototypical transformation between a structure representing healthy granule cells and the pathological state involves a decrease in the volume of granule cell nuclei, as well as an increase in the electron density, and its spatial heterogeneity. The latter can be explained by a higher ratio of heterochromatin to euchromatin. Similarly, many other structural properties can be derived from the data, reflecting both the natural polydispersity of the hip-

pocampal cytoarchitecture between different individuals in the physiological context, and the structural effects associated with AD-pathology.

Significance Statement We demonstrate multiscale phase-contrast X-ray computed tomography (CT) of *post mortem* human brain tissue. Large tissue volumes can be covered by parallel-beam CT, and combined with sub-cellular detail for selected regions scanned at high magnification. This has been repeated identically for a larger number of individuals, including both Alzheimer's diseased patients and a control group. Optimized phase retrieval, followed by automated segmentation based on machine learning, as well as feature identification and classification based on optimal transport theory indicates a pathway from healthy to pathological structure without prior hypothesis. This study provides a blueprint for studying the cytoarchitecture of the human brain and its alterations associated with neurodegenerative diseases.

4.1 Introduction

Brain mappings of the cyto- and myeloarchitecture in larger brain areas performed *post mortem* are required to advance our understanding of the human brain in quantitative terms. Beyond refinements of a brain atlas, they are also essential for later integration of *in vivo* functional observations with high-resolution structural data [2, 4, 5]. Mapping the brain, however, requires additional imaging approaches, which can visualize and quantify the three-dimensional (3d) architectonics, including data from more than a single individual [4]. The potential of phase-contrast X-ray tomography also known as phase-contrast computed-tomography (PC-CT) for 3d brain imaging has been recently demonstrated, both for small animals models [22, 24, 40, 45, 72], and the human brain [35, 37, 73, 74]. Since the entire 3d architecture on all scales is relevant for physiological functions and pathological mechanisms, multiscale implementations of PC-CT [27] are particularly suitable for brain mapping.

Complementary to genomics, proteomics and metabolics, structural data are also required to unravel mechanisms of neurodegenerative diseases. Such data must be comprehensive (large patient- and control-groups), quantitative and fully digital, amenable to advanced analysis including deep learning, and intrinsically three-dimensional. Alzheimer's disease (AD) is a case in point: Evidence for morphological changes in the hippocampus upon aging and disease can be found already *in vivo* with MRI. To inter-

pret such data based on a reference model, a 3d probabilistic atlas of the hippocampus was put forward in [2], combining *post mortem* MRI with histology. The authors concluded that, to test the hypothesis of differential involvement of hippocampal subfields in AD, a “more granular study” of the hippocampus in aging and disease would be required and hence higher-resolution and truly 3d data.

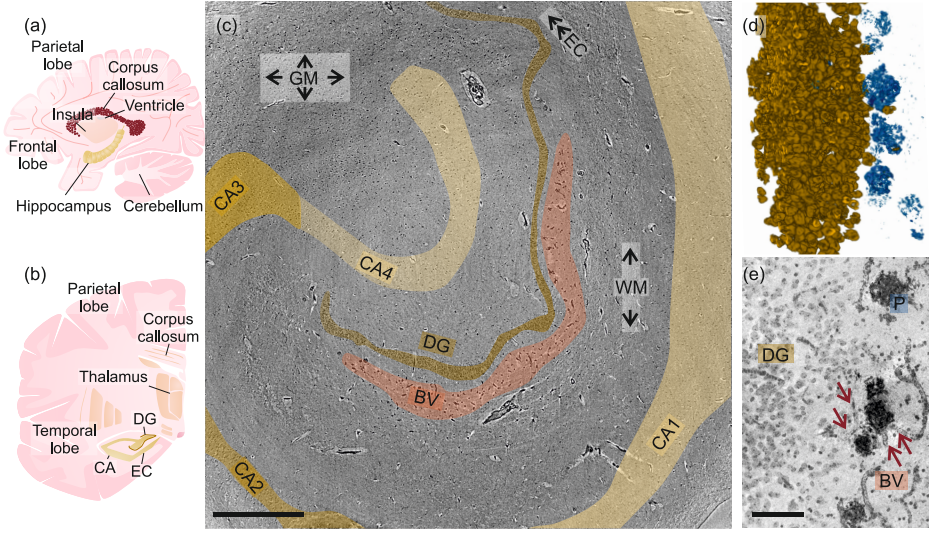


Fig. 4.1: Human hippocampus overview. (a & b) Schematics of the human hippocampus (gold) and its location, (a) in sagittal and (b) in frontal view. (c) Virtual slice through overview PC-CT data in EB-configuration. The different neuronal layers are outlined: dentate gyrus (DG); cornu ammonis (CA) differentiated into CA1, CA2, CA3 and CA4; white matter (WM); gray matter (GM) as well as the entorhinal cortex (EC). A region with calcified blood vessels (BV) is also indicated. (d & e) High-resolution PC-CT data from an AD patient. (d) Volume rendering of calcified plaques (blue) in close proximity to the DG (gold). (e) Calcified β -amyloid-plaques (P) and calcified BVs are observed only to one side of the DG, as shown here in a maximum intensity projection (16.2 μm thickness). Red arrows indicate the vascular connections between plaques. Scale bars: (c) 1 mm, (e) 30 μm .

To this end, we here present an advanced and multiscale implementation of PC-CT in combination with automated segmentation and statistical analysis of morphological features. In this way, a much-needed complement to conventional 2d histology is provided, sparing sample sectioning and staining. The signal is generated by the spatial variation of the real-valued part of the X-ray index of refraction $n = 1 - \delta + i\beta$, with δ being proportional to the electron density. Importantly, the advantage of PC-CT derives from the real-valued decrement being significantly larger than the imaginary,

absorption-accounting component β , *i.e.* $\delta/\beta \approx 10^3$ in the hard-X-ray regime. Image contrast is then efficiently formed by free-space propagation, *i.e.* self-interference of a partially coherent beam behind the object. The fact that this does not require any additional optics between the object and the detector provides a benefit both for dose efficiency and for resolution. Several PC-CT studies have already targeted hippocampal cytoarchitecture in transgenic mouse models for AD [6, 20, 45, 55, 59], which exhibit considerable contrast for a typical hallmark associated with this disease, namely β -amyloid plaques. In a recent study, we could also demonstrate the potential of PC-CT on paraffin-embedded hippocampal human tissue affected by AD, and evaluate its capability to visualize different pathologies, including plaques, depletion of neurons or possible recruitment of microglia to affected sites [73].

In this work, we study the 3d cytoarchitecture of the human hippocampus, which serves the formation of declarative long-term memory, *i.e.* remote episodic or remote semantic memory, but may also affect recent memory, emotions and vegetative functions [70]. Pathologically, the hippocampus is one of the regions first affected in AD [14]. As we show here, the throughput of PC-CT measurement, reconstruction, segmentation and analysis is sufficiently high to treat data from a larger pool, here consisting of *post mortem* paraffin embedded tissue blocks of several individuals, both of an AD and a control group (CTRL), categorized by neuropathological assessment based on the National Institute of Aging – Alzheimer’s Association (NIA-AA)-recommended ABC-staging [50]. [51] We specifically target the dentate gyrus (DG), and its AD-caused structural alterations. As recently shown, hippocampal neurogenesis and plasticity of the entire hippocampal circuitry are linked to the DG and are found to sharply drop in AD [51]. Further, we deliberately do not focus on plaques and tangles in AD, which have already been targeted by a high number of studies, but address in particular the nuclear structure of the DG-neurons, since recent evidence points to a nuclear origin of AD [30] including chromatin structures [78]. In addition, we also include 3d imaging examples of other parts and structures of the hippocampus, and provide the corresponding statistical analysis.

Fig. 4.1 shows a schematic of the hippocampus that is embedded in both left and right temporal lobe of the cerebral cortex, as a part of the limbic system. In (a), the hippocampus is sketched in the sagittal plane, where it forms an elongated structure of about 4 to 5.2 cm in length [46]. In (b), the frontal plane is shown, in which the appearance is often denoted as snail-shaped. Its characteristic functional units are shown in (c), most prominently including the *cornu ammonis* (CA) and the DG, which is a dense zone of granule cells. In the *polysynaptic* signal pathway relevant

in semantic memory formation, input signals from the *entorhinal cortex* (EC) reach first the DG, which is composed of elliptically shaped granular cells with millimeter-long dendrites. Connected through mossy fibers, information is further processed in the CA, whose neurons are characterized by their pyramidal-shaped bodies. The compartmentalization of the CA with commonly attributed sub-regions CA1 to 4 is not entirely standardized. The information exits the hippocampus to the inferior temporal cortex, the temporal pole and the prefrontal cortex, constituting the *gray matter* (GM). There are further pathways of information processing, involving myelinated tracts in the *white matter* (WM) that link the hippocampus to further brain regions. The physiological relevance of the hippocampus, with respect to several important signal pathways and its pivotal role in memory function and neurodegenerative diseases, in particular in AD, underpin the necessity to study its 3d structure with cellular and sub-cellular resolution.

To cover the hippocampal cytoarchitecture in a larger patient cohort, we increase the sample throughput with respect to earlier work [73] by an optimized recording strategy enabling a large sample pool at high and comparable data quality, and we implement a multiscale PC-CT workflow for human brain tissue, based on parallel-beam (PB) recordings at high field-of-view (FOV) combined with zooms into region-of-interest (ROI) scanned at high magnification based on cone beam geometry. We then use machine learning based on the V-net architecture to segment neurons, followed by optimal transport (OT) theory to unravel pathological alterations. Note that OT enables us to identify ‘movement’ in a patient cohort based on transport metrics in a structural feature space, which we define in the image segmentation step. OT also offers significant advantages over standard statistical tools such as t-testing of a single parameter, since it can compare the entire neuron population, by metrics quantifying changes in their distribution.

The implementation of PC-CT, notably regarding the multiscale configuration that comprises different zoom-levels, is detailed in Materials and Methods. Beginning with overview scans with a FOV of several millimeters in expanded-beam (EB) configuration as in Fig. 4.1 or in PB, sub-regions of the hippocampus are presented at the different zoom-levels in Results I: Multiscale Tomography of the Hippocampus. The structure of granule cell nuclei in the DG is then investigated in volumes of 10^8 to $10^9 \mu\text{m}^3$ at voxel size of $p_x \approx 160 \text{ nm}$, and in some cases even at $p_x \approx 50 \text{ nm}$, based on geometric magnification using a divergent and highly coherent beam exiting an X-ray waveguide (WG). In the high-resolution reconstructions, neurons and in particular DG-cell nuclei are segmented. Based on the segmentation masks, histograms of mor-

phological features are obtained, containing results on the order of 10,000 neurons for each tissue sample. Histograms of five selected features in autopsies of 20 individuals (11 subjects with intermediate to high AD neuropathologic change according to ref. 20, in the following referred to as AD; 7 controls; and 2 with diffuse presentation based on ABC-score) are then compared in tResults II: Geometric and Statistical Analysis, using the OT tools. In a very general manner, we propose an analysis workflow to identify a pathway from healthy to pathological structure.

4.2 Results I: Multiscale Tomography of the Hippocampus

Fig. 4.1(c) shows the PC-CT result obtained for the largest FOV, covering an 8-mm biopsy punch of a $2 \times 3 \times 0.3\text{-cm}^3$ tissue block, scanned in EB-configuration (SI Appendix, Tab. S1 & S2, and Fig. S1). The quintessential structure supporting all further identification of ROIs, as already summarized in the introduction, is easily recognized and labeled based on visual inspection of the 3d-data. Already at this coarse level, the granular cell band of the DG can be identified. It is bordered by a tract of particularly electron-dense blood vessels, indicative of calcifications. Note that calcified vasculature within the hippocampus was frequently observed in tissues of different subjects, both AD and CTRL. As presented in (d & e) for an AD-case, these emerge particularly electron dense, and may even traverse β -amyloid which then also show highly elevated electron density (as reported in [73]). In addition, other regions such as the pyramidal cell band of the CA, the WM and the EC can easily be located. Identification of these regions is important in view of subsequent extraction of further sub-volumes with a 1 mm-biopsy punch for the high-resolution scans. As a proof-of-principle that these large FOVs can also be scanned with smaller voxel sizes, the full 8 mm-punch was further scanned in PB-configuration (SI Appendix Tab. S2). Using dynamic stitching implemented by the *NRStitcher* (nonrigid stitching of terapixel-scale volumetric images) program [47], 7×7 individual scans were combined to again cover the entire 8-mm punch in a single large volume. By this approach, a tissue volume of 63 mm^3 was covered with submicrometer voxel size. Fig. 4.2 presents frontal plane slices through the stitched reconstruction volume. In (a), gray squares mark the single tomograms. With a few local ring artifacts only, structures can be successfully traced throughout the volume, well beyond the boundaries of a single scan. Fig. 4.2(b) illustrates the winding of the DG-band throughout the volume in two different frontal

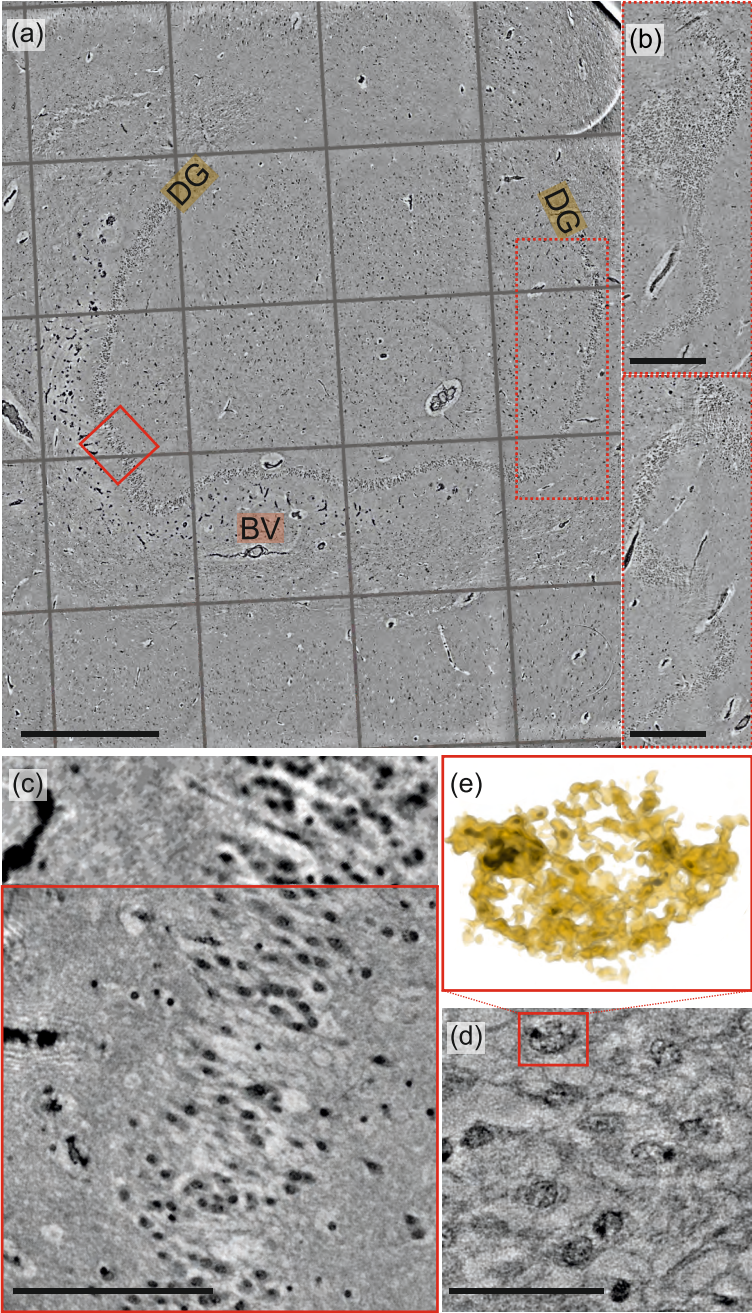


Fig. 4.2: (caption next page)

Fig. 4.2 (previous page): Multiscale PC-CT data. (a) Virtual slice through the stitched reconstruction volume of the entire 8-mm tissue sample obtained from 7×7 scans in PB-configuration. Labels indicate the ends of the DG-band in this slice, as well as calcified BVs. The red dashed box marks the region which is further detailed in (b), in two different parallel planes, demonstrating how the DG-band winds through the volume. (c, bottom) Detail view of the DG band, as obtained from a CB-scan recorded at $M \approx 40$, at the position marked by the solid red square in (a). For comparison of data quality and contrast, (c, top) shows the corresponding PB-data. (d) Highest zoom of the DG structure, recorded at $M \approx 130$. The nuclear envelope and heterochromatin become visible by median-filtered maximum intensity projection over $0.5 \mu\text{m}$. (e) A single nucleus is further highlighted by a full 3d rendering of the electron-density. Note that also here, darker areas are indicative of higher densities. Scale bars: (a) 1 mm, (b) 0.5 mm , (c) $100 \mu\text{m}$, (d) $30 \mu\text{m}$.

planes. This 3d morphology with its invaginations helps to accommodate a sufficiently high number of DG-cells. Based on the large FOV even in a single tomogram, the PB-data are particularly suitable to quantify the DG-band morphology and width (see Fig. 4.3, and further analysis summarized in SI Appendix, Fig. S3 and detailed in the text in SI Appendix). To image ROIs at higher magnification $M \simeq 40$ in cone-beam (CB) configuration and without local tomography artifacts, sub-volumes were extracted from the 8-mm block using a 1 mm-biopsy punch. Fig. 4.2(c) presents a slice through such a ROI, indicated by a red square in the overview scan. In this configuration, even the sub-structure of DG-cell nuclei can be unveiled. These details are even better resolved by further increasing the geometrical magnification to $M \simeq 130$, as shown in (d) for a slice and in (e) for a 3d-volume rendering of a single nucleus, based on its electron density.

Importantly, the image quality allows for semi-automatic segmentation of the granular cell nuclei using the *Ilastik* software [10], and a subsequent volume rendering of the annotated segmentation masks, using *Avizo Lite* (Thermo Fisher Scientific). Fig. 4.3 presents an example for a volumetric perspective, showing the overall bent shape of the DG-cell band in (a, gold), jointly with the vasculature (red). Holes in the DG band are due to major blood vessels penetrating the DG. Keeping the perspective, and applying this DG-mask to the PC-CT gray values, we can present volume renderings of different quantities: (b) normalized electron density P , (c) standardized relative variance $S = \sigma^2/\rho^2$ of the electron density within the nuclei, indicative for the prevalence of heterochromatin, and (d) the local cell density, averaged within a radius of $50 \mu\text{m}$. In this manner, the overall distribution and local inhomogeneities can be visualized.

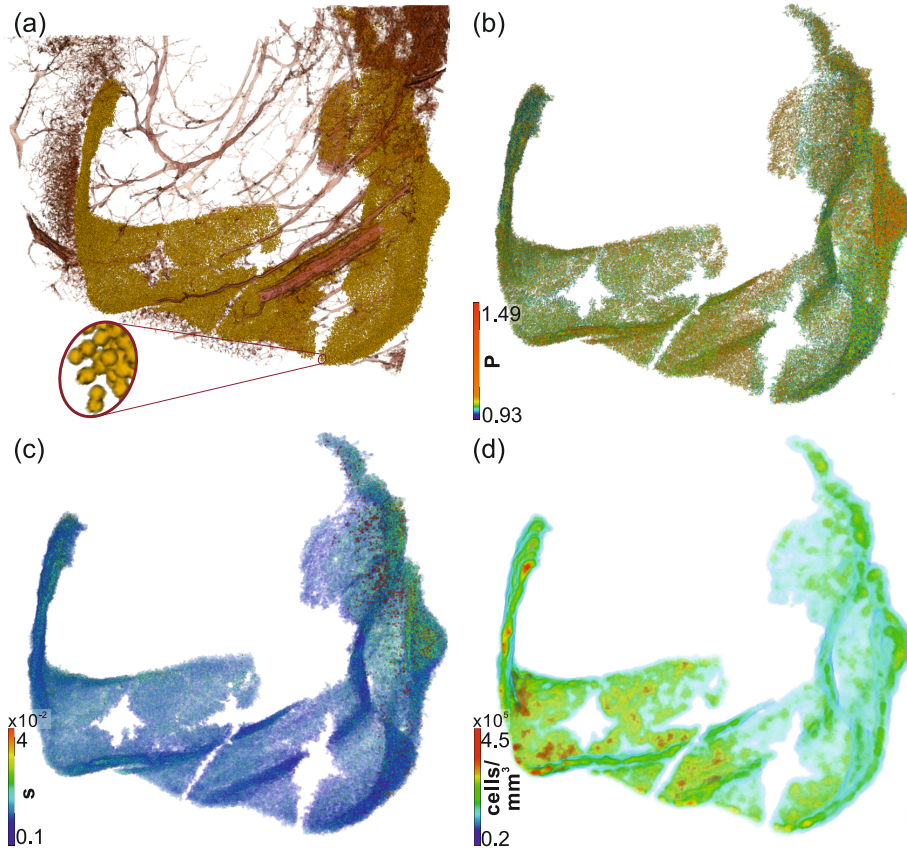


Fig. 4.3: Dentate gyrus (DG) overview. The DG-band in a section of 1.25 mm thickness (septotemporal axis) shows (a) segmented DG-cell nuclei (gold) and vasculature (red), and (b-d) rendering in false colors representing: (b) the normalized electron density P of the nuclei, (c) its variance S , and (d) the local granular cell density.

Next, we further illustrate high-resolution results obtained in CB-configuration for the examination of specific regions in the hippocampus such as CA1, DG, surrounding GM, and WM.

Cornu Ammonis 1 Fig. 4.4 shows exemplary results obtained for the cornu ammonis 1 (CA1) region, for a 1-mm sample that was extracted and scanned as detailed in SI Appendix, Tab. S2. The elongated, pyramidal shape that is typical of neurons in the CA-layer is well-visualized by the maximum intensity projections (MIPs) presented in (a-c). In each cell, body, nucleus and nucleolus can be differentiated. For some

cells, such as the one marked by the top arrow (a), the contrast between cell body and nucleus appears to reflect the position of the nuclear membrane, while for others (bottom arrow), the dominant effect is an overall increased electron density in the nucleus. Further, the density within the cytosol shows some variation. This is also observed for other cell types, as shown in Fig. 4.4(b), depicting the sub-structure of a satellite cell attached to a neuron. In line with the function of the CA-neurons for one-way signal processing throughout the hippocampus, the consistent polarization and orientation with the characteristic long dendrite is very well-visible throughout the 3d reconstruction volume. The contrast is sufficient to trace the large dendrites over several tens of micrometers as highlighted in Fig. 4.4(c). Using Ilastik, neuronal cell bodies and nuclei are segmented and 3d-rendered as shown in (d-f).

In the data of Fig. 4.4(c & e), areas of lower electron density (light gray values) are often observed around the neurons. To check whether this observation of lower electron density could eventually be an artifact of sample preparation, e.g. by the dehydration-and-embedding procedure of preparing formalin-fixed and paraffin-embedded (FFPE) tissue blocks, we varied the preparation and also scanned the tissue in hydrated state. For this purpose, a 1 mm-sample was taken from a tissue block, which was first chemically fixed with 10% formalin and then stored in phosphate-buffered saline at 4° C, and examined in its hydrated state, *i.e.* neither dehydrated nor paraffin-embedded. Interestingly, this showed that these area of decreased electron density are also present in the images of hydrated tissue (SI Appendix, Fig. S6).

Segmentation of pyramidal neurons was then applied to tissue samples from different subjects, both of the AD- and of the CTRL-group. Samples were extracted from the same position in the hippocampus. Note that pathological changes associated with AD are particularly pronounced in this region. Notably, tissue samples from three individuals diagnosed with AD (according to ABC staging; subjects 2, 6 and 21, aged 78 ± 11 y) were compared to four controls (subjects 16, 17, 20 and 21, aged 66 ± 20 y), and a further sample (subject 12). The results are reported in SI Appendix and visualized in SI Appendix, Fig. S4.

Gray Matter Fig. 4.4(g) shows a virtual slice (MIP) through hippocampal GM-tissue. For sample collection, the GM-region was identified based on histological analysis (stained by hematoxylin and eosin as well as Bielschowsky silver impregnation). Pyramidal cells are also segmented in this region, enabling again the evaluation of neuron density, neuronal morphology and orientation in full 3d.

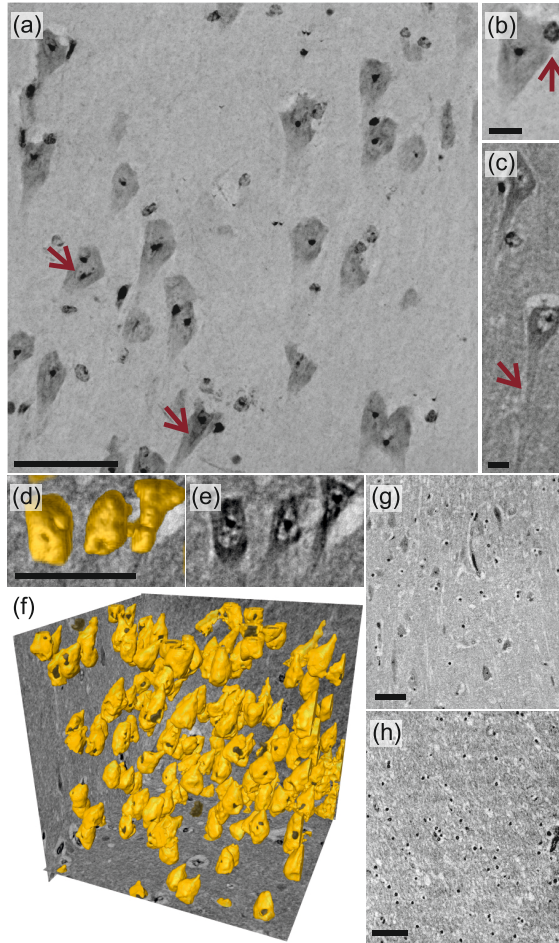


Fig. 4.4: CA1-region with pyramidal cells (CB-data). (a) Pyramidal cells with the typical uniaxial orientation are well-visualized by their electron density, when gray values are subjected to a maximum intensity projection (MIP), here over a thickness of 13 μm . The contrast is sufficient to distinguish cell bodies and nuclei, either by the visibility of the nuclear envelope (upper arrow) or an overall increased electron density within the nuclei (lower arrow). (b & c) MIPs over 8.7 μm thickness. (b) Pyramidal cell with a satellite cell attached (arrow). (c) Pyramidal cells are branched throughout the volume. (d & e) Volumetric segmentation of the cell bodies. (f) 3d-rendering of the cell bodies (gold) and the nuclei (brown) in the entire reconstruction volume. Gray-scaled orthoslices are included as a support for 3d visualization. (g) MIP of gray matter tissue, over 1 μm thickness. (h) MIP of white matter tissue, over 1.6 μm thickness. Scale bars: (a, d, e, g, h) 50 μm & (b, c) 10 μm .

White Matter Fig. 4.4(h) displays a cross-section through WM-tissue. Again, the position at which the sample was extracted by a biopsy punch in the FFPE block was chosen based on evaluation of neighboring histological sections (stained by hematoxylin and eosin as well as Bielschowsky silver impregnation). This tissue segment does not exhibit particular neurons as the CA and GM do, as expected, but appears rather fibrous, reflecting the myelinated fibers of the WM.

Dentate Gyrus The DG is a particularly substantial component in the information processing within the hippocampus. Fig. 4.5 shows a reconstruction of this region from data scanned in the CB-configuration. As exemplified in (a), sub-cellular details can be visualized. The virtual section is in the same plane as in Fig. 4.2. In (b), the volume is sectioned in a plane parallel to the DG-band, emphasizing its wall-like appearance. Granular cells exhibit a well-structured electron density within their nuclei, which is surrounded by regions of lower electron density (lighter gray values) in the cell body. Even interconnections between single cells can be noticed. The zoom-in highlights the particularly large variance of the electron density distribution in cell nuclei, which can be associated with heterochromatin.

Different features in the reconstruction volume of the DG were then identified and segmented, again using the interactive learning and segmentation toolkit Ilastik. Fig. 4.5(c) shows the volume-rendered segmentation of DG-cell nuclei. Based on the center-of-mass of the nuclei, a 3d cell density map was computed as shown in (d). The density obtained from the high-resolution scans in CB-configuration confirms the cell density analysis of the large FOV overviews recorded in the PB-configuration (Fig. 4.3(d)). The density ranges between 2 and $4.5 \cdot 10^5$ cells/mm³, which is in good agreement with the literature [12].

4.3 Results II: Geometric and Statistical Analysis

Histograms of Structural Properties of DG-nuclei

As a next step, we quantify the DG-cytoarchitecture in 3d to gain an understanding of its inter-subject variation both in the healthy physiological state and in the pathological context of AD. To this end, the DG-band in samples of 20 different subjects was scanned, reconstructed, segmented and analyzed. AD-cases were identified based on the ABC-score [50]. Notably, samples from 11 AD-subjects aged 76.6 ± 9.3 y, 7 CTRL-subjects aged 76.6 ± 7.0 y, and 2 further subjects with no group assignment were collected, as

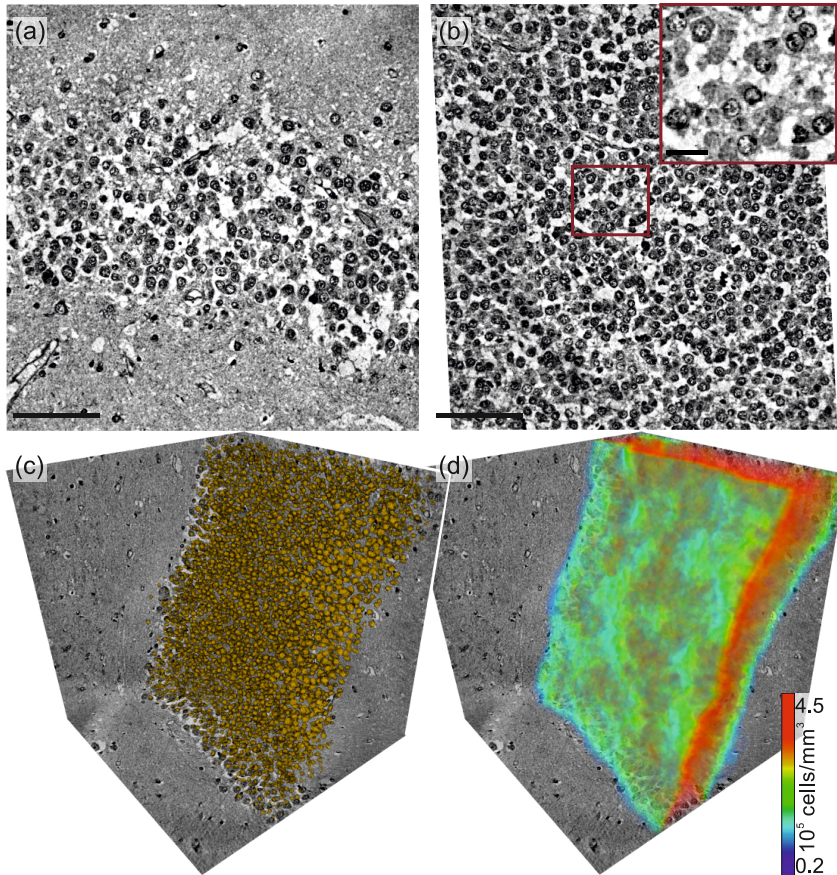


Fig. 4.5: Zoom into the DG-cell band (CB-data). (a) Transverse slice through the band. (b) Slice parallel to the DG-band. The red square marks a region that is shown in the zoom, and with gray scale chosen to highlight the structure of the nuclei, *i.e.*, the variance of electron density within the nuclei. (c) Volume rendering of DG-cell bodies. (d) Rendering with color indicating the local cell density (see colorbar). Scale bars: (a & b) 100 μm , (b, inset) 20 μm .

listed in SI Appendix, Tab. S1. Similarly to the multiscale workflow described above, 1-mm samples were extracted from each tissue block, and imaged first in PB- and then in CB-configuration. The following analysis is mainly based on the CB-data, due to the higher resolution capable of resolving nucleic structures, while the overview scans in PB-configuration helped in correct positioning of CB-scans and analysis robustness. The analysis of the PB-configuration data is given in the SI Appendix, Fig. and corresponding text sections.

Fig. 4.6 illustrates the segmentation of DG-neuronal nuclei (CB-data). In (a), the same region is shown before and after super-imposing the object mask, generated from the segmentation by the machine-learning workflow, described in (c). For each object in the segmentation output, *i.e.* from each DG-cell nucleus, several structural properties are evaluated for further analysis: (1) median of the electron density ρ (compactness parameter), (2) normalized variance of electron density $s = \sigma^2/\rho^2$ as a proxy for the spatial variations within the nucleus (heterogeneity parameter), (3) nuclei volume v (size parameter), (4) sphericity φ of the nucleus (form parameter), and (5) the number of neighbors nn within the local vicinity (neuron packing parameter). Here, object-vicinity was defined by a radius given as $\bar{x}_{nn} + 2 \cdot \text{MAD}_x = 13.5 \mu\text{m}$, where $\bar{x}_{nn} = 8.8 \mu\text{m}$ denotes the median of the next-neighbor distance distribution of all samples, and $\text{MAD}_x = 3.5 \mu\text{m}$ its median absolute deviation. Fig. 4.6(d) presents the resulting histograms for all five structural features, at the example of one subject belonging to the CTRL-group. In this particular case, the histograms contain data corresponding to a total of 3595 segmented nuclei in the reconstruction volume satisfying the following selection criteria applied to the segmentation output: Only objects with $v > 35 \mu\text{m}^3$, $0.6 \cdot \bar{x}_{nn} < x_{nn} < \bar{x}_{nn} + 3 \cdot \text{MAD}_x$, as well as lying within the $1.5 \times$ interquartile range of any of the five features, are considered for statistical evaluation. These criteria have been chosen to minimize bias from segmentation artifacts.

Inter-Subject Variation and Effects of AD

The segmentation of the granule cell nuclei and extraction of the five parameters per cell, as described above, are then carried out for all individuals, including AD-patients and CTRLs, based on the same automated workflow. For each property (parameter) and each individual, an entire histogram containing the data of all segmented granules is available. First, the different properties are compared independently, one-by-one. Fig. 4.7 presents results for electron density ρ , and the heterogeneity parameter s (see SI Appendix, Fig. S2 for all other parameters). The violin plots shown in (a) provide a quick overview, and illustrate the degree of intra- and inter-group variations of the histograms. Before addressing these differences at the level of the entire histograms, the median values of the distributions are compared for the two groups (AD and CTRL). The electron density is slightly higher for AD- than for CTRL-subjects; *i.e.* $\bar{\rho}_{\text{AD}} = 320.91 \text{ nm}^{-3}$ versus $\bar{\rho}_{\text{CTRL}} = 318.77 \text{ nm}^{-3}$, with a reduced volume, *i.e.* $\bar{v}_{\text{AD}} = 101.85 \mu\text{m}^3$ versus $\bar{v}_{\text{CTRL}} = 135.88 \mu\text{m}^3$, both indicating a trend to more compact nuclei, with *p*-values (*Welch's t-test* $p \approx 0.02$ and $p \approx 0.07$ for ρ and v , respectively). At the same time, the median of the heterogeneity parameter s increases from $\bar{s}_{\text{CTRL}} = 1.07 \cdot 10^{-5}$

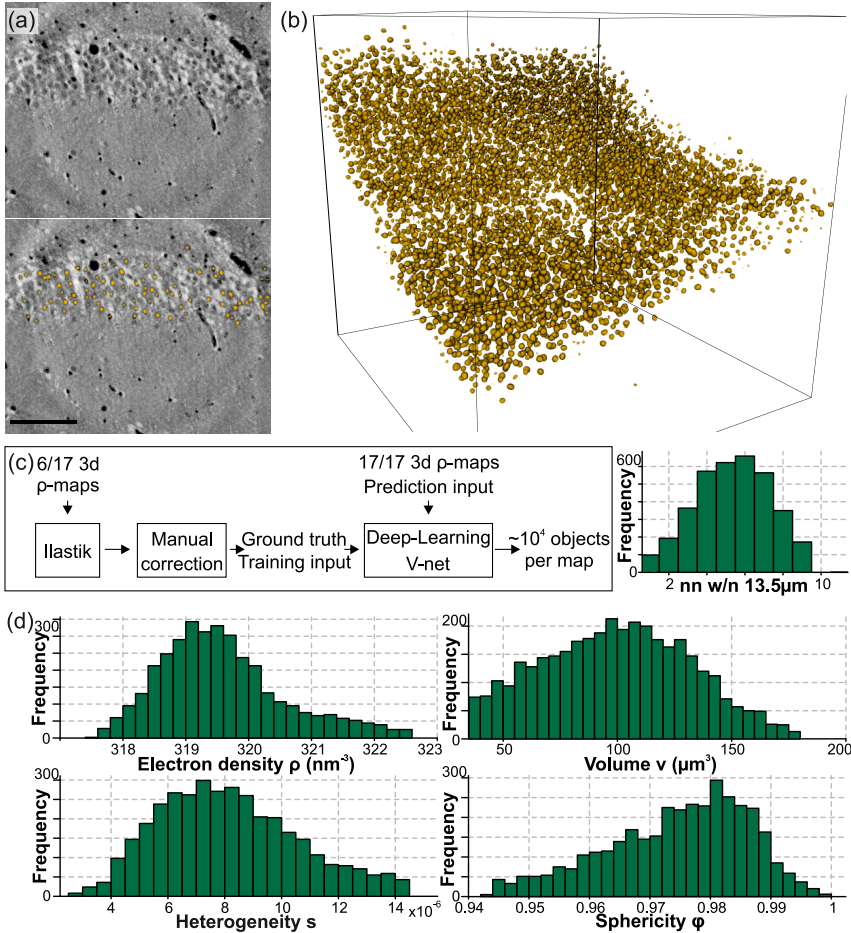


Fig. 4.6: Segmentation workflow for DG-nuclei. (a) Slice through exemplary 3d input data (CB-configuration), (top) without and (bottom) with mask annotations. (b) 3d-rendering of the mask, within a cubic volume of side length $400 \mu\text{m}$. (c) Flow diagram illustrating the steps of segmentation. (d) To each masked object (DG-cell nucleus), a number of properties can be attributed, resulting in respective histograms. Scale bar: $100 \mu\text{m}$.

to $\bar{s}_{\text{AD}} = 1.45 \cdot 10^{-5}$ in CTRL- versus AD-subjects, indicating a trend towards a more heterogeneous spatial structure of the nucleus in AD, but with $p \approx 0.17$, this difference in median values is not significant. Beyond comparison of the median values, however, entire granule populations should be compared between subjects and groups, which will lead us again to consider the changes in s as relevant in order to discriminate between pathological and healthy states (see further below). Taking into account the

entire neuron population is important, since the physiological functions may require a certain bandwidth of structural parameters, *i.e.*, a dispersion of properties associated with functional states of granules. It is therefore of interest to compare the inter- and intra-group differences also in view of the entire histograms, as quantified by the *Wasserstein*-metric (W). Fig. 4.7(b) shows a matrix of pairwise differences of the ρ distributions (“distance chart”), evaluated with W . The matrix is divided into four quadrants, showing differences between individuals within and between the groups. Notwithstanding the large variations at the subject level that are highlighted by this display, slightly increased differences can be noted already from visual inspection of the two quadrants comparing subjects across the groups.

To cope with the two major challenges of the data, the strong inter-subject variation, and the dispersion of neuron structural parameters of any single subject, we adopt a strategy, where each individual is represented by a point cloud in a five-dimensional space of structural parameters, denoted in the following as the *feature space*. The analysis of the point clouds below is motivated by the fact that inter-group structural differences for corresponding classification of AD- and CTRL-groups are expected to be better revealed in higher dimensions. Note that only for the special and very unlikely case that the point cloud distribution can be written as a factorized (separated) product to one-dimensional distributions, no information is lost, when treating each dimension separately. Already a simple projection to a two-dimensional sub-space, as exemplified in Fig. 4.7(c), shows that the point clouds do not separate (factorize), since the structure parameters are weakly correlated.

Classification of AD-Pathology vs. Control

The point clouds representing the granule cell population for each subject, as introduced above, are further analyzed in the five-dimensional feature space. First, we standardize the point clouds in each dimension (feature) separately by the population (*i.e.* the union of all sample point clouds) mean and standard variation. The standardized variables are denoted by the respective capital letter (P, S, V, Φ, NN). Then, each subject’s point cloud is approximated by a Gaussian distribution, with mean and covariance matrix given by the empirical mean and covariance matrix of the point cloud. This distribution can be conceptualized as an ellipsoid, centered at the mean, orientation of the principal axes given by the eigenbasis of the covariance matrix and their length by the square root of the corresponding eigenvalues. A natural metric on the set of Gaussian distributions is obtained by combining the Bures metric [26] on the covariance matrices with the Euclidean distance on the mean values. This yields the

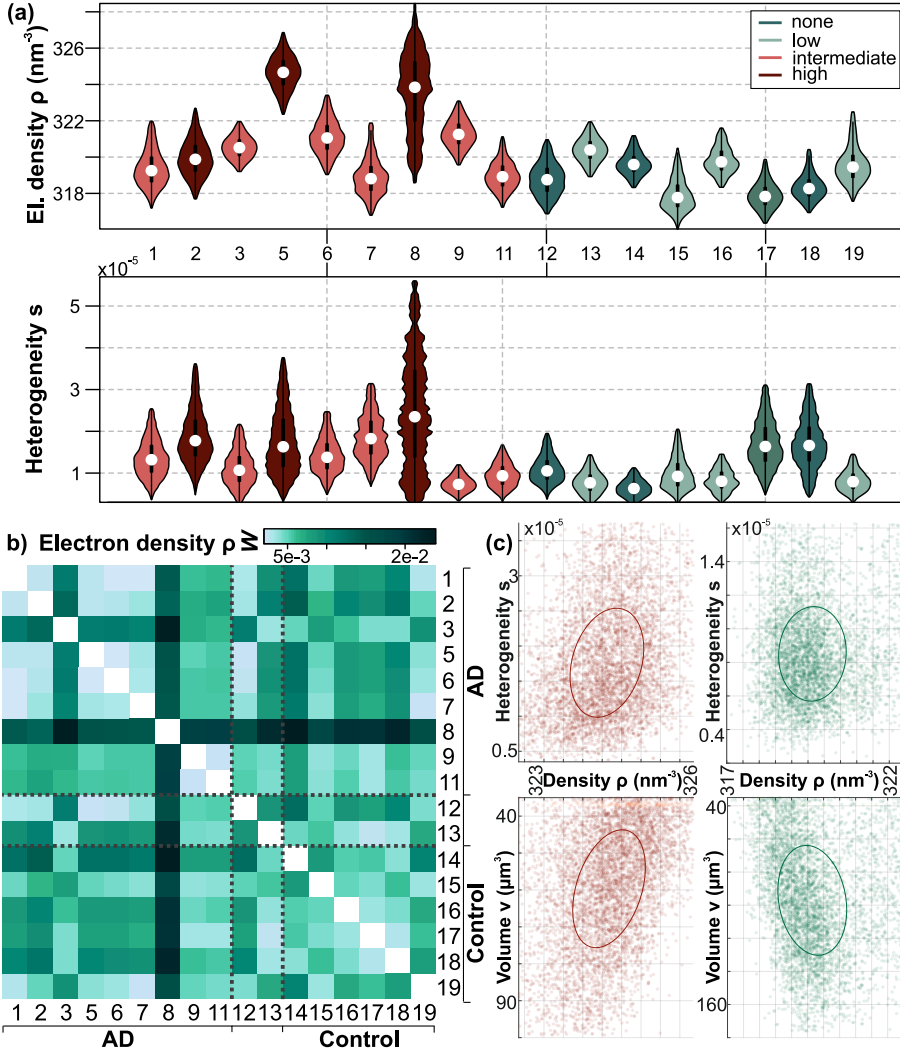


Fig. 4.7: (caption next page)

L^2 -OT distance, denoted by \mathcal{W} , between the two Gaussian distributions [58] which has recently become increasingly popular in data analysis applications [58, 67].

Fig. 4.8 reports on the point cloud analysis, and the corresponding classification in feature space. In (a), 2d-projections of the Gaussian distributions are visualized as ellipsoids, left for the AD-group (orange-red), and right for the CTRL-group (green). The distribution in the V/P plane (top), and the S/P plane (bottom) shows a larger diversity for the AD-group compared to the CTRL-group. The visualization of ellip-

Fig. 4.7 (previous page): Structural features of DG-cell nuclei. (a) Violin plots of electron density ρ and heterogeneity s , reflecting the histogram of the selected feature for each individual. The color scheme refers to the ABC-score from neuropathological staging. (b) Wasserstein-metric W calculated between any two patients and arranged in a matrix, as a measure of inter-histogram distances, here shown for ρ . Gray dashed lines separate groups. (c) Point clouds in the “feature space”, defined here by two selected features, illustrated for the example of two subjects (left: AD-group, right: CTRL-group), (top) s vs. ρ and (bottom) v vs. ρ . Each point corresponds to one neuron. Ellipsoids indicate the results of a PCA with half axis defining the principal axis, or equivalently the 1σ -intervals when fitting a two-dimensional Gaussian distribution to the point cloud.

soids in 2d also serves to illustrate the optimal transport cost: ellipsoids representing patients 15 and 19, for example, are quite distinct, which is reflected by $W = 0.86$ (V/P-plane), and $W = 0.74$ (S/P-plane), respectively. Contrarily, patients 15 and 12 are closer, evaluating to $W = 0.21$ (V/P-plane), and $W = 0.29$ (S/P-plane), respectively. The distances W between any two individuals is visualized in the matrix shown in (b), which can again be considered as a “distance chart”, now taking into account the full five-dimensionality of the feature space. Darker colors indicate a higher cost (distance), and hence a stronger dissimilarity between the 5d-ellipsoids of the corresponding subjects. Two patients stand out strongly: number 5 and 8, which are two AD-cases in an advanced state (both show an ABC-score of “high”, and have a distinct high B-score compared to one further subject ranked with ABC-score of “high”).

The OT-distance W can also be evaluated directly at the level of point clouds [58], making the Gaussian approximation an optional intermediate step. For the full point clouds one also obtains a “distance chart” analogous to that in Fig. 4.8(b). We perform the subsequent analysis both on full point clouds and with the Gaussian approximation. Every subject can now be interpreted as one point in “subject space” where distances are measured by W (with or without Gaussian approximation). While this space is not a linear vector space, it has the structure of a Riemannian manifold (intuitively, a curved hyper-surface). This manifold can then be approximated locally by its tangent space at a suitable reference point (usually the Riemannian center of mass of the samples) [77]. Thus, we have obtained an embedding of the subjects into the linear tangent space (where each individual is represented by one point, which in turn represents a point cloud or a Gaussian distribution on feature space), where we can now apply

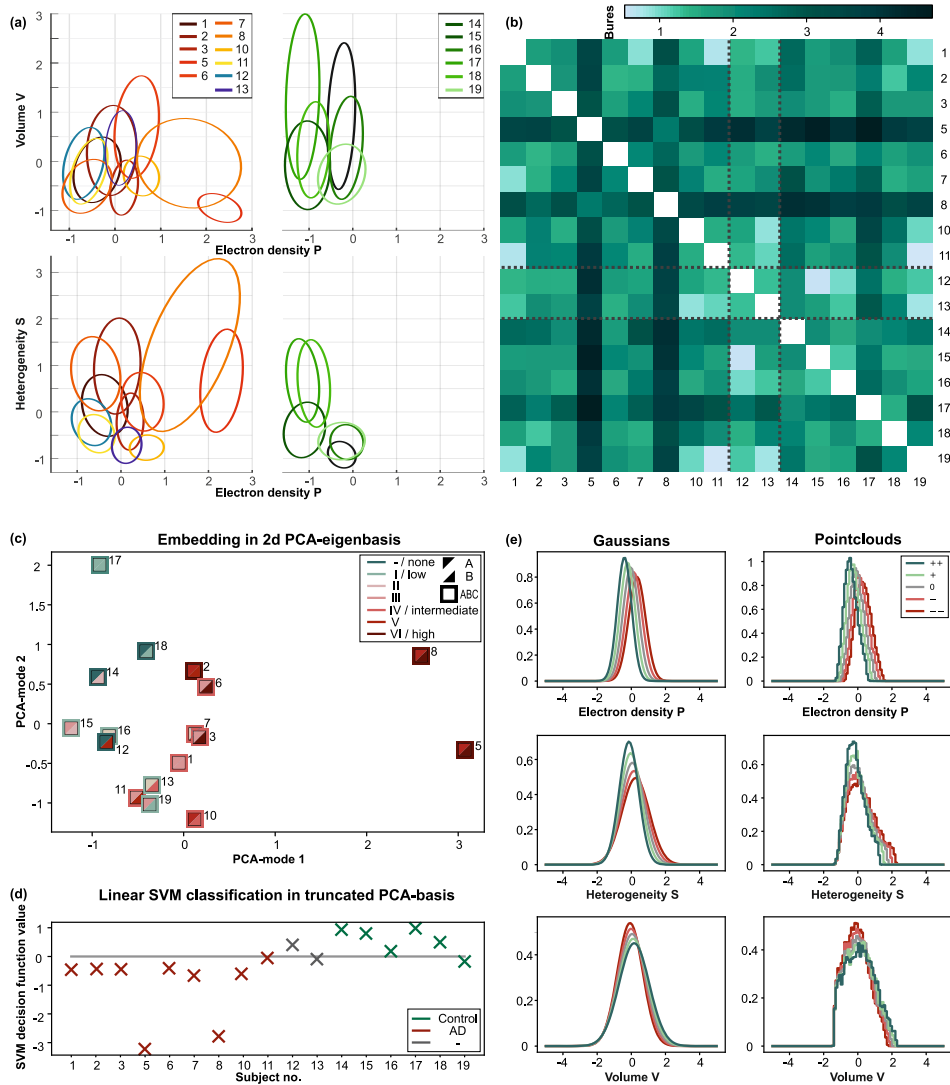


Fig. 4.8: (caption next page)

standard data analysis tools. Principal component analysis (PCA) can be used to identify the most dominant modes (directions) of variation in the subject point cloud (in the tangent space). Fig. 4.8(c) shows the coordinates of the patients with respect to the two dominant PCA-modes ($pca1, pca2$). It is important to note that the feature space and its lower dimensional (truncated) tangent space are implemented without any prior categorization into groups. Instead, the variance in the data itself is used to

Fig. 4.8 (previous page): Multi-dimensional analysis, optimal transport, and classification. (a) Ellipsoidal representations of the DG-cell nuclei in selected 2d sub-spaces of the full 5d feature space. Ellipsoids are shown for 17 different subjects, (left) subjects with AD and with no group assignment, and (right) CTRL, showing (top) volume V vs. electron density P , and (bottom) electron density variance S vs. P . (b) Matrix plot of the Bures-cost (“distance chart”), with each entry referring to the distance between the respective 5d-ellipsoids. With respect to the chosen metric, each subject can be located in a “subject space”, constructed from the ellipsoids. (c) PCA in a suitable tangent plane of this space yields the dominating components, along which the variance between the subjects is maximized. The PCA-components represent linear combinations of different features. Data points representing the different subjects are color coded according to Thal phases (upper left triangle), Braak stages (lower right triangle), and ABC score (frame), but this information is not used in the construction of the tangent space. (d) Linear SVM-analysis applied to the four most dominant PCA-components reveals a hyperplane separating both groups. (e) The evolution of histograms according to the first PCA-mode is found to describe the change from a healthy to a pathological state, indicating the “stereotypical transformation”, from CTRL (++) to AD (- -) tissue. The histograms obtained by (left) Gaussian approximation, and from (right) a full calculation taking into account every element of the point clouds are found to be in good agreement.

identify a pathway of maximum changes (*pca1*-mode). Based on the color-code of the data points reflecting the ABC-staging, we can already visually infer that this pathway also separates the patient groups. To quantify this further, a classification by a linear support vector machine (SVM) is performed, as shown in (d), using the four most dominant PCA-modes, which cover 92.4% or 88.7% of the data variance, in Gaussian approximation or on point clouds, respectively. The normal vector of the separating hyperplane that was obtained by the SVM can be interpreted as the main direction of discrimination between CTRL and AD in tangent space, and differs only by 15° from the direction of the *pca1*-mode. The shifts in the feature histograms corresponding to the direction of *pca1* are shown in (e) for the Gaussian approximation (left) and the point clouds (right), respectively, with colors indicating the shifts from CTRL-group (green) to AD-group (red), in a continuous manner. The evolution of the histograms (disease progression) is very similar for Gaussians and point clouds analysis, which can be regarded as a confirmation of validity and robustness. As a result, we can now indicate quintessential changes in the histograms for all features, as we move along the main axis discriminating pathology and control. These changes are (from physiological to pathological end) (1) increased density, (2) increased heterogeneity, and (3) smaller volume of the nuclei control.

4.4 Discussion

Pathological Progression and Validity of the Analysis The analysis presented above indicates that with pathological progression from CTRL to AD, DG-cell nuclei become more compact (increase of electron-density, reduction of volume) and exhibit higher heterogeneity (higher variance of electron density). These findings are revealed by a quantitative workflow that can be summarized as follows: (1) PC-CT of well-controlled regions of the human brain, for a considerable number of individuals; (2) automated segmentation and classification of many neurons based on machine learning and extraction of structural properties; (3) creation of a “feature space” based on single-cell properties, and the neuron population for each individual (one point in the feature space corresponds to a single cell and a point cloud to one patient); and (4) construction of a “subject space” based on the point clouds and their distances, as quantified by OT theory, and subsequent local linearization, PCA and SVM-analysis. In the subject space, a point corresponds to a single patient, and a point cloud to one group. Geometric analysis of the respective subject groups indicates the dominating “modes”, which encode a movement of cells in feature space that may correspond to the progression from physiological to pathological states. Since the full OT-analysis is numerically complex and relies on very recent mathematical work, we have also implemented a more conservative Gaussian approximation of the point clouds, which provides a fully established and numerically low-cost alternative to the full analysis. Importantly, the Gaussian approximation and the findings on point clouds are consistent, proving that the conclusions are robust with respect to smaller variations in the point distributions. At the same time, Fig. 4.8(e) shows that the prototypical change of a histogram for the heterogeneity S trends toward an asymmetric distribution for strong AD when estimated on the point clouds. In particular, the distribution exhibits a shoulder towards higher heterogeneity values, hinting at a sub-population of DG-neurons relevant in the pathology. In the Gaussian framework, this detail cannot be captured completely, but appears only as a broadening of the histogram. This nicely illustrates the more complete description provided by OT on the full point cloud.

Heterogeneity, Chromatin and AD Next, we raise the question of interpretation of these findings in the context of the aging brain and AD. We have to address in particular the increasing compactness and heterogeneity of the DG-cell nuclei, which were identified as a major marker for AD progression by the analysis. Note that OT is able to detect changes in a structural feature such as nuclear volume v , density ρ ,

or heterogeneity s also in cases where the average parameter - *i.e.* averaged over the neuron population of a patient - does not change significantly between groups, as tested by a t-test for example. This is because OT provides a measure for changes in the entire neuron population, and hence also takes into account a change in the distribution such as the broadening observed in Fig. 4.8(e). The observed changes in heterogeneity can be interpreted based on Fig.4.2(d-e), where we can recognize the typical structural patterns of heterochromatin as the dominating contribution to the variance of electron density, *i.e.* the heterogeneity S . This identification is plausible, since the noise contribution to S has been minimized by median filtering prior to the quantification of P and S . The attribution of s to heterochromatin patterns is also in agreement with chromosomal conformation studies by soft X-ray absorption tomography [42]. Hence, it is reasonable to draw the conclusion that the increase in heterogeneity is explained by an increasing ratio of heterochromatin to euchromatin, or more generally changes in chromatin conformation. In fact, the percentage of DNA in the euchromatin state is smaller in AD than in healthy tissue, as known from fractionation of DNA extracted from *post mortem* brains [21]. By PC-CT sub-nuclear structure can be assessed at the single neuron level in larger volumes of human brain tissue without slicing or staining. Currently, the topic of nuclear structure and AD receives much attention as chromatin organization has now been linked to dysregulation of genome architecture in aging and AD brain tissue [78]. Further, a nuclear origin of AD and dominant roles of nuclear tau protein and of nuclear lamins have been pointed out [31]. A specific contribution to the increased level of heterogeneity that we observe here could also be due to the formation of distinct heterochromatic structures designated as senescence-associated heterochromatic foci (SAHF). SAHF have first been reported for senescent human fibroblasts [53], and have been described as subnuclear heterochromatic compartments, which potentially silence genes that promote cell cycle progression [17]. More recently, SAHF formation and senescence have also been discussed in neurons and glial cells with respect to a putative role in AD [38]. An additional factor to the observed heterogeneity could be the nucleoplasmic reticulum that interrupts the smooth nuclear surface by tubular invaginations of the nuclear envelope and for which a significant expansion was reported in AD brain tissue [28], resulting from neurodegenerative laminopathy.

Structural Variability After discussing nucleic structure in view of a possible role in AD, we briefly address DG and hippocampal structure in a general context, in view of the average structural parameters and their inter-subject variability, also in the physiological regime. To this end, we have evaluated the average neuron density $\bar{\rho}_n$, the

Parameter (median over subject neuron population)	ALL		AD		CTRL		p^*
	mean	std	mean	std	mean	std	
Electron density ρ ($1/\text{nm}^3$)	320.06	2.00	320.91	2.10	318.77	0.92	0.020
Heterogeneity s ($\cdot 10^{-5}$)	1.30	0.50	1.45	0.50	1.07	0.45	0.165
Volume v (μm^3)	115.46	34.26	101.85	28.31	135.88	34.21	0.073
Sphericity φ	0.950	0.016	0.963	0.015	0.954	0.017	0.278
nn within radius of $13.5 \mu\text{m}$	4.93	1.39	5.44	1.42	4.17	0.983	0.061
Cell density $\bar{\rho}_n$ ($\cdot 10^5$ $1/\text{mm}^3$)	2.32	0.37	2.35	0.46	2.32	0.15	0.842
DG-band width d_{DG} (μm)	32.82	8.44	34.27	9.04	30.54	7.47	0.358
Next-neighbor dist. d_{NN} (μm)	14.29	1.01	13.88	0.95	15.04	0.65	0.009
nn within radius of $13.5 \mu\text{m}$	4.83	1.47	5.18	1.66	4.29	0.95	0.166

Table 4.1: The upper part refers to CB-data and the lower part to PB-data. For each subject, the median of the neuron population was calculated. p -values reflect group differences only with respect to the parameter median, not the entire neuron population, which is probed by OT. d_{NN} is derived from the structure factor maximum. The evaluation of the parameters is detailed in the SI Appendix, Methods, Structural parameters of DG-cell nuclei. NN: number of neighbors, *t-test (Welch).

local density fluctuations ζ_n as an indicator for possible local defects, the average width of the DG band d_{DG} , and the next-neighbor distance d_{NN} . Note that d_{NN} was quantified from the inverse of the peak position of the structure factor, which was computed from the nuclei center-of-mass positions (SI Appendix, Methods, Short-range order of DG-granular cells). The results are summarized in Tab. 4.1. Two observations are noteworthy: First, in contrast to the nucleic structure, the overall spatial distribution of DG-neurons, in terms of density, density fluctuations, and packing does not differ between groups (AD and CTRL), but was found to differ significantly between subjects. As a result of this study, we can now give accurate numbers for the structure of the human DG, notably its width $d_{\text{DG}} = 32.8 \mu\text{m}$, neuron density $\bar{\rho}_n = 2.32 \cdot 10^5 1/\text{mm}^3$, and the next-neighbor distance $d_{\text{NN}} = 14.29 \mu\text{m}$. In addition, we can quantify the inter-subject variance of these quantities. Defining the structural polydispersity for a structural parameter p as $P = \Delta p/p$, we find a surprisingly large value $P = 26\%$ for the width of the DG-band, while for neuron density and next-neighbor distance we have $P = 16\%$ and $P = 7\%$, respectively.

Accessibility and Scalability of PC-CT Finally, we provide a brief note on the accessibility, scalability and possible translation of PC-CT. The capabilities of PC-CT are currently substantially augmented, both in quantity and in quality, at almost all synchrotron radiation (SR) sources worldwide. Upgrades of electron storage ring and X-ray optics, in combination with dedicated beamlines designed for fully robotic sample handling and automated reconstruction will substantially increase resolution, image

quality and sample throughput. Furthermore, the current pandemic is catalyzing mail-in and remote beamtime operation. At the same time, ongoing instrumental progress enables at least partial translation of the method from SR to compact laboratory μ -CT, compatible with clinical use e.g. in the neuropathology units of university medical centers. Both developments will require or can at least significantly benefit from optimized PC-CT reconstruction, segmentation based on machine learning, and data analysis based on OT, as demonstrated here.

4.5 Materials and Methods

Sample Collection and Preparation Human hippocampus tissue was retrieved at routine autopsy in agreement with the ethics committee of the University Medical Center Göttingen. Following the protocol from clinical pathology routine, autopsy dissection blocks from 23 subjects were 10% paraformaldehyde-fixed, dehydrated and paraffin-embedded (FFPE). One FFPE-block measures about $2 \times 3 \times 0.3 \text{ cm}^3$. Following [50], we then classified subjects according to the ABC-score, accounting for (A) β -amyloid plaques according to Thal phases [71], (B) neurofibrillar tangles according to Braak stages [13, 14], and (C) for neuritic plaques according to the CERAD (consortium to establish a registry for Alzheimer’s disease) score [49]. Again following [50], subjects with an AD likelihood “intermediate” or “high” according to the compound ABC-score were classified as AD (11/20 subjects; 2/11 subject data sets were excluded from CB-analysis, as detailed in SI Appendix, Sample collection and preparation). Subjects with an AD likelihood “none” or “low” were classified as controls (7/20 subjects; 1/7 data sets were excluded from CB-analysis, for the same reason as above). For each subject analyzed in Results II: Geometric and Statistical Analysis, the neuropathological findings are listed in SI Appendix, Tab. S1. Note that 2/20 subjects were not assigned to any group due to their diffuse presentation in A, B, and C scores (subjects 12 and 13). For PC-CT analysis, cylindrical samples were then extracted from the FFPE blocks using either a 1- or 8-mm biopsy punch and inserted into polyimide tubes.

Experimental Setup The data presented in this work were recorded at the GINIX holo-tomography endstation of the P10 undulator beamline, Petra III, DESY, Hamburg, Germany [66], at a photon energy of 8.0 or 13.8 keV, selected by a Si(111) channel-cut monochromator. To cover the cytoarchitecture over a wide range of length scales, ranging from entire hippocampus structure in the frontal plane, down to ROIs within

the dentate gyrus at sub-cellular resolution, the instrument’s multiscale capability was used [27], comprising three different optical configurations. First, large FOVs up to about 8-mm were scanned in a beam which was focused by a Kirkpatrick-Baez (KB) mirror system and subsequently broadened by its divergence. This is denoted as EB-configuration. Second, intermediate FOVs up to about 1.5 mm were scanned in a PB-configuration, after moving the mirrors out of the beam path. Finally, small FOVs up to about 0.4 mm were scanned at highest resolution, using a compound optics of KB-mirrors and X-ray WGs (CB-configuration) [9, 74]. By adjusting the distance z_{01} between WG and sample, two different voxel sizes of $px \simeq 160$ nm and $px \simeq 50$ nm were chosen in this configuration, providing further zoom. The different configurations and parameters are further detailed in SI Appendix, Methods.

Reconstruction Projections were first corrected for empty beam and dark images, recorded before and after the tomography scans. Phase retrieval was performed by either the linearized *contrast-transfer-function* (CTF) scheme or the *non-linear Tikhonov* (NLT) algorithm [43]. Both are well-suited for the holographic regime corresponding to image formation at small Fresnel numbers $F = \frac{px^2}{z_{\text{eff}}\lambda} \ll 1$, with wavelength λ , and the effective propagation distance $z_{\text{eff}} = z_{12}/M$. After phase retrieval of the projections, tomographic reconstruction was performed by filtered back-projection (FBP), or a cone-beam (FDK; Feldkamp-Davis-Kress) algorithm, both as implemented in the ASTRA-toolbox [76]. Spatial resolution was determined using Fourier-Shell-correlation (FSC), after applying a Kaiser-Bessel-window of 7 pixels and a half-bit threshold. Based on the image quality metrics, 2/11 AD and 1/7 control CB-datasets were excluded from the analysis to keep the segmentation quality on a similar level for all data sets. Further details are given in SI Appendix, Methods.

Segmentation of DG-cell Nuclei For the PB-data, segmentation of DG-cell nuclei was carried out using the *Blobfinder*-tool of the segmentation and visualization package *Arivis* (Arivis AG). The CB-data were segmented with the interactive software package *Ilastik* [10], and a further manual optimization based on image filters and object removal based on visual control. These segmentations served as ground truth input for machine learning based on convolutional neural networks (CNN) implemented via the *Deep-learning V-net*, which is the three-dimensional generalization of the U-net design [64], as detailed in SI Appendix, Methods, Segmentation of DG-cell nuclei.

Structural Parameters of DG-cell Nuclei For segmented nuclei of the DG-cells, five features were selected for further analysis and computed based on the segmentation mask for each individual: median (over DG-neurons) of the nuclear electron density ρ , normalized nuclear electron density variance $s = \sigma^2 / \bar{\rho}^2$ (heterogeneity parameter), nuclear volume v , nuclear sphericity φ (shape parameter), and number of neighbors nn in a radius of $13.5 \mu\text{m}$, a value selected in between first and second coordination shell of the pair correlation function $g(r)$ [74]. The pairwise similarity (or equivalently distance) between the one-dimensional histograms (separately for each feature, Fig. 4.7) was computed using the *Wasserstein*-metric W of order $p = 2$, as implemented in [69].

Analysis based on Optimal Transport In the Gaussian approximation each individual is represented by a normal distribution $\mathcal{N}(\Sigma, \mu)$ with covariance matrix Σ and mean μ . The Bures metric between two covariance matrices was used as in [26] to construct an optimal transport map between the multi-dimensional normal distributions fitted to the point cloud data. Beyond this Gaussian approximation, point cloud optimal transport plans were also computed with entropic regularization and the Sinkhorn algorithm. Local linearization of the optimal transport metric is performed as described in [77], including the approximate extraction of an optimal transport map from the optimal transport plan between two point clouds. In the Gaussian approximation, the optimal transport center of mass (“barycenter”) was used as a reference for linearization, which can be computed efficiently with the fixed-point algorithm of [3], and also serve as a basis to sample 10^4 points from Gaussian distribution for point cloud analysis. Linear SVM-classification was performed with the implementation of [57]. Full details are given in SI Appendix, Methods, Analysis based on optimal transport.

Acknowledgments

We thank Michael Sprung, Markus Osterhoff and Bastian Hartmann for support at GINIX, and Thomas Jentschke and Jakob Frost for help with segmentation. Support by the Deutsche Forschungsgemeinschaft (DFG) (German Research Foundation) under Germany’s Excellence Strategy - EXC 2067/1-390729940 *Multiscale Bioimaging* and the German Federal Ministry of Education and Research through Grant 05K19MG2 *NeuroTomo* is gratefully acknowledged. J.F. and C.S. acknowledge funding by DFG

(TRR274-1) and the associated clinician scientist program.

There are no competing interests to declare.

4.6 SI Appendix

Sample Collection and Preparation Human hippocampus tissue was retrieved at routine autopsy in agreement with the ethics committee of the University Medical Center Göttingen. Following the protocol from clinical pathology routine, autopsy dissection blocks from 23 subjects (13 subjects for DG-samples only, 2 for CA1-samples only, 6 for DG- and CA1-samples, 1 for DG-, CA1- and WM-samples, and 1 subject for GM-sample; in total resulting in 20 DG-samples, 4 CA1-samples, 1 WM- and 1 GM-sample) were 10% PFA-fixed, dehydrated and paraffin-embedded (FFPE). One FFPE-block measures about $2 \times 3 \times 0.3 \text{ cm}^3$. Tab. 4.1 lists the sample numbers with neuropathological staging. Tissue of one further patient has been 10% PFA-fixed and stored in PBS, *i.e.* has not been dehydrated and paraffin-embedded, for hydrated examination (cf. Fig. 4.14). For PC-CT, cylindrical samples were extracted using either a 1 or 8 mm-biopsy punch and inserted into polyimide tubes. A note on the number of DG-samples: during the analysis of CB-data from DG-samples, 3/20 needed to be excluded since the corresponding tomographic acquisitions yielded inferior data quality and the automated segmentation quality was hence not on a comparable level (this concerns subjects 4, 9 and 20), while this was not necessary for PB-data, which is much more robust against beam fluctuations.

Neuropathological Staging Patients were diagnosed as AD patients following post-mortem analysis according to [13, 49, 50, 71]. Intraneuronal tangles as well as dystrophic neuritic plaques were analyzed in hippocampal, temporal, frontal and occipital sections stained with a phospho-tau antibody (monoclonal mouse at8, Thermo Fisher Scientific, 1:100, pretreatment steamer + citrate pH 6). The same hippocampal blocks were used for neuropathological staging and PC-CT. For staging of plaques, Bielschowsky silver impregnation and an amyloid-beta staining (monoclonal mouse anti amyloid-beta, 6E10, Zytomed Systems GmbH, 1:500 after pretreatment with formic acid, steamer + citrate pH 6) were performed. Following [50], we then classified patients according to the ABC-score, accounting for β -amyloid plaques according to Thal phases [71] (A), neurofibrillar tangles according to Braak stages [13, 14] (B), and for neuritic plaques according to the CERAD score [49] (C). The overall ABC-score is then

Subject no.	Age	Thal phase	A	Braak stage	B	CERAD score	C	CAA	ABC-based scoring	Group	Sex	PC-CT analysis of...
1	82	3	A2	3	B2	sparse	C1	1	intermediate	AD	f	DG
2	71	4-5	A3	5	B3	frequent	C3	0	high	AD	m	DG & CA1
3	74	3	A2	6	B3	moderate	C2	1	intermediate	AD	f	DG
4	84	3	A2	4	B2	sparse	C1	0	intermediate	AD	m	DG*
5	66	4-5	A3	6	B3	frequent	C3	1	high	AD	m	DG
6	72	3	A2	6	B3	moderate	C2	0	intermediate	AD	m	DG & CA1
7	83	1-2	A1	5	B3	moderate	C2	1	intermediate	AD	f	DG
8	91	4-5	A3	6	B3	frequent	C3	1	high	AD	m	DG
9	70	3	A2	5	B3	moderate	C2	1	intermediate	AD	f	DG*
10	62	4-5	A3	4	B2	moderate	C2	0	intermediate	AD	f	DG
11	87	3	A2	5	B3	sparse	C1	1	intermediate	AD	f	DG
12	86	0	A0	5	B3	not	C0	1	not	-	m	DG & CA1
13	87	1-2	A1	4	B2	not	C0	0	low	-	f	DG
14	84	0	A0	2	B1	not	C0	0	not	CTRL	f	DG
15	77	3	A2	2	B1	not	C0	0	low	CTRL	m	DG
16	74	1-2	A1	2	B1	not	C0	0	low	CTRL	f	DG & CA1
17	71	1	A1	1	B1	nd	nd	nd	N-L	CTRL	m	DG & CA1
18	65	0	A0	1	B1	not	C0	0	not	CTRL	m	DG
19	83	3	A2	1	B1	sparse	C1	0	low	CTRL	m	DG
20	82	0	A0	2	B1	not	C0	0	not	CTRL	m	DG* & CA1
21	91	4-5	A3	5	B3	moderate	C2	0	intermediate	AD	m	CA1
22	37	0	A0	1	B1	sparse	C0	0	not	CTRL	m	CA1

Table 4.1 (previous page): Sample list for neuropathological analysis: Columns give the assignment of sample numbers in the manuscript, the age, the A ($A\beta$ plaque score), B (NFT stage) and C (Neuritic plaque score), with the Thal phases [71], the Braak stage [13] and the CERAD score [49], respectively, the cerebral amyloid angiopathy (CAA) and the overall ABC-score according to [50], as well as the group assignment based on ABC and finally, which hippocampal region has been analyzed from the respective subject. * marks the CB-data sets which have been excluded from analysis, nd = not determined.

evaluated in terms of an AD likelihood based on a logic matrix with the individual entries, as defined in [50]. In this work, patients with a AD likelihood “intermediate” or “high” according to the compound ABC-score were classified as AD patients, again following [50]. One subject showed an amyloid pathology with cerebral amyloid angiopathy only while another subject displayed tau pathology only, with almost no amyloid depositions (subjects 12 and 13, respectively). Both are not assigned to any group. All results of the neuropathological staging are tabulated Tab. 4.1.

Experimental Setup The data presented in this work were recorded at the GINIX holo-tomography endstation of the P10 undulator beamline, Petra III, DESY, Hamburg [66], at a photon energy of 8.0 and 13.8 keV, selected by a Si(111) channel-cut monochromator. The beamline’s high brilliance $> 10^{21}$ ph/s mrad² mm² (0.1% BW) [7], and correspondingly high coherence, enables coherent nano-focusing, and hence high-resolution phase-contrast recordings in the holographic regime, as well as high-contrast and fast parallel-beam acquisitions. In order to cover the cytoarchitecture over a wide range of length scales, ranging from the entire hippocampus structure in frontal plane, down to regions-of-interest (ROIs) within the dentate gyrus at sub-cellular resolution, the instrument’s multiscale capability was used [27, 62], comprising three different optical configurations which are illustrated in Fig. 4.9. First, large field-of-views (FOVs) of up to about 8 mm were scanned in a beam which was focused by a Kirkpatrick-Baez (KB) mirror system and subsequently broadened by its divergence. This is denoted as expanded beam (EB) configuration. Second, intermediate FOVs of up to about 1.5 mm were scanned in a parallel beam (PB) configuration, after moving the mirrors out of the beam path. Finally, small FOVs of up to about 0.4 mm were scanned at highest resolution, using a compound optics of KB-mirrors and X-ray waveguides (WG) [9, 74] (cone-beam configuration, CB). By adjusting the distance z_{01} between WG and sample, two different voxel sizes of $px \simeq 160$ nm and $px \simeq 50$ nm were

chosen in this configuration, providing further zoom. The reconstructed volumes of all recordings could be precisely registered with respect to each other, enabling a zoom into specific ROIs. The three configurations with their respective optical components, detector technologies, and tomographic acquisition schemes are presented in Tab. 4.2, and described in more detail below.

EB-Configuration X-rays were focused by Kirkpatrick-Baez (KB) mirrors onto a $3\text{ }\mu\text{m}$ pinhole, fabricated by focused-ion-milling, and acting as a spatial filter. This helped to suppress the stripe artifacts typically associated with the KB-farfield [62]. The sample stage was installed in the expanded beam at $z_{01} \approx 5.1\text{ m}$ behind the focus. The projections were recorded with a sCMOS detector (pco.edge, Optique Peter, $50\text{ }\mu\text{m}$ -LuAg-scintillator, $6.5\text{ }\mu\text{m}$ physical pixel size and $2\times$ interchangeable lenses) at a position of $z_{02} \approx 5.4\text{ m}$. This configuration was used for PC-CT measurements of a 8 mm cylindrical tissue sample, covering the characteristic anatomical regions, notably the DG and the CA. The sample fit entirely into the FOV $8.3\text{ mm}\times 6.7\text{ mm}$. Data from this configuration are presented in Fig. 1(c), where the CA1-4 fields, the DG, WM and further GM as well as vasculature can be clearly identified.

PB-Configuration After removing the KB-mirrors, the pinhole, as well as various foils and windows of the beamline [27], the parallel undulator beam was used for PC-CT (Fig. 4.9). The sample was installed on a fully motorized tomography stage with air bearing (UPR-160 Air, Micos, Germany). Given the accuracy and reproducibility of the rotation, it was possible to acquire projections in a continuous scan, *i.e.* projections with a short exposure time were taken during continuous rotation of the sample [27]. 1501 projections were acquired at a propagation distance $z_{12} = 220\text{ mm}$ with an acquisition time of 0.035 s , using the microscope camera system described above with the $10\times$ objective. This resulted in a FOV of $1.7\text{ mm}\times 1.3\text{ mm}$ at $0.65\text{ }\mu\text{m}$ voxel size. This configuration was used both for punch biopsies of 1 mm diameter covered in a single scan, as well as to map multi-mm sized tissue samples by stitching and merging of several individual tomograms (Fig. 2).

CB-Configuration For cone-beam (CB) PC-CT with high spatial resolution, the beam was focused by KB-mirrors to approx. $310 \times 320\text{ nm}^2$, and coupled into an X-ray waveguide (WG) for further reduction of beam size, and for coherence and wavefront filtering. The waveguides consist of empty channels (10^2 nm lateral entrance/exit

width) fabricated by e-beam lithography and wafer bonding [29, 39, 54, 65]. At low-E X-rays (*i.e.* ≤ 8 keV), a WG with a 1 mm-guiding layer consisting of Si was selected, at high-E X-rays (≥ 13.8 keV), Ge was chosen with 0.2 mm depth; see also Tab. 4.2 for specifications of the WG-systems. The WG provides a secondary source of sub-50 nm spot size, and a beam with high spatial coherence and a smooth wavefront, which is decoupled from upstream optical components of the beamline. The geometric magnification of $M = \frac{z_{02}}{z_{01}} \approx 41$, or $M \approx 132$, respectively, was adjusted by the motorized sample tower (same as PB-configuration). Projections were recorded with a fiber-coupled sCMOS Camera (Zyla 5.5 HF, Andor) positioned at $z_{02} \approx 5.1$ m, with 2560×2160 pixels of $6.5 \mu\text{m}$ pixel size, and $15 \mu\text{m}$ -Gadox-scintillator. Biopsy punches of 1 mm cross section were scanned with a FOV of $0.4 \text{ mm} \times 0.4 \text{ mm}$ and a voxel sizes of approx. 160 nm (values for $M \approx 41$), which allowed investigations with sub-cellular resolution, regarding in particular the structure of the DG-cell nuclei (cf. Fig. 2(b & c)).

Phase Retrieval and Object Reconstruction Phase retrieval has been carried out after correcting for empty-beam and dark images, recorded before and after the tomography scans. For the EB-configuration, empty-beam recordings were analyzed by *principal component analysis* (PCA) prior to flat-field correction [62]. Phase retrieval was performed by either the linearized *contrast-transfer-function* (CTF) scheme or by the *non-linear Tikhonov* (NLT) algorithm [43]. Both are well-suited for the holographic regime corresponding to image formation at small Fresnel numbers $F = \frac{px^2}{z_{\text{eff}}\lambda} \ll 1$, with wavelength λ , and the effective propagation distance $z_{\text{eff}} = z_{12}/M$. For homogeneous objects with coupled ratio $\frac{\delta}{\beta}$ of the decrements of the index of refraction $n = 1 - \delta + i\beta$, the phase Φ in the object plane is obtained from the flat-field corrected projections I_{exp} by [19, 75, 79]

$$\Phi(\vec{r}_{\perp}) = \mathcal{F}_{\perp}^{-1} \left(\frac{\sum_{n=1}^N \xi_n \cdot \mathcal{F}_{\perp} (I_{\text{exp}}(\vec{r}_{\perp}, z_n) - 1)}{\sum_{n=1}^N 2 \cdot \xi_n^2 + \alpha(\vec{k}_{\perp})} \right),$$

$$\xi_n = \sin(\chi_n) + \frac{\delta}{\beta} \cos(\chi_n),$$

where \vec{r}_{\perp} denotes the position vector in the object plane, and \vec{k} the squared spatial frequency in natural units $\chi_n = \frac{\lambda_n z_n k_{x,y}^2}{4\pi}$. In phase retrieval, the optical property of the tissue $\frac{\delta}{\beta}$ is treated as an effective parameter, chosen based on inspection. The

zero-crossings of the denominator are regularized by the function $\alpha(\vec{k}_\perp)$. To further stabilize phase retrieval, multiple datasets ($N = 2-4$) at different, carefully chosen χ_n were recorded, based on variation of z_{01} . When the linearization inherent in CTF-reconstruction failed, we utilized the iterative NLT-algorithm which can be regarded as a non-linear generalization [43]. In fact, the NLT was used for most of the data collected in CB-configuration, in particular the entire scan series used for the statistical DG-analysis. After phase retrieval of the projections, tomographic reconstruction was performed by filtered back-projection (FBP), or a cone-beam (FDK) algorithm, both as implemented in the ASTRA-toolbox [1, 56, 76]. Post-processing included a ring-filter step as in [36] (“additive”/“A” approach) or [52] (“wavelet”/“W”). Alternatively, in the datasets of PB-configuration which encompassed full 360°-scans, ring-artifacts were treated by respective “replacement” (“R”). Spatial resolution was determined using Fourier-Shell-correlation (FSC) [16], after applying a Kaiser-Bessel-window of 7 pixels and a half-bit threshold. If desired, gray values could be converted to electron density ρ ($\text{e}^-/\mu\text{m}^3$) using tabulated values [34] as detailed in [63], based on the X-ray energy and the fact that the tissues were fully penetrated by paraffin ($\text{C}_{30}\text{H}_{62}$, 0.9 g/cm^3 , $\rho \approx 3.1 \cdot 10^2 \text{ nm}^{-3}$, under the assumption that the maximum of the tomographic gray value histogram can be assigned to the impregnation material). Based on the image quality metrics, 2/10 AD subjects and 1/10 control CB-datasets were excluded from the analysis to keep the segmentation quality on a similar level for all data sets (subjects 4, 9 and 20).

Segmentation of CA1-neurons Segmentation of pyramidal neurons in the CA1-region required a segmentation algorithm compatible with low contrast and variable cellular morphology. At the same time, there was not sufficient data available for the deep learning approach, as used for the DG-cell nuclei. We therefore turned to the *Chan-Vese level-set* algorithm [18], which determines the object contour (mask) based on minimizing an energy functional, including contributions due to gray value deviations from the average values in- and outside the object, its surface and its volume. In this work, the python level-set implementation of the *simple insight toolkit* [44] was used.

Segmentation of DG-Cell Nuclei For the PB-data, segmentation of DG-cell nuclei was carried out using the *Blobfinder*-tool of the segmentation and visualization package *Arivis* (Arivis AG). To this end, the *Draw Object*-tool was first used to roughly restrict the ROI to the DG. The *Blobfinder* was then applied to this volume (diameter: $7.2 \mu\text{m}$,

probability threshold: 18.3%, split sensitivity: 30.9%). Subsequently, the *Feature Filter* was used to remove objects of size ($\leq 2.5 \cdot 10^3 \mu\text{m}^3$), sphericity (≤ 0.25) or intensity. Finally, a python script was written to remove cells outside the DG-band based on criteria involving next-neighbor distances.

The CB-data, in which the DG-cell nuclei are much better resolved, required a more detailed object mask, retrieved as follows: First, four datasets were segmented with the interactive software package Ilastik [10], and a further manual optimization based on image filters and object removal based on visual control. These segmentations served as ground truth input for machine learning based on convolutional neural networks (CNN) implemented via the *Deep-learning V-net*, which is the three-dimensional generalization of the U-net design [64]. Starting with the segmentations of the four datasets, the V-net has been trained in several passages to introduce revised ground truth data: output probability maps were thresholded (individually for each sample), fine-tuned (manually), and used as revised ground truths. In this work, three passages were conducted: in passage (1) three data sets have been used for training and one for validation, in (2) four for training and two for validation, in (3) six for training and two for validation. Overall, the V-net architecture from [48] was adapted. The Adam optimizer together with the dice loss function was monitored in the training procedure to cope with the class imbalance between cell and background voxels. In order to account for differences in image quality, data augmentation was applied. Training was carried out on a single NVIDIA Quadro RTX 8000. To fit the GPU memory, data sets were rebinned to a size of 512^3 voxels, from which single subvolumes of 256^3 voxels were used for both training and validation data, resulting in a binary dice coefficient on the validation set of 81%.

Note that for the volume rendering of the DG-band and β -amyloid plaques in Fig. 1(d), data segmentation was solely based on the Ilastik software.

Computation of Local Cell Density Using the segmentation masks, each single object (*i.e.* cell nucleus) was identified and represented by its center-of-mass (COM). The resulting 3d-array M_p hence has non-zero entries only at the COM positions. The local density on a given coarse-graining scale r was then computed by convolution between COM-positions and a sphere with radius r . The local density at any point is proportional to the number of spheres reaching this point and the volume of the test sphere. To avoid artifacts from sharp interfaces, the spheres were smoothed by Gaussian filtering. Denoting the smoothed sphere (convolution kernel) as M_r , the convolution is implemented in Fourier space based on multiplication of the Fast Fourier

transforms (FFT) of M_p and M_r . The cell density ρ_{pr} (objects per volume element) in real space is then obtained by the inverse FFT followed by a proper normalization, which can be written as

$$\rho_{pr} = \frac{1}{px^3} \cdot \frac{\Re(\mathcal{F}^{-1}(\mathcal{F}(M_p) \cdot \mathcal{F}(M_r)))}{\Re(\mathcal{F}^{-1}(\mathcal{F}(J) \cdot \mathcal{F}(M_r)))},$$

where J denotes an array of ones of the same size as M_p , $\mathcal{F}(\cdot)$ denotes the Fast Fourier transform, and $\Re(\cdot)$ extracts the real part of a complex argument. For the PB data, a radius $r = 52 \mu\text{m}$, was chosen. This workflow has been adapted from [74].

Short-Range Order of DG-Granular Cells Apart from cell density and the shape of the DG-band, the local short range order of granule cells can be analyzed, similar to structural analysis of liquids or amorphous solids in condensed matter. Such an approach based either on the pair-correlation function $g(r)$ or its Fourier transform given by a structure factor $S(q)$ was already adapted in [74] for the granule layer of human cerebellum. Here, we used the structure factor

$$S(\mathbf{q}) = \left\langle \frac{1}{N} \cdot \left| \sum_{j=1}^N e^{i\mathbf{q} \cdot \mathbf{p}_j} \right|^2 \right\rangle_{\phi, \theta},$$

computed for an array of points \mathbf{q} in Fourier space (scattering vectors) based on the spatial COM coordinates \mathbf{p} of the DG-cell nuclei (segmentation masks of PB-data), with the total number of cells N . After radial averaging in \mathbf{q} -space, the structure factors $S(\mathbf{q})$ are presented in Fig. 4.11(g). Solid lines (red, green) are given by the group-wise (AD, CTRL) median, with half-transparent areas covering the 1σ -intervals of each group.

Structural Parameters of DG-Cell Nuclei For segmented nuclei of the DG-cells, five features were selected for further analysis, and computed based on the segmentation mask for each individual: median (over DG-neurons) of the nuclear electron density ρ , normalized nuclear electron density variance $s = \sigma^2/\bar{\rho}^2$ (heterogeneity parameter), nuclear volume v , nuclear sphericity φ (shape parameter), and number of neighbors nn in a radius of $13.5 \mu\text{m}$, a value selected in between first and second coordination shell of the pair correlation function $g(r)$, see also [74]. The pairwise similarity (or equivalently distance) between the one-dimensional histograms (separately for each feature, Fig. 6) was computed using the 1d-Wasserstein metric W of

order $p = 2$, as implemented in [69]. In addition, we also computed distances based on the *Kullback-Leibler-Divergence* (*KLD*), defined as [11, 41, 61].

$$KLD[h(\beta)||h(\alpha)] = \sum_{i=1}^N h(\beta_i) \log \left(\frac{h(\beta_i)}{h(\alpha_i)} \right) .$$

In most cases, this yielded similar results, but with the additional problem of the *KLD* being ill-defined for zero values of the discretized probability distributions (zero bins). The metrics/measures were applied to each two histograms $h(\alpha)$, $h(\beta)$ with $N = 70$ bins resulting from $\sim 10^4$ objects per subject and feature. Also note that $h(\alpha)$ and $h(\beta)$ have been normalized prior to input.

Furthermore, based on the PB-datasets which span a much larger FOV than the CB, further parameters have been computed and are presented in the lower part of Tab. 1 in the main article. These parameters concern the overall DG-band structure, and not single DG-cells. (i) From the 3d local cell density masks (defined in the SI Appendix, Methods, “Computation of local cell density”), median and standard deviation of the local cell density are denoted by $\bar{\rho}_n$ and ζ_n , respectively. ζ_n is also referred to as “local density fluctuations”, and is an indicator for possible local defects. (ii) The DG-band width d_{DG} of each data set is based on the binary 3d-mask of the DG, to which then a distance analysis tool has been applied: for each voxel within the DG, this yields the distance to the closest voxel outside the DG. The central line, extracted by skeletonization, indicates the local thickness, from which the median is computed to obtain d_{DG} . (iii) Analysis of the structure factor (see SI Appendix, Methods “Short-range order of DG-granular cells”) yields the next-neighbor distance d_{NN} .

Presentation of Gaussian Ellipsoids The point clouds in n dimensions (nd) were described by nd ellipsoids, obtained as follows: the $n \times n$ -covariance matrix and the respective nd -vector of mean values were obtained for a given point cloud. An ellipsoid was then centered around the mean (or equivalently the COM) of the point cloud, with ellipsoidal half axes (magnitude and directions) given by the eigenvectors of the covariance matrix (square root of eigenvalue and unit eigen vector). This is equivalent to least-square fitting to a multi-dimensional Gaussian distribution, with standard deviation (1σ -interval) represented by the half axes of the ellipsoids. The graphical functions were implemented with MATLAB functions presented in [60].

Analysis based on Optimal Transport In the Gaussian approximation each individual is represented by a normal distribution $\mathcal{N}(\Sigma, \mu)$ with covariance matrix Σ and mean μ . The Bures metric between two covariance matrices is given by [15, 26]

$$\mathcal{B}(\Sigma_\alpha, \Sigma_\beta) = \sqrt{\text{tr} \left(\Sigma_\alpha + \Sigma_\beta - 2 \left(\Sigma_\alpha^{1/2} \Sigma_\beta \Sigma_\alpha^{1/2} \right)^{1/2} \right)},$$

and the L^2 -optimal transport distance between two normal distributions $\mathcal{N}(\Sigma_\alpha, \mu_\alpha)$ and $\mathcal{N}(\Sigma_\beta, \mu_\beta)$ can be expressed as [58]

$$\mathcal{W}_2^2(\alpha, \beta) = \|\mu_\alpha - \mu_\beta\|^2 + \mathcal{B}(\Sigma_\alpha, \Sigma_\beta)^2,$$

the optimal transport map from α to β is given by

$$T_{\alpha, \beta} : x \mapsto \mu_\beta + \Sigma_\alpha^{-1/2} \left(\Sigma_\alpha^{1/2} \Sigma_\beta \Sigma_\alpha^{1/2} \right)^{1/2} \Sigma_\alpha^{-1/2} \cdot (x - \mu_\alpha).$$

For point clouds, optimal transport plans between the normalized empirical measures were computed with entropic regularization and the Sinkhorn algorithm using the implementation of [68], with a final regularization parameter of $\varepsilon = 10^{-6}$ and a plan threshold of 10^{-10} which results in high quality approximate solutions where the scale of entropic blur is considerably below the typical nearest neighbour distance of the point clouds. Local linearization of the optimal transport metric is performed as described in [77], including the approximate extraction of an optimal transport map T from the optimal transport plan between two point clouds. In the Gaussian approximation, the optimal transport center of mass (“barycenter”) was used as reference for linearization, which can be computed efficiently with the fixed-point algorithm of [3]. For point clouds we sampled 10^4 points from the Gaussian barycenter as an approximate reference point. SVM-classification was done with the implementation of [57]. Note that we only used a *linear* (i.e. without kernel functions) SVM on four PCA-modes to avoid any risk of overfitting. Our main motivation was to extract a robust discriminating axis that lends itself to subsequent medical interpretation.

SI Additional Datasets and Analysis

DG-Cell Nuclei Fig. 4.10 presents additional plots on the statistical analysis of DG-cell nuclei (CB-data). This includes the histograms (violin plots) shown in (a) for the structural parameters (“features”) volume v , sphericity φ and next neighbors nn

within a radius of $13.5\ \mu\text{m}$, which are not shown in the main manuscript, for reasons of space restrictions. In (b), a correlation matrix is presented showing the correlation between any two elements of the set of features, for all subjects. Noteworthy are a positive correlation between density and volume ρ & v , and a negative one between heterogeneity and sphericity s & φ , *i.e.* large nuclei tend to be denser, and nuclei with larger heterogeneity (higher heterochromatin-to-euchromatin-ratio) tend to be more elongated and hence less spherical. These correlations are observed for all subjects. In (c), the “distance charts” (Wasserstein-metric, W) between individuals are shown for all features except ρ , which had already been included in the main manuscript. These heatmaps again convey the large inter-subject variation within and across groups. This is further quantified by the corresponding plots of W -values (for each feature), computed for single individuals with respect to their entire group population. For the heterogeneity parameter s , the in-control-group distances are found to be significantly smaller than distances involving AD-data. A similar trend is found for the sphericity φ and the packing parameter nn , where the distances within the CTRL-group are smaller than for the AD- or the cross-group case. Finally, (e) shows a graph representation [25] of distances based on the Bures-cost \mathcal{W} . Note that on the group-level, as shown in the main manuscript, the distances are better revealed when all features are treated jointly in the five-dimensional feature space, as quantified here by \mathcal{W} .

Next, Fig. 4.11 presents statistical analysis of DG-cell nuclei, as segmented in the large volume reconstructions obtained by the PB-configuration. The larger field-of-view (FOV) results in a larger section of the DG-band which can be captured. Hence, in particular the width of the DG-band d_{DG} and its standard deviation d_{σ} , as well as the local “packing” parameter nn can be well-assessed from this data. In (a), the corresponding box-whisker plots are shown. The width of the DG-band is slightly widened, but does not significantly change in the AD-group with respect to CTRL. Interestingly, nn seems much more tightly controlled in the CTRL-group, *i.e.* the physiological regime, while the dispersion of nn values is much higher in the AD-group, *i.e.* the local ordering differs substantially between members of this group. In (b), the feature histograms are presented for all patients in form of a violin plot. Since the larger FOV compared to CB-configuration comes at cost of resolution, a segmented nucleus is now sampled by much fewer voxels, and the structural features within the nuclei are no longer well-assessed. In particular, we cannot expect the variance in electron density, *i.e.* the heterogeneity parameter s , to capture the sub-structure of the nucleus. Also, volume v and sphericity φ can be extracted only with much higher sampling errors. The corresponding “sampling artifact” also introduces bias in

estimating v and φ , as can be seen by comparison with the high-resolution CB-data which can be regarded as “ground truth”. This may also affect the correlation plot of v , φ and s , which are shown in (c), and the corresponding W -metric, calculated for 1d-feature distributions between each two individuals as shown in (e), and presented as box-whisker-plots for inter- and intra-group behavior, see (d). Contrarily, the results of ρ and nn, also depicted in (d-e), can be considered robust with respect to sampling. Here we note that in particular, the distances (W) within the CTRL-group are much smaller than within the AD-group or across groups, again indicating a much more tightly controlled parameter nn in the physiological regime, and a possible positional disordering effect of DG-neurons in AD. The smaller distances between patients of the CTRL-group is confirmed by the distance chart shown in (f), presenting the 5d Bures-cost \mathcal{W} . However, we have to keep in mind that also poorly sampled features contribute here. In (g) more analysis is included on the local packing. Instead of counting the number of neighboring neurons (nuclei) within a certain shell, as for the definition of nn, we now ask for the typical distance distribution of neighbors, as described by a structure factor $S(\mathbf{q})$ computed from the nuclear positions, see SI Appendix, Methods above. Compared to CTRL, the AD-curve shows a broader dip and a less prominent peak, indicative of a reduced short range order of nuclear positions. In addition, the AD-group exhibits larger inter-subject variation, as illustrated by the shaded 1σ -intervals, again underlining a tighter control of DG-structure in CTRL than in AD.

Cornu Ammonis 1 Fig. 4.12 summarizes the analysis of pyramidal neurons in the CA1-region. *Post mortem* biopsy punch samples from 8 different subjects were scanned: 3 subjects diagnosed with AD (based on ABC-score; subjects 2, 6 and 21, aged 78 ± 11 years), 4 subjects of the control group (subjects 16, 17, 20 and 22, aged 66 ± 20 years), and a further sample (subject 12). For this purpose, all samples were collected from the same location within the hippocampus. The segmentation of neurons was carried out as detailed in SI Appendix, Methods. The segmentation quality is illustrated in Fig. 4.12(a). Here, gold-rendered structures mark voxels included in the segmentation mask. In (b), histograms for the same structural features as for the DG-analysis in the main text were evaluated: (1) median of electron density ρ ($\text{e}^-/\mu\text{m}^3$), (2) its relative variance $s = \sigma^2/\bar{\rho}^2$, (3) object volume v and (4) sphericity φ , as well as (5) number of neighboring neurons nn within a radius of $120 \mu\text{m}$. Fig. 4.12(c) illustrates the correlations between different features. For example, in all subjects, smaller volume of the pyramidal neurons correlates negatively with sphericity. Visual inspection of

the histograms in (b) may indicate a slight group-specific segregation for φ and nn. This is corroborated, when taking the distances between the entire feature histograms into account (W), either in form of the distance chart (Fig. 4.12(d)), or by comparing distances for single individuals with respect to their overall group distribution (Fig. 4.12(e)). Again, φ and nn show a marginally significant pattern, while the other features are dominated by the inter-subject variation with no significant effect on the group level. Fig. 4.12(f) and (g) illustrate the Bures-cost, taking all features into account. While this completes the analysis, we must be cautious about drawing conclusions here, since only 3-4 subjects of each group have been measured, and including a younger patient (aged 37 years). Further, datasets have been recorded at slightly different configurations, in particular regarding the X-ray energy and WG-optics, which may result in different image quality.

Multiscale Implementation The multiscale implementation presented in the main article includes the stitching of many individual tomographic scans. For completeness, Fig. 4.13 presents a full slice through the entire 7×7 tomographic reconstructions (stitched) covering the entire 8 mm cylindrical punch of hippocampal tissue recorded in PB-configuration.

Hydrated Tissue While formalin-fixed paraffin-embedded (FFPE) tissue which is the standard in histology and pathology has been used for this work, we have also explored the image quality for hydrated (PBS), formalin-fixed tissue. Fig. 4.14 shows a corresponding reconstruction (CA1-region, CTRL-group, CB-configuration). While the noise is higher than for FFPE-preparation, we can still well recognize cellular bodies, nuclei and apical dendrites of the pyramidal neurons. Interestingly, tissue gaps around neurons are also observed at this stage of sample preparation, without any tissue dehydration or paraffin embedding.

Translation to Laboratory μ CT In view of future applications of the approach presented here for neuro-pathology it is important to know to which extent PC-CT can be translated to laboratory μ CT instrumentation, more readily available in a clinical setting. Fig. 4.15 shows reconstructions from laboratory datasets, acquired with a μ PC-CT setup [8, 72]. X-rays were generated by a liquid-metal jet source (Excillum Inc.) with $K_{\alpha, \text{Ga}} = 9.5$ keV. The sample and detector stages were fully motorized. Scans were recorded in two different configurations, serving a multiscale implementation:

Overview scans with $7.7 \times 9.7 \text{ mm}^2$ FOV and $px = 5 \text{ }\mu\text{m}$, were realized using a DEXELA flat panel CMOS detector ($150 \text{ }\mu\text{m}$, $75 \text{ }\mu\text{m}$ pixels) and large magnification ($z_{01} = 121 \text{ mm}$, $z_{02} = 1.82 \text{ m}$). In this configuration, the X-ray source was operated at 70 kV, 100 W, and $9 \times 9 \text{ }\mu\text{m}^2$ source spot size (circular). 1201 projections were recorded over 185° , each with $5 \times 1 \text{ s}$ acquisition time. For the high-resolution configuration, the sample stage was moved to $z_{01} = 158 \text{ mm}$, and a Rigaku XSight Micron detector (lens-coupled CCD, $10\times$ optics, $5.5 \text{ }\mu\text{m}$ pixels) was installed at $z_{02} = 193 \text{ mm}$, resulting in a FOV of $1.2 \times 1.6 \text{ mm}^2$ and $px = 0.46 \text{ }\mu\text{m}$. Source settings were adjusted to 40 kV, 57.7 W, and $10 \times 10 \text{ }\mu\text{m}^2$ source spot size (circular). In this configuration, 1001 projections over 181° with 1 s were acquired. Phase retrieval was performed with *Modified-Bronnikov algorithm (MBA)* [32, 33] and *Bronnikov-Aided correction (BAC)* [23]. For overview scans, $\alpha = 0.025$, $\gamma = 1$ and for high-resolution scans, $\alpha = 0.005$ and $\gamma = 1$ were chosen. Further data processing was carried out as presented in the main text, *i.e.* with the wavelet ring correction in overview scans and the additive filter in high-resolution, followed by FDK-based tomographic reconstruction.

Configuration	EB	PB	CB
X-ray optics	KB & pinhole	-	KB & Waveguide (Si/Ge)
Detector	sCMOS with 50 μm -LuAg-scin., 2 \times optics	sCMOS with 50 μm -LuAg-scin., 10 \times optics	sCMOS with 15 μm -Gadox-scin.
z_{02} / z_{01} (mm)	5400 / 5060	220 / 88 $\cdot 10^3$	5100 / 125 = $M \approx 41$ or 5100 / 40 = $M \approx 128$
FOV $h \times v$ (mm ²)	8.3 \times 6.7	1.7 \times 1.3	0.4 \times 0.4 or 0.13 \times 0.13
px (μm)	3.06	0.65	0.162 or 0.051
F	0.3240	0.0220	0.0013 or 0.0008
Number of projections	1 \times 2000	1 \times 1500	1-4 \times 1501
Number of empty-beam projections	100	150	1-4 \times 2 \times 100
Exposure time per projection (s)	1	0.035 (cont.)	≤ 1

Table 4.2: Optical configuration and parameters for multiscale PC-CT.

Configuration	EB	PB			CB		
Energy (keV)	13.8	13.8	8.0	8.0	13.8	8.0	14.8
px (μm)	3.06	0.65	0.65	0.123	0.167	0.200	0.051
Phase retrieval *	CTF (1)	CTF (1)	CTF (1)	CTF (1/3)	CTF (4)	NLT (1)	NLT (4)
δ/β	20	33	30	35 / 50	35	130	115
Tomography	FBP	FBP	FBP	FBP	FDK	FBP	FBP
Ring removal	W	A	R	A/W	A	A/W	A
FSC (μm)	6.4	4.2**	1.6	0.963	0.385	1.268	0.219
Fig.	1(c)	2(a)	-	-	5	2(c)	2(d)

Table 4.3: Phase retrieval and reconstruction parameters. * number of measurement planes, ** local tomography (8 mm-biopsy punch).

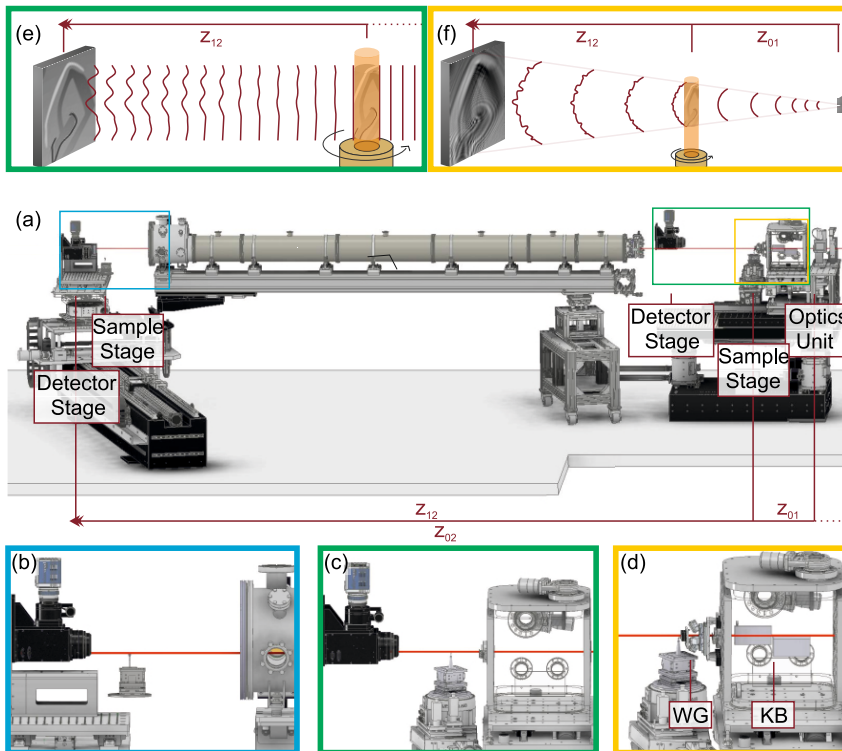


Fig. 4.9: Schematics of the setups. (a) Overview of the GINIX-endstation for multiscale PC-CT: direction of X-rays travel is from right to left. Depending on the configuration (marked by colored boxes), either of two sample and detector stages is utilized. (b) In EB-configuration, the stages installed further downstream are used. Note that the optics unit - not shown in this zoom-in - shapes the beam via the KB-mirrors and a pinhole. (c) In PB-configuration, optics from the optics unit are removed, and the upstream stages are inserted. (d) In CB-configuration, again KB-mirrors focus the X-rays onto a CB. The sample installed at the upstream sample stage is imaged with the camera > 5 m downstream. (e & f) Schematics of the X-rays free-space propagation: image formation in (e) parallel-beam geometry as in (c), (f) cone-beam geometry leading to effective geometrical magnification as exploited in (d).

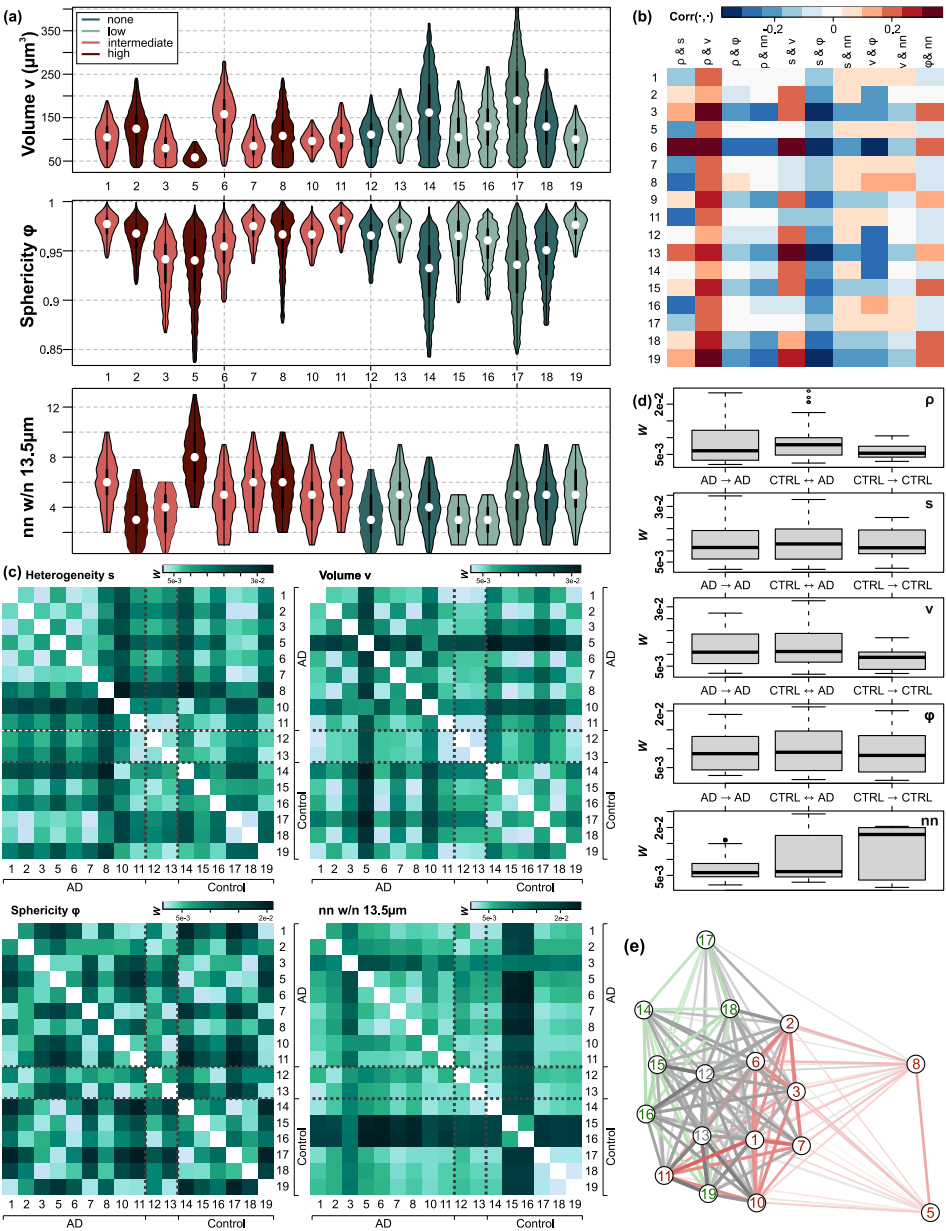


Fig. 4.10: (caption next page)

Fig. 4.10 (previous page): Nuclei of DG-granular cells – supplementary analysis of CB-data. (a) Violin plots of structural features for each subject, (top to bottom): nuclear volume v , sphericity φ and number of neighboring objects (nn) within a radius of $13.5 \mu\text{m}$. The color scheme corresponds to the ABC-score. (b) Feature-feature-correlation (columns), evaluated for different subjects (rows). (c) Matrices of Wasserstein-measures (W), (c, top left) heterogeneity parameter s , (top right) nuclear volume v , (bottom left) sphericity φ , (bottom right) nn, and (d) Scatter plots of W -values, calculated for each individual with respect to its entire group (with subject 12 and 13 excluded). (e) Bures-cost \mathcal{W} in 5d-space represented as a graph: bold connections and close node proximity correspond to lower \mathcal{W} . Connections between controls are colored “green”, between AD-individuals “red” and inter-groups “gray” (including subjects with no group assignment).

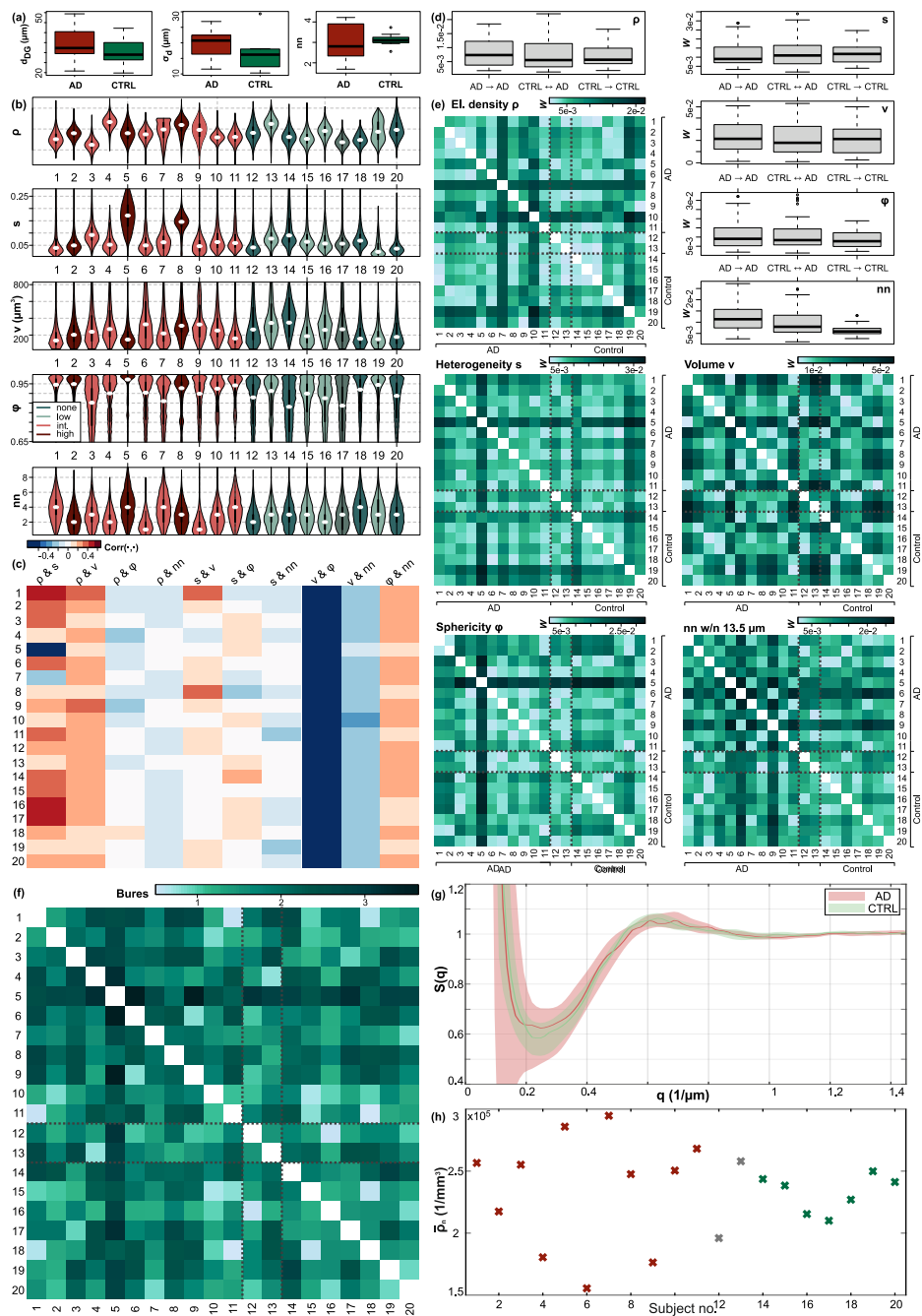


Fig. 4.11: (caption next page)

Fig. 4.11 (previous page): Nuclei of DG-granular cells – supplementary analysis of PB-data. (a) Box-whisker plots of (left) granular cell bandwidth d_{DG} , (center) its variance σ_d , and (right) number of neighboring objects (nn) within a radius of $13.5 \mu\text{m}$; each (left, red) grouped for AD-subjects, (right, green) for controls according to ABC-score. (b) Violin plots of structural features (top to bottom): median electron-density ρ and heterogeneity s , nuclear volume v , sphericity φ , and nn within $13.5 \mu\text{m}$. The color scheme corresponds to the respective ABC-score. (c) Feature-feature-correlation (columns), evaluated for different subjects (rows). (d) Plots of Wasserstein-values (W), calculated for each individual with respect to its entire group (with the exclusion of subjects 12 and 13). (e) Matrices of W -measures, for all five features. (f) Matrices of W -measures. (e) Bures-cost \mathcal{W} in 5d. (g) Structure factor $S(q)$ computed from the centers-of-mass of DG-cell nuclei masks (see SI Appendix, Methods, Structural parameters of DG-cell nuclei). Lines indicate the group-wise median, half-transparent areas the 1σ -intervals. The positions of the scattering peak indicate the next neighbor distances d_{NN} , namely $d_{\text{NN}} = 13.88 \mu\text{m}$, and $d_{\text{NN}} = 15.04 \mu\text{m}$, for AD and CTRL, respectively. However, the modulation of $S(q)$, *i.e.* the dip and the peak are less pronounced for AD, indicating a reduced short range order compared to in healthy tissue. (h) Group-averaged cell densities (red: AD, green: CTRL, gray: with no group assignment), obtained from density maps evaluated within the cell band only by applying a density threshold (10^5 1/mm^3 , see SI Appendix, Methods, Computation of local cell density). AD exhibits a larger variance compared to CTRL.

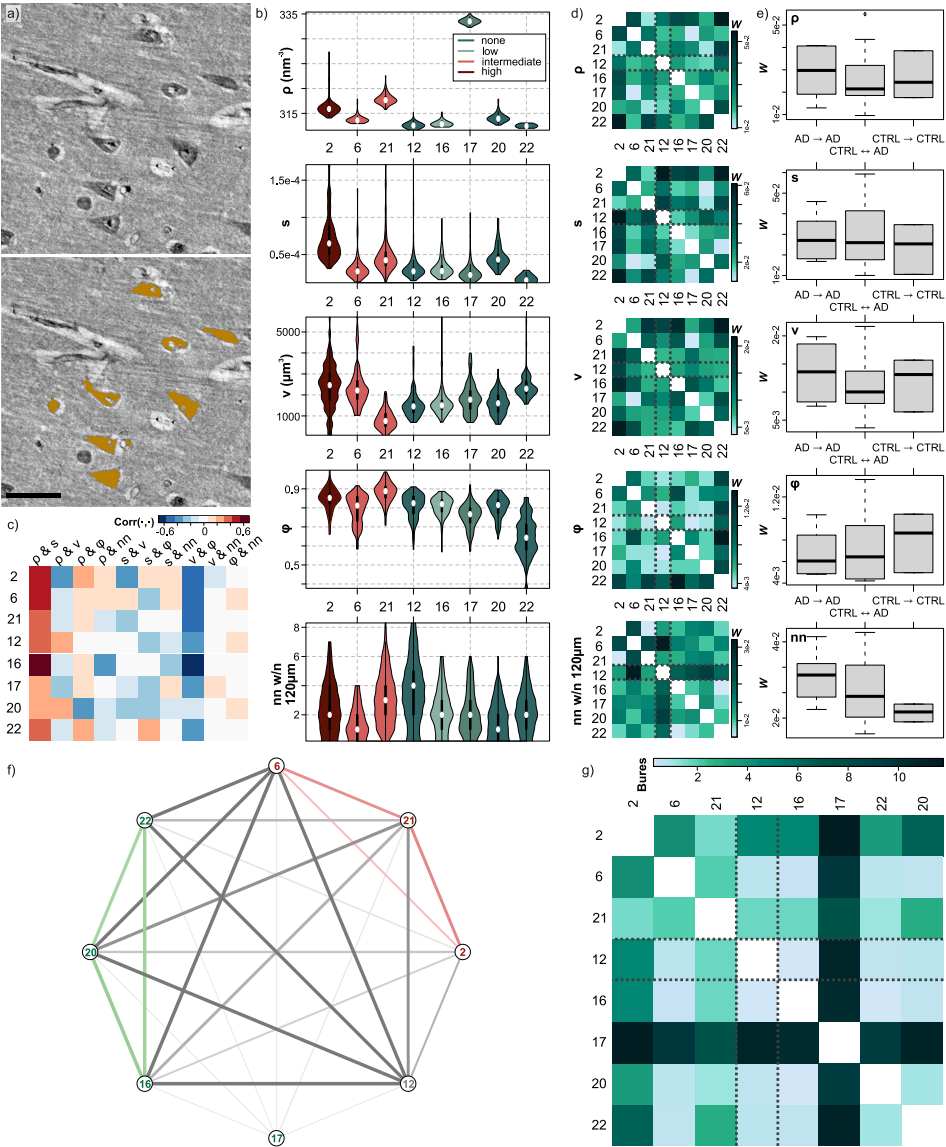


Fig. 4.12: (caption next page)

Fig. 4.12 (previous page): Pyramidal neurons in CA1 – statistical analysis. (a) Virtual sectioning to illustrate segmentation of pyramidal neurons. Scale bar: 50 μm . (b) Violin plots of the five selected features, where the color scheme indicates the ABC-score of the respective subject. (c) Feature-feature-correlation (columns), evaluated for different subjects (rows). (d) Matrices of Wasserstein-measures (W), for all five features. (e) Plots of W -measures, evaluated for single individuals with respect to their entire group distributions (with the exclusion of subject 12). (g) Bures-cost \mathcal{W} in 5d. (f & g) Presentation of the Bures-cost \mathcal{W} (computed in 5d), (f) as graph where thicker and shorter connections indicate lower cost (red: AD, green: CTRL, gray: with no group assignment), and (g) as distance chart.

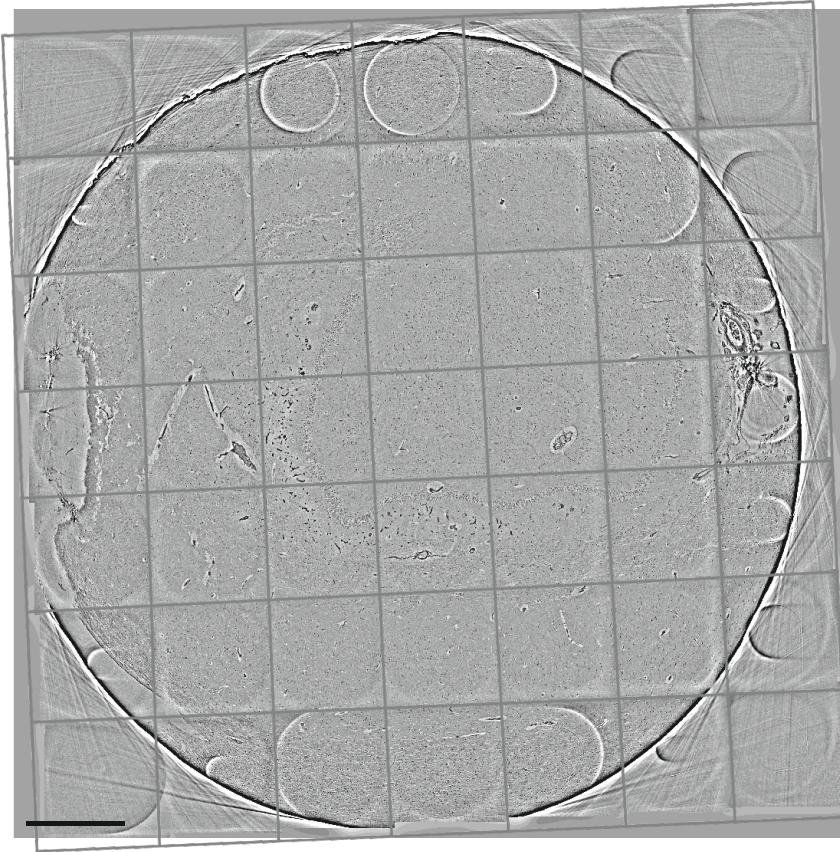


Fig. 4.13: Stitching of tomographic data sets for multiscale analysis. A full slice through the entire 7×7 tomographic reconstructions is shown covering the entire 8 mm cylindrical punch of hippocampal tissue recorded in PB-configuration. Scale bar: 1 mm.

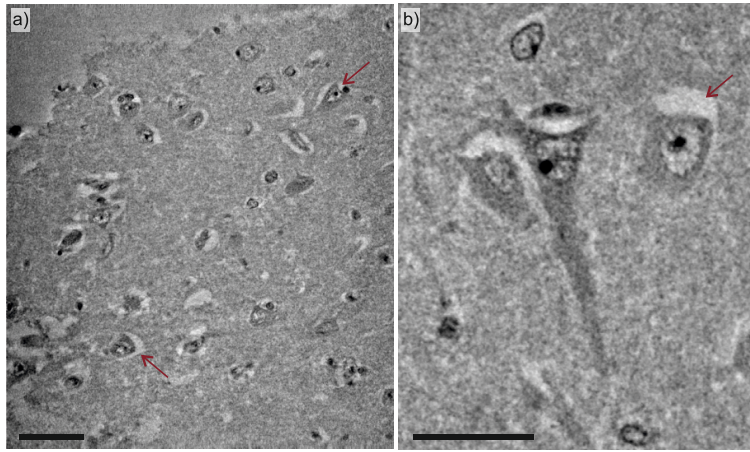


Fig. 4.14: Reconstruction of hydrated (PBS), formalin-fixed tissue. The example of a biopsy punch into the CA1-region (CTRL-group) recorded in CB-configuration) is shown, demonstrating that cellular bodies, nuclei and apical dendrites of the pyramidal neurons, are also resolved for this preparation, without tissue dehydration and paraffin embedding. Interestingly, tissue gaps around neurons are also observed at this stage of sample preparation. Scale bars: (a) 50 μm , (b) 30 μm .

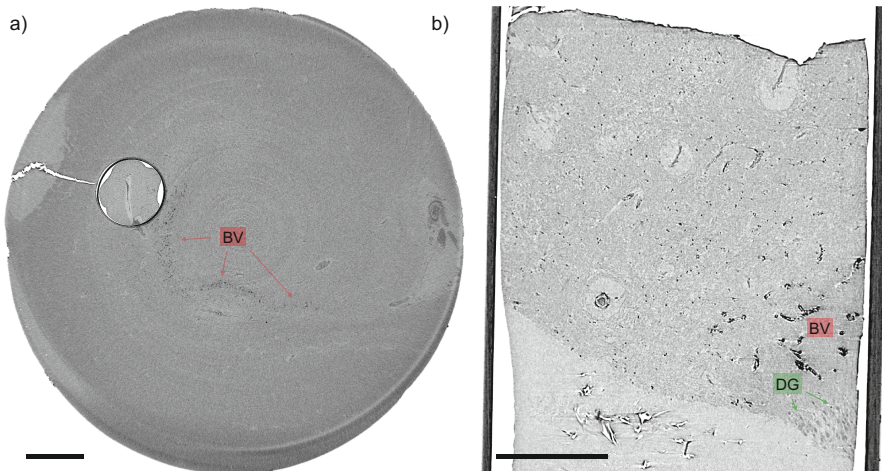


Fig. 4.15: PC-CT with laboratory μCT instrumentation. The same tissue block which was used for demonstrating the multiscale imaging workflow in the main text is shown. Experimental details are described in SI Appendix, Methods. (a) Overview scan of the 8 mm-tissue block, with the higher resolution dataset of the 1 mm-biopsy punch merged into the volume. (b) Virtual slice through the reconstruction volume of the 1mm-biopsy punch, with labeled anatomical features such as calcified blood vessels (BV) and the DG-cell band. Scale bars: (a) 1 mm, (b) 300 μm .

Bibliography

- [1] W. van Aarle, W. J. Palenstijn, J. De Beenhouwer, T. Altantzis, S. Bals, K. J. Batenburg, and J. Sijbers. “The ASTRA Toolbox: A platform for advanced algorithm development in electron tomography.” In: *Ultramicroscopy* 157 (2015), pp. 35–47.
- [2] D. H. Adler, L. E. M. Wisse, R. Ittyerah, J. B. Pluta, S.-L. Ding, L. Xie, J. Wang, S. Kadivar, J. L. Robinson, T. Schuck, J. Q. Trojanowski, M. Grossman, J. A. Detre, M. A. Elliott, J. B. Toledo, W. Liu, S. Pickup, M. I. Miller, S. R. Das, D. A. Wolk, and P. A. Yushkevich. “Characterizing the human hippocampus in aging and Alzheimer’s disease using a computational atlas derived from ex vivo MRI and histology.” In: *Proceedings of the National Academy of Sciences* 115.16 (2018), pp. 4252–4257.
- [3] P. C. Álvarez-Esteban, E. del Barrio, J. Cuesta-Albertos, and C. Matrán. “A fixed-point approach to barycenters in Wasserstein space.” In: *Journal of Mathematical Analysis and Applications* 441.2 (2016), pp. 744–762.
- [4] K. Amunts, M. Hawrylycz, D. V. Essen, J. V. Horn, N. Harel, J.-B. Poline, F. D. Martino, J. Bjaalie, G. Dehaene-Lambertz, S. Dehaene, P. Valdes-Sosa, B. Thirion, K. Zilles, S. Hill, M. Abrams, P. Tass, W. Vanduffel, A. Evans, and S. Eickhoff. “Interoperable atlases of the human brain.” In: *NeuroImage* 99 (2014), pp. 525–532.
- [5] K. Amunts and K. Zilles. “Architectonic Mapping of the Human Brain beyond Brodmann.” In: *Neuron* 88.6 (2015), pp. 1086–1107.
- [6] A. Astolfo, A. Lathuiliere, V. Laversenne, B. Schneider, and M. Stampanoni. “Amyloid- β plaque deposition measured using propagation-based X-ray phase contrast CT imaging.” In: *Journal of Synchrotron Radiation* 23.3 (2016), pp. 813–819.
- [7] K. Balewski, K. Brefeld, W. Decking, H. Franz, R. Röhlberger, and E. Weckert. *PETRA III: A Low Emittance Synchrotron Radiation Source*. Tech. rep. DESY, Hamburg, Germany, 2004.

- [8] M. Bartels, V. H. Hernandez, M. Krenkel, T. Moser, and T. Salditt. "Phase contrast tomography of the mouse cochlea at microfocus x-ray sources." In: *Appl. Phys. Lett.* 103.8, 083703 (2013), p. 083703.
- [9] M. Bartels, M. Krenkel, J. Haber, R. Wilke, and T. Salditt. "X-ray holographic imaging of hydrated biological cells in solution." In: *Physical Review Letters* 114.4 (2015), p. 048103.
- [10] S. Berg, D. Kutra, T. Kroeger, C. N. Straehle, B. X. Kausler, C. Haubold, M. Schiegg, J. Ales, T. Beier, M. Rudy, et al. "Ilastik: interactive machine learning for (bio) image analysis." In: *Nature Methods* 16 (2019), pp. 1–7.
- [11] J. M. Bernardo and R. Rueda. "Bayesian hypothesis testing: A reference approach." In: *International Statistical Review* 70.3 (2002), pp. 351–372.
- [12] M. Boldrini, A. N. Santiago, R. Hen, A. J. Dwork, G. B. Rosoklija, H. Tamir, V. Arango, and J. J. Mann. "Hippocampal Granule Neuron Number and Dentate Gyrus Volume in Antidepressant-Treated and Untreated Major Depression." In: *Neuropsychopharmacology* 38.6 (2013), pp. 1068–1077.
- [13] H. Braak, I. Alafuzoff, T. Arzberger, H. Kretschmar, and K. Del Tredici. "Staging of Alzheimer disease-associated neurofibrillary pathology using paraffin sections and immunocytochemistry." In: *Acta Neuropathologica* 112.4 (2006), pp. 389–404.
- [14] H. Braak and E. Braak. "Neuropathological staging of Alzheimer-related changes." In: *Acta Neuropathologica* 82.4 (1991), pp. 239–259.
- [15] D. Bures. "An extension of Kakutani's theorem on infinite product measures to the tensor product of semifinite w^* -algebras." In: *Transactions of the American Mathematical Society* 135 (1969), pp. 199–212.
- [16] T. Butz. *Fouriertransformation für Fußgänger*. Vieweg+Teubner Verlag / Springer Fachmedien Wiesbaden GmbH, Wiesbaden, 2012.
- [17] S. Castro-Obregón. "Lamin B receptor: role on chromatin structure, cellular senescence and possibly aging." In: *Biochemical Journal* 477.14 (2020), pp. 2715–2720.
- [18] T. F. Chan and L. A. Vese. "Active contours without edges." In: *IEEE Transactions on Image Processing* 10.2 (2001), pp. 266–277.

- [19] P. Cloetens, W. Ludwig, J. Baruchel, D. Van Dyck, J. Van Landuyt, J. Guigay, and M. Schlenker. “Holotomography: Quantitative phase tomography with micrometer resolution using hard synchrotron radiation x rays.” In: *Applied Physics Letters* 75.19 (1999), pp. 2912–2914.
- [20] D. M. Connor, H. Benveniste, F. A. Dilmanian, M. F. Kritzer, L. M. Miller, and Z. Zhong. “Computed tomography of amyloid plaques in a mouse model of Alzheimer’s disease using diffraction enhanced imaging.” In: *NeuroImage* 46.4 (2009), pp. 908–914.
- [21] D. Crapper, S. Quittkat, and U. De Boni. “Altered chromatin conformation in Alzheimer’s disease.” In: *Brain: a Journal of Neurology* 102.3 (1979), p. 483.
- [22] L. C. Croton, K. S. Morgan, D. M. Paganin, L. T. Kerr, M. J. Wallace, K. J. Crossley, S. L. Miller, N. Yagi, K. Uesugi, S. B. Hooper, et al. “In situ phase contrast X-ray brain CT.” In: *Scientific Reports* 8.1 (2018), pp. 1–12.
- [23] Y. De Witte, M. Boone, J. Vlassenbroeck, M. Dierick, and L. Van Hoorebeke. “Bronnikov-aided correction for x-ray computed tomography.” In: *JOSA A* 26.4 (2009), pp. 890–894.
- [24] E. L. Dyer, W. G. Roncal, J. A. Prasad, H. L. Fernandes, D. Gürsoy, V. De Andrade, K. Fezzaa, X. Xiao, J. T. Vogelstein, C. Jacobsen, et al. “Quantifying mesoscale neuroanatomy using x-ray microtomography.” In: *eNeuro* 4.5 (2017).
- [25] S. Epskamp, A. O. J. Cramer, L. J. Waldorp, V. D. Schmittmann, and D. Borsboom. “qgraph: Network Visualizations of Relationships in Psychometric Data.” In: *Journal of Statistical Software* 48.4 (2012), pp. 1–18.
- [26] P. J. Forrester and M. Kieburg. “Relating the Bures measure to the Cauchy two-matrix model.” In: *Communications in Mathematical Physics* 342.1 (2016), pp. 151–187.
- [27] J. Frohn, D. Pinkert-Leetsch, J. Missbach-Güntner, M. Reichardt, M. Osterhoff, F. Alves, and T. Salditt. “3D virtual histology of human pancreatic tissue by multiscale phase-contrast X-ray tomography.” In: *Journal of Synchrotron Radiation* 27.6 (2020), pp. 1707–1719.
- [28] B. Frost. “Alzheimer’s disease: An acquired neurodegenerative laminopathy.” In: *Nucleus* 7.3 (2016), pp. 275–283.
- [29] K. Giewekemeyer, H. Neubauer, S. Kalbfleisch, S. P. Krüger, and T. Salditt. “Holographic and diffractive x-ray imaging using waveguides as quasi-point sources.” In: *New Journal of Physics* 12.3 (2010), p. 035008.

- [30] L. Gil, S. A. Nino, G. Capdeville, and M. E. Jiménez-Capdeville. "Aging and Alzheimer's disease connection: Nuclear Tau and lamin A." In: *Neuroscience Letters* 749 (2021), p. 135741.
- [31] L. Gil, S. A. Niño, E. Chi-Ahumada, I. Rodríguez-Leyva, C. Guerrero, A. B. Rebolledo, J. A. Arias, and M. E. Jiménez-Capdeville. "Perinuclear Lamin A and Nucleoplasmic Lamin B2 Characterize Two Types of Hippocampal Neurons through Alzheimer's Disease Progression." In: *International Journal of Molecular Sciences* 21.5 (2020), p. 1841.
- [32] A. Groso, R. Abela, and M. Stampanoni. "Implementation of a fast method for high resolution phase contrast tomography." In: *Optics Express* 14.18 (2006), pp. 8103–8110.
- [33] A. Groso, M. Stampanoni, R. Abela, P. Schneider, S. Linga, and R. Müller. "Phase contrast tomography: an alternative approach." In: *Applied Physics Letters* 88.21 (2006), p. 214104.
- [34] B. Henke, E. Gullikson, and J. Davis. *X-ray interactions: photoabsorption, scattering, transmission, and reflection at E=50-30000 eV, Z=1-92, Atomic Data and Nuclear Data Tables*. Database 2. Center for X-Ray Optics, Lawrence Berkeley National Laboratory, 1993.
- [35] S. E. Hieber, C. Bikis, A. Khimchenko, G. Schweighauser, J. Hench, N. Chicherova, G. Schulz, and B. Müller. "Tomographic brain imaging with nucleolar detail and automatic cell counting." In: *Scientific Reports* 6 (2016), p. 32156.
- [36] R. A. Ketcham. "New algorithms for ring artifact removal." In: *Proc. SPIE* 6318 (2006), 63180O.
- [37] A. Khimchenko, C. Bikis, A. Pacureanu, S. E. Hieber, P. Thalmann, H. Deyhle, G. Schweighauser, J. Hench, S. Frank, M. Müller-Gerbl, et al. "Hard X-Ray Nanoholotomography: Large-Scale, Label-Free, 3D Neuroimaging beyond Optical Limit." In: *Advanced Science* 5 (2018), p. 1700694.
- [38] M. Kritsilis, S. V Rizou, P. N. Koutsoudaki, K. Evangelou, V. G. Gorgoulis, and D. Papadopoulos. "Ageing, cellular senescence and neurodegenerative disease." In: *International Journal of Molecular Sciences* 19.10 (2018), p. 2937.
- [39] S. P. Krüger, K. Giewekemeyer, S. Kalbfleisch, M. Bartels, H. Neubauer, and T. Salditt. "Sub-15 nm beam confinement by two crossed x-ray waveguides." In: *Optics Express* 18.13 (2010), pp. 13492–13501.

- [40] A. T. Kuan, J. S. Phelps, L. A. Thomas, T. M. Nguyen, J. Han, C.-L. Chen, A. W. Azevedo, J. C. Tuthill, J. Funke, P. Cloetens, et al. "Dense neuronal reconstruction through X-ray holographic nano-tomography." In: *Nature Neuroscience* 23.12 (2020), pp. 1637–1643.
- [41] S. Kullback and R. A. Leibler. "On information and sufficiency." In: *The Annals of Mathematical Statistics* 22.1 (1951), pp. 79–86.
- [42] M. A. Le Gros, E. J. Clowney, A. Magklara, A. Yen, E. Markenscoff-Papadimitriou, B. Colquitt, M. Myllys, M. Kellis, S. Lomvardas, and C. A. Larabell. "Soft X-ray tomography reveals gradual chromatin compaction and reorganization during neurogenesis in vivo." In: *Cell reports* 17.8 (2016), pp. 2125–2136.
- [43] L. M. Lohse, A.-L. Robisch, M. Töpperwien, S. Maretzke, M. Krenkel, J. Hagemann, and T. Salditt. "A phase-retrieval toolbox for X-ray holography and tomography." In: *Journal of Synchrotron Radiation* 27.3 (2020).
- [44] B. C. Lowekamp, D. T. Chen, L. Ibáñez, and D. Blezek. "The design of SimpleITK." In: *Frontiers in Neuroinformatics* 7 (2013), p. 45.
- [45] L. Massimi, I. Bukreeva, G. Santamaria, M. Fratini, A. Corbelli, F. Brun, S. Fumagalli, L. Maugeri, A. Pacureanu, P. Cloetens, et al. "Exploring Alzheimer's disease mouse brain through X-ray phase contrast tomography: From the cell to the organ." In: *NeuroImage* 184 (2019), pp. 490–495.
- [46] T. L. McHugh, A. J. Saykin, H. A. Wishart, L. A. Flashman, H. B. Cleavinger, L. A. Rabin, A. C. Mamourian, and L. Shen. "Hippocampal Volume and Shape Analysis in an Older Adult Population." In: *The Clinical Neuropsychologist* 21.1 (2007), pp. 130–145.
- [47] A. Miettinen, I. V. Oikonomidis, A. Bonnin, and M. Stampanoni. "NRStitcher: non-rigid stitching of terapixel-scale volumetric images." In: *Bioinformatics* 35.24 (2019). Ed. by R. Murphy, pp. 5290–5297.
- [48] F. Milletari, N. Navab, and S.-A. Ahmadi. "V-net: Fully convolutional neural networks for volumetric medical image segmentation." In: *2016 fourth international conference on 3D vision (3DV)*. IEEE. 2016, pp. 565–571.
- [49] S. S. Mirra, A. Heyman, D. McKeel, S. Sumi, B. J. Crain, L. Brownlee, F. Vogel, J. Hughes, G. Van Belle, L. Berg, et al. "The Consortium to Establish a Registry for Alzheimer's Disease (CERAD): Part II. Standardization of the neuropathologic assessment of Alzheimer's disease." In: *Neurology* 41.4 (1991), pp. 479–479.

- [50] T. J. Montine, C. H. Phelps, T. G. Beach, E. H. Bigio, N. J. Cairns, D. W. Dickson, C. Duyckaerts, M. P. Frosch, E. Masliah, S. S. Mirra, et al. "National Institute on Aging–Alzheimer’s Association guidelines for the neuropathologic assessment of Alzheimer’s disease: a practical approach." In: *Acta Neuropathologica* 123.1 (2012), pp. 1–11.
- [51] E. P. Moreno-Jiménez, M. Flor-García, J. Terreros-Roncal, A. Rábano, F. Cafini, N. Pallas-Bazarra, J. Ávila, and M. Llorens-Martín. "Adult hippocampal neurogenesis is abundant in neurologically healthy subjects and drops sharply in patients with Alzheimer’s disease." In: *Nature Medicine* 25.4 (2019), pp. 554–560.
- [52] B. Münch, P. Trtik, F. Marone, and M. Stampanoni. "Stripe and ring artifact removal with combined wavelet-Fourier filtering." In: *Optics Express* 17.10 (2009), pp. 8567–8591.
- [53] M. Narita, S. Nuñez, E. Heard, M. Narita, A. W. Lin, S. A. Hearn, D. L. Spector, G. J. Hannon, and S. W. Lowe. "Rb-mediated heterochromatin formation and silencing of E2F target genes during cellular senescence." In: *Cell* 113.6 (2003), pp. 703–716.
- [54] H. Neubauer, S. Hoffmann, M. Kanbach, J. Haber, S. Kalbfleisch, S. Krüger, and T. Salditt. "High aspect ratio x-ray waveguide channels fabricated by e-beam lithography and wafer bonding." In: *Journal of applied physics* 115.21 (2014), p. 214305.
- [55] K. Noda-Saita, A. Yoneyama, Y. Shitaka, Y. Hirai, K. Terai, J. Wu, T. Takeda, K. Hyodo, N. Osakabe, T. Yamaguchi, et al. "Quantitative analysis of amyloid plaques in a mouse model of Alzheimer’s disease by phase-contrast X-ray computed tomography." In: *Neuroscience* 138.4 (2006), pp. 1205–1213.
- [56] W. J. Palenstijn, K. J. Batenburg, and J. Sijbers. "The ASTRA tomography toolbox." In: *13th International Conference on Computational and Mathematical Methods in Science and Engineering. CMMSE*. 2013.
- [57] F. Pedregosa, G. Varoquaux, A. Gramfort, V. Michel, B. Thirion, O. Grisel, M. Blondel, P. Prettenhofer, R. Weiss, V. Dubourg, J. Vanderplas, A. Passos, D. Cournapeau, M. Brucher, M. Perrot, and E. Duchesnay. "Scikit-learn: Machine Learning in Python." In: *Journal of Machine Learning Research* 12 (2011), pp. 2825–2830.

- [58] G. Peyré, M. Cuturi, et al. “Computational optimal transport: With applications to data science.” In: *Foundations and Trends® in Machine Learning* 11.5-6 (2019), pp. 355–607.
- [59] B. R. Pinzer, M. Cacquevel, P. Modregger, S. McDonald, J. Bensadoun, T. Thuerling, P. Aebischer, and M. Stamparoni. “Imaging brain amyloid deposition using grating-based differential phase contrast tomography.” In: *NeuroImage* 61.4 (2012), pp. 1336–1346.
- [60] *plot_gaussian_ellipsoid*. https://www.mathworks.com/matlabcentral/fileexchange/16543-plot_gaussian_ellipsoid.
- [61] R Core Team. *R: A Language and Environment for Statistical Computing*. R Foundation for Statistical Computing, Vienna, Austria, 2013.
- [62] M. Reichardt, J. Frohn, A. Khan, F. Alves, and T. Salditt. “Multi-scale X-ray phase-contrast tomography of murine heart tissue.” In: *Biomedical Optics Express* 11.5 (2020), pp. 2633–2651.
- [63] A.-L. Robisch, M. Eckermann, M. Töpperwien, F. van der Meer, C. Stadelmann-Nessler, and T. Salditt. “Nanoscale x-ray holotomography of human brain tissue with phase retrieval based on multienergy recordings.” In: *Journal of Medical Imaging* 7.1 (2020), p. 013501.
- [64] O. Ronneberger, P. Fischer, and T. Brox. “U-Net: Convolutional Networks for Biomedical Image Segmentation.” In: *Medical Image Computing and Computer-Assisted Intervention – MICCAI 2015*. Ed. by N. Navab, J. Hornegger, W. M. Wells, and A. F. Frangi. Cham: Springer International Publishing, 2015, pp. 234–241.
- [65] T. Salditt, S. Krüger, C. Fuhse, and C. Bähitz. “High-transmission planar x-ray waveguides.” In: *Physical Review Letters* 100.18 (2008), p. 184801.
- [66] T. Salditt, M. Osterhoff, M. Krenkel, R. N. Wilke, M. Priebe, M. Bartels, S. Kalbfleisch, and M. Sprung. “Compound focusing mirror and X-ray waveguide optics for coherent imaging and nano-diffraction.” In: *Journal of Synchrotron Radiation* 22.4 (2015), pp. 867–878.
- [67] F. Santambrogio. *Optimal Transport for Applied Mathematicians*. Vol. 87. Progress in Nonlinear Differential Equations and Their Applications. Birkhäuser Boston, 2015.
- [68] B. Schmitzer. “Stabilized sparse scaling algorithms for entropy regularized transport problems.” In: *SIAM Journal on Scientific Computing* 41.3 (2019), A1443–A1481.

- [69] D. Schuhmacher, B. Bähre, C. Gottschlich, V. Hartmann, F. Heinemann, and B. Schmitzer. *transport: Computation of Optimal Transport Plans and Wasserstein Distances*. 2020.
- [70] L. R. Squire. “Memory and the hippocampus: a synthesis from findings with rats, monkeys, and humans.” In: *Psychological Review* 99.2 (1992), p. 195.
- [71] D. R. Thal, U. Rüb, M. Orantes, and H. Braak. “Phases of A β -deposition in the human brain and its relevance for the development of AD.” In: *Neurology* 58.12 (2002), pp. 1791–1800.
- [72] M. Töpperwien, M. Krenkel, D. Vincenz, F. Stöber, A. M. Oelschlegel, J. Goldschmidt, and T. Salditt. “Three-dimensional mouse brain cytoarchitecture revealed by laboratory-based x-ray phase-contrast tomography.” In: *Scientific Reports* 7.1 (2017), pp. 1–8.
- [73] M. Töpperwien, F. van der Meer, C. Stadelmann, and T. Salditt. “Correlative x-ray phase-contrast tomography and histology of human brain tissue affected by Alzheimer’s disease.” In: *NeuroImage* 210 (2020), p. 116523.
- [74] M. Töpperwien, F. van der Meer, C. Stadelmann, and T. Salditt. “Three-dimensional virtual histology of human cerebellum by X-ray phase-contrast tomography.” In: *Proceedings of the National Academy of Sciences* 115.27 (2018), pp. 6940–6945.
- [75] L. Turner, B. Dhal, J. Hayes, A. Mancuso, K. Nugent, D. Paterson, R. Scholten, C. Tran, and A. Peele. “X-ray phase imaging: Demonstration of extended conditions for homogeneous objects.” In: *Optics Express* 12.13 (2004), pp. 2960–2965.
- [76] W. Van Aarle, W. J. Palenstijn, J. Cant, E. Janssens, F. Bleichrodt, A. Dabravolski, J. De Beenhouwer, K. J. Batenburg, and J. Sijbers. “Fast and flexible X-ray tomography using the ASTRA toolbox.” In: *Optics Express* 24.22 (2016), pp. 25129–25147.
- [77] W. Wang, D. Slepčev, S. Basu, J. A. Ozolek, and G. K. Rohde. “A linear optimal transportation framework for quantifying and visualizing variations in sets of images.” In: *International Journal of Computer Vision* 101.2 (2013), pp. 254–269.
- [78] W. Winick-Ng and R. J. Rylett. “Into the fourth dimension: dysregulation of genome architecture in aging and Alzheimer’s disease.” In: *Frontiers in Molecular Neuroscience* 11 (2018), p. 60.

-
- [79] S. Zabler, P. Cloetens, J.-P. Guigay, J. Baruchel, and M. Schlenker. "Optimization of phase contrast imaging using hard x rays." In: *Review of Scientific Instruments* 76.7 (2005), p. 073705.

Towards Correlative Imaging of Neuronal Tissue by Phase-Contrast X-ray Tomography and SEM

5

Marina Eckermann, Torben Ruhwedel, Wiebke Möbius and Tim Salditt

Reproduced from Proc. SPIE Optics + Photonics – Developments in X-Ray Tomography XIII (2021), **1184005**, 29-36.

The mammalian brain shows a complex and hierarchical architecture, whose assessment at all functionally relevant scales requires the establishment of multiomics approaches. In this work, we propose a correlative workflow, which is based on large-scale overview PC-CT scans using the extended beams offered by laboratory μ CT sources and parallel beam synchrotron radiation (SR), with subsequent zooms into specific regions-of-interest using cone-beam recordings with nanofocused laboratory sources or SR, and finally SEM in controlled and well-identified sub-volumes obtained before. We demonstrate the workflow at the example of rOTO-stained murine corpus callosum tissue, a brain region rich in myelinated nerve fibers. Based on two different and complementary techniques, PC-CT and scanning electron microscopy (SEM), we approach the establishment of a correlative imaging workflow. As we show here, the workflow can be applied (i) in a correlative study, in order to add further quantitative value, for instance, or (ii) in a multiscale approach, to which PC-CT can contribute volume throughput, while SEM can contribute resolution. The findings from this work demonstrate the complementary strength of each modality in terms of resolution (SEM) and FOV or volume throughput (PC-CT).

5.1 Introduction

The functions of the mammalian brain require a complex and hierarchical architecture, composed of neurons and neuroglial cells. While the first make up the neuronal network connected by synapses, the latter provide a wealth of supporting functions, and in particular form the myelin sheath around myelinated axons and nerve projections which can extend over several centimeters [17, 23]. In order to assess brain tissue at all functionally relevant scales, the establishment of multiomics approaches is required [1]. For fundamental neuroscience, unraveling the connectome in specific brain regions is an extremely important goal, which no longer seems unrealistic based on progress in electron microscopy [7, 8], and sample preparation, including infiltration with metal solutions and subsequent staining, in particular the rOTO protocol [9].

Beyond the physiological regime, pathological changes of brain tissue in neurodegenerative diseases, for instance, are highly important and require three-dimensional (3d) structural probes with sub-cellular resolution in order to assess cellular shapes and organelles such as the myelin sheaths, which is of special interest in diseases such as multiple sclerosis (MS). MS is an inflammatory disease resulting in axonal demyelination and eventual remyelination. To probe such damages and repair mechanisms, ultrastructure preservation during tissue preparation is essential. Due to changes in osmolarity, purely formalin-based tissue fixation is considered insufficient to study neuronal ultrastructure, which can to some degree be absorbed by the addition of glutaraldehyde, or should be entirely replaced by high-pressure freezing if possible [12, 16]. In particular for human tissue, tissue preservation techniques are limited, since rapid and standardized fixation protocols are not realistic and autolysis onset cannot be excluded. In order to first control for such artifacts due to preparation, and to then assess and analyze the fixated, stained or labeled tissue, it is helpful to compare and eventually correlate images recorded by different modalities. This has for example already been exploited for grating-based phase-contrast tomography and histology in [2, 13], or propagation-based phase-contrast computed-tomography (PC-CT) and histology in [22].

In this work, we study murine corpus callosum (CC) tissue, a white matter brain region with high occurrence of myelinated nerve fibers, by two different and complementary techniques, PC-CT and scanning electron microscopy (SEM), towards establishing a correlative imaging workflow. We use rOTO-staining which has already been demonstrated to enable state-of-the-art connectomic studies by transmission-EM (TEM) and focused ion-beam SEM (FIB-SEM) [7, 8] and has also been proven to be compatible

with X-ray tomography [11]. We investigate under which conditions and parameters of photon energy, resolution, field of view (FOV), and image quality, mammalian brain tissue stained by the rOTO-protocol[9] can also be probed by PC-CT, following our earlier work in [3]. Here, we in particular aim at a correlative workflow, based on (i) large-scale overview PC-CT scans using the extended beams offered by laboratory μ CT sources, followed by (ii) scans with parallel beam (PB) synchrotron radiation (SR), and (iii) zooms into specific regions-of-interest (ROIs) based on cone-beam (CB) recordings with nanofocused SR, and finally (iv) SEM on sections of regions identified in sub-volumes before. This sequence is obvious, owing to the fact that PC-CT is non-destructive while SEM relies on the preparation of sections. At the same time, large FOV pre-characterization is helpful to find the “needle in a haystack”. For the purpose of PC-CT and SEM correlative imaging, the rOTO-protocol[9] can be regarded as a prerequisite since it is uniquely suited for connectomics of (neuronal) tissues by FIB-SEM. Hence, the experimental PC-CT parameters, in particular photon energy E and FOV, have to be adapted to this requirement. Note that imaging of neuronal tissue by PC-CT does not demand metal staining *per se*, and that on the contrary the native electron density contrast of unstained but fixed tissue can give sufficient contrast to image the cytoarchitecture [21]. While it can be expected that rOTO-stain enhances the contrast and also achievable resolution in PC-CT, the increased absorption can limit the sample diameter and hence the practical FOV to a few mm or require to increase E . While the energy range $E \simeq 7\ldots 14$ keV is well-suited for biopsy punch tissue samples up to a few mm in cross-section, higher E in combination with metal-stained samples could lead to increased background for example by fluorescence or scattering, which are no longer optimal for low electron density components of the tissue. Furthermore, the deposited dose will increase considerably. As we show here, these challenges can be well-met, e.g. by the $E = 17.1$ keV SR-scans demonstrated here, as well as by broad bandpass laboratory radiation.

Feasibility and compatibility given, we then also ask to which extend PC-CT and SEM are complementary. Based on the much higher resolution of SEM, it can be questioned whether PC-CT offers particular advantages for metal-stained tissue samples, other than being nondestructive. As we show here, the FOV and throughput at reasonable scan times still offer a significant and valuable advantage of PC-CT when larger mm-sized volumes have to be assessed. In a correlative study, PC-CT can contribute volume, while SEM can contribute resolution. In the images provided here for the example of murine corpus callosum (CC) tissue, we can also assess the window of resolution and FOV where both methods overlap, and how identical features appear in image

contrast for both techniques, respectively.

5.2 Methods

5.2.1 Sample Preparation

For PC-CT and SEM measurements, the exact same sample, with identical embedding and mounting, has been utilized. Murine corpus callosum (CC) was chosen as sample tissue for its abundance of dense myelinated structures. The particular sample presented here was selected from a series of samples, for which the preparation and PC-CT parameters were described in detail before [3]. In short, male C57Bl6N mice at the age of 10 weeks were sacrificed in agreement with the ethics committee of Max-Planck-Institute for Experimental Medicine by cervical dislocation. Tissue was fixed by immersion in solution containing 2.5% glutaraldehyde, 4% formaldehyde and 0.5% NaCl in 0.1 M phosphate buffer. Staining procedure followed a modification of the *reduced osmium, thiocarbohydrazide, osmium* (rOTO) protocol, which elevates membrane penetration of OsO_4 [9]. Samples were washed in 0.1 M phosphate buffer (3×15 mins at 4°C), and then incubated in 2% OsO_4 and 0.25% $\text{K}_4[\text{Fe}(\text{CN})_6]$ (3 h at 4°C) to reduce the OsO_4 to OsO_2 . After washing with ddH_2O , samples were incubated with 0.1% thiocarbohydrazide (in ddH_2O , for 1 h at RT). Samples were subsequently treated with 2% OsO_4 (90 min), and after washing with ddH_2O , further contrasted with 2.5% uranyl acetate (overnight at 4°C), followed by several washes with ddH_2O . Samples were then dehydrated with increasing concentrations of acetone in water (30%, 50%, 70% and 90%, for 20 mins each at RT), and incubated in 100% acetone (3×15 min). For embedding, tissues were incubated with increasing concentrations of EPON resin mixed with acetone (2:1, 1:1 1:2, for 2 h each at RT) prior to incubation with pure EPON resin (overnight at RT) and polymerization (24 h at 60°C), for which the sample was mounted in a 1 mm-kapton tube on a brass pin. Note that after completed polymerization, the kapton tube has been removed from the EPON surface.

5.2.2 Propagation-based Phase-Contrast Tomography

Different implementations of propagation-based phase-contrast tomography (PC-CT), with four zoom levels in total, have been utilized: In this work, μCT -Overview and μCT -zoom1 data have been recorded with a table-top nanofocus PC-CT setup (EasyTom, with voxel sizes of $1\text{ }\mu\text{m}$ and $0.35\text{ }\mu\text{m}$, respectively), and SR-Zoom1 and SR-Zoom2

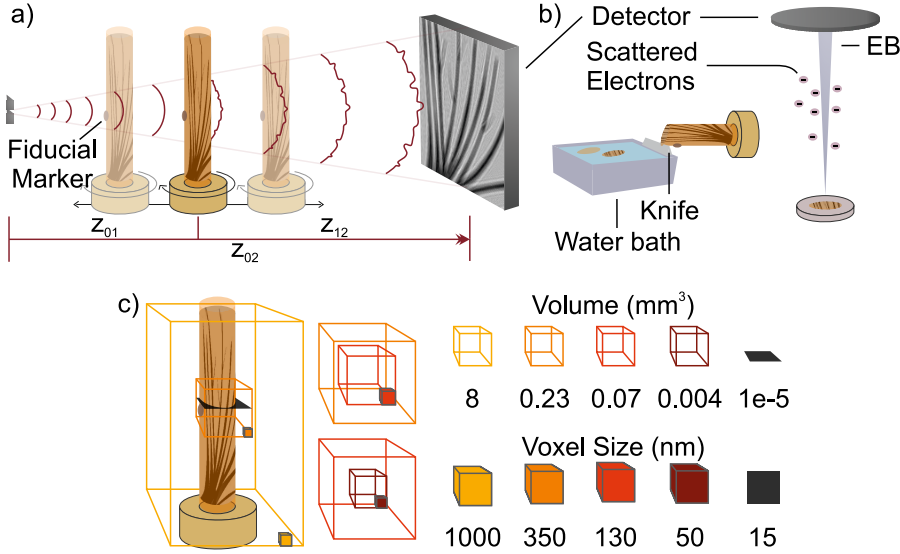


Fig. 5.1: Correlative imaging workflow. (a) Propagation-based phase-contrast tomography (PC-CT): X-rays penetrate the sample mounted on a tomography stage at z_{01} . The near-field diffraction pattern (or inline hologram) of the sample is recorded by the detector positioned at z_{02} . A fiducial marker helps to identify the ROI. (b) SEM: A sample-ROI which was selected based on the previous PC-CT results, exposed by trimming using a diamond knife followed by sectioning and imaging using a SEM. In SEM, the sample is scanned by an electron beam (EB), and the scattered electrons provide the image contrast. (c) Depiction of the multiscale imaging workflow: with PC-CT, the sample can be scanned at different zoom-levels, covering the entire sample with coarse sampling (yellow box) down to a selected ROI with small voxels (darker shades of red), and further by SEM imaging (black).

data with a synchrotron holography PC-CT setup (ID16A, ESRF, with voxel sizes of 130 nm and 50 nm, respectively [4]). Fig. 5.1(a) depicts the experimental principle, and the experimental parameters are briefly summarized in Tab. 5.1, with more details and results given in [3].

Note that the volume throughput and data quality can be modified by adjustment of experimental parameters, and that other setups can be used as well, such as the parallel-beam (SR-Overview) [3, 6] or cone-beam (SR-Zoom3) [3, 6, 22] configurations at the GINIX-endstation, P10 (DESY, Hamburg), or home-built PC-CT setups (for instance liquid metal jet setup (μ CT-Zoom2) [10, 20], or setups with nanofocus [3, 5] or microfocus rotating anode sources [14]).

	μ CT-Overview	μ CT-Zoom1	SR-Zoom1	SR-Zoom2
# projections	1568	3008	2000	2000
Energy (keV)	60	60	17.1	17.1
Exp. time (s)	12×1.7	5×10	4×0.2	4×0.2
Voxel Size (nm)	0.99e3	350	130	50
Phase retrieval	simple	simple	CG	CG

Table 5.1: Experimental and reconstruction parameters for PC-CT measurements. Note that for μ CT-Overview and μ CT-Zoom1 scans, the X-ray spectrum spans the entire range of bremsstrahlung, and the given energy denotes its upper limit. For SR-Zoom1 and SR-Zoom2, data have been acquired at four defocus distances, and phase retrieval has been carried out with an iterative contrast transfer function approach (CTF; conjugated gradients, CG). For μ CT-Overview and μ CT-Zoom1 data, phase has been retrieved using the implemented simple phase filter (RX-Solutions, EasyTom).

5.2.3 Scanning Electron Microscopy

Scanning Electron Microscopy (SEM) has been carried out with the Zeiss Crossbeam 540-47-27 device [18, 19]. The selected region was first exposed with a microtome (Trim90, Diatome), then sliced into $200\mu\text{m}$ -sections (Histo Knife, Diatome Ltd, Switzerland), mounted on a silicon wafer and coated with carbon. Large tile scans were obtained by detection of the backscattered electrons.

In this work, a single 2d sample slice has been examined with the SEM, covering a relatively large area ($851 \times 838 \mu\text{m}^2$) with small voxel sizes (15 nm). To capture the entire area, 23 single scans of $184.32 \times 184.32 \mu\text{m}^2$ were recorded at 1.5 keV and subsequently stitched. The tile time was 1715.4 s and the dwell time 10 μs . Since back-scattered electrons were chosen as a signal, no energy window/filter was available.

5.2.4 Multiscale and Multimodal Imaging

Fig. 5.1(c) delineates the multiscale and multimodal workflow proposed in this work: first, a suitable PC-CT configuration is chosen to efficiently image the entire sample in 3d (yellow box). Consecutively, a selected subvolume, referred to as regions of interest (ROIs), is sampled with increased resolution, indicated with shades of red. Finally, the selected region is identified based on the fiducial marker, exposed, and imaged by SEM. To the right of Fig. 5.1(c), the FOV and voxel sizes at each step are depicted as they were applied in this work. Note that while we propose the used of fiducial markers for future work, the identification in the present work was based only on the cytoarchitecture

itself, based on successive microtome sectioning and optical microscopy, combined with visual identification in the PC-CT reconstruction.

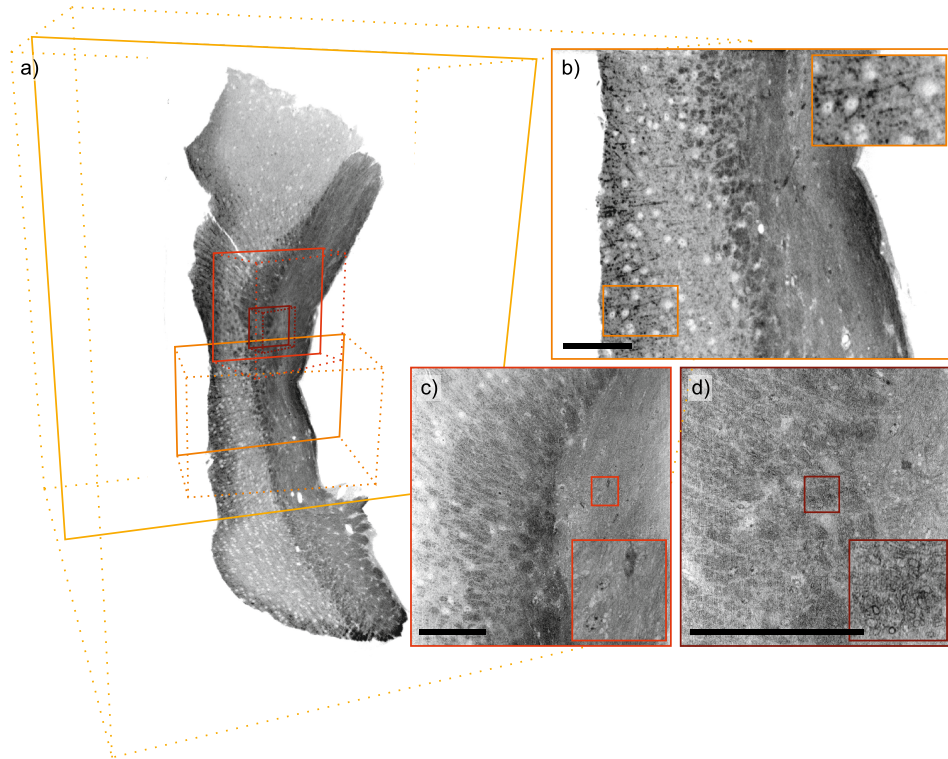


Fig. 5.2: Slices from multiscale PC-CT of a rOTO-prepared murine Corpus Callosum (CC): (a) μ CT-Overview data with indications of selected ROI-scans, where dashed lines indicate imaging volumes, and solid lines 2d slices. (b-d) Slices from zoom-in ROI-scans μ CT-Zoom1, SR-Zoom1 and SR-Zoom2 as marked in (a), where (b-c) are 1 μ m maximum intensity projections (MIPs). Scalebars: 100 μ m.

5.3 Results

Fig. 5.2 shows the PC-CT results. Following the workflow from sec. 5.2.4, (a) depicts the overview scan data (yellow), with smaller boxes indicating the positions of the ROI-scans. Note that dashed lines represent scan volumes, while solid lines indicate virtual 2d slices of the respective volume. Hence, ROI-volume boxes end where they intersect with the 2d-slice of the overview scan (yellow solid lines). The ROI-slices in

(b-d) follow the same color scheme, with (b) μ CT-Zoom1 (orange), (c) SR-Zoom1 (red) and (d) SR-Zoom2 data (dark red).

On all imaging scales, the anatomical structure of the CC can be identified: on the larger scales (a-b), the massive strands of myelinated axons can be distinguished individually, while smaller axons are likely to simply result in an elevated background level. Neurons appear in negative contrast (lighter gray values). At sub- μ m resolution (c-d), the contrast is increasingly shifted towards membranous structures, as highlighted in the insets for cell nuclei and myelin sheaths, respectively.

Fig. 5.3 shows the SEM results. The entire scan area is depicted in (a), where the grid-pattern can be attributed to the stitching of single SEM scans. Compared to PC-CT the voxel size of 15 nm is extremely small, and contrast extends down to the finest sub-cellular structures, without local averaging PC-CT which emphasizes more extended structures. The high level of detail is demonstrated with the insets on vasculature. A multi-walled membranous structure with individually resolved membranes can be identified. In (b), cellular nuclei next to a blood vessel and, a wealth of neighboring myelinated axons appear in cross-section view. Within the nuclei, the distribution of heterochromatin is contrasted particularly well.

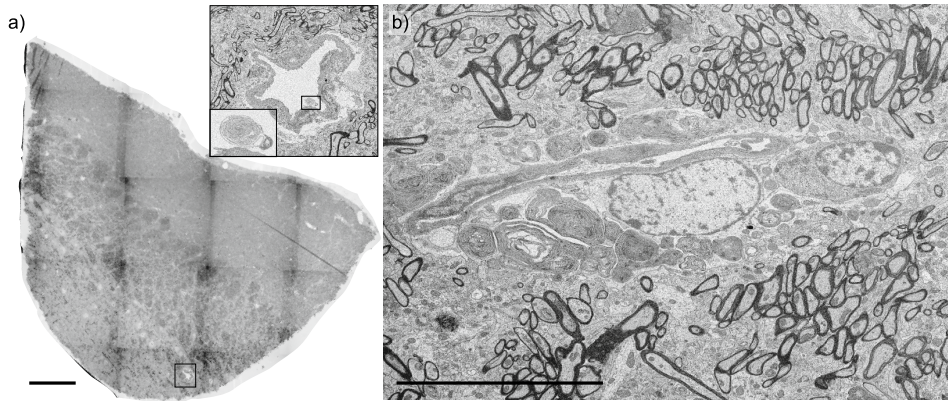


Fig. 5.3: SEM of the same rOTO-prepared murine CC-sample. (a) Overview of stitched data, (insets) zooms into a vasculature structure demonstrating the capability to distinguish delicate membranous structures. (b) A region with cellular features, such as nucleoli and nuclei in the center, surrounded by and myelinated axons. Scale bars: (a) 100 μ m, (b) 20 μ m.

Fig. 5.4 shows the two modalities side-by-side for comparison. A slice through the volume rendering of the μ CT-Overview data indicates the spatial location of the SEM data. In this cross-section view, the same tissue structures can be identified by both

imaging modalities, at a larger scale in (b) and at sub- μm resolution in (c). In (d-e), the differences in appearance of cell nuclei, when imaged by μCT -Zoom1, SEM and SR-Zoom2, respectively, can be particularly well assessed.

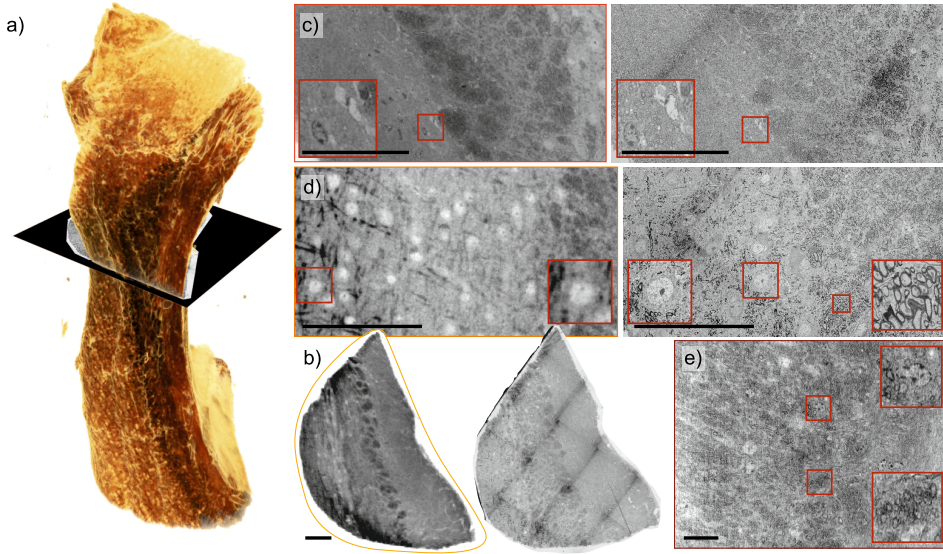


Fig. 5.4: Correlative SEM & PC-CT. (a) Volume rendering of μCT -Overview data with the slice indicating the position of SEM imaging. (b, left) PC-CT and (right) SEM data on the overview level. (c, right) Exact SEM slice matching with (left) PC-CT data (SR-Zoom1), which is a $1\ \mu\text{m}$ MIP. (d, left) PC-CT slice showing myelinated fibers and neuronal cell bodies (μCT -Zoom1), in comparison with their appearance in (right) SEM. (e) With SR-Zoom2, in a different PC-CT imaging regime, neuronal cell bodies more closely resemble the SEM data (d, right). Scale bars: (b-d) $100\ \mu\text{m}$, (e) $20\ \mu\text{m}$.

As a supplement for a further evaluation of correlative imaging with SEM and PC-CT, Tab. 5.2 details the volume throughput for each setup, namely the scanned volume per time. When access is available, SR-Overview scans can help to identify structures at the μm -level, with a considerably fast volume throughput, which will result in a similar data quality as with μCT -Overview [3]. Zoom-setups can be chosen depending on the setup availability and the desired feature contrast accentuation. With its so far unparalleled level of structural details, SEM, or FIB-SEM as a next step, however, remains the method of choice to inspect carefully selected regions at sub-organelle resolution, as required for connectomics.

Setup	Voxel Size (nm)	Volume Size (px)	Scan Duration (h)	Volume Throughput (mm ³ /h)
μCT-Overview	1000	1979 × 1979 × 2040	9	887.7 × 10 ⁻³
SR-Overview	650	2160 × 2160 × 2160	0.02	142
μCT-Zoom1	350	2019 × 2019 × 1298	46	4.9 × 10 ⁻³
μCT-Zoom2	450	3326 × 3326 × 2504	15	168.3 × 10 ⁻³
SR-Zoom1	130	3216 × 3216 × 3216	4	18.3 × 10 ⁻³
SR-Zoom2	50	3216 × 3216 × 3216	4	1.0 × 10 ⁻³
SR-Zoom3	170	2560 × 2560 × 2160	4	17.4 × 10 ⁻³
SEM	15	56736 × 55835 × 1	15	7.1 × 10 ⁻⁷

Table 5.2: Volume throughput for different imaging configurations. Setup notations are detailed in Sec. 5.2.2.

5.4 Discussion and Outlook

First of all, the results show that rOTO-stained neuronal tissue can be used for PC-CT and SEM alike, under the exact same conditions of staining, embedding and mounting. The example images and reconstruction volumes indicate the complementary strength of each modality in terms of resolution (SEM) and FOV or volume throughput (PC-CT). To specify this, it is useful to define a range of length scales, which one could also denote as a window of length scales, *i.e.* an interval W , bounded by the resolution and the FOV which can be covered within a given time, considered as reasonable. If resolution is not quantitatively assessed (as in this work), a small multiple of the voxel size can be taken as a proxy. A range of length scales can be covered well by both modalities, *i.e.* the overlap window $O = W_{\text{SEM}} \cap W_{\text{CT}}$. This overlap of both techniques will probably still increase in future. This is to be expected, since the resolution of SR PC-CT can still be scaled based on increasing brilliance, better detector technology, and improved reconstruction algorithms. At the same time the FOV of SEM may also increase following further progress in instrumentation, including further optimisation of ion and electron sources, and scanning speed. A large O is desirable not only to confirm the correct identification of a ROI, but also for the sake of truly correlative imaging, rather than just multiscale or comparative imaging.

To this end, gray values must be correlated. While the gray values in SEM are difficult to trace back to a simple sample quantity, since the back-scattering cross section is not quantitatively known for a given composition and structure, PC-CT with synchrotron radiation can in principle yield quantitative electron density values in each voxel [15].

This may not only help to “calibrate” and better understand SEM signals, for example in terms of quantitative metal concentration, but also to differentiate cellular or tissue components based on a two-dimensional gray value chart. For the present example of neuronal tissue, one may for instance be interested in the identification of different cells, including for example different types of glias. PC-CT before (unstained), and after rOTO stain (heavy metal labelled), followed by (FIB-)SEM would even yield a three-dimensional gray value vector to better segment and differentiate components. In this respect, note that structural correlation with PC-CT has been demonstrated in a 2d SEM-scan here. This is important in order to validate the correlation over a relatively large, mm^2 -sized area. Of course, following this proof-of-concept work, specific cellular features may be of particular interest as a next step. Owing to the 3d-extension of such features, the volume throughput in SEM will be exploited in a laterally confined, but in-depth extended 3d SEM-scan, in correlation with 3d PC-CT. Instead of O , consideration of its complementary in terms of W_{SEM} and W_{CT} can also add particular value, as quantified by the union $W = W_{\text{SEM}} \cup W_{\text{CT}}$, which gives for the present example already a quite considerable extension $W = [15 \text{ nm} \dots 1.5 \text{ mm}]$. Here, it is worth noting that even a combination of only laboratory μCT and SEM can nicely cover a sample with sufficient O and impressive W , even without the special efforts involved in SR-experiments, such as beamtime proposals etc. Furthermore, both modalities are available as commercial instruments, and could be nicely combined in an imaging facility.

What then, one may ask, would be the special benefit of SEM correlative imaging with PC-CT? At this point, we note that the volume throughput based on continuous scanning is extremely high, and that hence, by stitching of sub-volumes W can be tremendously increased to entire brain regions. At the same time, the resolution and hence O can be kept high. Finally, one could conceive instruments, where the (FIB-)SEM is integrated into a beamline, and where correlative and multiscale workflows take advantage of robotic sample exchange and fiducial markers, which can be summarized as “targeting”: First identifying the ROI in a mm^3 -sized sample by PC-CT, which is then targeted with physical sectioning (microtome) and imaged by large tile scans (SEM only), and finally targeted by 3d FIB-SEM of a selected smaller ROI. Scaling up capabilities accordingly, would truly open up new windows for neuroscience. Such an approach would provide anatomical and histological “context” for connectomics, and sub-cellular resolution for research on neurodegenerative diseases, where high resolution has to be combined with efficient screening for affected lesions.

Acknowledgments

We thank Peter Cloetens for excellent support at ID16a and a related collaboration. Support by the Deutsche Forschungsgemeinschaft (DFG, German Research Foundation) under Germany's Excellence Strategy - EXC 2067/1-390729940 *Multiscale Bioimaging* and the German Federal Ministry of Education and Research (BMBF) through grant No. 05K19MG2 *NeuroTomo*, are gratefully acknowledged.

Bibliography

- [1] A. Badhwar, G. P. McFall, S. Sapkota, S. E. Black, H. Chertkow, S. Duchesne, M. Masellis, L. Li, R. A. Dixon, and P. Bellec. “A multiomics approach to heterogeneity in Alzheimer’s disease: focused review and roadmap.” In: *Brain* 143.5 (2020), pp. 1315–1331.
- [2] M. Busse, M. Müller, M. A. Kimm, S. Ferstl, S. Allner, K. Achterhold, J. Herzen, and F. Pfeiffer. “Three-dimensional virtual histology enabled through cytoplasm-specific X-ray stain for microscopic and nanoscopic computed tomography.” In: *Proceedings of the National Academy of Sciences* 115.10 (2018), pp. 2293–2298.
- [3] M. Eckermann, F. van der Meer, P. Cloetens, T. Ruhwedel, W. Möbius, C. Stadelmann, and T. Salditt. “3d virtual histology of the Cerebral Cortex based on Phase-Contrast X-ray tomography.” N.D.
- [4] M. Eckermann, P. Cloetens, J. Reichmann, M. Osterhoff, T. Salditt, and M. Osterhoff. *3d structure of the human dentate gyrus by holo-tomography: Alzheimer disease vs Control*.
- [5] M. Eckermann, M. Töpperwien, A.-L. Robisch, F. van der Meer, C. Stadelmann, and T. Salditt. “Phase-contrast X-Ray Tomography of Neuronal Tissue at Laboratory Sources With Submicron Resolution.” In: *Journal of medical imaging (Bellingham, Wash.)* 7.1 (2020), p. 013502.
- [6] J. Frohn, D. Pinkert-Leetsch, J. Missbach-Güntner, M. Reichardt, M. Osterhoff, F. Alves, and T. Salditt. “3D virtual histology of human pancreatic tissue by multiscale phase-contrast X-ray tomography.” In: *Journal of Synchrotron Radiation* 27.6 (2020), pp. 1707–1719.
- [7] M. Helmstaedter. “Cellular-resolution connectomics: challenges of dense neural circuit reconstruction.” In: *Nature Methods* 10.6 (2013), pp. 501–507.
- [8] M. Helmstaedter, K. L. Briggman, S. C. Turaga, V. Jain, H. S. Seung, and W. Denk. “Connectomic reconstruction of the inner plexiform layer in the mouse retina.” In: *Nature* 500.7461 (2013), pp. 168–174.

- [9] Y. Hua, P. Laserstein, and M. Helmstaedter. “Large-volume en-bloc staining for electron microscopy-based connectomics.” In: *Nature Communications* 6.1 (2015), p. 7923.
- [10] M. Krenkel, M. Töpperwien, C. Dullin, F. Alves, and T. Salditt. “Propagation-based phase-contrast tomography for high-resolution lung imaging with laboratory sources.” In: *AIP Advances* 6.3 (2016), p. 035007.
- [11] A. T. Kuan, J. S. Phelps, L. A. Thomas, T. M. Nguyen, J. Han, C.-L. Chen, A. W. Azevedo, J. C. Tuthill, J. Funke, P. Cloetens, et al. “Dense neuronal reconstruction through X-ray holographic nano-tomography.” In: *Nature Neuroscience* 23.12 (2020), pp. 1637–1643.
- [12] W. Möbius, K.-A. Nave, and H. B. Werner. “Electron microscopy of myelin: Structure preservation by high-pressure freezing.” In: *Brain Research* 1641 (2016), pp. 92–100.
- [13] M. Müller, M. A. Kimm, S. Ferstl, S. Allner, K. Achterhold, J. Herzen, F. Pfeiffer, and M. Busse. “Nucleus-specific X-ray stain for 3D virtual histology.” In: *Scientific Reports* 8.1 (2018), pp. 1–10.
- [14] M. Reichardt, J. Frohn, M. Toepperwien, J.-D. Nicolas, A. Markus, F. Alves, and T. Salditt. “Nanoscale holographic tomography of heart tissue with x-ray waveguide optics.” In: *Developments in X-Ray Tomography XI*. Vol. 10391. International Society for Optics and Photonics. 2017, p. 1039105.
- [15] A.-L. Robisch, M. Eckermann, M. Töpperwien, F. van der Meer, C. Stadelmann-Nessler, and T. Salditt. “Nanoscale x-ray holotomography of human brain tissue with phase retrieval based on multienergy recordings.” In: *Journal of Medical Imaging* 7.1 (2020), p. 013501.
- [16] P. Rostaing, E. Real, L. Siksou, J.-P. Lechaise, T. Boudier, T. M. Boeckers, F. Gertler, E. D. Gundelfinger, A. Triller, and S. Marty. “Analysis of synaptic ultrastructure without fixative using high-pressure freezing and tomography.” In: *European Journal of Neuroscience* 24.12 (2006), pp. 3463–3474.
- [17] M. Rubinov and O. Sporns. “Complex network measures of brain connectivity: uses and interpretations.” In: *NeuroImage* 52.3 (2010), pp. 1059–1069.
- [18] A. M. Steyer, T. Ruhwedel, and W. Möbius. “Biological sample preparation by high-pressure freezing, microwave-assisted contrast enhancement, and minimal resin embedding for volume imaging.” In: *Journal of Visualized Experiments* 145 (2019).

- [19] A. M. Steyer, A. Schertel, C. Nardis, and W. Möbius. “FIB-SEM of mouse nervous tissue: Fast and slow sample preparation.” In: *Methods in cell biology* 152 (2019), pp. 1–21.
- [20] M. Töpperwien, M. Krenkel, D. Vincenz, F. Stöber, A. M. Oelschlegel, J. Goldschmidt, and T. Salditt. “Three-dimensional mouse brain cytoarchitecture revealed by laboratory-based x-ray phase-contrast tomography.” In: *Scientific Reports* 7.1 (2017), pp. 1–8.
- [21] M. Töpperwien, A. Markus, F. Alves, and T. Salditt. “Contrast enhancement for visualizing neuronal cytoarchitecture by propagation-based x-ray phase-contrast tomography.” In: *NeuroImage* 199 (2019), pp. 70–80.
- [22] M. Töpperwien, F. van der Meer, C. Stadelmann, and T. Salditt. “Correlative x-ray phase-contrast tomography and histology of human brain tissue affected by Alzheimer’s disease.” In: *NeuroImage* 210 (2020), p. 116523.
- [23] K. M. Tye and K. Deisseroth. “Optogenetic investigation of neural circuits underlying brain disease in animal models.” In: *Nature Reviews Neuroscience* 13.4 (2012), pp. 251–266.

Conclusion and Outlook

6

In this work, the characterization of neuronal cyto-architecture by PC-CT imaging at sub- μm resolution has been pursued. For this purpose, sample preparation methods have been optimized, reconstruction schemes fine-tuned, new technologies translated to the lab, and novel segmentation and analysis schemes have been established.

In order to study structural features, their presence is an obvious but crucial prerequisite. Correlative imaging with a method which is already established for visualizing the features of interest can be used to verify their presence in a tissue sample. In Ch. 5, PC-CT and subsequent SEM were conducted on the exact same sample. This work shows that structural preservation by immersion fixation at 4°C is sufficient when the target image resolution is in the range of about 50-100 nm. Contrarily, the preservation of ultrastructure by high-pressure freezing appears to be relevant at smaller voxel sizes [12]. In Ch. 5, structural preservation has not only been achieved by chemical fixation with formalin and glutaraldehyde, but also by a heavy metal stain based on osmium. These findings can be compared to our earlier work [4], which reported poor structure visibility in heavy-metal stained murine brain tissue. The major differences between the two studies are in the sample preparation protocols: in [4], staining of $\lesssim 0.5$ mm tissue slices was conducted at room temperature for several minutes only, while in Ch. 5 (and in parts of Ch. 3), $\lesssim 1$ mm-sized tissue volumes were treated at 4°C for several hours. This suggests that, while the amount of stain within the tissues was most likely sufficient to generate image contrast, it was insufficient for adequate tissue fixation in [4]. Also, higher temperatures might have had a negative impact on structural preservation, consistent with [5]. These findings contribute to the establishment of sample preparation protocols for sub- μm PC-CT alone or in correlative use with other experimental modalities. In this context, it would be interesting to further explore the structural preservation in human tissues, which faces intrinsic limitations as discussed in Sec. 1.3.3. The direct comparison between murine and human cortical tissue in Ch. 3 indicates a better preservation in the murine tissue preparation as expected. The wide range of sample preparation techniques which are suitable for PC-CT can help to

better understand the processes of the single steps [10].

Given sufficient feature preservation, it is worthwhile to take a closer look at the FSC-based spatial resolution reported in Ch. 2 and 4, to point out future directions for PC-CT development. In order to achieve particularly high resolution in laboratory PC-CT scans, the setup “TINa” has been designed, based on a nanofocus X-ray source (cf. Ch. 2 & A.2). In unstained and paraffin-embedded soft tissue, a FSC-based resolution of about $1\ \mu\text{m}$ has been reached (in a 3d-volume; $0.90\ \mu\text{m}$ in a reconstructed 2d-slice within the 3d-volume). This sets the state-of-the-art and narrows the gap between PC-CT setups at accelerator- and laboratory-based X-ray sources. The discrepancy between the resolution in a 3d-volume and a reconstructed 2d-slice indicates that the large X-ray cone-beam (CB) angle degraded the quality in FDK-tomographic reconstruction (cf. Sec. 1.5.2). To further assess how the setup conditions take effect, the spatial resolution has been measured for a range of X-ray source spot sizes s and pixel sizes px . First of all, a halved s led to the same FSC-result, and elevated the feature contrast as expected for phase-contrast image-formation at a smaller Fresnel number Fr . Furthermore, reducing the pixel size by more than 50% reduced the FSC-value only by 10%, and required 4-times the scan duration and more than 7-times the radiation dose. Considering the extended scan duration, these findings indicate stability issues, which are also reported for a very similar setup and attributed to a temperature drift [11]. In part, these stability issues may be ascribed to the X-ray source itself, which has since been upgraded and is now equipped with a more-stable high-voltage generator. For further improvements, comparative measurements between laboratory nanofocus setups as in Ch. 3 can be fruitful: the commercial EasyTom Nano-setup (RX Solutions) is particularly distinguished by a sophisticated source spot analysis and correction scheme. For the home-built TINa-setup, an interleaving-and-registration scheme has been implemented: The registration is made on a highly contrasted feature, for which the sample is translated. However, on the sub- μm -scale, sample-stage motor imprecisions are observed, which can not adequately be compensated by simple projection-registration in strong CB-geometry. It seems to be advisable to follow the RX Solutions scheme, in which reference projections are recorded prior to a tomographic scan without additional sample translation.

Also for the “GINIX”-setup in CB-configuration (cf. Ch. 4), the spatial resolution does not scale with the geometric magnification $M = \frac{z_{02}}{z_{01}}$, which results in $px = \frac{6.5\ \mu\text{m}}{M}$ for the camera used. For $px = 167\ \text{nm}$, a resolution of $2.3 \cdot px$ has been achieved, which corresponds to the expected PSF of the sCMOS camera. However, increasing M such that $px = 50\ \text{nm}$ led to a resolution of $4.4 \cdot px$. There are several possible reasons for

this observation. For one, the reported FSC-values in Ch. 4 indicate that the invested dose plays an important role in the overall image quality. Low photon flux, for instance, induces inconsistencies in PC-CT data sets, which can to some degree be compensated for by iterative methods [6, 8]. Regarding inconsistencies, also the sample diameter is a relevant parameter (cf. Sec. 1.3.1 and 1.5). Furthermore, higher stability in terms of vibrations and temperature drift as reported in [2] can increase tomographic data consistency, which can be achieved by active cooling of setup components or a sample cryo-environment [13]. This is especially important for high-flux experiments in view of the high proportion of absorption (cf. Fig. 1.6a), compare P.E. with R.S.). For holographic imaging with a similar configuration of the GINIX-setup, a FSC-based resolution of 11.2 nm has recently been reported [14]. The resolution was achieved by a joint iterative reconstruction scheme which uses both far- and near-field images, recorded with a single-photon counting detector at a higher numerical aperture¹. This proves that these setup components are capable of higher resolution scans, and points to limitations in further instrumentation, or adequate phase retrieval or tomographic reconstruction.

For the parallel-beam (PB) setup in Ch. 4, a spatial resolution of 1.6 μm was measured for a 1 mm sample within a 1.5 mm field-of-view (FOV), while for the identical sample in an 8 mm tissue block, the resolution was 4.2 μm . These data have been acquired in a continuous rotation instead of the step-and-shoot scheme, which apparently does not fully compensate for the ROI-problem in PB-geometry (cf. discussion in Sec. 1.5.6). Therefore, the following workflow is suggested in order to maximize the spatial resolution in cone-beam PC-CT: First, overview scans of mm-sized blocks should be recorded to identify a feature of interest. This feature should then be extracted in a way that the final sample width does not exceed the FOV of the zoom tomography. Optionally, artifacts from strong phase shifts at sample edges are prevented by embedding with additional material (paraffin, for instance). Possibly, given suitable instrumentation at beamlines, the location of this feature of interest can first be marked in a software and then automatically trimmed.

In this thesis, it has been demonstrated that sample throughput can be upscaled with PC-CT, such that 3d cellular structures of $N \gtrsim 20$ individuals can be studied “in their full native dimensionality” [3]. In Ch. 4, the key steps were identified as (i)

¹A higher numerical aperture allows to encode smaller structural features in the data. The larger physical pixel size of single-photon counting detectors leads to a higher photon flux per pixel, with a particularly small detector- PSF (approximately $1 \cdot px$).

(semi-)automatic segmentation, (ii) defining any number of structural properties, and (iii) accessing entire point clouds in a robust way using optimal transport (OT). OT enables the definition of (iv) a “tangent space”, where each individual is represented by a single data point. Hence, in the tangent space, multiscale phenomena are studied as an interconnected entirety, such that the statistical significance does not rely on the isolated study of single criteria anymore. Thereby, this workflow can substantially contribute to the testing and developing of hypothesis in biomedical research. In order to fully establish OT as a statistical analysis tool, it is necessary to develop its equivalent to the p -value of a Student’s t -test which quantifies the significance of a hypothesis. For instance, in an earlier study [9], tissue samples from Parkinson’s diseased patients and a control group were analyzed with XRD and XRF (X-ray diffraction, X-ray fluorescence). In contrast to the expectations of the authors, no group-related significance in copper-burden was found; neither based on t -test analysis, nor based on statistical measures which incorporate random effects. However, the abundance of trace elements in individuals is not purely random, but is affected by external factors such as medication. Also, the presence of trace elements should not be analyzed in isolation, but contextualized with other features. In the future, such studies can evaluate the phenomena intercorrelatively by OT analysis. Further directions include the complementation of the feature space, whose M vectors are defined by the M structural properties, by the correlative use of imaging methods. These additional imaging methods can be selected as desired: examples thereof are XRD and XRF, which are both well-suited for tomography applications [7]. XRD could help to uncover the structure of (pathological) aggregations. Due to the fluorescent excitation by X-rays, XRF is suitable to localize, identify and quantify trace elements within a sample. The overload of metals in human brain tissue is associated with *neurotoxicity*, since it may induce oxidative stress, mitochondrial dysfunction, or protein misfolding [1]. Hence, the quantification of elemental deposits in neuronal tissue is of particular interest in neurodegenerative diseases. Beyond the complementing strategy, PC-CT can be combined with a further method to correlate identical structures. This can deepen the understanding of contrast mechanisms in PC-CT. Examples are given in Fig. 1.4 for joint usage with Histology, or in Ch. 5 with SEM. Sec. A.1 describes a first implementation of correlative XRF computed-tomography (XRF-CT) with PC-CT at the GINIX-endstation, P10-beamline, DESY.

At this stage, PC-CT can capture the wide ranges of scales in neuronal tissues, in joint usage with advanced analysis workflows and optionally completed by additional methods (in experiment or sample preparation). Advancements in X-ray technology

increase the photon flux provided by both laboratory- and accelerator-based sources, which is beneficial for volume throughput and setup stability. In particular laboratory-based PC-CT benefits from a higher flux, along with low demands on tissue preparation and setup compactness. These factors make it well-suited for its integration into the clinics for rapid-section diagnosis during surgery, or as a standard tool for (pre-)clinical studies. Suitable stains or correlative methodologies can enable feature identification and their contextualization in 3d. For example, next steps could be the morphological characterization of possible neuronal subpopulations, and the identification of glial cell types to study their roles in entire networks. This could be combined with the correlation of $A\beta$ -plaques with τ -tangles in 3d to further elucidate AD-pathology. Regarding circuit connectivity, the strength of PC-CT is its ready access to multiple spatial *and* topological scales. OT-analysis may not only be applied to pathological groups, but also to neuronal circuits in order to characterize brain hierarchy on topological scales. Thus, we are getting closer to characterizing the complexity of the brain.

Bibliography

- [1] P. Chen, M. R. Miah, and M. Aschner. “Metals and neurodegeneration.” In: *F1000Research* 5 (2016).
- [2] V. De Andrade, V. Nikitin, M. Wojcik, A. Deriy, S. Bean, D. Shu, T. Mooney, K. Peterson, P. Kc, K. Li, S. Ali, K. Fezzaa, D. Gürsoy, C. Arico, S. Ouendi, D. Troadec, P. Simon, F. De Carlo, and C. Lethien. “Fast X-ray Nanotomography with Sub-10 nm Resolution as a Powerful Imaging Tool for Nanotechnology and Energy Storage Applications.” In: *Advanced Materials* 33.21 (2021), p. 2008653.
- [3] M. Eckermann, J. Frohn, M. Reichardt, M. Osterhoff, M. Sprung, F. Westermeier, A. Tzankov, C. Werlein, M. Kühnel, D. Jonigk, et al. “3D virtual pathohistology of lung tissue from Covid-19 patients based on phase contrast X-ray tomography.” In: *Elife* 9 (2020), e60408.
- [4] M. Eckermann, M. Töpperwien, T. Ruhwedel, W. Möbius, and T. Salditt. “Evaluation of different heavy-metal stains and embedding media for phase contrast tomography of neuronal tissue.” In: *Developments in X-Ray Tomography XII*. Vol. 11113. International Society for Optics and Photonics. 2019, 111130N.
- [5] I. Ferrer, A. Martinez, S. Boluda, P. Parchi, and M. Barrachina. “Brain banks: benefits, limitations and cautions concerning the use of post-mortem brain tissue for molecular studies.” In: *Cell and Tissue Banking* 9.3 (2008), p. 181.
- [6] S. Flenner, M. Storm, A. Kubec, E. Longo, F. Döring, D. M. Pelt, C. David, M. Müller, and I. Greving. “Pushing the temporal resolution in absorption and Zernike phase contrast nanotomography: enabling fast in situ experiments.” In: *Journal of Synchrotron Radiation* 27.5 (2020).
- [7] T. A. Grünewald, M. Liebi, N. K. Wittig, A. Johannes, T. Sikjaer, L. Rejnmark, Z. Gao, M. Rosenthal, M. Guizar-Sicairos, H. Birkedal, et al. “Mapping the 3D orientation of nanocrystals and nanostructures in human bone: Indications of novel structural features.” In: *Science advances* 6.24 (2020), eaba4171.

- [8] J. Hagemann and T. Salditt. “The fluence–resolution relationship in holographic and coherent diffractive imaging.” In: *Journal of Applied Crystallography* 50.2 (2017), pp. 531–538.
- [9] K. Joppe, J.-D. Nicolas, T. A. Grünewald, M. Eckermann, T. Salditt, and P. Lingor. “Elemental quantification and analysis of structural abnormalities in neurons from Parkinson’s-diseased brains by X-ray fluorescence microscopy and diffraction.” In: *Biomedical Optics Express* 11.7 (2020), pp. 3423–3443.
- [10] G. Rodgers, C. Tanner, G. Schulz, A. Migga, T. Weitkamp, W. Kuo, M. Scheel, M. Osterwalder, V. Kurtcuoglu, and B. Müller. “Impact of fixation and paraffin embedding on mouse brain morphology: a synchrotron radiation-based tomography study.” In: *Developments in X-Ray Tomography XIII*. International Society for Optics and Photonics. 2021.
- [11] J. Romell, V. W. Jie, A. Miettinen, E. Baird, and H. M. Hertz. “Laboratory phase-contrast nanotomography of unstained *Bombus terrestris* compound eyes.” In: *Journal of Microscopy* (2021).
- [12] P. Rostaing, E. Real, L. Siksou, J.-P. Lechaire, T. Boudier, T. M. Boeckers, F. Gertler, E. D. Gundelfinger, A. Triller, and S. Marty. “Analysis of synaptic ultrastructure without fixative using high-pressure freezing and tomography.” In: *European Journal of Neuroscience* 24.12 (2006), pp. 3463–3474.
- [13] J. C. da Silva, A. Pacureanu, Y. Yang, F. Fus, M. Hubert, L. Bloch, M. Salome, S. Bohic, and P. Cloetens. “High-energy cryo x-ray nano-imaging at the ID16A beamline of ESRF.” In: *X-Ray Nanoimaging: Instruments and Methods III*. Vol. 10389. International Society for Optics and Photonics. 2017, 103890F.
- [14] J. Soltau, M. Vassholz, M. Osterhoff, and T. Salditt. “Inline holography with hard x-rays at sub-15 nm resolution.” In: *Optica* 8 (2021), pp. 818–823.

Appendix



A.1 Towards X-ray Fluorescence Tomography

The concentration of chemical elements with spatial resolution can be relevant for questions and hypotheses in the field of neuroscience. Metal overload in human brain tissue can induce “neurotoxicity” due to oxidative stress, mitochondrial dysfunction, or protein misfolding [4]. “Metalloproteins” have metal binding sites, and the family of amyloid precursor proteins (APP) is an example thereof. Owing to the regulating role of these proteins in cellular metal homeostasis, knowledge of the spatial prevalence of metals can help to unravel neurodegenerative disease mechanisms [6]. As such, in Alzheimer’s Disease (AD), higher amounts of A β -deposits have been associated with reduced levels of copper (Cu) [14]. Furthermore, iron (Fe) deposits may be linked to neuropathology in Multiple Sclerosis [9]. Hence, the iron content in calcified vasculature is targeted in this proof-of-concept experiment [20].

Just like the electron-density map from PC-CT, X-ray Fluorescence CT (XRF-CT) yields concentration maps of trace elements [5, 18]. The underlying phenomenon is the X-ray induced emission of characteristic radiation by the specimen. With XRF, up to 10-15 elements can be distinguished [7]. Beyond XRF of naturally deposited trace elements [6], it can also be conducted on nanobody-labelled samples [11]. The advantage of probing with hard X-rays lies in their relatively high tissue penetration depth. The current state of implementing correlative imaging by PC-CT and XRF at the GINIX-endstation is summarized in the following. Note that the analysis scheme has been developed together with Dr. Anna-Lena Robisch. Directions for next steps can be found at the end of this chapter, in the “Discussion and Outlook”-paragraph.

Experimental Setup In this proof-of-concept experiment, a 1 mm cylindric specimen from a FFPE-prepared tissue block of a normal human hippocampus, enclosed by a polyimide tube, was sampled. PC-CT and XRF-CT scans were conducted at the same synchrotron endstation, with an additional PC-CT scan at the laboratory liquid-metal jet setup (“JuLiA”, at 40 keV, 50 s exposure per projection at 1001 angular positions,

$40 \times 10 \mu\text{m}^2$ spot and $0.47 \mu\text{m}$ pixel size, i.e. in inverse high-resolution geometry [21]). Synchrotron data have been collected at the GINIX-endstation (P10 beamline, DESY, Hamburg), during run79.

Fig. A.1(a-c) shows the schematics of the setup. For PC-CT, the sample was probed in cone-beam geometry, with high geometric magnification ($M \approx 40$) using a compound optics of KB-mirrors and X-ray waveguides (WG) [2, 17]. The X-ray energy was set to 7.5 keV, and projections were acquired at 1201 angular positions and 4 defocus

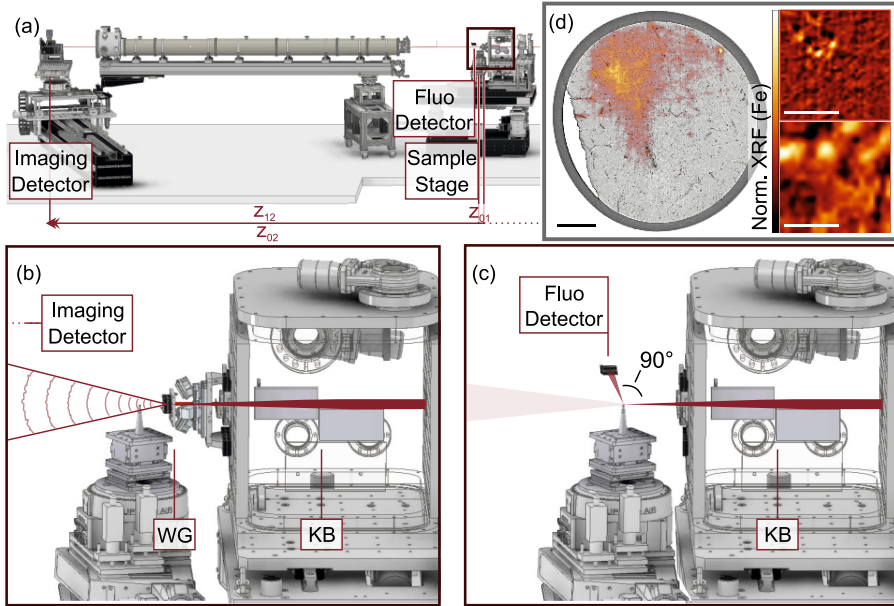


Fig. A.1: Schematics of the GINIX-setup for correlative imaging by XRF-CT and PC-CT. (a) Overview of the endstation, where the X-ray beam enters the setup from the right, and first passes the optics unit which includes the KB-mirrors. For PC-CT imaging in high geometric magnification, a waveguide (WG) in the KB-focus serves as coherent mode filter, with the sample at z_{01} downstream on an air-bearing rotation sample stage, and the imaging detector at $z_{02} \gg z_{01}$ behind the WG or at z_{12} behind the sample, respectively. The MCA (“Fluo Detector”) is in close proximity to the sample stage, at 90° with respect to the beam path. (b) Zoom into the PC-CT setup shows the sample in the defocus position. (c) Zoom into the XRF-CT setup, for which the WG has been removed and the sample inserted into the KB-focus. (d) Overlay of laboratory PC-CT (MIP over $5 \mu\text{m}$) data with XRF-CT reconstructions for the Fe-K_α -peak. XRF-CT data correlate well with the vasculature in the PC-CT slice. Reconstructed slices from further XRF-CT scans are presented to the right, and detailed in Sec. A.1. Scale bars: (d, left) $200 \mu\text{m}$, (right, top) $20 \mu\text{m}$, (right, bottom) $5 \mu\text{m}$.

distances. During PC-CT, the WG-entry was positioned in the KB-focal spot. For XRF-CT scans, the WG-stage was removed from the setup and the sample was translated upstream by $|z_{01}|$, into the KB-focus ($300 \times 350 \mu\text{m}^2$, $h \times v$). Orthogonal to the X-ray beam path, in the KB-focal plane, a multi-channel analyzer (MCA) was integrated for fluorescence detection (Ketek GmbH, 65 mm^2 SDD-chip collimated to 50 mm^2 , energy resolution with $\text{FWHM} \leq 139 \text{ eV}$, and $450 \mu\text{m}$ active thickness). The X-ray energy was set to 8 keV .

Fig. A.1(d) shows a part of the reconstructed slices¹, as a preview. Note that the XRF-reconstruction of the Fe-K_α peak shows plausible agreement with the PC-CT data. However, as detailed further below, radiation-induced sample damage lead to inconsistency in sinograms (cf. Fig. A.2(a)) and hence to flawed reconstructions.

Acquisition Scheme The XRF-CT acquisition is a scanning procedure: An X-ray probe with a limited spatial extension excites sample features *locally*, and the fluorescent emission signal is recorded by 0d-detector (MCA). The 1d projections are recorded by step-wise displacement of the sample. Besides the X-ray spot size, the resolution in XRF-CT is determined by the step size, and the FOV

```
1 numAngles = 18;
2 step = 180/numAngles;
3
4 for (iii=0;iii<=numAngles;iii++){
5     umv stzrot iii*step
6     dscan maccy -1 1 400 0.5
7 }
```

Code A.1: Acquisition scheme of XRFtomo01: cover the entire sample and identify a ROI.

by the number of data points (multiplied by the step size). As for conventional CT scans, such projections are recorded at a number of angles θ , here covering a range of $[0^\circ, 180^\circ]$.

A technical note on the choice of motor for 1d projection scanning: The GINIX tomography stage is equipped with two pairs of motors for positioning of the rotational axis (“stx”, “sty”), and two pairs of motors for positioning of the sample (“cx”, “cy”). The sample positioning accuracy with respect to the probe is higher for cx and cy than it is for stx and sty. However, as their orientation with respect to the setup depends on θ , the dummy motor “maccy” is utilized, which moves cx and cy such that the overall sample repositioning is parallel with sty (perpendicular with the X-ray beam).

¹In Fig. A.1(d), PC-CT data have been recorded with the laboratory setup. Correlative images with WG-based PC-CT can be found in Fig. A.3.

```

1 umvr sty -0.0804
2 umvr cx 0.2239
3 umvr cy 0.2146
4
5 numAngles = 60;
6 step = 180/numAngles;
7
8 for (iii=0;iii<=numAngles;iii++){
9     umv stzrot iii*step
10    dscan maccy -0.02 0.02 40 1
11 }

```

Code A.2: XRFtomo02: ROI-scan at zoom-level 2 (40 μm FOV with 0.98 μm step size).

```

1 umvr cx -0.004
2 umvr cy 0.005
3
4 numAngles = 150;
5 step = 180/numAngles;
6
7 for (iii=0;iii<=numAngles;iii++){
8     umv stzrot iii*step
9     dscan maccy -0.05 0.05 100 1
10 }

```

Code A.4: XRFtomo04: ROI-scan at zoom-level 1 (100 μm FOV with 0.99 μm step size).

```

1 umvr cx 0.004
2 umvr cy -0.005
3
4 numAngles = 30;
5 step = 180/numAngles;
6
7 for (iii=0;iii<=numAngles;iii++){
8     umv stzrot iii*step
9     dscan maccy -0.005 0.005 20 10
10 }

```

Code A.3: XRFtomo03: ROI-scan at zoom-level 3 (10 μm FOV with 0.48 μm step size).

```

1 umv stzrot 0
2 dscan maccy -1 1 400 1
3
4 umv stzrot 180
5 dscan maccy -1 1 400 1
6
7 umv stzrot 90
8 dscan maccy -1 1 400 1
9
10 umv stzrot 270
11 dscan maccy -1 1 400 1

```

Code A.5: Sparse angular-sampling XRF-CT: scans at orthogonal angular positions (at 0°, 90°, 180°, 270°) covering a FOV of 2 mm which exceeds the sample diameter (1 mm), in order to identify the center of rotation.

Codes A.1-A.5 show the SPEC-macros. Note that their order follows the sequence of scans performed during run79, which may facilitate data identification. First, a ROI with a fluorescent feature was localized in XRFtomo01, Code A.1. This feature was highlighted in XRFtomo02-04, see Code A.2-A.4. Finally, the center of rotation for tomographic reconstruction was identified with the scan presented in Code A.5. Further note that these scans serve tomographic reconstruction of 2d planes. In order

to reconstruct 3d volumes, additional scanning in parallel with the rotation axis is required.

Data Reconstruction Code A.6 shows a Matlab script for tomographic reconstruction of XRF data. It starts with loading the toolbox [13] and XRF-CT scan specifications. The tomographic data are stored in the 3d array “fluoDat”, where the first dimension contains the angular position, the second the lateral scan data and the third the counts per energy channel. Here, the actual angular and lateral positions from the encoder are utilized. Note that it is important to correct the counts by the detector deadtime “dt-Corr”, which is stored in the SPEC file. Fig. A.2(a) depicts the spectrum of XRFtomo02, with prominent peaks at the probe energy and the Fe- K_{α} line at 6.4 keV [10]. The sinogram is based on the total counts in the channels of interest, see (b). Here, the entire spectrum can be utilized, which is dominated by the probe peak, or single regimes can be selected, such as the Fe- K_{α} regime ($Z_{\text{Fe}} = 26$). The center of rotation has been identified beforehand, based on the data from Code A.5 as illustrated in Fig. A.2(c & d): the projection data at $\theta = 0^{\circ}$ (“reference scan”) are compared with the flipped and shifted data at $\theta = 180^{\circ}$ (“match scan”). Here, the profile clearly features the 1 mm sample tube and demonstrates that the detected signal originates from the sample. Finally, basic tomographic reconstruction is done, using the inverse Radon transform. Since the angular data are strongly undersampled, sinograms can be additionally filtered beforehand.

Fig. A.3 shows correlative overlays between the XRF-CT data 1-3 and the laboratory PC-CT. The PC-CT data have been collected before the XRF-CT scans. While the Fe- K_{α} -map matches considerably well with the vasculature identified with PC-CT, the correlation is less prompt for the ROI-scans XRFtomo02-03. This can not only be attributed to the error-prone local tomography, but may also be ascribed to radiation damage, which is highlighted in the next paragraph.

Manual Feature Correlation The correlative data shown in Fig. A.3 have been identified manually, supported by the motor positions cx , cy and sty . In particular the identification of the XRF-CT plane along the rotation axis was facilitate by the fact that the sample suffered from radiation damage as a result of the numerous exposures to the KB-beam focus, which can easily reach $5 \cdot 10^{11}$ ph/s. Again, Fig. A.4(a) shows the slice from laboratory PC-CT, with a red square which marks the position of the synchrotron PC-CT scan *after* XRF-CT. These PC-CT data are presented in (b), with a perpendicular slice in (c). (b) reveals that most of the tissue features heavily degraded

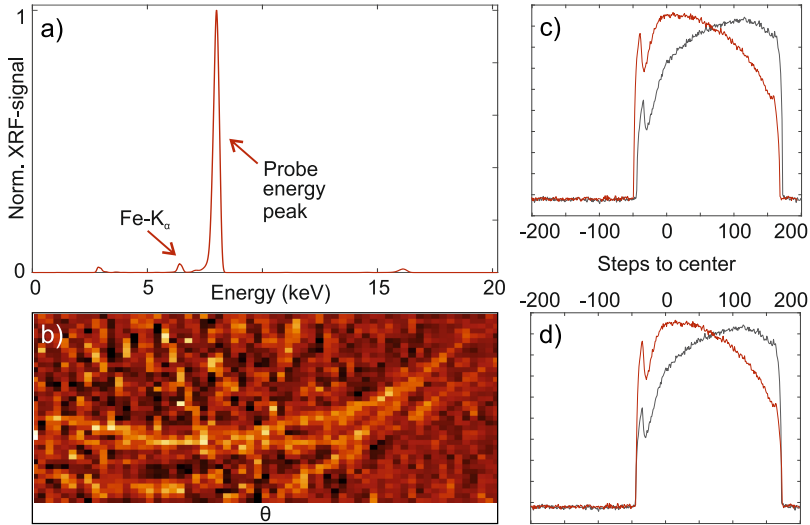


Fig. A.2: XRF-CT reconstruction. (a) Plot of the spectrum of XRFtomo02, with the sinogram in (b). (c & d) Plots of the projections at $\theta = 0^\circ$ (“reference scan”) and the flipped at $\theta = 180^\circ$ (“match scan”). In (c) the center of rotation is off about 5 pixels, in (d) it is well-centered.

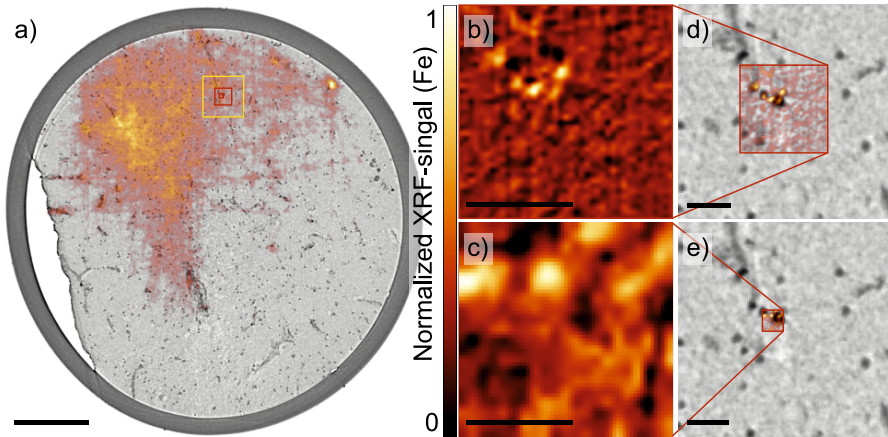


Fig. A.3: Overlay of laboratory PC-CT (MIP over $5\ \mu\text{m}$) data with XRF-CT reconstructions for the $\text{Fe-K}\alpha$ -peak. (a) XRFtomo01 correlates well with the vasculature in the PC-CT slice. From the motor positions, the location of XRFtomo04 was identified (yellow square), as well as of XRFtomo02-03 (red squares), which are detailed in (b & d) and (c & e), respectively. Scale bars: (a) $200\ \mu\text{m}$, (b, d & e) $20\ \mu\text{m}$, (c) $5\ \mu\text{m}$.

due to in-focus scanning. (c) demonstrates that this observation is limited to a region of $5\ \mu\text{m}$ thickness, and that outside features are well-preserved. It remains unclear at which point of the sequence of XRF-CT scans the radiation damage set in. Again, a yellow square in (a) marks the region of XRFtomo04. The insets show the XRF-CT slice and in combination with the PC-CT data, according to the motor positions. With the low degree of correlation, the low degree of features in the XRF-CT slice and the fact that XRFtomo04 has been conducted as the final scan, the radiation damage stands out at this point.

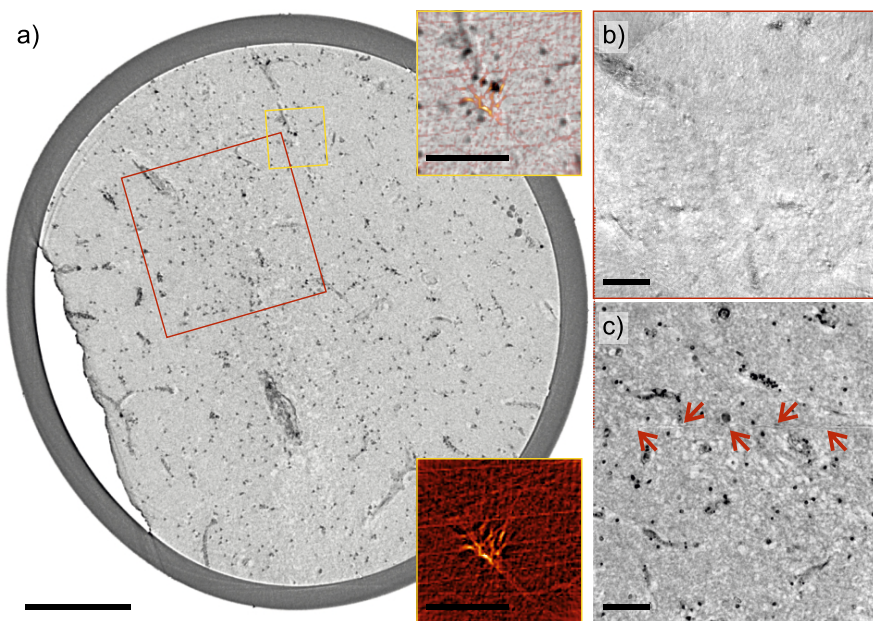


Fig. A.4: Radiation damage from extensive XRF-CT scanning: (a) A wealth of features emerges in the laboratory PC-CT scan *before* the XRF-CT scans. The yellow square indicates the position of XRFtomo04, shown in the insets. The red square marks the position of the synchrotron PC-CT scan *after* the sequence of XRF-CT scans, and the data are shown in (b), and in perpendicular view in (c). The target area of the probe comes out prominently as a $5\ \mu\text{m}$ -thick horizontal line of radiation damage in (c), with heavy sacrifice in features in (b). Scale bars: (a) $200\ \mu\text{m}$, (otherwise) $50\ \mu\text{m}$.

Automatic Correlation Further to manual data correlation, a concept for automatic correlation has been developed, in order to identify XRF-CT positions in PC-CT data based on a Matlab script, see Code A.7. In this procedure, four parameters are tuned: relative rotation, horizontal and vertical shifts, as well as the position of the slice. After

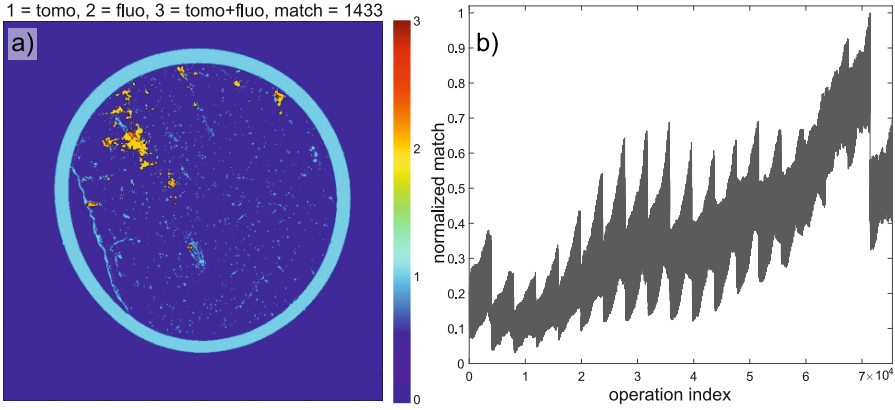


Fig. A.5: Automatic feature correlation of exemplary XRF-CT with PC-CT data: (a) Output of the Matlab script in Code A.7, and (b) plot of the masks-correlation parameter “match”.

loading the toolbox and both datasets, the first part consists of finding rough ranges of these four parameters by manual tuning. For correlation, appropriate thresholds for both datasets are identified, such that features are adequately delineated in the masks. Subsequently, in a sequence of *for*-loops, the four parameters are varied within these ranges. For each combination of parameters, the correlation indicator “match” is calculated as follows: thresholded features from PC-CT are assigned the value “1”, XRF-CT features “2”, and when a pixel is true for “1” and “2”, it is assigned a “3” (a “true” in the overall match map “m”). The array “match” is then assigned the number of pixels with value “true” in “m”. Note that the sample polyimide container is disregarded here, as “mask” is applied. Fig. A.5(a) shows an exemplary live output. Finally, for the set of parameters for which “match” is maximum (cf. Fig. A.5(b)), both maps match best.

Discussion and Outlook In this experiment, calcified blood vessels were probed by correlative XRF-CT and PC-CT. The X-ray energy was set to 8 keV, thus exciting elements with $Z \leq 27$. For future experiments in neurodegenerative studies, the X-ray beam energy can be selected according to the metalloprotein of interest [1]. Additionally, Tab. A.1 can serve as a basis: it lists the trace elements in a *normal* human brain with their mole percentage as reported in [16], and further the respective atomic number Z , the K 1s electron binding energy and the K_{α} emission line. Note that, as reviewed in [8], the measured quantity of trace elements strongly depends on the experimental procedure, and shall give only a first idea at this point. In this perspective,

	Cerebellum (%)	Hippocampus (%)	Frontal Cortex (%)	Z	K 1s (keV)	K_{α} (keV)
Na	35.5	45.7	34.0	11	1.07	1.0
K	33.7	24.9	30.0	19	3.61	3.3
P	22.4	23.9	29.3	15	2.15	2.0
Ca	2.1	1.2	1.7	20	4.04	3.7
Mg	3.99	1.86	2.54	12	1.30	1.3
Al	1.34	1.62	1.64	13	1.56	1.5
Fe	0.45	0.18	0.34	26	7.11	6.4
Si	0.28	0.58	0.35	14	1.84	1.7
Zn	0.07	0.04	0.04	30	9.66	8.6
Cu	0.07	0.02	0.02	29	8.98	8.0

Table A.1: Trace elements in human brain tissue according to [16]. Their mole percentage is given for selected brain regions. K 1s electron binding energies and K_{α} emission lines were taken from [10].

advanced XRF can potentially contribute to the quantification of trace elements in human tissues. Regarding the probe, a higher probe energy excites higher- Z elements with higher K_{α} emission lines, and induces less energy deposition inside the sample. In this context, the maximum sample diameter is limited by its X-ray absorption: in [11], the authors argue the maximum sample thickness from the fact that it shows 50% X-ray transmission. For the irradiation of 1 mm paraffin ($C_{30}H_{62}$) with X-rays of 8 keV, about 43% transmission can be expected [10]. However, in [11], X-rays with an energy of 24.1 keV were utilized. For a higher probe energy, the fluorescence signal stems from higher- Z atoms, which have their major emission lines at a higher energy than those of lower- Z atoms. For atoms with $Z \leq 19$, self-absorption becomes problematic [7]. Experiments in which lower emission energies are expected, can benefit from a fly tube between the sample and the detector. In [6], 2d XRF imaging has been conducted on 12 μm -thick, unstained and air-dried brain slices of APP and APLP2 knock-out mice at 10 keV. The sample diameter for future XRF-experiments

at the GINIX-endstation should possibly be reconsidered, as well as the embedding material in view of radiation damage. In this context, the total dose deposition in the sample should be evaluated in detail. Furthermore, in order to better account for self-absorption, 360°-tomography scans are preferred to 180° [12]. For the same reason, the readily availability of an imaging detector should also be exploited in order to collect “transmission maps” [7].

Concerning the tomographic reconstructions in Fig. A.1(d), a simple inverse Radon transformation with an additional sinogram filter to account for sparse angular sampling has been applied ². The CNR in XRF-data is of particular concern [7], and reduced noise has been reported for iterative tomographic reconstruction [3].

```

1 %% Add HoloTomoToolbox (10.1107/S1600577520002398)
2
3 %% Prepare - fluo data
4 filePrefix = 'HH_P6916-4_p1_fluo03'; % scan prefix
5 prePath = ['S:/Messzeiten/2018/GINIX/run79/data/raw/20181027/']; % data
   path
6 detector = 'mca'; % detector name
7 getDumpName = @(number) fullfile([prePath, '/', detector, '/', filePrefix], '
   dump', sprintf(['_%04i.dat.txt'], number));
8
9 offset = 0; % data number offset for this scan in the directory
10 numAngles = 61; % number of projection angles
11 numPositions = 41; % number of lateral scan positions
12 numChannels = 4096; % number of energy bins
13 fluoDat = zeros(numAngles, numPositions, numChannels);
14 thetas = zeros(numAngles, 1);
15 position = zeros(numPositions, 1);
16
17 %% Read in - mca data
18 specScan = 31; % offset for scan number in spec files
19 specColumn = 26; % column of dead time correction factor in spec files
20
21 for ang=1:numAngles
22     disp(ang);
23     specScan = specScan+1;
24     % read deadtime correction factor
25     dtCorr = unspec([prePath, 'spec/'], filePrefix, specScan, specColumn);
26
27     for dat=1:numPositions

```

²Consulting the angular sampling criteria from Sec. 1.5.3, it becomes clear that this criteria is satisfied for scans Code A.2-A.4, but not for A.1. The filter consists of a Ram-Lak filter to which a cutoff has been applied in real space.

```

28     datNum = (ang-1)*numPositions+dat+offset;
29     filePath = [prePath,detector,'/',filePrefix,'/',filePrefix,'_',
sprintf('%04d',datNum),'.dat'];
30     FID=fopen(filePath);
31     dataCell = textscan(FID, '%f%f%f','CommentStyle','#');
32     fclose(FID);
33
34     % read projection angle, lateral dummy motor
35     thetas(ang) = wwas(getDumpName(datNum),'stzrot');
36     position(dat) = wwas(getDumpName(datNum),'maccy');
37
38     counts = dataCell{3}/dtCorr(dat);
39     fluoDat(ang,dat,:) = squeeze(counts);
40 end
41 end
42
43 %% Assign energy bins
44 spectrum = squeeze(sum(sum(fluoDat,1),2));
45 ChPrimary = find(spectrum==max(spectrum)); % energy channel of probe
46 ChFe = find(spectrum==max(spectrum(1000:ChPrimary-150))); % energy channel
    of Fe, Kalpha (doublecheck!)
47
48 %% Reconstruct XRF-CT slice - all channels
49 shift = 0; % use shift from sparse angular-sampling fluotomo
50 padval = 20; % sinogram padding
51 sino = sum(fluoDat(ang, :, :), 3)';
52
53 % fft filter optimized for undersampled angles < pi/2*nx
54 sino = filter_fewangles(padarray(sino,[padval,0],'replicate'),10);
55
56 figure(1)
57 showImage(sino)
58 colormap hot
59
60 sino = sub_circshift(sino,[shift 0]);
61 slice = iradon(sino,thetas,'linear','Ram-Lak',1,numPositions);
62
63 figure(2)
64 showImage(imresize(slice,3))
65 colormap hot
66
67 %% Reconstruct XRF-CT slice - Fe-channel
68 sinoFe = sum(fluoDat(angle, :, ChFe-34:ChFe+34), 3)';
69 sinoFe = filter_fewangles(padarray(sinoFe,[padval,0],'replicate'),10);
70

```

```

71 figure(3)
72 showImage(sinoFe)
73 colormap hot
74
75 sinoFe = sub_circshift(sinoFe,[shift 0]);
76 sliceFe = iradon(sinoFe,thetas,'linear','Ram-Lak',1,numPositions);
77
78 figure(4)
79 showImage(imresize(sliceFe,3))
80 colormap hot
81
82 %% Emphasize Fe localizations
83 figure(5)
84 showImage(slice+50*sliceFe)
85 colormap hot

```

Code A.6: Matlab code to reconstruct XRF-CT slices.

```

1 %% Add HoloTomoToolbox (10.1107/S1600577520002398)
2
3 %% Read in
4 fluoOverview = ... ; % XRF-CT data
5 slices = ...; % PC-CT data
6
7 %% Bring XRF and PC data to same pixel size & scale
8 pixelSizeFluo = ...;
9 pixelSizePC = ...;
10 fluoOverview = imresize(fluoOverview, pixelSizeFluo/pixelSizePC)/ max(
    fluoOverview(:));
11
12 %% Find correct orientation of PC-CT data - first (rough) manual alignment
13 shiftV = ...; % adjust vertical shift
14 shiftH = ...; % adjust horizontal shift
15 rot = ...; % adjust rotation
16 thrFluo = ...; % find appropriate mask threshold for fluotomo data
17 fluoBin = cut2Darray(imrotate(circshift(fluoOverview,[shiftV shiftH]),rot)
    , size(stmp,2), size(stmp,1));
18 fluoBin = fluoBin.*(fluoBin>thrFluo);
19
20 sliceNo = ...; % select slice number
21 thrPC = ...; % find appropriate mask threshold for PC-CT data
22 stmp = slices(:,:,sliceNo);
23 stmp = stmp / max(stmp(:));
24 stmpBin = stmp>thrPC;
25
26 % Overlay both slices

```

```

27 figure(1)
28 image_s(stmpBin+2*fluoBin)
29 axis equal tight
30 colormap jet
31
32 %% Find suitable range of slices that fit to XRF-Data
33 halfRange = 10; % adjust this parameter if appropriate
34 slices2corr = slices(:, :, sliceNo - halfRange : sliceNo + halfRange) ;
35 slices2corr = slices2corr ./ max(max(slices2corr));
36
37 %% Create circular mask to disregard Kapton tube during automatic matching
38 radius = ...; % adjust radius of mask
39 centerV = ...; % adjust center position of mask
40 centerH = ...;
41 [xx,yy] = ndgrid((1:size(slices,1))-centerV,(1:size(slices,2))-centerH);
42 mask = (xx.^2 + yy.^2)>radius^2;
43 image_s(mask.*stmp)
44
45 %% Automatic feature matching
46 clear match
47
48 % Set ranges according to first manual matching
49 rotStart = ...; rotEnd = ...; % interval for rot. alignment
50 rotStep = 1; % adjust this parameter if appropriate
51 shiftVertStart = ...; shiftVertEnd = ...; % interval for vert. shift
    alignment
52 shiftVertStep = 2; % adjust this parameter if appropriate
53 shiftHorStart = ...; shiftHorEnd = ...; % interval for hori. shift
    alignment
54 shiftHorStep = 2; % adjust this parameter if appropriate
55
56 for rot = rotStart:rotStep:rotEnd
57     disp(rot)
58     tic
59     for shiftV = shiftVertStart:shiftVertStep:shiftVertEnd
60         for shiftH = shiftHorStart:shiftHorStep:shiftHorEnd
61             fluoShift = (cut2Darray(imrotate(circshift(fluoOverview,[
    shiftV shiftH])), rot), size(stmp,2), size(stmp,1)) ) ;
62             for idx = 2 : size(slices2corr,3)-1
63                 stmp = mean(slices2corr(:,:,idx-1:idx+1),3);
64                 mfluo = fluoShift > thrFluo ;
65                 mstmp = stmp > thrPC ;
66
67                 % live viewer
68                 figure(1)

```

```

69         showImage((mstmp + 2*mfluo))
70         m = mstmp + 2*mfluo == 3;
71         match((rot-(rotStart-rotStep))/rotStep,(shiftV-(
shiftVertStart-shiftVertStep))/shiftVertStep,(shiftH-(shiftHorStart-
shiftHorStep))/shiftHorStep,idx-1) = sum(m(:))-sum(sum(m.*mask));
72
73         t = sprintf('%s%i', '1 = tomo, 2 = fluo, 3 = tomo+fluo,
match = ', match((rot-(rotStart-rotStep))/rotStep,(shiftV-(
shiftVertStart-shiftVertStep))/shiftVertStep,(shiftH-(shiftHorStart-
shiftHorStep))/shiftHorStep,idx-1));
74         title(t)
75         colorbar; colormap jet; drawnow()
76     end
77 end
78 end
79 toc
80 end
81
82 %% Plot correlation parameter
83 figure(2)
84 plot(match(:)/max(match(:)))
85 xlim([0,length(match(:))-1])
86 ylim([0 1.02])
87
88 %% Get index of maximum agreement, and index of second maximum
89 [rotIndMax shiftVIndMax shiftHIndMax sliceIndMax]=ind2sub([size(match,1)
size(match,2) size(match,3) size(match,4)],find(match(:)==max(max(
match(:)))));
90 scndmax = match;
91 scndmax(find(match(:)==max(match(:))))=0;
92 [rotIndMax2 shiftVIndMax2 shiftHIndMax2 sliceIndMax2]=ind2sub([size(match,
1) size(match,2) size(match,3) size(match,4)],find(scndmax==max(
scndmax(:)))));
93
94 %% Compute rotation, vertical and horizontal shift and slice number from
the respective index
95 rotMax = rotIndMax*rotStep+shiftVertStart-shiftVertStep;
96 rotMax2 = shiftVIndMax*shiftVertStep+shiftVertStart-shiftVertStep;
97 shiftVMax = shiftVIndMax*shiftVertStep+shiftVertStart-shiftVertStep;
98 shiftVMax2 = shiftVIndMax2*shiftVertStep+shiftVertStart-shiftVertStep;
99 shiftHMax = shiftHIndMax*shiftHorStep+shiftHorStart-shiftHorStep;
100 shiftHMax2 = shiftHIndMax2*shiftHorStep+shiftHorStart-shiftHorStep;
101 sliceMax = sliceIndMax+1; % refers to array: slices2corr
102 sliceMax2 = sliceIndMax2+1; % refers to array: slices2corr
103

```

```

104 %% Save workspace
105 save('workspace_correlation')

```

Code A.7: Matlab code to automatically correlate XRF-CT with PC-CT data.

A.2 Further Details on Working with the Nanofocus PC-CT Setup TINA

In the course of this thesis, the TINA-setup (“Transmission Anode Imaging at the Nanoscale”) was designed for PC-CT experiments at sub- μm voxel size. Its characteristic hardware consists of Excillum’s NanoTube X-ray source and a single-photon counting detector Timepix (X-ray Imaging Europe Hexa H05-W0154, 500 μm Si-sensor, 516×774 pixels of 55 μm). Alternatively, the scintillator-based detector Thyia is also integrated (Photonic Science FDS Serial Number 316310, 5 μm LuAg:Ce scintillator, 2208×2744 pixels of 4.54 μm). Further details on the setup and first results can be found in Ch. 2. Note that the data from Ch. 2 stem from the NanoTube N1 source, which has been upgraded in November 2020 to NanoTube N2 for reasons of increased flux and spot stability. Post-upgrade results can be found in Ch. 3.

Owing to the fact that TINA is designed for high-resolution PC-CT at a particularly short source-sample distance z_{01} , the setup shows some peculiarities. In the following, a collection of useful hints for working with this setup, and introductions into the PC-CT data acquisition as well as reconstruction are given.

Hints for the Alignment Procedure

- Conventionally, a TEM-grid is used for rotation axis alignment at the different PC-CT setups at the Institute for X-ray Physics. If $z_{01} \lesssim 1.5$ mm, the TEM-grid can not be used for alignment procedures during which the sample is rotated, since its diameter is 3 mm. In these cases, the TEM-grid should be used for the nick angle alignment (“mat_align_nick(...”), and then exchanged for a tungsten needle to continue with the estimation of the effective pixel size and the lateral rotation axis alignment (“mat_pixelsize(...”, “mat_align_rotaxis(...”).
- For the TINA-setup, TEM-grids on Huber pins have been customized: a slit in the pin allows to mount the grid central to the pin for increased alignment precision.
- The TEM-grid is very thin and may be twisted, such that it is advantageous to use its lower part, close to the pin.

- In order to not get lost in the periodicity of the TEM-grid, its outer frame should be in the FOV.
- Bear in mind that the Timepix detector has a dummy motor “thl”, which sets the energy threshold (in keV) in the software “Pixelman”. It was found that thl= 5 is appropriate to mitigate hot pixels and not miss essential image information.

Acquisition Scheme Code A.8 shows an exemplary PC-CT SPEC-macro at the TINa-setup. Depending on the exact configuration (width of sample which limits the minimal z_{01} , in combination with the desired pixel size determining the corresponding source-detector distance z_{02}), the photon flux in the detector plane z_{02} can be low such that long exposures, on the order of tens of seconds, are necessary. In order to also reduce the characteristic ring artifacts, which occur in reconstructions with Timepix-data, it proved advantageous to record several identical tomography scans (sets, “nsets”) and afterwards register and combine the projections to a single dataset with effective long exposures per projection. Further, for reasons of overall stability, empty images are recorded with the “cy” motor at “szrot= 0”. Still, imprecisions in the cy-position have been found to accumulate. In order to correct for these imprecisions, and potential source spot drift, reference recordings (“doreference”, “numref”) have been introduced. When these shall be used, it is important to choose “cx_ref” and “cy_ref” such that a strong feature (sample edge, for instance) is in the center of the FOV at 0° and 90°, respectively³. Another utility of the reference scans is the facilitated identification of the center of rotation during tomographic reconstruction. Finally, dark images can be collected, but are not required for single-photon counting detectors.

```

1 # Tomoscan macro
2 # Filename: *newfile*
3 # Started on day month dd hh:mm:ss yyyy
4 # Total counting time: xx h
5
6 # Start position
7 x_start = ...;
8 y_start = ...;
9 z_start = ...;
10 cx_start = ...;
11 cy_start = ...;
12 rot_start = ...;

```

³Reference images are only recorded at 0° and 180°. The centering at 90° is still required to maintain the geometric magnification for all reference images.

```

13 cx_ref = ...; # choose ref. pos. s.t. strong feature (edge) is centered
14
15 # Scan parameters
16 numflats = 50; # number of flats
17 numdarks = 10; # number of darks
18 numaccumulations = 1; # number of consecutive, identical projections
19 ctime = 1.4; # acquisition time
20 range = 192; # angular projection range
21 nprojs = 1200; # number of projections
22 interpolate = 0; # move projections to interpolate module gaps with data?
23 nsets = 6; # number of consecutive tomo scans
24 doreference = 1; # take reference projections?
25 numref = 10; # number of reference projections
26
27 # Move to start position
28 umv sx x_start
29 umv sy y_start
30 umv sz z_start
31 umv cx cx_start
32 umv cy cy_start
33 umv szrot 0
34 umv thl 5 # energy threshold timepix (keV)
35
36 # Tomo scan
37 for (i_set=1;i_set<=nsets;i_set++){
38     # Take empty images
39     mat_newflat numflats ctime
40
41     # Take reference projections
42     if (doreference == 1){
43         umv cx cx_ref
44         umv cy cy_ref
45         loopscan numref/2 ctime
46         umv cx cx_start
47         umv cy cy_start
48         ascan szrot rot_start range numref ctime
49     }
50     umv szrot 0
51
52     # Tomo scan
53     step = range/nprojs
54     if (interpolate == 0){
55         ascan szrot rot_start range nprojs ctime
56     }
57     else{

```

```

58     umvr sz psize()*5/1000
59     for (z_rot=rot_start;z_rot<=range;z_rot+=(2*step)){
60         umvr sz -psize()*10/1000
61         umv szrot z_rot
62         sleep(1)
63         ct ctime
64         umvr sz psize()*10/1000
65         umv szrot z_rot+step
66         sleep(1)
67         ct ctime
68     }
69     umv sz z_start
70 }
71
72 # Take reference projections
73 if (doreference == 1){
74     umv szrot 180
75     umv cx cx_ref
76     umv cy cy_ref
77     loopscan numref/2 ctime
78     umv cx cx_start
79     umv cy cy_start
80     umv szrot 0
81 }
82 }
83 umv szrot 0
84
85 # Take reference projections
86 if (doreference == 1){
87     umv cx cx_ref
88     umv cy cy_ref
89     loopscan numref/2 ctime
90     umv cx cx_start
91     umv cy cy_start;}
92
93 # Take empty images
94 mat_newflat numflats ctime
95
96 jxs_off
97
98 # Take dark images
99 sleep(300)
100 loopscan numdarks ctime

```

Code A.8: SPEC macro for PC-CT measurements with TiNa.

Recommendations for the Choice of Experimental Parameters In particular for the studies in Ch. 2 and 3, experimental parameters for different settings have been optimized. Tab. A.2 details these settings for the TINa-setup, and, since it may be useful as well, Tab. A.3 for the other in-house nanofocus PC-CT setup “EasyTom” (EasyTom Nano with CCD-camera, RX Solutions, [19]).

	<i>Overview</i>	<i>Detailed I</i>	<i>Detailed IIa</i>	<i>Detailed IIb</i>
Acc. Voltage (kV)	60	60	60	60
Spot Size (μm)	1.00	0.50	0.30	0.30
N_{proj}	1201	1201	1201	1201
N_{sets}	1	4	6	14
z_{01} (mm)	3.5	1.5	1.1	1.4
z_{02} (mm)	200	200	200	218
px (μm)	1.00	0.41	0.30	0.35
ct (s)	1.3	1.8	7.5	9
t_{tot} (h)	3	3	12	46

Table A.2: Recommended settings for three different zoom-levels at the TINa Nano setup. Note that z_{01} can be adjusted depending on the sample size, and that z_{02} and ct may be adapted accordingly. Further, *Overview*, *Detailed I* and *Detailed IIa* have been optimized for NanoTube N1 (ct has been updated for the usage of N2), and *Detailed IIb* for NanoTube N2.

Reconstruction Script Due to the special data recording scheme introduced above, reconstruction of TINa-data follows an adapted procedure, see Code A.9. The Matlab-script consist in large part of the correct data assignment, processing (including module gap interpolation and flat image correction), and shift correction based on reference images (including matching the projection angles “thetas”/“thetasIdx”, interpolation, and visual inspection and saving of the output).

Note that often, the sample exceeds the projection FOV, which makes the identification of the center of rotation challenging. In such cases, the reference images can give a first approach towards the correct value, which should be further finetuned in test reconstructions.

```

1 %% Scan parameters
2 year = '2021';
3 runname = '2021_04_27';

```

	<i>Overview</i>	<i>Detailed</i>
Acc. Voltage (kV)	60	60
Spot Mode	“middle”	“small”
N_{proj}	3008	1568
Proj. Scheme	6 turns + ref.	6 turns + ref.
z_{01} (mm)	5	5
z_{02} (mm)	98	278
px (μm)	0.99	0.35
ct (s)	12×1.7	5×10
t_{tot} (h)	9	46

Table A.3: Recommended settings for two different zoom-levels at the EasyTom Nano setup. Note that the acceleration voltage has been optimized for heavy metal stained samples (ROTO, OsO₄). For small focal spot mode, the X-ray beam should be focused manually.

```

4 runnameDark = runname;
5 detector = 'TIMEPIX';
6 detector = lower(detector);
7
8 filePrefix = ...;
9 filePrefixDark = filePrefix; # change if darks have different location
10
11 rotMotor = 'szrot';
12 angRange = 192;
13 numProjs = 1200;
14 interpolate = 0;
15 nsets = 6;
16 doRef = 1;
17 numRef = 10;
18
19 numAverage = 1;
20 numFlats = 50;
21 numDarks = 10;
22 numAngles = numProjs+1;
23 numRef = numRef+1;
24
25 z02 = 202.7;
26 z01Corr = 0; % in mm; correction offset for source-sample distance wrt to
    sx motor position
27

```

```

28 %% Load toolboxes and set paths
29 % Add HoloTomoToolbox (10.1107/S1600577520002398)
30 % Add ASTRA-toolbox (10.1016/j.ultramic.2015.05.002, 10.1364/OE.24.025129)
31 prePath = 'B:/' ; % mount of TiNa network drive
32
33 dataPath = fullfile(prePath, year, 'tina' , runname, 'detectors', detector
    , filePrefix);
34 darkPath = fullfile(prePath, year, 'tina' , runnameDark, 'detectors',
    detector, filePrefixDark);
35
36 %% Set up image reader for the specified detector
37 imageReader = getImageReaderIRP(detector);
38
39 switch(lower(detector))
40     case 'thya'
41         fileEnding = '%i.tif'; dumpEnding = '%05i.tif.txt';
42         dx = 4.5e-6;
43     case 'timepix'
44         fileEnding = '%05i.raw'; dumpEnding = '%05i.raw.txt';
45         dx = 55e-6;
46 end
47
48 fileName = [filePrefix,fileEnding];
49 dumpName = [filePrefix,dumpEnding];
50 getFileName = @(number) fullfile(dataPath, sprintf(fileName,number));
51 getDumpName = @(number) fullfile(dataPath,'dump',sprintf(dumpName,number))
    ;
52
53 fileNameDark = [filePrefixDark,fileEnding];
54 getFileNameDark = @(number) fullfile(darkPath, sprintf(fileNameDark,number)
    );
55
56 %% Read first projection to check if path is correct
57 raw = imageReader(getFileName(numFlats+1));
58 showImage(raw);
59 colormap gray
60
61 %% Set image numbers
62 clear emptynumbers;
63 emptynumbers{1} = 1:numFlats;
64
65 if doRef == 1
66     refnumbers{1} = numFlats+1:numFlats+doRef*round((numRef-1)/2);
67     refnumbers{2} = numFlats+doRef*round((numRef-1)*1.5)+numAngles+2:
        numFlats+doRef*round((numRef-1)*2)+numAngles+1;

```

```

68     refnumbers{3} = numFlats+doRef*round(0.5*(numRef-1))+1:numFlats+doRef*
        round(1.5*(numRef-1))+1;
69 end
70
71 % first image of tomo scan
72 numFirstangle = numFlats+doRef*round(numRef*1.5-1)+1;
73 numLastangle = numFlats+doRef*round(numRef*1.5-1)+numAngles*numAverage;
74
75 % first image at each projection angle
76 rawnumbers = numFirstangle:numAverage:numLastangle;
77
78 % empty images after tomo scan
79 emptynumbers{2} = numLastangle+1:numLastangle+numFlats;
80
81 % darkfields
82 darknumbers = numFlats + (nsets+1)*(numFlats+numAngles+doRef*numRef)-
        numAngles + doRef*round((numRef-1)/2) : numFlats + (nsets+1)*
        (numFlats+numAngles+doRef*numRef)-numAngles + doRef*round((numRef-1)/2
        ) + numDarks -1;
83 % darknumbers = ...; % otherwise insert here manually
84
85 %% Read darkfields
86 darks = zeros([size(raw), numDarks], 'single');
87 for indDark=1: numel(darknumbers)
88     tmp = imageReader(getFileName(darknumbers(indDark)));
89     darks(:, :, indDark) = tmp;
90     fprintf('. ');
91 end
92 fprintf('\n');
93 dark = median(darks,3);
94 % dark = 0; % use this if no darks are available
95
96 %% for-loop to read data from different tomo-scans
97 binningFactor=1; % factor for binning of detector pixels, factor 1 does
        nothing
98 projs = zeros([size(raw,1)/binningFactor,size(raw,2)/binningFactor,
        numAngles,nsets], 'single');
99 thetas = zeros([numAngles,nsets], 'single');
100
101 if doRef == 1
102     shifts = zeros([2,nsets+1], 'single');
103     projsRef = zeros([size(raw,1)/binningFactor,size(raw,2)/binningFactor,
        numRef,nsets], 'single');
104     projsRefStat = zeros([size(raw,1)/binningFactor,size(raw,2)/
        binningFactor,2,nsets+1], 'single');

```

```

105     thetasRef = zeros([numRef,nsets],'single');
106 end
107
108 for iScan=1:nsets
109     % read empty images
110     emptys = cell(numel(emptynumbers),1);
111
112     for j=1:numel(emptynumbers)
113         x = 0;
114         emptys{j} = zeros(size(raw));
115         for indEmpty=1:numel(emptynumbers{j})
116             % read image
117             if (iScan==nsets)
118                 if (j==1)
119                     tmp = imageReader(getFileName(413+emptynumbers{j}(
120 indEmpty)+10+(numAngles+numFlats+doRef*(2*numRef-1))*(iScan-1)+round
121 ((numRef-1)/2)));
122                     else
123                         tmp = imageReader(getFileName(413+emptynumbers{j}(
124 indEmpty)+20+(numAngles+numFlats+doRef*(2*numRef-1))*(iScan-1)+round
125 ((numRef-1)/2)));
126                     end
127                 else
128                     tmp = imageReader(getFileName(emptynumbers{j}(indEmpty)+(
129 numAngles+numFlats+doRef*(2*numRef-1))*(iScan-1)));
130                 end
131                 emptys{j} = emptys{j} + tmp;
132                 x=x+1;
133                 fprintf('.');
134             end
135             fprintf('\n');
136             emptys{j} = emptys{j}/x;
137         end
138     end
139
140 % read reference images
141 if doRef == 1
142     settingsOutliers.threshold = 1.5;
143     for ii = 1:2
144         tmp = zeros(size(raw),'single');
145         for indRef = 1:round((numRef-1)/2)
146             number = refnumbers{ii}(indRef);
147             if (iScan==nsets)
148                 raw = imageReader(getFileName(413+15+number+(numAngles
149 +numFlats+doRef*(2*numRef-1))*(iScan-1)));

```

```

144         else
145             raw = imageReader(getFileName(number+(numAngles+
numFlats+doRef*(2*numRef-1))*(iScan-1)));
146         end
147
148         if binningFactor~=1
149             raw = imresize((raw-dark)./(emptys{1}-dark),1/
binningFactor);
150         else
151             raw = (raw-dark)./(emptys{1}-dark);
152         end
153         tmp = tmp+raw;
154     end
155     tmp = tmp/round((numRef-1)/2);
156
157     for l=1:size(tmp,1) % treat detector gaps
158         tmp(l,253:263) = interp1([1,2,10,11],[tmp(l,253),tmp(l,254
),tmp(l,262),tmp(l,263)],[1:11]);
159         tmp(l,512:522) = interp1([1,2,10,11],[tmp(l,512),tmp(l,513
),tmp(l,521),tmp(l,522)],[1:11]);
160     end
161     for l=1:size(tmp,2)
162         tmp(253:264,l) = transpose(interp1([1,2,11,12],[tmp(253,l)
,tmp(254,l),tmp(263,l),tmp(264,l)],[1:12]));
163     end
164
165     projsRefStat(:,:,ii,iScan) = removeOutliers(tmp,
settingsOutliers);
166
167     if iScan==nsets % last scan has an additional set of reference
images
168         tmp = zeros(size(raw),'single');
169         for indRef = 1:round((numRef-1)/2)
170             number = refnumbers{ii}(indRef);
171             raw = imageReader(getFileName(darknumbers(1)-round((
numRef-1)/2)-1+indRef-numFlats));
172             if binningFactor~=1
173                 raw = imresize((raw-dark)./(emptys{1}-dark),1/
binningFactor);
174             else
175                 raw = (raw-dark)./(emptys{1}-dark);
176             end
177             tmp = tmp+raw;
178         end
179         tmp = tmp/round((numRef-1)/2);

```

```

180
181         for l=1:size(tmp,1) % treat detector gaps
182             tmp(1,253:263) = interp1([1,2,10,11],[tmp(1,253),tmp
(1,254),tmp(1,262),tmp(1,263)], [1:11]);
183             tmp(1,512:522) = interp1([1,2,10,11],[tmp(1,512),tmp
(1,513),tmp(1,521),tmp(1,522)], [1:11]);
184         end
185         for l=1:size(tmp,2)
186             tmp(253:264,1) = transpose(interp1([1,2,11,12],[tmp(
253,1),tmp(254,1),tmp(263,1),tmp(264,1)], [1:12]));
187         end
188
189         projsRefStat(:, :, ii, iScan+1) = removeOutliers(tmp,
settingsOutliers);
190     end
191 end
192
193     for indRef = 1:numRef
194         number = refnumbers{3}(indRef);
195         if (iScan==nsets)
196             raw = imageReader(getFileName(413+15+number+(numAngles+
numFlats+doRef*(2*numRef-1))*(iScan-1)));
197         else
198             raw = imageReader(getFileName(number+(numAngles+numFlats+
doRef*(2*numRef-1))*(iScan-1)));
199         end
200
201         if binningFactor~=1
202             raw = imresize((raw-dark)./(emptys{1}-dark), 1/
binningFactor);
203         else
204             raw = (raw-dark)./(emptys{1}-dark);
205         end
206         thetasRef(indRef, iScan) = wwas(getDumpName(number+(numAngles+
numFlats+doRef*(2*numRef-1))*(iScan-1)), rotMotor);
207
208         for l=1:size(raw,1) % treat detector gaps
209             raw(1,253:263) = interp1([1,2,10,11],[raw(1,253),raw(1,254
),raw(1,262),raw(1,263)], [1:11]);
210             raw(1,512:522) = interp1([1,2,10,11],[raw(1,512),raw(1,513
),raw(1,521),raw(1,522)], [1:11]);
211         end
212         for l=1:size(raw,2)
213             raw(253:264,1) = transpose(interp1([1,2,11,12],[raw(253,1)
,raw(254,1),raw(263,1),raw(264,1)], [1:12]));

```

```

214         end
215
216         projsRef(:, :, indRef, iScan) = removeOutliers(raw,
settingsOutliers);
217     end
218 end
219
220 % read projection data
221 for indProj = 1:numAngles
222     % initialize
223     raw = zeros(size(raw));
224     x = 0;
225
226     % read images and average
227     number = rawnumbers(indProj);
228     for indRaw = 1:numAverage
229         % read it
230         if (iScan==nsets)
231             tmpFrame = imageReader(getFileName(413+15+number+(indRaw-1
)+(numAngles+numFlats+doRef*(2*numRef-1))*(iScan-1)));
232         else
233             tmpFrame = imageReader(getFileName(number+(indRaw-1)+(
numAngles+numFlats+doRef*(2*numRef-1))*(iScan-1)));
234         end
235
236         raw = raw + tmpFrame;
237         x=x+1;
238     end
239     raw = raw / x;
240
241     fprintf('In Tomo % 4i Winkel % 4i von % 4i gelesen\n', iScan, indProj,
numAngles);
242
243     % linear empty correction
244     anteil = (indProj-1)/(numAngles-1);
245     empty = (1-anteil)*emptys{1} + anteil*emptys{2};
246
247     % write projections to array
248     if binningFactor~=1
249         raw = imresize((raw-dark)./(empty-dark), 1/binningFactor);
250     else
251         raw = (raw-dark)./(empty-dark);
252     end
253
254     for l=1:size(raw,1) % treat detector gaps

```

```

255         raw(1,253:263) = interp1([1,2,10,11],[raw(1,253),raw(1,254),
raw(1,262),raw(1,263)], [1:11]);
256         raw(1,512:522) = interp1([1,2,10,11],[raw(1,512),raw(1,513),
raw(1,521),raw(1,522)], [1:11]);
257     end
258     for l=1:size(raw,2)
259         raw(253:264,l) = transpose(interp1([1,2,11,12],[raw(253,l),raw
(254,l),raw(263,l),raw(264,l)], [1:12]));
260     end
261
262     projs(:,:,indProj,iScan) = raw;
263
264     if (iScan==nsets)
265         thetas(indProj,iScan) = wwas(getDumpName(413+15+number+(indRaw
-1)+(numAngles+numFlats+doRef*(2*numRef-1))*(iScan-1)),rotMotor);
266     else
267         thetas(indProj,iScan) = wwas(getDumpName(number+(indRaw-1)+(
numAngles+numFlats+doRef*(2*numRef-1))*(iScan-1)),rotMotor);
268     end
269
270 end
271
272 projsFilt(:,:,:,iScan) = projs(:,:,:,iScan);
273 settingsOutliers.threshold = 1.5; % remove hotpixel
274 parfor indProj=1:numAngles
275     projsFilt(:,:,indProj,iScan) = removeOutliers(projs(:,:,indProj,
iScan),settingsOutliers);
276 end
277 end
278
279 %% Match projection angles for the different scans
280 for iScan=1:nsets
281     if doRef == 1
282         for indRef = 1:numRef
283             thetasIdx(indRef,iScan) = find(round(thetas(:,iScan),2)==round
(thetasRef(indRef,2),2),1);
284         end
285     end
286 end
287
288 for iScan=1:nsets
289     % do shift correction with reference projections - assume linear drift
290     if doRef == 1
291         projsShift = projsFilt;
292         settings = struct;

```

```

293     settings.upsampling = 5;
294     settings.cutLeft = 275;
295     settings.cutRight = 275;
296     settings.cutTop = 270;
297     settings.cutBottom = 20;
298     settings.sigmaLowpass = 0;
299
300     [~,shifts(:,iScan+1),~,~] = alignImages(projsRefStat(:, :, 1, iScan+1
301 ),projsRefStat(:, :, 1, iScan),settings);
302
303     shiftsInterpV = interp1q([1 numAngles].',[shifts(1,iScan) shifts(1
304 ,iScan+1)].',[1:numAngles].');
305     shiftsInterpH = interp1q([1 numAngles].',[shifts(2,iScan) shifts(2
306 ,iScan+1)].',[1:numAngles].');
307
308     projsRC(:, :, :, iScan) = projsShift(:, :, :, iScan);
309     parfor indProj=1:numAngles
310         projsRC(:, :, indProj, iScan) = shiftRotateImage(projsShift(:, :,
311 indProj, iScan), [shiftsInterpV(indProj),shiftsInterpH(indProj)], 0);
312         disp(indProj);
313     end
314 end
315
316 %% First check aligned projections
317 if doRef == 1
318     iSet = 1;
319     for indRef = 1:numRef
320         subplot(2,1,1)
321         showImage(projsRef(:, :, indRef, iSet))
322         caxis([0.2373 0.3104])
323         subplot(2,1,2)
324         showImage(projsShift(:, :, thetasIdx(indRef, iSet), iSet))
325         caxis([0.2373 0.3104])
326         title('before reference shift')
327         pause(1)
328         showImage(projsRC(:, :, thetasIdx(indRef, iSet), iSet))
329         caxis([0.2373 0.3104])
330         title('after reference shift')
331         pause(1)
332     end
333 end
334
335 %% Then replace and average
336 if doRef == 1

```

```

334     projsShift = projsRC;
335 end
336 projsAve = median(projsShift,4);
337 thetas = double(squeeze(median(thetas,2)));
338
339 %% Save projections
340
341 %% Align rotation axis manually - roughly
342 % determine parameters manually
343 shiftAxis = 0;
344 shifty = 0;
345 detectorTilt = 0;
346
347 settings.shiftx = shiftAxis;
348 settings.shifty = shifty;
349 settings.tiltAngle = detectorTilt;
350 proj0Degrees = projsRefStat(:, :, 1, 1);
351 proj180Degrees = projsRefStat(:, :, 2, 1);
352
353 % check result
354 showImage(checkRotaxis(proj0Degrees,proj180Degrees,settings));
355
356 %% Recommended: align rotation axis via tomographic reconstruction
357 slicenumber1 = -200;
358 slicenumber2 = 200;
359 x = 0;
360
361 for xxx = -8:8
362     %% position of rotation axis and detector tilt
363     %find out the shift of the rotation axis by comparing different shifts
364     for
365         %a slice ABOVE the vertical center
366         shiftAxis = shiftx+xxx;
367
368         projsAstra = circshiftSubPixel(projsAve,[0 shiftAxis 0]);
369
370         % offset indicates the position relative to the central line
371         settingsAstra.offset = slicenumber1; % exchange for slicenumber2
372         settingsAstra.outputSize = 774;
373
374         tic
375         x = x+1; disp(x)
376         slicesTmp{x} = astraFDK(projsAstra,thetas,z01,z02,dx*1000,
377             settingsAstra);
378         toc

```

```

377 end
378
379 %% Find the correct rotation axis shift by visual inspection
380 figure(1)
381 showImage(-imgaussfilt(slicesTmp{28},1.5))
382 title(sprintf('Current rotation axis shift: %4.1f + %4.1f',shiftx,xxx))
383 colormap gray; zoom(1.3);
384
385 %% Tilt projections: enter shifts here
386 shift1 = 0; % shift at slicenumber1
387 shift2 = 0; % shift at slicenumber2
388 detectorTilt = atand((shift1-shift2)/(slicenumber1-slicenumber2));
389 shiftAxis = 0; % shift in central slice
390
391 clear projs
392 parfor indProj = 1:size(projsAve,3)
393     disp(indProj);
394     projs(:,:,indProj) = shiftRotateImage(projsAve(:,:,indProj), [0,
        shiftAxis], detectorTilt);
395 end
396
397 %% Save final projections
398
399 %% determine geometric parameters - Fresnel number
400 % source-sample distance
401 z01 = wwas(getDumpName(numFirstangle),'sx') + z01Corr;
402
403 % effective pixel size
404 M = z02/z01;
405 dx = binningFactor*dx;
406 dx_eff = dx/M;
407
408 % effective propagation distance
409 z12 = (z02-z01)/1000;
410 z_eff = z12/M;
411
412 % weighted mean energy of the x-ray spectrum in keV (timepix @20cm)
413 E = 9.11; % see Eckermann et al., JMI (2020)
414 lambda = 12.398/E*1e-10; % wave length
415
416 % Fresnel number:
417 F = dx_eff^2/(lambda*z_eff);
418 fprintf('Fresnel number: %4.5f\n',F);
419 save('parameters.mat','thetas','z01','z02','dx','F');
420

```

```

421 %% PHASE RECONSTRUCTION
422 % with BAC, according to HoloTomoToolbox-scripts
423
424 %% Are the horizontal stripes in the sinogram mitigated?
425 sinoPre=squeeze(projsAve(round(end/2),:,:));
426 sinoPost=sinoPre;
427 sinoPost(sinoPost==inf)=max(sinoPost(sinoPost~=inf));
428 sinoPost = sinoPost-repmat(mean(sinoPost,2),1,size(sinoPost,2));
429
430 figure(1)
431 subplot(2,1,1)
432 showImage(sinoPre)
433 title('Before correction');
434 subplot(2,1,2)
435 showImage(sinoPost)
436 title('After correction');
437
438 %% If yes, run this
439 for k=1:size(projsAve,1)
440     sino=squeeze(projsAve(k,:,:));
441     sino(sino==inf)=max(sino(sino~=inf));
442     projsAve(k,:,:) = sino-repmat(mean(sino,2),1,size(sino,2));
443 end
444
445 %% TOMO-RECONSTRUCTION
446 % according to HoloTomoToolbox-scripts
447
448 %% Save reconstructed slices
449 %% Recommendation: smoothen slices
450 filterSigma = 0.9; % standard deviation in pixels
451 slicesF = imgaussfilt3(slices,filterSigma);

```

Code A.9: Matlab script for PC-CT reconstruction of TINa data.

A.3 Measurements and Analysis of the X-ray Spectrum

The analysis scheme in this section has been developed together with Dr. Anna-Lena Robisch.

Characterization of the X-ray Spectrum As a part of the commissioning process of the TINa setup, the source spectrum was characterized under consideration of air scattering and photon sensitivity of the imaging detector.

The X-ray spectrum was assessed with an energy-resolving XR-100CdTe detector (Amptek, Bedford) with a sensor thickness of 1 mm, positioned at a distance z_{Amptek} from the source. A first measurement series served the calibration of the spectral bins. To this end, reference materials such as molybdenum (Mo) or nickel (Ni) foils, with $K_{\alpha} = 17.48$ keV and $K_{\alpha} = 7.48$ keV respectively [10], are suitable. The entrance window of the energy-resolving detector was positioned at 90° with respect to the optical axis, and the foils at 45° , in order to access their fluorescence signal in absence of the X-ray source spectrum. Subsequently, with the detector in parallel (*i.e.* at 0°) and foils removed, the source spectrum itself was recorded. Hereby, settings such as z_{Amptek} , exposure time and gain were chosen to meet a considerable photon flux.

The analysis script of the data is outlined in Code A.10. In the first part, the detector bins are assigned energy levels in [keV] according to the calibration measurements. As a next step, tabulated X-ray properties of air, as the propagation medium, and the sensor material of the imaging detector are included, based on either β from the complex refractive index or the absorption coefficient μ [15]. The energy bins of the tabulated values are then rescaled to match the bins of the energy-resolving detector, and utilized to calculate the energy-dependent absorption proportion according to Beer-Lambert's law [15]. Finally, the recorded X-ray spectrum is corrected for the difference in propagation path (since the energy-resolving and the imaging detector most probably are positioned at $z_{\text{Amptek}} \neq z_{02}$), and the sensor material efficiency.

```

1 %% Geometric configuration:
2 zAmptek = 1; % source-Amptek distance in m
3 z02 = 0.2; % source-Imaging detector distance in m
4 z01 = 1e-3; % source-sample distance in m
5
6 %% Load & scale spectrum measured by amptek
7 filename = 'tina_spektrum_gain20_300sec.txt';
8 fid = fopen(filename);
9 data = textscan(fid,'%f %f %f', 'CollectOutput',true);
10 countsAmptek = data{1}(1:end,1);
11 fclose('all');
12
13 % Utilize calibration data points
14 Ni = [252.05 7.48]; % Ni line Channel, Ni line [keV]
15 Mo = [532.69 17.48]; % Mo line Channel, Mo line [keV]
16

```

```

17 % bin width in keV
18 binsE = (Mo(2)-Ni(2)) / (Mo(1)-Ni(1));
19
20 % energy axis
21 energyAmptek = linspace(0, 2048, 2048) * binsE; % Number of channels
    Amptek: 2048
22 offsetAmptek = 1.0 ;
23 energyAmptek = [energyAmptek(1:end)]' - offsetAmptek;
24
25 % normalize spectrum
26 countsAmptek = countsAmptek / max(countsAmptek);
27
28 %% Load & process tabulated transmission in air
29 % CXRO - beta -> linear attenuation coefficient:  $\mu = 4\pi\beta/\lambda$ 
30
31 % read in data
32 filename = 'IndexRefraction_Air_CXRO.txt';
33 fid = fopen(filename);
34 data = textscan(fid,'%f %f %f', 'CollectOutput',true);
35 betaCXRO = data{1}(1:end,3);
36 energyCXRO = data{1}(1:end,1)*1e-3; % keV
37 muCXRO = 4*pi*betaCXRO./(1.2398e-9./energyCXRO);
38 fclose('all');
39
40 % extract relevant mu
41 idx = find(energyCXRO >= 30 , 1, 'first'); % 30 keV is the cutoff for
    tabulated data
42 energyCXRO = energyCXRO(1 : idx);
43 muCXRO = muCXRO(1 : idx);
44
45 % interpolate to linear energy axis
46 EAir = []; muAir = [];
47 binWidth = min(diff(energyCXRO));
48
49 for currBin = 1 : numel(energyCXRO)-1
50     currBinWidth = energyCXRO(currBin+1) - energyCXRO(currBin);
51     scale = currBinWidth / binWidth;
52     ETmp = energyCXRO(currBin : currBin+1);
53     muTmp = muCXRO(currBin : currBin+1);
54     ETmp = imresize(ETmp, [scale,1],'bilinear');
55     muTmp = imresize(muTmp, [scale,1],'bilinear');
56     for iii = 1 : numel(ETmp)
57         EAir = [EAir ETmp(iii)];
58         muAir = [muAir muTmp(iii)];
59     end

```

```

60 end
61
62 % remove data points that are of the same value
63 [EAir,ia,ic] = unique(EAir,'first');
64 muAir = muAir(ia);
65
66 %% Adjust tabulated data for absorption in air to amptek spectrum
67 countsAmptek = countsAmptek + 0.1;
68
69 % crop Amptek spectrum
70 idx = find(energyAmptek >= EAir(1),1,'first');
71 energyAmptek = energyAmptek(idx:end);
72 countsAmptek = countsAmptek(idx:end);
73 countsAmptek(energyAmptek > EAir(end)) = 0;
74 energyAmptek(energyAmptek > EAir(end)) = 0;
75 energyAmptek = nonzeros(energyAmptek);
76 countsAmptek = nonzeros(countsAmptek) - 0.1;
77
78 % interpolate absorption coefficient to used number of bins in amptek
79 % spectrum
80 EAir = imresize( EAir, [1, numel(energyAmptek)], 'bilinear');
81 muAir = imresize( muAir, [1, numel(energyAmptek)], 'bilinear');
82
83 % compute detection efficiency of imaging detector
84 deltaDefocusDistance = zAmptek-z02;
85 transmissionAir = exp(-muAir*deltaDefocusDistance)';
86
87 %% Load & process imaging detector specifications
88 % CXRO - beta -> linear attenuation coefficient:  $\mu = 4\pi\beta/\lambda$ 
89
90 % read in data
91 filename = 'IndexRefraction_Si_CXRO.txt'; % make sure to use the same
    energy bins or adjust skript accordingly
92 fid = fopen(filename);
93 data = textscan(fid,'%f %f %f', 'CollectOutput',true);
94 betaCXRO = data{1}(1:end,3);
95 energyCXRO = data{1}(1:end,1)*1e-3; %keV
96 muCXRO = 4*pi*betaCXRO./(1.2398e-9./energyCXRO);
97 fclose('all') ;
98
99 % extract relevant mu
100 idx = find(energyCXRO >= 30 , 1, 'first'); % 30 keV is the cutoff for
    tabulated data
101 energyCXRO = energyCXRO(1 : idx);
102 muCXRO = muCXRO(1 : idx);

```

```

103
104 % interpolate to linear energy axis
105 EDet = []; muDet = [];
106 binWidth = min(diff(energyCXRO));
107
108 for currBin = 1 : numel(energyCXRO)-1
109     currBinWidth = energyCXRO(currBin+1) - energyCXRO(currBin);
110     scale = currBinWidth / binWidth;
111     ETmp = energyCXRO(currBin : currBin+1);
112     muTmp = muCXRO(currBin : currBin+1);
113     ETmp = imresize(ETmp, [scale,1], 'bilinear');
114     muTmp = imresize(muTmp, [scale,1], 'bilinear');
115     for iii = 1 : numel(ETmp)
116         EDet = [EDet ETmp(iii)];
117         muDet = [muDet muTmp(iii)];
118     end
119 end
120
121 % remove data points that are of the same value
122 [EDet,ia,ic] = unique(EDet,'first');
123 muDet = muDet(ia);
124
125 %% Adjust tabulated data for absorption coefficient (imaging detector) to
    amptek spectrum
126 % interpolate absorption coefficient to the number of used bins in amptek
    % spectrum
127 EDet = imresize( EDet, [1, numel(energyAmptek)], 'bilinear');
128 muDet = imresize( muDet, [1, numel(energyAmptek)], 'bilinear');
129
130
131 % compute detection efficiency of imaging detector
132 sensorThickness = 500e-6;
133 efficiency = 1 - exp(-muDet*sensorThickness)';
134
135 %% normalize spectrum wrt spectrum at Imaging detector
136 countsAmptek = countsAmptek / max((2-transmissionAir).*countsAmptek);
137
138 %% compute weighted spectrum
139 weightedCounts = (2-transmissionAir).*efficiency.*countsAmptek;

```

Code A.10: Matlab code to compute the imaging spectrum.

Plotting the X-ray Spectra In order to visualize the effect of the aforementioned corrections on the X-ray spectrum, the originally measured spectrum and the one with corrections applied are plotted together. Further, the respective mean weighted energy

is specified. The implementation is detailed in Code A.11.

```

1 %% plot spectrum
2 figure(1); clf
3 xlabel('Energy [keV]')
4 ylabel('I/I_{max}')
5 axis([4.5 max(energyAmptek) 0 1])
6
7 % weighted mean energy
8 weightedMeanE = sum(energyAmptek.*countsAmptek) / sum(countsAmptek);
9 line([weightedMeanE weightedMeanE], [0 1], 'color', 'k', 'LineWidth', 1.5,
    'LineStyle', '--');
10 info = sprintf('%.2f%s', string(weightedMeanE) , ' keV');
11 set(0,'defaultAxesFontSize',12)
12 text(15.5,0.85,info,'Color',[0.4 0.4 0.2]);
13 hold on
14
15 airWeightedMeanE = sum((2-transmissionAir).*countsAmptek.*energyAmptek) /
    sum((2-transmissionAir).*countsAmptek);
16 line([airWeightedMeanE airWeightedMeanE], [0 1], 'Color','k', 'LineWidth',1.
    5, 'LineStyle', '--');
17 info = sprintf('%.2f%s', string(airWeightedMeanE) , ' keV');
18 text(14.4,0.75 ,info,'Color',[0.2 0.4 0.4]);
19
20 effWeightedMeanE = sum((2-transmissionAir).*efficiency.*countsAmptek.*
    energyAmptek) / sum((2-transmissionAir).*efficiency.*countsAmptek);
21 line([effWeightedMeanE effWeightedMeanE], [0 1], 'Color','k', 'LineWidth',1.
    5, 'LineStyle', '--');
22 info = sprintf('%.2f%s', string(effWeightedMeanE) , ' keV');
23 text(11.8,0.61,info,'Color',[0.5 0.5 0]);
24
25 % normalize spectra
26 countsAmptek = countsAmptek / max((2-transmissionAir).*countsAmptek);
27
28 plot(energyAmptek,countsAmptek,'LineWidth',2,'Color',[0.4 0.4 0.2]);
29 plot(energyAmptek,(2-transmissionAir).*countsAmptek,'LineWidth',2,'Color'
    ,[0.2 0.4 0.4]);
30 plot(energyAmptek,(2-transmissionAir).*efficiency.*countsAmptek,'LineWidth
    ',2,'Color',[0.5 0.5 0]);
31 text(17,0.5,'Measured spectrum','Color',[0.4 0.4 0.2]);
32 text(17,0.4,'Spectrum corrected for air','Color',[0.2 0.4 0.4]);
33 text(17,0.3,'Spectrum weighted by efficiency','Color',[0.5 0.5 0]);

```

Code A.11: Matlab code to plot the imaging spectrum.

Dose Calculation The computation of the dose in Code A.12 is based on the preceding spectrum characterizations and the utilization of a photon-counting imaging detector, but may be adjusted accordingly if either of these is not fulfilled.

Based on a flat field image from the (tomographic) scan and the X-ray spectrum, the photon flux in the imaging detector plane z_{02} and from that in the sample plane z_{01} is calculated.

The dose D is defined as the overall absorbed energy, hence

$$D = \sum_E \frac{I_0 t E}{d(E) \cdot \rho A} \cdot N_{\text{proj}} N_{\text{tomos}},$$

with flux I_0 , exposure time per projection t , sample density ρ and illuminated area A , number of tomographic projections N_{proj} and number of tomographic scans N_{tomos} . Note that the energy spectrum E and the stopping power $d(E)$ are Matlab arrays. As in Code A.10, tabulated values are used as input for $d(E)$, including rescaling of energy intervals.

```

1 %% Get imaging detector flat field & total number of photons
2 flat = ...;
3 countedPhotons = sum(flat(:));
4
5 %% Remove weight from spectrum
6 exposureTime = 5; % exp. time of flat in s
7 rateImDet = countedPhotons * weightedCounts / (exposureTime * sum(
8     weightedCounts));
9 fluxImDet = sum(rateImDet); % ph/s in detector plane
10 % to account for sample-detector path in air
11 rateSample = countedPhotons * (2-exp(-muAir*(z02-z01))) .* countsAmptek /
12     (exposureTime * sum((2-exp(-muAir*(z02-z01))) .* countsAmptek));
13 fluxSample = sum(rateSample); % ph/s in sample plane
14
15 %%
16 fprintf(sprintf('%s%.2f%s\n', 'total number of detected mega-photons per
17     second ', fluxImDet/1e6, ''))
18 fprintf(sprintf('%s%.2f%s\n', 'total number of mega-photons per second in
19     sample plane ', fluxSample/1e6, ''))
20
21 %% Estimate dose
22 I_0 = fluxSample; % ph/s
23 t = exposureTime; % exp. time in s
24 E = (2-exp(-muAir*(z02-z01))) .* countsAmptek .* energyAmptek; % get
25     energy from spectrum
26 rho = ...; % density sample in kg/m3

```

```

22 numPixelX = 774; % number of pixels Imaging detector
23 numPixelY = 516;
24 px = 55e-6; % physical pixel size
25 FOV = numPixelX*numPixelY*(px/z01)^2;
26 numProjs = ...; % projections per tomo
27 numTomos = ...; % number of tomo scans
28
29 %% Get stopping power
30 fid = fopen(...); % txt-file
31 data = textscan(fid,'%f %f %f', 'CollectOutput',true);
32 stoppingCXRO = data{1}(1:end,2);
33 energyCXRO = data{1}(1:end,1)*1e-3; % in keV
34 fclose('all');
35
36 % extract relevant mu
37 idx = find(energyCXRO >= 30 , 1, 'first'); % 30 keV is the cutoff for
    tabulated data
38 energyCXRO = energyCXRO(1:idx);
39 stoppingCXRO = stoppingCXRO(1:idx);
40
41 % interpolate to linear energy axis
42 ESample = []; stoppingSample = [];
43 binWidth = min(diff(energyCXRO));
44
45 for currBin = 1 : numel(energyCXRO)-1
46     currBinWidth = energyCXRO(currBin+1) - energyCXRO(currBin);
47     scale = currBinWidth / binWidth;
48     ETmp = energyCXRO(currBin : currBin+1);
49     muTmp = muCXRO(currBin : currBin+1);
50     ETmp = imresize(ETmp, [scale,1],'bilinear');
51     muTmp = imresize(muTmp, [scale,1],'bilinear');
52
53     for iii = 1 : numel(ETmp)
54         ESample = [ESample ETmp(iii)];
55         stoppingSample = [stoppingSample muTmp(iii)];
56     end
57 end
58
59 % remove data points that are of the same value
60 [ESample,ia,ic] = unique(ESample,'first');
61 stoppingSample = stoppingSample(ia);
62
63 % interpolate absorption coefficient to used number of bins in amptek
64 % spectrum
65 ESample = imresize( ESample, [1, numel(energyAmptek)], 'bilinear');

```

```
66 stoppingSample = imresize( stoppingSample, [1, numel(energyAmptek)], '  
    bilinear');  
67  
68 %% Compute total dose  
69 D = I_0*t*E./(stoppingSample*rho*FOV) *numProjs*numDists
```

Code A.12: Matlab code to compute the total dose (based on the previously computed spectrum).

Bibliography

- [1] L. Banci and I. Bertini. *Metallomics and the Cell*. Springer, 2013.
- [2] M. Bartels, M. Krenkel, P. Cloetens, W. Möbius, and T. Salditt. “Myelinated mouse nerves studied by X-ray phase contrast zoom tomography.” In: *Journal of Structural Biology* 192.3 (2015), pp. 561–568.
- [3] D. Bourassa, S.-C. Gleber, S. Vogt, H. Yi, F. Will, H. Richter, C. H. Shin, and C. J. Fahrni. “3D imaging of transition metals in the zebrafish embryo by X-ray fluorescence microtomography.” In: *Metallomics* 6.9 (2014), pp. 1648–1655.
- [4] P. Chen, M. R. Miah, and M. Aschner. “Metals and neurodegeneration.” In: *F1000Research* 5 (2016).
- [5] M. Chukalina, A. Simionovici, A. Snigirev, and T. Jeffries. “Quantitative characterization of microsamples by x-ray fluorescence tomography.” In: *X-Ray Spectrometry: An International Journal* 31.6 (2002), pp. 448–450.
- [6] G. D. Ciccotosto, S. A. James, M. Altissimo, D. Paterson, S. Vogt, B. Lai, M. D. de Jonge, D. L. Howard, A. I. Bush, and R. Cappai. “Quantitation and localization of intracellular redox active metals by X-ray fluorescence microscopy in cortical neurons derived from APP and APLP2 knockout tissue.” In: *Metallomics* 6.10 (2014), pp. 1894–1904.
- [7] M. D. De Jonge and S. Vogt. “Hard X-ray fluorescence tomography—an emerging tool for structural visualization.” In: *Current opinion in structural biology* 20.5 (2010), pp. 606–614.
- [8] C. Grochowski, E. Blicharska, P. Krukow, K. Jonak, M. Maciejewski, D. Szczepanek, K. Jonak, J. Flieger, and R. Maciejewski. “Analysis of trace elements in human brain: its aim, methods, and concentration levels.” In: *Frontiers in Chemistry* 7 (2019), p. 115.
- [9] S. Hametner, I. Wimmer, L. Haider, S. Pfeifenbring, W. Brück, and H. Lassmann. “Iron and neurodegeneration in the multiple sclerosis brain.” In: *Annals of Neurology* 74.6 (2013), pp. 848–861.

- [10] B. Henke, E. Gullikson, and J. Davis. *X-ray interactions: photoabsorption, scattering, transmission, and reflection at $E=50\text{--}30000\text{ eV}$, $Z=1\text{--}92$* , Atomic Data and Nuclear Data Tables. Database 2. Center for X-Ray Optics, Lawrence Berkeley National Laboratory, 1993.
- [11] H. M. Hertz, J. C. Larsson, U. Lundström, D. H. Larsson, and C. Vogt. “Laboratory x-ray fluorescence tomography for high-resolution nanoparticle bio-imaging.” In: *Optics letters* 39.9 (2014), pp. 2790–2793.
- [12] P. J. La Riviere, P. Vargas, M. Newville, and S. R. Sutton. “Reduced-scan schemes for X-ray fluorescence computed tomography.” In: *IEEE Transactions on Nuclear Science* 54.5 (2007), pp. 1535–1542.
- [13] L. M. Lohse, A.-L. Robisch, M. Töpperwien, S. Maretzke, M. Krenkel, J. Hagemann, and T. Salditt. “A phase-retrieval toolbox for X-ray holography and tomography.” In: *Journal of Synchrotron Radiation* 27.3 (2020).
- [14] C. J. Maynard, R. Cappai, I. Volitakis, R. A. Cherny, A. R. White, K. Beyreuther, C. L. Masters, A. I. Bush, and Q.-X. Li. “Overexpression of Alzheimer’s disease amyloid- β opposes the age-dependent elevations of brain copper and iron.” In: *Journal of Biological Chemistry* 277.47 (2002), pp. 44670–44676.
- [15] D. Paganin et al. *Coherent X-ray optics*. 6. Oxford University Press on Demand, 2006.
- [16] M. Rajan, K. J. Rao, B. Mamatha, R. Rao, P. Shanmugavelu, R. B. Menon, and M. Pavithran. “Quantification of trace elements in normal human brain by inductively coupled plasma atomic emission spectrometry.” In: *Journal of the Neurological Sciences* 146.2 (1997), pp. 153–166.
- [17] T. Salditt, M. Osterhoff, M. Krenkel, R. N. Wilke, M. Priebe, M. Bartels, S. Kalbfleisch, and M. Sprung. “Compound focusing mirror and X-ray waveguide optics for coherent imaging and nano-diffraction.” In: *Journal of Synchrotron Radiation* 22.4 (2015), pp. 867–878.
- [18] C. G. Schroer. “Reconstructing x-ray fluorescence microtomograms.” In: *Applied Physics Letters* 79.12 (2001), pp. 1912–1914.
- [19] R. Solutions. *EasyTom Nano*. 2021.
- [20] H. Spatz. “Über den Eisennachweis im Gehirn, besonders in Zentren des extrapyramidal-motorischen Systems. I. Teil.” In: *Zeitschrift für die gesamte Neurologie und Psychiatrie* 77.1 (1922), pp. 261–390.

-
- [21] M. Töpperwien, M. Krenkel, D. Vincenz, F. Stöber, A. M. Oelschlegel, J. Goldschmidt, and T. Salditt. “Three-dimensional mouse brain cytoarchitecture revealed by laboratory-based x-ray phase-contrast tomography.” In: *Scientific Reports* 7.1 (2017), pp. 1–8.

Author Contributions

Author Contributions Chapter 2 The manuscript was written by M. Eckermann and T. Salditt, with input from M. Töpperwien, A.-L. Robisch and C. Stadelmann. The experiment and data analysis were performed by M. Eckermann and A.-L. Robisch, guided by T. Salditt. Tissue samples were provided by F. v.d. Meer and C. Stadelmann.

Author Contributions Chapter 3 The manuscript was mainly written by M. Eckermann and T. Salditt, with substantial input from P. Cloetens and C. Stadelmann. The experiments were performed by M. Eckermann, with valuable support by P. Cloetens. Data analysis was conducted by M. Eckermann, with substantial input by T. Salditt. Murine tissue samples were provided by T. Ruhwedel and W. Möbius, and human tissue samples by F. v.d. Meer and C. Stadelmann, along with data interpretation.

Author Contributions Chapter 4 The manuscript was mainly written by M. Eckermann and T. Salditt, with substantial input from B. Schmitzer and C. Stadelmann. The experiments were performed by M. Eckermann and T. Salditt. Data analysis was performed by M. Eckermann, guided by T. Salditt and B. Schmitzer. Optimal transport analysis was designed by B. Schmitzer. Machine-learning tools were provided by O. Hansen. Samples and neuropathological data interpretation were contributed by F. v.d. Meer, J. Franz and C. Stadelmann.

Author Contributions Chapter 5 The manuscript was written by M. Eckermann and T. Salditt, with input from T. Ruhwedel and W. Möbius. X-ray experiments were performed by M. Eckermann and T. Salditt. SEM-imaging was conducted by T. Ruhwedel. Data analysis was performed by M. Eckermann and T. Ruhwedel. Samples were provided by T. Ruhwedel and W. Möbius.

List of Publications

- M. Eckermann, B. Schmitzer, F. van der Meer, J. Franz, O. Hansen, C. Stadelmann & T. Salditt. 3d Virtual Histology of the Human Hippocampus based on Phase-Contrast Computed-Tomography. PNAS 118.48 (2021).
- M. Eckermann, T. Ruhwedel, W. Möbius & T. Salditt. Towards Correlative Imaging of Neuronal Tissue by Phase-Contrast X-ray Tomography and SEM. Developments in X-Ray Tomography XIII. International Society for Optics and Photonics Vol. 1184005 (2021).
- M. Eckermann, F. van der Meer, P. Cloetens, T. Ruhwedel, W. Möbius, C. Stadelmann & T. Salditt. 3d Virtual Histology of the Cerebral Cortex based on Phase-Contrast X-ray Tomography. Biomedical Optics Express 12.12 (2021): 7582-7598.
- J. Kemppainen, B. Scales, K. R. Haghighi, J. Takalo, N. Mansour, J. McManus, G. Leko, P. Saari, J. Hurcomb, A. Antohi, J.-P. Suuronen, F. Blanchard, R. C. Hardie, Z. Song, M. Hampton, M. Eckermann, F. Westermeier, J. Frohn, H. Hoekstra, C.-H. Lee, M. Huttula, R. Mokso & M. Juusola. Binocular Mirror-Symmetric Microsaccadic Sampling Enables Drosophila Hyperacute 3D-Vision. PNAS (2022, in press).
- B. Veress, N. Peruzzi, M. Eckermann, J. Frohn, T. Salditt, M. Bech & B. Ohlsson. The Structure of the Myenteric Plexus in Normal and Diseased Human Ileum Analyzed by Three-Dimensional X-ray Tomography. (under review).
- M. Eckermann, N. Peruzzi, J. Frohn, M. Bech, E. Englund, B. Veress, T. Salditt, L.B. Dahlin & B. Ohlsson. 3d Phase-Contrast Nanotomography of Unstained Human Skin Biopsies May Identify Morphological Differences in the Dermis and Epidermis between Subjects. Skin Research and Technology 27.3 (2021): 316-323.
- M. Eckermann*, J. Frohn*, M. Reichardt*, M. Osterhoff, M. Sprung, F. Westermeier, A. Tzankov, M. Kühnel, D. Jonigk & T. Salditt. 3d Virtual Patho-Histology of Lung Tissue from Covid-19 Patients based on Phase Contrast X-ray Tomography. Elife 9 (2020): e60408.

* shared first authorship

- K. Joppe, J.-D. Nicolas, T. A. Grünwald, M. Eckermann, T. Salditt & P. Lingor. Elemental Quantification and Analysis of Structural Abnormalities in Neurons from Parkinson's-diseased Brains by X-ray Fluorescence Microscopy and Diffraction. *Biomedical Optics Express* 11.7 (2020): 3423-3443.
- H. M. Kjer, M. Andersson, Y. He, A. Pacureanu, T. Salditt, M. Eckermann, M. Töpperwien, M. L. Elkjær, Z. Illes, B. Pakkenberg, M. Ptito, V. Andersen Dahl, A. Bjorholm Dahl & T. B. Dyrby. Multiscale - Multimodal Brain Imaging: Combining MRI and X-ray Synchrotron Radiation Imaging Reveals Axon Crossing as Sheet-like Laminars by Non-Straight Axon Fasciculi Trajectories. (in preparation).
- N. Peruzzi, B. Veress, L.B. Dahlin, T. Salditt, M. Andersson, M. Eckermann, J. Frohn, A.-L. Robisch, M. Bec & B. Ohlsson. 3D Analysis of the Myenteric Plexus of the Human Bowel by X-ray Phase-Contrast Tomography – a Future Method?. *Scandinavian Journal of Gastroenterology* 55.10 (2020): 1261-1267.
- G. E. Barbone, A. Bravin, A. Mittone, A. Pacureanu, G. Mascio, P. Di Pietro, M. J. Kraiger, M. Eckermann, M. Romano, M. H. De Angelis, P. Cloetens, V. Bruno, G. Battaglia & P. Coan. X-ray Multiscale 3D Neuroimaging to Quantify Cellular Ageing and Neurodegeneration Post-Mortem in a Model of Alzheimer's Disease. (under review).
- A.-L. Robisch, M. Eckermann, M. Töpperwien, F. van der Meer, C. Stadelmann & T. Salditt. Nanoscale X-ray Holotomography of Human Brain Tissue with Phase Retrieval based on Multienergy Recordings. *Journal of Medical Imaging* 7.1 (2020): 013501.
- M. Eckermann, M. Töpperwien, A.-L. Robisch, F. van der Meer, C. Stadelmann & T. Salditt. Phase-Contrast X-ray Tomography of Neuronal Tissue at Laboratory Sources with Submicron Resolution. *Journal of Medical Imaging* 7.1 (2020): 013502.
- M. Eckermann, M. Töpperwien, T. Ruhwedel, W. Möbius & T. Salditt. Evaluation of Different Heavy-Metal Stains and Embedding Media for Phase Contrast Tomography of Neuronal Tissue. *Developments in X-Ray Tomography XII. International Society for Optics and Photonics* Vol. 11113. (2019).
- M. Osterhoff, A.-L. Robisch, J. Soltau, M. Eckermann, S. Kalbfleisch, D. Carbone, U. Johansson & T. Salditt. Focus Characterization of the NanoMAX Kirkpatrick-Baez Mirror System. *Journal of Synchrotron Radiation* 26.4 (2019): 1173-1180.

- E. H. Yang, J. Rode, M. A. Howlader, M. Eckermann, J. T. Santos, D. Hernandez Armada, R. Zheng, C. Zou & C. W. Cairo. Galectin-3 Alters the Lateral Mobility and Clustering of β 1-Integrin Receptors. PLoS One 12.10 (2017): e0184378.
- M. Bernhardt, J.-D. Nicolas, M. Eckermann, B. Eltzner, F. Rehfeldt & T. Salditt (2017). Anisotropic X-ray Scattering and Orientation Fields in Cardiac Tissue Cells. New Journal of Physics 19.1 (2017): 013012.

Danksagung

An dieser Stelle möchte ich mich bei vielen Menschen bedanken, die auf verschiedene Weisen entscheidend zu dieser Arbeit beigetragen haben.

Zuallererst möchte ich mich ganz besonders bei Prof. Dr. Tim Salditt für dieses spannende Dissertationsthema, seine herausragende Betreuung, die tolle Infrastruktur in der Arbeitsgruppe, und das entgegengebrachte Vertrauen bedanken. Tim, deine Begeisterungsfähigkeit hat mich stets motiviert, und deine besondere Art, Dinge zu betrachten inspiriert.

Außerdem möchte ich Prof. Dr. Christine Stadelmann-Nessler für die Co-Betreuung und das Gutachten dieser Arbeit danken, ganz besonders aber für die tolle Kollaboration: vielen Dank für die spannenden neurowissenschaftlichen Projekte, und die Einblicke die ich dadurch gewinnen durfte, sowie das Zurverfügungstellen der wertvollen humanen Proben.

Ich möchte mich auch bei Prof. Dr. Sarah Köster für die tolle Co-Betreuung bedanken. Besonders die persönliche Förderung weiß ich wirklich zu schätzen.

Prof. Dr. Bernhard Schmitzer danke ich für die Bereitschaft, diese Arbeit zu prüfen, aber besonders für seinen spontanen und engagierten Einstieg in das Alzheimerprojekt, was durch seinen Beitrag der Optimaler-Transport-Analyse entscheidend geprägt wurde.

Auch Prof. Dr. Florentin Wörgötter und Prof. Dr. Stefan Klumpp danke ich für das Prüfen dieser Arbeit.

Ich möchte mich beim gesamten Institut für Röntgenphysik für die außergewöhnliche wissenschaftliche und soziale Atmosphäre bedanken. Jeder Einzelne trägt dazu bei, und dafür möchte ich mich wirklich bei jedem bedanken. Seien es wissenschaftliche Diskussionen oder Veranstaltungen, gemeinsame Pausen oder sonstige Aktivitäten, mit euch habe ich die Zeit immer genossen. Ich bin stolz, Teil des Instituts sein zu dürfen!

Besonders bei den intensiven Phasen der Messzeiten, ob in Grenoble, Lund oder Hamburg, konnte ich durch euch so viel lernen, und es war unterm Strich zwar eine harte,

aber auch immer schöne Zeit. Besonders möchte ich Markus Osterhoff, Jan Goemann, Jasper Frohn, Jan-David Nicolas, Anna-Lena Robisch, Mareike Töpferwien, Jakob Reichmann, Jannis Schaeper und meinen Bürokollegen Marius Reichardt hervorheben. Wenn es um GINIX-Messzeiten geht, dürfen natürlich auch nicht Fabian Westermeier und Michael Sprung fehlen, vielen Dank euch beiden! Auch Kerstin Pluschke, Eva Hetzel und Michaela Ständer danke ich. Danke an Thomas Jentschke, Jakob Frost und Ove Hansen für die Unterstützung in der Datensegmentierung. Für die vielen Stunden gemeinsamer Laborarbeit, sei es an Tomographieaufbauten oder auch bei der Probenpräparation, danke ich Susanne Hengst, Bastian Hartmann, Mike Kanbach, Peter Luley und Jochen Herbst.

Zudem möchte ich mich auch bei der Gemeinschaft des Hertha Sponer Colleges bedanken.

Mein ganz herzlicher Dank gilt Franziska van der Meer. Ich denke gerne an unsere gemeinsamen Diskussionen mit Tim und Christine zurück. Franziska, deine Begeisterungsfähigkeit für Mikroglia und Oligodendrozyten hat mich wirklich inspiriert, und ist stets eine Quelle der Motivation für mich.

Bei Torben Ruhwedel und Wiebke Möbius bedanke ich mich für die tolle Kollaboration rund um gefärbtes Neurogewebe.

Ich möchte mich für die tolle Unterstützung beim Verfassen dieser Arbeit, durch Korrekturlesen wie durch fachliche Diskussionen, bedanken bei Mareike Töpferwien, Johannes Hagemann, Leon Lohse, Charlotte Neuhaus, Linda Rojin, Lydia Maus, Malte Vassholz, Carolina Thomas und Chiara Cassini.

Zu guter Letzt möchte ich mich bei den mir nahestehenden Personen, insbesondere meiner gesamten Familie, bedanken, die immer aufrichtig für mich da sind. Mein besonderer Dank gilt hier Florian Eckermann für seine bedingungslose Unterstützung. Kerstin und Heiner Eckermann, Mama und Papa, neben eurer andauernden Unterstützung habt ihr mir schon früh Werte wie Zielstrebigkeit und Urteilsvermögen vermittelt - ohne die Ausdauer, die ich dadurch gelernt habe, wäre diese Arbeit nicht möglich gewesen. Ich bin euch zutiefst dankbar.

Curriculum Vitae

Marina Eckermann

Born on 10 April 1993 in Göttingen

Education and Professional Experience

- 07/2020 - 10/2021 *Member of the Hertha Sponer College (HSC)*
Multiscale Bioimaging Cluster of Excellence
- 10/2017 - 10/2021 *Doctoral Studies in Physics*
Georg-August-Universität, Göttingen
Institut für Röntgenphysik
Group of Prof. Dr. Tim Salditt
- 02 - 03/2017 *Guest Scientist*
European Synchrotron Radiation Facility (ESRF), Grenoble (Fr)
- 01 - 03/2016 *Academic Research Internship*
University of Alberta, Edmonton (CA)
U. of Alberta Research Experience (UARE), Faculty of Chemistry
- 04/2015 - 09/2017 *Master of Science in Physics*
Ludwig-Maximilians-Universität, München
with special qualification in Medical Physics
Title of thesis: "Development of advanced image processing
methods for X-ray phase contrast neuro-CT experiments"
- 10/2014 - 03/2015 *Industrial Research Internship*
Carl Zeiss Meditec AG, Oberkochen
- 10/2011 - 08/2014 *Bachelor of Science in Physics*
Georg-August-Universität, Göttingen
Title of thesis: "Scanning small-angle X-ray diffractive imaging of
cardiomyocyte cells"
- 06/2011 *Abitur*, Grotefend-Gymnasium Münden, Hann. Münden

To bring physiology and pathology of the human brain into better micro-anatomical and histological context, studies with different methodologies are required. Established techniques such as electron microscopy or histology show limitations in view of invasiveness, labor-intensive and artifact-prone sample preparation, as well as an adequate ratio between resolution and volume throughput. For this reason, X-ray phase-contrast tomography (PC-CT) has been proposed as a three-dimensional non-destructive imaging technique, which requires less effort in sample preparation and can assess larger volumes. Furthermore, it offers quantitative electron density based contrast even for unstained tissue. Up to now, however, PC-CT studies fell short in number of samples, so that structural alterations caused by neurodegenerative diseases cannot be distinguished from physiological inter-subject variations.

In this thesis, the scalability of PC-CT with respect to the required number of samples and resolution-to-volume-throughput is demonstrated, and the methodology is advanced with respect to data acquisition, processing and segmentation. In addition to the human cerebellum, cortex and hippocampus are studied. Concerning quantification and analysis of PC-CT data, this work introduces optimal transport analysis to obtain quantitative metrics of the cyto-architecture and to identify changes due to neurodegenerative diseases. For the case of Alzheimer's disease, this workflow reveals a yet undescribed compactification of granular cells in the human hippocampus. This thesis also provides optimized configurations to study neural tissues with laboratory instrumentation, and – finally – provides new correlative imaging approaches, in particular with scanning electron microscopy.



GEORG-AUGUST-UNIVERSITÄT
GÖTTINGEN

ISBN 978-3-86395-528-1
ISSN 2191-9860
eISSN 2512-6326

Universitätsverlag Göttingen